Maine Marine Composites

2 Portland Fish Pier, Suite 211
Portland, ME 04101-4699
tel: 207.774.9616
fax: 207.221.1416
www.mainemarinecomposites.com

PROJECT TITLE:	
Fatigue Design Methodologies Applicable to Complex Fixed and Floating Offshore Wind Turbines	
Client/Client Ref: Bureau of Safety and Environmental Enforcement	Document Title: Final Report
Project No: Contract E13PC00019	Project Document No: E13PC00019_Final_Report.docx

Rev.	Effective Date	Description	Made by	Checked by	Approved by
0	08-Sept-15	Draft Final Report	All	RHA/KT/CG	
	11-Sept-15	Final Report	All	RHA/KT/CG	

NOTES:

Contents

1 Abstract

This document is the Final Report delivered under BSEE Contract E13PC00019.

This report begins by summarizing historical work in fatigue mechanisms such as abrasion, corrosion and snap loads, especially as applied to steel chains and wire ropes. The report describes four case studies in which software tools were used to simulate prototype floating offshore wind turbine systems (FOWT) in an attempt to predict motions, fatigue damage and extreme strains to the mooring components on such system. The project team used several different software tools, NREL FAST, Orcina OrcaFlex, Ocean Dynamics Charm3D and ANSYS Aqwa to perform these analyses. Results from these software tools were compared with each other and with measured data in order to evaluate the effectiveness of these tools. A special study was performed using corrosion and abrasion data provided by the USCG on their Aid to Navigation (ATON) buoys, and new techniques for predicting material loss through corrosion and abrasion mechanisms were demonstrated. Finally conclusions and recommendations are provided regarding the difficulty of predicting the fatigue life and failure mechanisms in FOWT mooring systems using existing software tools.

2 Introduction

This project is focused on one renewable energy technology that has captured a great deal of attention within the United States and worldwide: floating offshore wind turbines (FOWT). These systems consist of a wind turbine, a tower, a floating structure, and a mooring system. Typically they are moored in relatively shallow water, 50m to 300m deep. Unique aspects of the FOWT mooring system that challenge applicability of established offshore mooring practices are:

1. Economics: The emerging FOWT industry cannot afford to use the heavy, complex components prescribed for oil industry applications. Similarly the affordability of expensive mooring laying vessels is doubtful. Thus mooring and foundation systems that are made up of standard components and installed in a straightforward manner should be given preference.
2. Platform size: FOWT are significantly lighter platforms compared to conventional O&G platforms and provide real-estate allowance for minimal infrastructure. This has important consequences, including lack of tensioning winches and storage for excess mooring lines.
3. Water depth: FOWT operate in shallower waters than typical offshore platforms. This has important consequences on mooring line length and distance between the platform and anchors. Importantly, the pre-tension that can be supported by shorter lines is less.
4. Site permitting: Environmental regulations and permitting is a complex bureaucratic process, which may not give due regard to design conditions ideally suited for deployment of a mooring system. Consequently, mooring lines and foundation systems may be subject to significant wear.

Two key factors that can affect fatigue life of FOWT mooring systems have been identified and focused on in this project: snap (shock) loads and chain abrasion. Failure modes in shallow-water mooring systems include the fatigue of chain links near the touchdown point, long-term damage due to cyclic and shock-induced tension variation, and damage due to the abrasion of the laid length dragging transversely on the seafloor.

A straightforward way to estimate fatigue damage can be implemented by the rainflow counting method, which was introduced by Matsuishi and Endo (1968). From the tension history of mooring line, the stress cycles are calculated and the rainflow counting method is used to give an estimate of fatigue damage.

The fatigue accumulation is then computed by the linear Palmgren-Miner law based on specific S-N curves as Equation (1).

$$D(t) = \sum_i \frac{n_i S_i^m}{\alpha} \qquad (1)$$

where n_i is the number of stress cycle ranges and S_i, α and m are material-dependent S-N curve parameters. Both the rainflow method for counting tension cycles and the Palmgren-Miner rule for cumulatively calculating for fatigue damage can be performed using software developed for fatigue analysis. However, the effect of impulsive snap events on fatigue life, and the ability of the standard assessment methods to incorporate these effects are not well known.

One possible approach to include the snap effects is to use a dual narrow-band approach such as recommended by DNV (OS-E301). DNV's suggestion is to use this approach for wave frequency and low frequency ranges weighted by a correction factor that depends on the stress ranges. Similarly, low cycle high stress range effect like snap loads could be incorporated. This approach was attempted in some of the software tools used in this project.

2.1 Project Goals

A major challenge in the design of FOWTs is predicting the life of the mooring system. Most analysis tools for the study of fatigue of FOWT are developed as hybrids of software for floating structures with aerodynamics codes that were developed initially for land-based wind turbines, and later migrated to fixed-support wind turbines in coastal waters. Mooring analysis in many of the software tools are rudimentary and focused on the ultimate strength requirements needed to withstand an extreme environment. It is crucial to evaluate the ability of these software tools to predict fatigue induced failures, incorporating unique factors described above.

The original goals of the project are

1. Evaluate fatigue design criteria for offshore wind turbine support structures,
2. Study fatigue design methodologies applicable to complex fixed and floating offshore wind turbines support structures, and
3. Recommend a rational, practical, fatigue design method for offshore wind turbine support structures.

These goals translated into searching answers for the following questions:

- Are existing design methods capable of predicting the fatigue life of mooring systems for Floating Offshore Wind Turbines (FOWT)?
- As implemented in commercial software analysis tools, are these methods complete and accurate?
- Is there sufficient and accurate environmental data so that existing software tools can predict fatigue life accurately?

To answer these questions the following tasks were executed:

- A list of software design tools and systems was created:
  - Software tools had to be available for commercial use.
  - The tools should be the most common choice for domestic and international companies.
  - The project team had to be able to acquire the software tools for use in the project.
- A set of FOWT case studies were identified to test the software tools.
  - Published design information had to be available for each case study
  - Performance information including FOWT motion and mooring line tension had to be available for each case study

- Design tools were used to model the individual FOWT designs and results were compared with measured data provided by project partners.
- Observations and conclusions were made regarding the ability of existing design tools to predict the fatigue life of FOWT designs. Those observations and conclusions include:
    - Accuracy of predictions from design tools
    - Ease or difficulty in using design tools, including barriers to providing accurate input data.
    - Recommendations for future research topics related to the fatigue life and failure modes of FOWT mooring systems.
    - Comments on the accuracy and completeness of classification society design rules. Suggestions for changes or possible improvements to the rules.

2.2 Case Studies

Four case studies were selected for this report:

- Kabashima Island Spar FOWT. A 1KW scale model was deployed in a small harbor in Japan, and the performance results were published. The project team modeled this FOWT using Aqwa/OrcaFlex+FAST and succeeded in predicting motion and fatigue life. The team attempted to model this FOWT using Charm3D, but with limited success. The team continues to speak with the developers of Charm3D to try to simulate the spar FOWT successfully. The team has been communicating with Prof. Utsunomiya at Kyushu University about collaborative research projects and data exchanges.
- USCG Aid to Navigation Buoy (ATON). The design team has been working with the USCG to collect data on the chain mooring systems on ATON buoys. The USCG provided data from the logs of the USCG Abbie Burgess and chain samples cut from retrieved chain assemblies. The project team has simulated the seafloor motion of the chain to model the chain abrasion. The simulations were time consuming and the results were open to interpretation, but the decision was made to use this data for model calibration, and then to test the model using data collected from the USCG Willow in Baltimore next month.
- DeepCwind Semi-Submersible. The behavior of the 1/50th Scale model is well documented and data is available from the University of Maine. The DeepCwind model was tested in the MARIN tank, and the performance data has been scaled to model a full-size turbine system. The project team was successful in modeling and simulating the motion of the DeepCwind semisubmersible, and in estimating the fatigue life of this system. Two software systems were used in this case study, Aqwa/OrcaFlex+Fast and Charm3D+Matlab. Further, the time-domain tension data imported into the WAFO toolbox to predict the fatigue damage of the system, so three different fatigue analysis tools were employed in total
- VolturnUS 1/8-Scale Semi-Submersible. The next step in the University of Maine ASCC floating offshore wind project was to build and deploy a 1/8 scale model of the targeted

2MW system. The large scale prototype was constructed and deployed near Castine, Maine for about a year. This project team built simulation models of the 1/8-scale FOWT and worked with the ASCC laboratory to analyze field data collected from the 1/8-scale system. Fully-coupled versions of OrcaFlex+FAST and Charm3D+FAST were used to analyze the system and results compared favorably with measure data provided by the University of Maine.

The project team ran extensive simulations and analyses in each case study, exploring the impact of fatigue on the design of the system. Various fatigue methodologies were tested including classical fatigue analysis using the Miner-Palmgren hypothesis. Fatigue in the mooring system on a full-scale model of the DeepCwind FOWT was calculated using the methods described in the American Petroleum Institute (API) standard RP 2SK including frequency-domain and time-domain based algorithms. There was wide variation in fatigue life predictions using the different methods. Furthermore there was significant variation in fatigue life predictions using the same method as implemented using different software tools.

The project team devoted significant resources to studying the effects of seafloor abrasion on mooring chains. As there are no mooring system software packages that model this effect directly, scripts were developed to use the OrcaFlex system to study the effect of abrasion on shortened fatigue life. An energy-based algorithm was developed and demonstrated. This algorithm uses existing marine motion simulation software to predict abrasion loss in catenary mooring chains.

3 Slack lines and Snap Loading

A light displacement platform (e.g. FOWT) in shallow water, supported by mooring lines with light to moderate pre-tension, can be exposed to slack line events (line tension close to zero) and hence snap loads during re-engagement. Snap type impact indicates a spike in tension following a slack event over a very short duration. Limited research has been conducted to study snap events on mooring lines of FOWTs in the past (Masciola et al., 2013). In the context of marine operations, DNV (1996) defines a criterion to avoid snap condition on a crane wire lifting or lowering an object into the sea. The total force on the wire is described as:

$$F_{total} = F_{st} \pm F_{dyn} \quad (2)$$

where F_{st} is the static force and F_{dyn} is the dynamic force on the wire. DNV (2011) allows for a 10% margin for safety and defines the criteria to avoid snap loads as:

$$F_{dyn} \leq 0.9F_{st} \quad (3)$$

Following DNV (2011) a criterion to avoid snap condition in mooring lines as:

$$T \leq 0.9T_0 \quad (4)$$

Where subscript 0 denotes static or pre- tension in a mooring line.

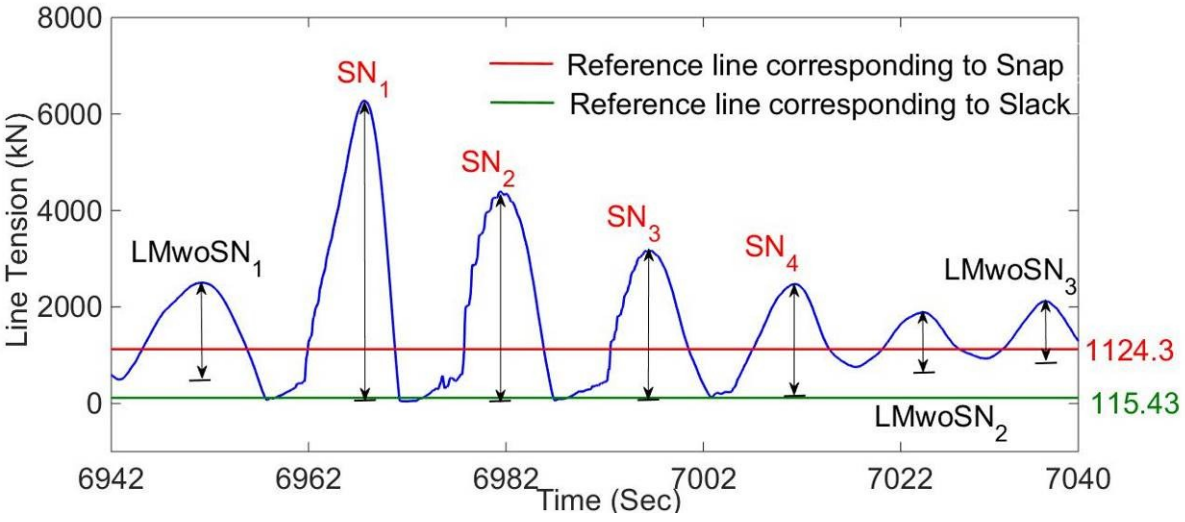

Figure 1 Sample experimental time history of mooring line tension.

Figure 1 illustrates a sample time history of line tension vs. time from experimental test data for a semi-submersible FOWT in a 100 year storm condition. The static pretension in the line is 1124.3 kN. A slack condition is defined to occur when line tension is less than 112.4 ± 3 kN ($10 \pm 0.3\%$ of F_{st}). The allowance of 0.3% accounts for some variation in the mean tension noted

in the experiments. A snap condition can be defined to occur when the tension in the mooring line goes from a slack condition to a value greater than the static tension (1124 kN). More description of this condition may be found in Hsu et al. (2015).

The effect of snap loads on fatigue life is an important issue when designing offshore floating systems. Both over-prediction and under-prediction of the fatigue life can lead to unexpected costs and consequences. Liu (1981) has observed that, although the measured snap load in the Open Diving Bell (ODB) handling system was low, the ODB handling system was not safe for long-term operation in sea-states two or higher due to its short fatigue life. Niedzwecki and Thampi (1991) have observed a marine cable system should be able to sustain one or more snap load cycles without a catastrophic cable breakage. However, these snap load cycles can be expected to reduce the useful life of the cable components of the system. Salancy et al. (1997) have observed that the hawsers used to connect tankers to the SPM buoys can have severe fatigue problems, and they can cause serious problems when they break by snapping back. The authors have also suggested that hawsers should be replaced every six months to avoid fatigue problems. Gobat and Grosenbaugh (2001) have noted that snap loads and increased chain wear along the bottom may decrease the fatigue life, requiring the design life to be shortened or that heavier mooring materials be used. The authors have also found that loading shocks, which lead to snap loads, only occurred in storm excitation conditions. Unloading shocks occurred in both calm and storm conditions, though wear on the mooring lines was likely to be less in mild conditions.

In order to get a clear picture of the mooring line failure, many statistical methods have been used to predict the fatigue failure probability. Some researchers have sought to define safety factors for mooring line systems. Liu (1981) has observed that snap loading has a high probability of occurrence even at low sea-states in at-sea tests of diving bell operations. Hovde and Moan (1997) have proposed a probabilistic failure approach for TLPs which estimates the probability of failure directly instead of assuming that an accepted probability level is achieved by the use of safety factors. A case study shows that the probability of failure due to extreme tension or fatigue is roughly of the order of 0.6% for 25 years. Shah et al. (2005) have showed that for both slack and taut mooring systems, the probability of failure increases for more narrow-banded sea-states. Heredia-Zavoni (2012) has provided a brief description of fatigue limit states and the failure of a mooring line due to fatigue. The author has made an important assertion about the complex coupling between fatigue limit states and ultimate limit states. Large consequences can occur when a number of pre-damaged mooring lines fail during an extreme event and lead to the failure of the entire mooring system. For this reason, the risk assessment for the fatigue limit state must also account for the probability of failure associated with the ultimate limit state because the undamaged mooring lines will experience an increased demand during the extreme event due to the failures of the pre-damaged lines. This connection could be relevant for snap events, because the snap can inherently weaken the mooring line, thus causing it to fail prematurely in an extreme event.

4 Corrosion and Abrasion: Historical Review

Experience has demonstrated several factors that are significant in mooring system failure. Allan et al. (2013) makes note of the fact that line failures typically occur at higher rates in the early and late stages of mooring lifetime. Kiecke and Zhang (2011) have conducted a study of the Constitution truss spar in the Gulf of Mexico and concluded that the estimated fatigue damage accumulated in winter and sudden storms over a 20 year period account for only 20% of the damage that was seen in the most severe 10 hour period of Hurricane Ike.

Ma (2013) observes that in many cases of mooring line failure, the failure mechanism was previously unknown or unconsidered, including out-of-plane bending, chain twisting, poor welding, and pitting. While innovation in mooring technology appears to be rare due to desire for risk aversion, Fletcher et al. (2010) have outlined advancements to improved strength, creep, corrosion and wear behavior. These high level observations demonstrate the need for developing an understanding of failure and fatigue mechanisms for floating offshore wind technology.

4.1 Corrosion Allowances in Offshore Mooring Design

Mooring degradation due to corrosion and abrasion is accounted for in many offshore standards in the form of an annual diameter reduction rate. Corrosion and abrasion are designed for in current operating codes and standards by increasing mooring chain size to offset a predicted material loss to corrosion and abrasion.

These diameter reduction rates, summarized in Table 1 for several of the most applicable offshore standards for floating offshore wind turbines, are very broad in their scope. There is rarely distinction between corrosive and abrasive degradation, and no accounting for the diversity of degradation mechanisms that exist in different regions of the world.

A review of applicable standards and code requirements shows that a typical range of corrosion and abrasion rate allowance is from 0.2 to 0.4 mm/yr. in the splash zone and touchdown zone, and allowances of 0.1 to 0.3 mm/yr. in the catenary zone (DNV-OS-E301; API-RP-2SK). A more stringent requirement of 0.8 mm/yr. for the Norwegian continental shelf is called for in DNV-OS-E301. BS6349-1 recommends water temperature and mollusk presence be accounted for as well.

Table 1: Summary of design allowances for corrosion and abrasion from several offshore classification societies.

Reference		Diameter Reduction Guidelines	Notes
Class NK OFWT Section 6.2.6	Splash Zone	0.2-0.4 mm/yr.	
	Mid-Line	0.1-0.2 mm/yr.	
	Seafloor Contact Zone	0.2-04 mm/yr.	
DNV OS-E301 Section E200	Splash Zone	0.4 mm/yr.	Assuming ROV inspection according to DNV-OSS-102 Ch.3 Sec.6 B800
	Catenary	0.3 mm/yr.	
	Bottom	0.4 mm/yr.	
	Splash Zone	0.2 mm/yr.	Assuming inspection according to DNV-OSS-102 Ch.3 Sec.6
	Catenary	0.2 mm/yr.	
	Bottom	0.3 mm/yr.	
	Splash Zone	0.8 mm/yr.	Norwegian Shelf
	Catenary	0.2 mm/yr.	
	Bottom	0.2 mm/yr.	
ABS FOWT Chapter 8 Section 3	Use allowances suggested in API RP 2SK		
API RP 2SK Section 7.6	Splash Zone	0.2-0.4 mm/yr.	
	Mid-Line	0.1-0.2 mm/yr.	
	Thrash Zone	0.2-0.4 mm/yr.	

A number of sources (such as Fontaine et al, 2012; Morandini et al, 2009) have suggested that the corrosion and abrasion allowances in current operating standards and recommended practices are not conservative and in some cases inadequate. Examining a case study in West African waters, Fontaine et al (2012) concluded that:

> "The corrosion losses for the chain links are much higher than predicted from corrosion rates recommended in existing codes and Class Rules. If confirmed by further investigations this suggests that revision of code rules may be appropriate, including allowances also to account for effects such as seawater temperature, water velocity and water quality."

DNV-OS-E304 indicates that wire rope mooring components must be protected in such a way that corrosion is not significant and that "…fatigue life approaches that in air." This is to be done through a combination of sacrificial coating, blocking compound, and sheathing or jacketing.

Guidelines for replacement of mooring components due to excessive corrosion or abrasion are discussed in DNV-OSS-101 and DNV-OS-E301. DNV-OS-E301 indicates that soil contact is unacceptable for fiber rope. Otten and Leite (2013) discuss a case study in which fiber mooring lines contacted the seabed during installation. Furthermore DNV-OSS-101 indicates that for mooring chain, a cross-sectional area loss of 81% (corresponding to a 10% diameter loss) due to corrosion or abrasion requires replacement of the link.

Fatigue S-N curves for different mooring components are discussed in DNV-OS-E301 and an S-N curve is shown in Figure 2. Comparable T-N curves are discussed in API-RP-2SK.

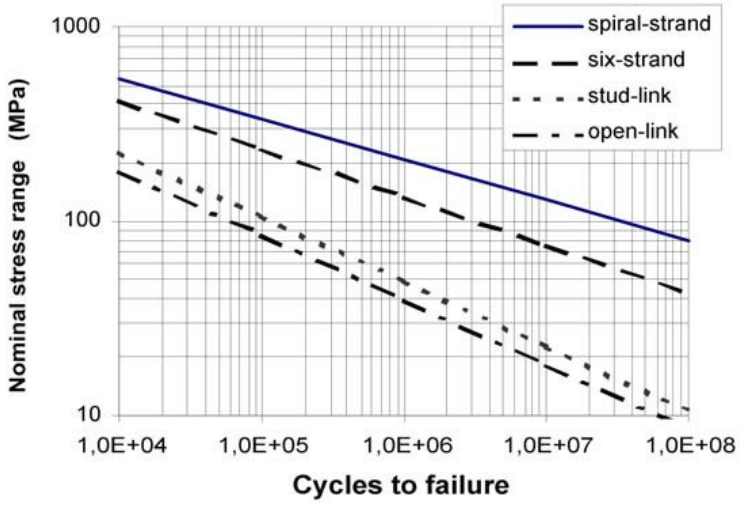

Figure 2: S-N curve for mooring fatigue (DNV-OS-E301).

4.2 Mooring Chain

4.2.1 Factors Contributing to Corrosion

Corrosion damage can occur in a number of forms. Uhlig (1985) identifies five main types of corrosion. Of primary significance in offshore applications are *uniform corrosion*, which refers to rust and tarnishing damage that occurs uniformly over a surface, *pitting corrosion*, which is more localized, and *corrosive fatigue*, which occurs when corrosion works in tandem with cyclical fatigue stresses. Uniform corrosion is typically reported as a rate, such as mm/year. Uhlig (1985) suggests that, very broadly, a corrosion rate less than 0.15 mm/year is typically acceptable, while a corrosion rate greater than 1.5 mm/year is not acceptable. Anything in between this range is suitable with proper design.

Pitting is a localized corrosion that forms pockets which can be shallow or deep, and wide or narrow (Uhlig, 1985). This can be reported with a pitting factor, which is the ratio of pit depth to the uniform corrosion depth. Pitting can also occur when fretting corrosion takes place.

In a corrosive environment, metals do not benefit from the fatigue limit that they enjoy elsewhere, and so the presence of a corrosive environment will cause failure if cyclical stresses are applied, no matter how large the amplitude of the stresses (Uhlig, 1985). Similarly, a metal may fail when a constant stress is applied in a corrosive environment (the loads or stresses need not be cyclic).

Corrosion impacts the strength of mooring systems by degrading the chain and increasing the stresses upon the system. Standards for offshore mooring design do not adequately account for environmental factors when providing guidance on rates of corrosion.

A number of mechanisms leading to corrosion are identified in the literature. These include water temperature, oxygen concentration, water flow velocity, nitrogen content, water depth, and microbiologically influenced corrosion (Fontaine et al, 2009; Melchers, 2005; Fontaine et al, 2012). Note that some of these factors are related. For example nitrogen content increases microbiologically influenced corrosion (MIC), and water depth is related to dissolved oxygen

content. The splash zone has been identified as the area of most significant corrosion from dissolved oxygen (Duggal and Fontenot, 2010; Figure 9). Brown (2013; Figure 10) has found, through inspection of an FPSO, that locations of flash welds are vulnerable to pitting corrosion.

Both the temperature and average velocity of water have significant impacts on corrosion rates. Higher water velocity has the effect of increasing corrosion rate in the early stages by influencing how rust layers are able to develop. Mean water temperature has been found to have an exponential effect on the corrosion rate (Melchers, 2005). The effect of temperature on corrosion is significant throughout the entire exposure life.

The rates at which microbiologically influenced corrosion occurs is explored by Melchers and Wells (2006) using a theoretical approach. Corrosion governed by microbiological factors occurs in later phases, once a rust layer has developed. The limiting factor for microbiologically influenced corrosion is in the availability of nutrients. The nutrient effect occurs primarily in the later phases of corrosion, after significant exposure time on the order of several years. This includes a transient stage and a steady state stage, as well as an intermediate transition between the two. While significant theoretical development is presented, the experimental data appears to be fairly limited and therefore any mathematical or empirical models that may be developed to predict corrosion rates at these stages will suffer from significant uncertainty.

Stiff et al (1996) have shown that corrosion can reduce lifetimes of mooring chains by up to three times, and seems to lead to different failure mechanisms than chain fatigue in air.

Fontaine et al (2009) have found, through empirical modeling of steel wire ropes, that corrosion rate is exponentially dependent on water temperature, and linearly dependent on dissolved oxygen concentration and water flow velocity. Also important is the rope location in the water (splash zone, catenary zone, etc.). Another model of corrosion over time for offshore steel is developed by Melchers (2005). This work shows that corrosion behavior over time is broken into five discrete phases, in each of which corrosion is governed by different mechanisms and follows a different trend.

Observations of several offshore systems such as in West African waters (Fontaine et al, 2012) have shown that measured corrosion rates have occurred at higher rates than rates laid out in various recommended practices. This floating production unit has experienced a 35% reduction in cross-sectional area of mooring chain links due to corrosion, which was found to correspond to a decrease in strength to 80-90% of the original breaking load. The conclusion of Fontaine et al (2012) is that locally high nitrogen content in the water has increased MIC.

4.2.2 Prediction of Corrosion

A review of corrosion prediction models for offshore systems is presented by Melchers (2008). A predictive model is presented (also discussed by Melchers, 2005) that treats corrosion as a random variable, neglecting preventative measures. The model divides corrosion into four phases. The first phase occurs over the first days-weeks of exposure of the metal to seawater when the chemical processes that lead to rust build up are initiated. In the next two phases a rust layer develops. The limiting factor in determining how quickly rusting occurs is the availability of oxygen. The key chemical reaction is the oxidation of iron. At some point the build-up of rust makes oxygen less readily available.

The later phases are controlled by bacterial corrosion. It is suggested that Sulphate-Reducing Bacteria (SRB) cause the most significant corrosion damage. SRB live in anaerobic conditions and

require nutrients including iron, carbon, and nitrogen. Nitrogen is considered the rate-limiting factor. It is through the metabolism of SRB that corroding elements are produced.

In addition to uniform corrosion, pitting corrosion models are discussed by Melchers (2008). Pitting corrosion prediction is approached from a statistical perspective, where it is clear that the key factor in terms of strength loss is the depth of the largest pit. This may be predicted using extreme value statistics.

In another paper by Melchers, Moan, and Gao (2007), a predictive model is described that is directly applicable to mooring chain. The inherent assumption of this model is that the chain is "constantly working," i.e. there is enough motion and tension between chain links that significant rust build-up is prevented. The relative motion between chain links is assumed to cause enough abrasion that most of the rust is removed, and oxygen availability on the steel surface is not inhibited. This assumption is a small step in attempting to predict the interaction between corrosion and abrasion for offshore mooring systems.

Predictive corrosion models have been developed by other authors in the literature as well. Qin and Cui (2003) present a three-stage model for predicting corrosion of steel ship plate. The rate at which corrosion takes place is defined with a Weibull function, and occurs in the following stages:

1. Corrosion protection systems are effective and no corrosion takes place
2. Corrosion accelerates as pitting generates in the flaws of the CPS
3. Corrosion decelerates as the rust layer and biomass build up prevent oxygen diffusion.

Paik, Kim, and Lee (1998) present a similar model which assumes that the length of coating protection may be treated as a normal variable, with an exponentially defined corrosion rate. Nominal parameters for corrosion curves are presented.

Guedes Soares et al. (2005) published a predictive corrosion model for offshore steel, dependent on environmental factors. The baseline model for predicting corrosion is a three-phase model, which is then modified by local environmental factors. Environmental factors considered include salinity, water temperature, dissolved oxygen content, water pH, and water velocity.

4.2.3 Interlink Abrasion

The literature on abrasion and wear of chain mooring systems has proven to be far less complete than for corrosion. A number of causes for abrasion have been reported and hypothesized, though there is limited guidance on how they might be modeled. Some of these mechanisms are discussed below.

Shoup and Mueller (1984) present a thorough case study of mooring failure of a CALM buoy along with experiments that show that wear of the chain links was the failure mechanism. A simple model for prediction of link wear using Archard's wear equation is presented:

$$V = \sum_{i=1}^{N-1} \left(\frac{F_{i+1} + F_i}{2} \right) |\phi_{i+1} - \phi_i| \left(\frac{\pi}{180} \right) (r)(K_i) \quad (5)$$

Where V is the wear volume, F is the chain tension, φ is the roll angle, r is the chain radius, K is a wear coefficient, and N is the number of time steps in the simulation or measurement (Shoup and Mueller, 1984). This equation is dependent on relative motion and tension between chain links, both of which may be simulated using available software tools.

The equation is also dependent upon a wear coefficient that must be calibrated experimentally. However a calibration of the model presented by Shoup and Mueller (1984) from available data sources, such as USCG buoys, would be of value.

Several papers, including Shoup and Mueller (1984) and Yaghin and Melchers (2015), have provided results of experimental testing of interlink chain abrasion. Both of these studies conclude that chain is drastically less susceptible to abrasion when submersed than in air. Yaghin and Melchers (2015) also conclude that breaking strength of chain decreases at a similar rate to the rate of diameter reduction during interlink abrasion.

Shoup and Mueller (1984) experimentally conclude that the wear coefficient is a function of the load applied, which provides additional complication to Archard's Equation. As seen in the equation above, if the wear coefficient is a function of the load applied, then additional nonlinearity is introduced to any wear calculations or predictions.

A report by Brown et al (2010) on a second phase of the Mooring Integrity JIP outlines a more detailed procedure that may be used to estimate wear between mooring chain links. This model is similarly dependent upon Archard's wear equation. The work conducted in this JIP lays out the first practical method for estimating interlink chain abrasion, including providing a practical way to convert from volume degradation, as predicted through Archard's Equation, to diameter loss, as needed for stress calculation.

Tokubuchi and Takayama (2011) have examined methods to encase catenary chain links in rubber, which serves to limit abrasive damage, as well as absorb shocks when chain links are compressed together. This proposal is found to be effective but expensive.

4.3 Fiber & Wire Rope Mooring

4.3.1 Corrosion

Strength loss of wire ropes is predicted by measuring loss of cross-sectional area due to general corrosion and maximum pit depth from pitting corrosion (Melchers, 2005). Strength loss of wire ropes in sea water compared to wire ropes in air has been experimentally measured to be as high as 80% (Potts et al, 1988). However no measured strength loss was found with steel wire ropes immersed in seawater for up to 80 weeks (Potts et al, 1988). A number of sources indicate that the driving mechanism in the amount of strength loss due to corrosion is the degradation of protective zinc. T-N curves developed by Kobayashi et al (1987) show that at high cycles, failure limits of TLP tendons in seawater is significantly lower than in air. However this difference is not observed when either cathodic protection or coatings (or preferably both) are used.

A semi-empirical model is laid out by Fontaine et al (2009) for the rate of zinc dissolution of 6-strand wire rope in seawater. This model describes three phases of galvanization:

1. Protective coating
2. Primarily protective coating with galvanic protection for exposed sections
3. Primarily galvanic protection

The model laid out by Fontaine et al (2009) is dependent on water temperature, oxygen concentration, water velocity, and wire location. Calibrated coefficients of this model are not presented, although the model appears to compare favorably to the available data.

4.3.2 Creep of Fiber Ropes

Elongation leading to creep-rupture is a fatigue mechanism that must be considered for high modulus polyethylene (HMPE) rope and may lead to line failure. Vlasblom and Bosman (2006) have conducted experiments studying elongation percent of various HMPE ropes commonly used in mooring systems. It is recommended that for HMPE mooring systems, a 10% permanent elongation rate be used as a failure criterion. This represents a conservative indication of transition away from steady-state creep and into rapid creep and the beginning of creep rupture. Banfield et al (2005) and Seo et al (1997) have suggested that creep rupture is not a significant factor in high-load fatigue of polyester mooring systems.

4.3.3 External Abrasion

External damage to fiber ropes was simulated by Ayers and Aksu (2011). Findings showed that damage leading to failure of 10% of fibers reduced breaking strength 3.5 times more than allowable margins. The conclusion, therefore, is that any partially damaged subrope should be considered fully damaged. Ridge et al (2001) examine bending fatigue endurance for wire ropes over a number of damaged conditions. Their findings indicate that external abrasion does not contribute a significant reduction to bending fatigue. Abrasion of hawsers on pulleys, rollers, and fairleads was shown by Markussen et al (1984) to be a significant mechanism of fatigue, especially for fixed/seized rollers and fairleads and high contact angles.

Gobat and Grosenbaugh (2001) have studied the behavior of catenary lines in the touchdown zone, finding that at high excitation frequencies the interaction with the seabed causes the catenary line to experience a shock, when the speed at the touchdown exceeds the transverse speed of the mooring line. This finding is applicable both to snap load events and to seafloor abrasion.

4.3.4 Soil Ingression

Soil particle ingression into polyester mooring lines decreases strength by increasing internal abrasion. Ayers and Del Vecchio (2013) cite laboratory decreases in strength of polyester mooring lines of 13-40% due to soil ingression. These rates are observed for clay soil after 100,000 loading cycles. Ayers and Del Vecchio (2013) also discuss observations by Petrobras that indicate strength losses of 20-31% due to soil contamination in mooring rope.

Otten and Leite (2013) report on tests that were carried out to ascertain the remaining strength in a polyester mooring line that was dropped to the seafloor during installation of the Thunder Hawk semi-submersible. While soil ingression was observed during SEM observations, strength and fatigue tests showed that over 90% of the original strength of the line was maintained.

4.3.5 Internal Abrasion

Internal abrasion is a result of relative motion of individual strands of ropes. A varying load due to environmental factors causes a change in helix angle of internal subropes, which leads to relative motion between subropes and induces internal abrasion (Banfield et al, 2005). Compared with external abrasion, the surfaces in contact internally are considered smooth (Seo et al, 1997).

Flory and Banfield (2006) have identified internal abrasion as the critical failure mechanism for polyester ropes, based on the results of the Durability of Polyester Ropes JIP. They have shown that internal abrasion is most severe when low mean tensions and large cycling amplitudes are applied. Due to the nonlinear stretch vs. tension behavior of polyester ropes, internal abrasion under high mean loads is not found to be as significant. This is supported by Ayers and Aksu (2011), who suggest that cyclic loadings from 20-60% of the breaking limit is the optimal operating range.

Banfield et al (2000) suggest that internal abrasion will begin to take effect after millions of cycles, where a typical 20-year offshore mooring installation may experience cycle numbers on the order of 60 million. A comparison of T-N curves and cycles to failure have shown a 50-fold increase in fatigue strength for polyester ropes compared with steel rope (Banfield et al, 2005; Flory and Banfield, 2006). Banfield et al (2005) develop T-N curves for polyester rope and propose a formulaic design curve.

4.4 Inspection

Regular inspection of mooring components is one of the best ways to ensure long term survival. Allen et al (2013) review methodology for inspecting mooring systems for abrasion and corrosion damage. Visual inspections are used to identify potential problems, using ROV or deck inspections. Underwater measurements may establish reductions in cross-sectional area, which can be compared with design expectations in corrosion/abrasion loss. Note that this must be done regularly to establish corrosion and abrasion rates. Finally 3D modeling allows for more detailed FEA analysis. Hall and Trower (2011) note that chain moorings have too many links for individual examination, and therefore support the practice of focusing inspection on splash zone, touchdown zone, and wire connection regions.

5 Project Design

5.1 Data Collection Efforts

A critical component of this project is the collection of real-world data to validate software design tools. Practical difficulty of collecting real world data includes problems with types of sensors, units of data in post-processed data sets, completeness or lack of completeness of datasets (e.g. actual currents and tide levels at time of data), synchronization and completeness of data from different sensor sources, importance of redundancy of sensors with respect to reliable data collection, and care in post-processing data especially with respect to the intended final use of the data. The main obstacle to collecting real-world data is that there are no FOWT wind farms – all of the FOWT efforts are either in the prototype and testing phase or they are concentrated on one or two utility scale floating turbines that only have been deployed for a year or two, thus no reliable information on inspection and replacement of damaged mooring lines. Hence the team resorted to exemplar data from smaller scale cases or similar systems.

The DeepCwind Consortium led by the University of Maine is composed of several academic and industry participants. With the support of the US Department of Energy, the consortium conducted model tests on three generic FOWT structures: a semi-submersible, a spar and a tension leg platform. The semi-submersible data was made available for the study.

In addition, the team searched for data available in the public domain and found considerable information on a spar FOWT that is currently deployed off Kyushu in Japan. This data was utilized in the study.

The research team worked with the United States Coast Guard (USCG) to analyze maintenance data regarding mooring chains on Aid To Navigation (ATON) buoys. This effort has been underway for a number of months and one of the case studies in this report is related to that effort. Even though the ATON data was essentially public and not sensitive from a security standpoint, a lot of effort was spent to identify USCG personnel who could release the appropriate data to the project team. As the USCG does not have an active data collection program as part of its mission objectives, the design team had to be creative with respect to collecting data from multiple sources to form a complete environmental picture of each ATON buoy. Furthermore, as no SW analysis tools exist that an predict the failure modes and fatigue life of single point ATON buoy mooring systems, the team had to develop new ways of analyzing the data.

The project team had an agreement to work with the Univ. of Maine on analyses of the 1/8 scale model VolturnUS FOWT system. The VolturnUS 1:8 is an eighth scale of a 6 MW prototype floating wind turbine that was deployed in Castine, Maine, USA in May 2013, and decommissioned in Sept 2014, for an 18-month autonomous offshore deployment. The goal of the testing was to de-risk the deployment of a full-scale system. A comprehensive instrumentation package monitored key performance characteristics of the system, including turbine power, thrust, hull motions, and metocean conditions. Three sample 1-hour data from various loading conditions were made available for this project.

5.1.1 Scaling Factors

In comparing simulation results with small scale experimental data, scaling factors are important considerations. It is a challenge to develop a scale model of a system as complex as a FOWT

because different physical properties scale at different rates. It is not possible to simultaneously maintain Froude and Reynolds numbers between a full-size and model scale FOWT. Froude number similitude is chosen for FOWT scaling, so that the gravitational effects of waves are maintained, bur special care must be taken to assure that physical characteristics that are Reynolds-scaled phenomena are modeled so as to create the proper forces. As described in Martin (2009) the scaling relationships are determined by three rules:

1. Froude number similitude is employed from prototype to scale model.
2. Froude scaled wind is employed during basin model testing.
3. The wind turbine tip speed ratio, TSR, is to be maintained from prototype to scale model.

The first rule guarantees that the dominant factor in wave mechanics, inertia, is modeled properly. If the turbine dynamics are insensitive to Reynolds phenomena, then the second rule guarantees that the wind force to wave force ratio is maintained from model scale to full size operation. The third rule guarantees that the turbine rotational speed and other system excitation frequencies related to rotor imbalance will scale properly. Further, the third rule results in properly scaled turbine thrust forces and rotor torque. As above, this assumes that the FOWT airfoil section lift and drag coefficients have a low dependence on Reynolds number. Table 2 summarizes the scale factors for various parameters according to these rules.

Table 2 Scale Factors for Floating Offshore Wind Turbines (Martin, 2009)

Parameter	Unit(s)	Scale Factor
Length (e.g. displacement, wave height and length)	L	λ
Area	L^2	λ^2
Volume	L^3	λ^3
Density	M/L^3	1
Mass	M	λ^3
Time (e.g. wave period)	T	$\lambda^{0.5}$
Frequency (e.g. rotor rotational speed, structural)	T^{-1}	$\lambda^{-0.5}$
Velocity (e.g. wind speed, wave celerity)	LT^{-1}	$\lambda^{0.5}$
Acceleration	LT^{-2}	1
Force (e.g. wind, wave, structural)	MLT^{-2}	λ^3
Moment (e.g. structural, rotor torque)	ML^2T^{-2}	λ^4
Power	ML^2T^{-3}	$\lambda^{3.5}$
Stress	$ML^{-1}T^{-2}$	λ
Mass moment of inertia	ML^2	λ^5
Area moment of inertia	L^4	λ^4

A result of this set of scaling rules is that converting wind speed from full size to model scale requires a scale factor of $\lambda^{0.5}$, converting significant wave height requires a scale factor of λ, and converting the wave period requires a scale factor of $\lambda^{0.5}$. For the Survival Load Case which has

very high winds and high seas, the sea height scales by 0.125, while the wind speed scales by the much larger value of 0.354. Accordingly the equivalent storm condition for the 1/8-scale VolturnUS system will appear to have a much higher ratio of wind to waves than does the full-size system, even though the two are scaled properly.

5.2 Software Tools Used in Study

5.2.1 FAST

The FAST software tool developed by the National Renewable Energy Laboratory (NREL) is a program system to simulate performance of wind turbines. Modules within the program simulate the aerodynamics of turbine blades, wind drag due to rotor thrust and drag from the turbine mast, the generator system, and other major components of a turbine system. The FAST system has been extended by incorporating the HydroDyn module to simulate floating platforms and mooring line dynamics for floating wind turbines. Input/output for FAST is via text files.

The main FAST program manages the time-clock and the flow of information between modules. The main program manages the equations of motion, kinematics, kinetics and turbine control algorithms. FAST also models the flexure of system components such as the tower, rotor blades and the drive-train. The AeroDyn module models wind resistance, rotor blade airflow and stall mechanisms. The HydroDyn module models floating platforms and simple mooring systems. This module is replaced with OrcaFlex in the FAST – FASTlink – OrcaFlex system.

Table 3 FAST is implemented as a Fortran-90 program packaged with three library files

Module	Type	Version	Purpose
FAST	Executable program	v7.02.00d-bjj, 20-Feb-2013	Main program, controls time-step, integration. Calls modules to calculate aerodynamics and hydrodynamics NOTE: Includes HydroDyn module
AeroDyn	Library	v13.00.01a-bjj, 16-Feb-2012	Calculates aerodynamic loads on wind turbine blade elements
InflowWind	Library	v1.02.001-mlb, 2-Apr-2013	Read and process inflow winds, pass results to AeroDyn
NWTC	Library	v1.07.00b-mlb, 10-Jan-2013	Common I/O interface for FAST and other National Wind Technology Center (NWTC) software tools

5.2.1.1 Extending FAST

The University of Maine VolturnUS system has a simple blade pitch control that keeps the rotor spinning at a constant RPM. Modeled on the OC3 Hywind floating wind turbine, a proportional-integral (PI) control system uses the integral of rotor velocity error to change the blade pitch. This helps to guarantee constant power output from the FOWT in the face of changing wind conditions.

The FAST software system does not support blade pitch control directly. Instead, the user must edit a Fortran 90 file called "UserSubs.F90," implementing their custom control law. This file

replaces a file provided in the FAST software release, and the user must recompile and link the object files to create their FAST program with pitch control.

The FAST source code files are supplied as are make-files to build the program in a Linux environment. A Windows programmer using Microsoft Visual Studio and Intel Fortran has to build their own project and solution system, modeling it on the contents of the Linux make files. While this is not difficult, it is beyond the capabilities of most engineers, especially since most engineers lack a Fortran compiler and knowledge of the Fortran language. On the other hand GNU-Fortran is open source and free, so the capital cost of building a custom version of FAST is limited only by the availability of skilled programmers.

5.2.2 OrcaFlex

OrcaFlex is a time-domain multibody hydrodynamics simulator developed by Orcina, Ltd., optimized for simulation of floating bodies connected by solid structures and lines. Mooring lines are modeled using finite element techniques. The OrcaFlex model includes axial and radial stiffness, added mass and damping, seafloor friction and other physical effects. OrcaFlex is an accurate and efficient simulator for complex systems including free floating and fixed structures, submerged structures and interconnection lines.

OrcaFlex includes a graphical user interfaces and a dialog-box-based interface to specify mechanical properties. OrcaFlex includes powerful post-process capabilities including spectral analyses, static and animated displays, and charts of all important system values and derived values.

Although OrcaFlex does not include a potential flow module to calculate added mass and damping for floating objects, it has the ability to import hydrodynamic databases generated by ANSYS Aqwa. The user has the choice of using potential flow models for floating objects, or to use hydrostatic models augmented by Morison drag coefficients.

5.2.3 FASTLink (OrcaFlex + FAST)

It is common to use the FAST and OrcaFlex tools independently, passing the results from a FAST simulation into OrcaFlex in one direction, but a more accurate solution might be obtained by coupling the two programs together. The combined system should be able to calculate the interaction between the wind system and the wave and current system to better compute complete system dynamics. A major goal of this project is to test that ability, comparing measured performance results with simulation results.

Currently FAST approximates the mooring forces on an offshore floating wind turbine with a quasi-static cable model HydroDyn that accounts for cable weight, but not its inertia. By linking FAST with OrcaFlex using the FASTlink coupling module the quasi-static cable model can be replaced with OrcaFlex's dynamic cable model which includes cable inertia, drag, and fluid added mass. The source code modifications needed to couple FAST with OrcaFlex were developed by Antoine Pfieffer, of Principle Power, in collaboration with Orcina, the creators of OrcaFlex.

OrcaFlex replaces the HydroDyn module within FAST. HydroDyn is responsible for calculating the:

- Hydrodynamic force on the platform, which includes the radiation, diffraction added mass and quadratic drag terms

- Mooring line restoring forces via a quasi-static approximation methods using a closed-form continuous cable analytical model

In the FAST-FASTlink- OrcaFlex software system, at every time-step:

- FAST passes the vessel position and velocity vectors into OrcaFlex.
- OrcaFlex calculates line tension, hydrodynamic added mass matrix, and non-acceleration dependent hydrodynamic forces.
- OrcaFlex passes the added mass matrix and total force / moment applied to the platform back to FAST.
- The resulting platform motion is solved in FAST.

There are a number of issues related to coupling FAST and OrcaFlex:

- Reference Frames: The user must define OrcaFlex mooring lines relative to the FAST reference frame, which in turn is parallel to the calm water surface.
- Accounting for Gravity: All masses are declared in FAST, and all OrcaFlex masses are set to zero.
- Integration Time-Step: FAST controls the time-step. The OrcaFlex time-step must be set to the same value as the FAST time-step.

Platform weight and buoyancy are handled inconsistently in the FAST – FASTlink – OrcaFlex software system, and this can cause problems with quasistatic stability. If the system does not achieve the necessary static stability before the transient analysis starts, the user may have to add an applied force to the OrcaFlex model such that this force is equal to the undisplaced buoyancy of the platform. With some iteration static stability usually can be achieved.

In this project, the platform natural frequencies can be used to confirm that FAST and OrcaFlex are connected properly. Simulated and measured loads in mooring lines are compared in both the time and frequency domain to insure that the dynamic simulation is working properly.

5.2.4 Charm3D

Efforts initiated at Texas A&M University (TAMU) with the support of Houston oil industry resulted in the development of the Charm3D, a software system that can perform coupled time domain analyses for offshore systems, including floaters, moorings, risers and foundations. Charm3D has a user-friendly interface. The system includes a preprocessor, WAMIT (2013), a boundary element module, to calculate added mass and damping databases to model the response of floating structures in waves. Mooring components and risers are modeled with a non-linear finite element formulation.

Model templates exist for platforms that are widely used, e.g. TLP, spar, semi-submersible and FPSO. Apart from this, users can input their hull form and data.

The program has been continuously developed for emerging markets by the vendor Offshore Dynamics, Inc. Recently, the program has been extended for FOWT analysis, and a module for linking with FAST is being added. Furthermore, a module for fatigue analysis of floating structures is also reportedly in the beta testing stage.

5.2.5 Charm3D-FAST

As summarized in ABS (2012), TAMU developed a data passing scheme to link CHARM3D and FAST. In the original implementation Charm3D calculated the platform motions based on

environmental conditions and input on the hull-tower loads from FAST. In turn, FAST calculated the aerodynamic loads and turbine loads. The balanced platform motions at the hull-tower interface were sent to FAST, which would then compute the dynamic loads on the turbine and update the hull-tower interface loads.

Charm3D includes a hull and riser hydrodynamic analysis module called Hull and Riser/mooring Program (HARP), which uses the well known diffraction/radiation 3D panel program WAMIT (Lee et al. 1991) to calculate the hydrodynamic coefficients (added mass and radiation damping), the first order wave frequency and second order sum and difference frequency wave excitation forces. From the HARP output, the water-plane area, the displacement volume, the center of buoyancy and the restoring coefficients are obtained. Based on these data, the vertical static equilibrium of the floating structure is checked.

The nonlinear finite element method (FEM) is used on the mooring/riser module. The upper ends of the mooring lines/ risers are connected to the fairlead through generalized elastic connection conditions. Charm3D transfers the calculated hydrodynamic force due to wave and current loading, mooring line tension into time domain and feeds them into FAST, an aero-rotor-tower-control program developed by the National Renewable Energy Laboratory (NREL). The resultant aerodynamic forces and the forces due to elastic deformation of the tower are lumped at the interface between the tower base and the floating structure and exported as an external force input to Charm3D. Charm3D calculates all the external forces acting on the platform and then feeds 6 DOF platform dynamics back to FAST. (Shim and Kim, 2008; Bae and Kim, 2013).

Control of the integration time-step is a major issue when coupling multiple simulators. Often activities modeled by one simulator operate at much different frequencies than in another simulator. The first step in coupling simulators is to select one simulator to control the time-step, usually the simulator handling the fastest events. If the time-step is set by the simulator with the highest frequency events, then the combined system will be inefficient because the other simulator is forced to operate with a shorter time interval than would be necessary for accurate results. In the Charm3D-FAST integration the time-steps for each simulator are set separately, typically with FAST running multiple steps for each Charm3D step.

As reported in Bae and Kim (2011) and Bae, et al. (2011a, 2011b), the division of labor between FAST and Charm3D was revised such that FAST calculates the dynamic responses of the turbine components, tower and floating hull structure, and CHARM3D calculates the hydrodynamic wave and drift frequency forces, viscous forces on Morison members, radiation damping forces, and mooring restoring forces (Figure 3). FAST solves for 6-DOF motions at the hull-tower interface by combining tower forces and forces calculated by Charm3D. The resultant displacements, velocities, and accelerations of the hull platform are passed to CHARM3D at each step.

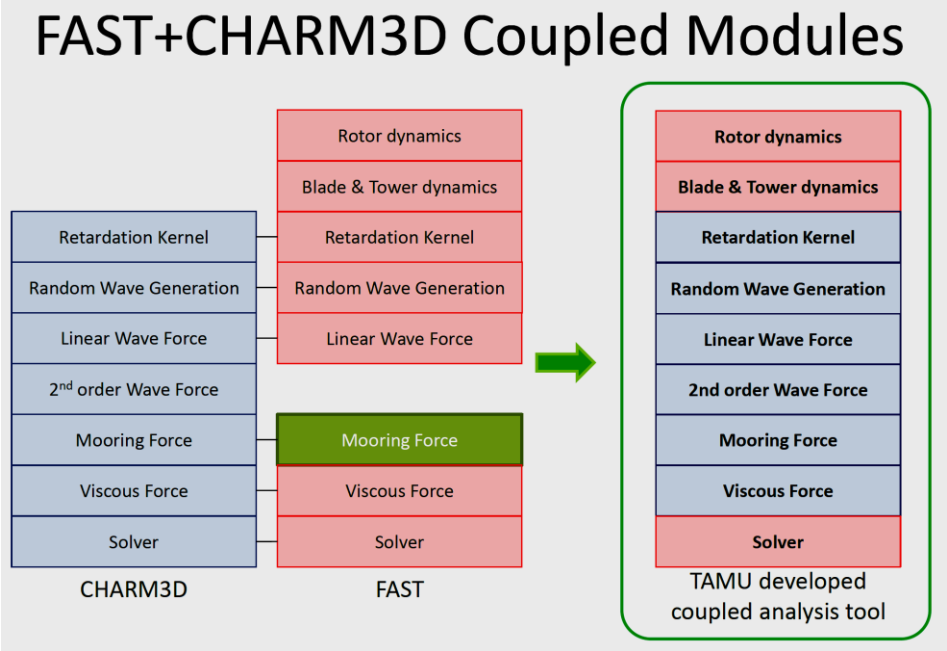

Figure 3 Texas A&M University developed a SW system coupling Charm3D and FAST (Kim, 2012)

5.2.5.1 Extending Charm3d-FAST

To model some of the FOWT cases studied here, a simple proportional-integral controller for blade pitch control must be implemented in the version of FAST that is coupled with Charm3D. The Charm3D-FAST system uses a custom version of FAST, tailored to operate with Charm3D, and end users do not have direct access to the source code for that version of FAST. Instead TAMU and Offshore Dynamics, Inc., the developers of Charm3D, packaged certain functions, including a blade pitch control module, in an external dynamic link library (DISCON.DLL) that can be replaced by the user.

The pitch control algorithm was used to create a custom DLL for Charm3D-FAST. The file DISCON.DLL was compiled and built using Intel Composer XE 2015.

5.3 Fatigue Damage Prediction

OrcaFlex offers three types of fatigue analyses (see Orcina, 2013 for additional detail):

Rainflow Fatigue Analysis: Rainflow fatigue analysis requires time domain simulations be carried out for each cell of the irregular wave scatter table. OrcaFlex conducts rainflow counting of the mooring tension time history. From these rainflow cycles, Miner's Rule is used to estimate the total damage and expected lifetime of the mooring component under consideration. Miner's Rule states that:

$$damage = \sum_{i=1}^{k} \frac{n_i}{N_i} \qquad (6)$$

In this equation, n_i is the number of cycles counted at a given stress or tension range, N_i is the

number of cycles to failure at that stress or tension range (determined in OrcaFlex from a user-specified S-N or T-N curve), and i and k are indices for the tension bins in the analysis.

Typically it is assumed that if the damage exceeds unity, then the system will fail (although appropriate thresholds may be specified in OrcaFlex to account for safety factors, etc.). If damage is calculated for a year, then the expected lifetime until failure can be determined by inverting the damage (i.e. lifetime=1/damage).

Rainflow fatigue is the most computationally expensive fatigue analysis method, but also the most accurate. Orcina recommends that each irregular wave simulation have a duration of at least 20 minutes.

Regular Wave Fatigue: For regular wave fatigue analysis, an irregular wave scatter table may be converted to a regular wave scatter table. OrcaFlex includes capabilities to do this conversion and to calculate the number of encounters for each wave condition in the scatter table (see Orcina, 2013 for discussion).

Simulations are conducted in OrcaFlex or FAST+OrcaFlex for each wave condition in the scatter table to determine the steady state response of the system. In the fatigue calculation only the response for the final wave period of the simulation is used.

Fatigue damage and lifetime expectation are calculated using the same methodology as before. A key parameter in accurate regular wave fatigue analysis is determining the number of wave periods required to establish a steady state response.

Spectral Fatigue: OrcaFlex includes functionality to conduct spectral fatigue analysis. For several reasons, computation speed being primary among them, the makers of OrcaFlex no longer recommend this method for mooring fatigue analysis in OrcaFlex. According to the User Manual (Orcina, 2013):

"The advent of multi-core processors and the wave scatter conversion facility mean that regular wave fatigue is often just as fast as spectral fatigue analysis, as well as giving much more reliable and accurate answers. Because of this we no longer recommend the use of spectral fatigue analysis in OrcaFlex."

For this reason it was decided that a spectral fatigue analysis would be of little value for the current project, and so it was not conducted.

T-N Curve: Each fatigue analysis method applies a T-N curve to the response history, and uses the Palmgren-Miner Rule to determine damage and expected lifetime for the mooring. For this analysis an appropriate T-N curve was obtained from API RP 2SK, section 6.2.1, page 25:

$$N = KR^{-M} \quad (7)$$

The T-N curve is a function of empirical parameters *M* and *K*, as well as the ratio of tension to mean breaking load (MBL), *R*. For stud-less, grade R3S chain, *M=3.0*, and *K=316*. Three values of MBL were analyzed: the MBL at the nominal chain size, the MBL assuming 50% lifetime corrosion, and the MBL assuming 100% lifetime corrosion. The API MBL of the nominal chain diameter of 77 mm is 5586.4 kN. If the chain is assumed to corrode at 0.4 mm/yr. (recommended design value in API RP 2SK), then the diameter will be 69 mm after a 20 year lifetime. The MBL of 69 mm chain is 4561.8 kN. Finally, if the corroded chain size at 50% of the

lifetime is assumed (recommended by DNV OS-E301), then the chain diameter is 73 mm and the MBL is 5063.5 kN.

The WAFO Matlab toolbox was explored as an alternative option for fatigue analysis. WAFO was developed by Lund University and was first released in 2000. Numerous routines have been developed for statistical analysis of waves, fatigue, and extreme events. From an input time series, turning points are calculated from WAFOs *dat2tp* routine. From the turning points, it is possible to find the rainflow cycles using a rainflow counting algorithm in WAFO. Routines have also been developed to filter rainflow cycles to remove low amplitude cycles, which allows for elimination of cycles below the fatigue limit. In addition to calculation of rainflow cycles and matrices from a data series, it is possible to compute a theoretical rainflow matrix from a series of min-max cycles. Finally, for purposes of fatigue, either a calculated and a theoretical rainflow matrix (or series of rainflow cycles) are used to estimate fatigue damage using the Palmgren-Miner hypothesis.

$$D(t) = \sum_{t_k<t} K\left(S_k^{RFC}\right)^{\beta} \quad (8)$$

Where:

D is the cumulative damage

K and *beta* are parameters of the S-N curve

S(RFC) is the rainflow cycle data

Another avenue explored for some aspects of this study is the code for Rainflow counting algorithm by Adam Nieslony from Matlab file exchange center, http://www.mathworks.com/matlabcentral/fileexchange/authors/7825

6 Case Studies

6.1 Kyushu University Spar Wind Turbine

6.1.1 Introduction

As part of a demonstration project funded by the Japanese Ministry of the Environment, researchers at Kyushu University and the Toda Corporation have deployed two scale model FOWTs and one full scale FOWT. A 1:10 scale model (1kW rated power) was deployed in the Sasebo Shipyard in southern Japan, and is reported in depth in Utsunomiya et al. (2010). A 100kW, 1:2 scale model was installed June 9-11, 2012 off the coast of Kabashima Island (Utsunomiya et al., 2012). The full scale model, a 2MW downwind spar, was deployed off of Kabashima Island in 2013 (Utsunomiya et al., 2013). The dynamic motion of each of the prototype spar models has been extensively studied. A thorough discussion of the dynamic response of the 1:10 scale model during several sea-states is presented by Utsunomiya et al. (2010). The response of the 1:2 scale model during power generation (Utsunomiya et al., 2014), during a typhoon (Utsunomiya et al., 2013), and with the objective of studying in-house modeling tools (Utsunomiya et al., 2012) have all been reported. This work of Utsunomiya et al. (2010) is of high enough quality that a case study of the 1:10 scale model was developed and validated for purposes of preliminary analysis.

There are two primary objectives of this case study. The first is to develop a complete computer model of the FOWT case study. As has been discussed in previous reports, the first component is an accurate model of the submerged platform for frequency domain analysis to determine the platform's linear response. This is done in ANSYS Aqwa. The second component is a complex mooring model, developed in OrcaFlex, to simulate the moored system response in the time domain.

The second primary objective of this case study is to perform a preliminary validation of each of these tools. This is done for the spar and the coupled simulation using field measurements for the 1:10 scale spar reported by Utsunomiya et al. (2010). Design information for the commercial turbine was also used for preliminary validation of the FAST model (http://www.awing-i.com/english/index.html).

6.1.2 Design Creation

The spar is designed as a 1:10 scale of a full scale 2MW FOWT. The platform has a design draft just over 7 m and a maximum diameter of 0.92 m. Geometric details are presented in Utsunomiya et al. (2010). For the current project, a CAD model of the spar was developed in ANSYS Design Modeler with known dimensions of the spar (Figure 4). This CAD model is used for radiation/diffraction analysis in ANSYS Aqwa in the frequency domain. As such, geometric information is only necessary for the submerged portion of the model.

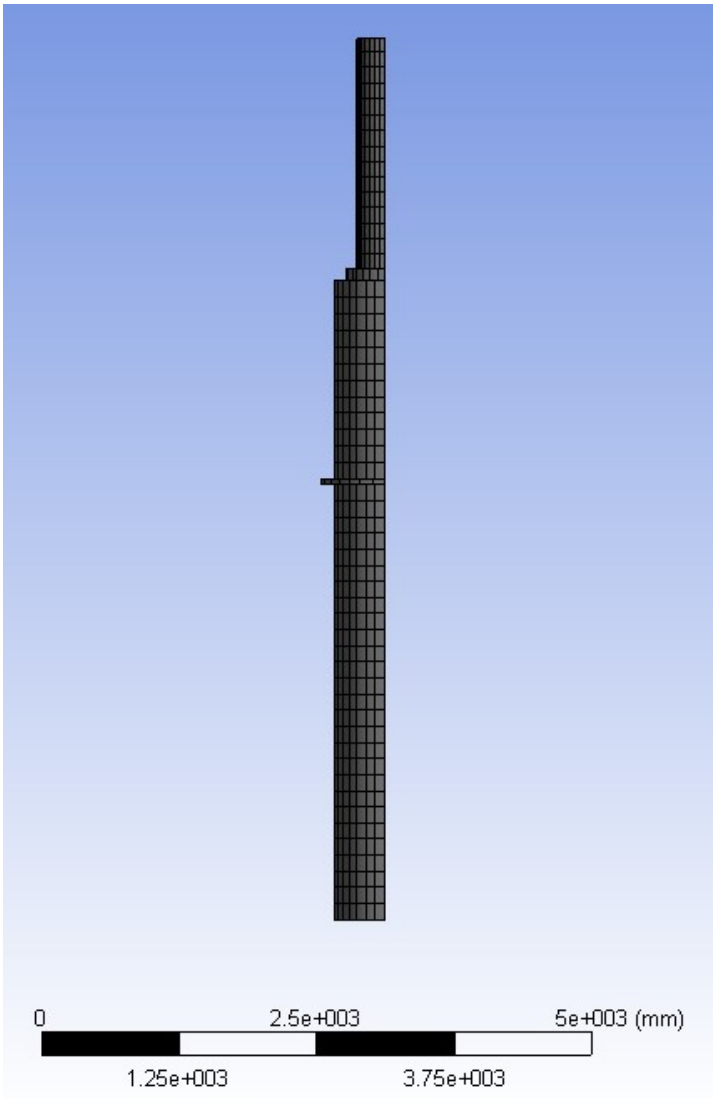

Figure 4: ANSYS-Aqwa mesh of the spar used for radiation/diffraction analysis.

In addition to the radiation/diffraction analysis done to determine the response of the system, Morison drag coefficients were included in the model. This was done in OrcaFlex using buoy elements connected to the platform. The buoy elements have no effect on the platform other than to add Morison drag. A similar procedure was used to model Morison drag on the Hywind Spar FOWT model developed as an example case study, reported by Masciola et al. (2011).

The system employs three catenary mooring chains for stationkeeping. The chain used in the field was 16 mm studless chain (Utsunomiya et al., 2010). The scope of the catenary chains was not measured. However, chain tension was measured as a function of water depth, which varied significantly due to tidal action. From basic catenary equations and assumptions, it is a simple matter to determine the scope of the mooring system once the tension, depth and chain weight are known. Using first principle assumptions and available information, the mooring system design was replicated and assembled in OrcaFlex. The mooring model in OrcaFlex is seen in Figure 5.

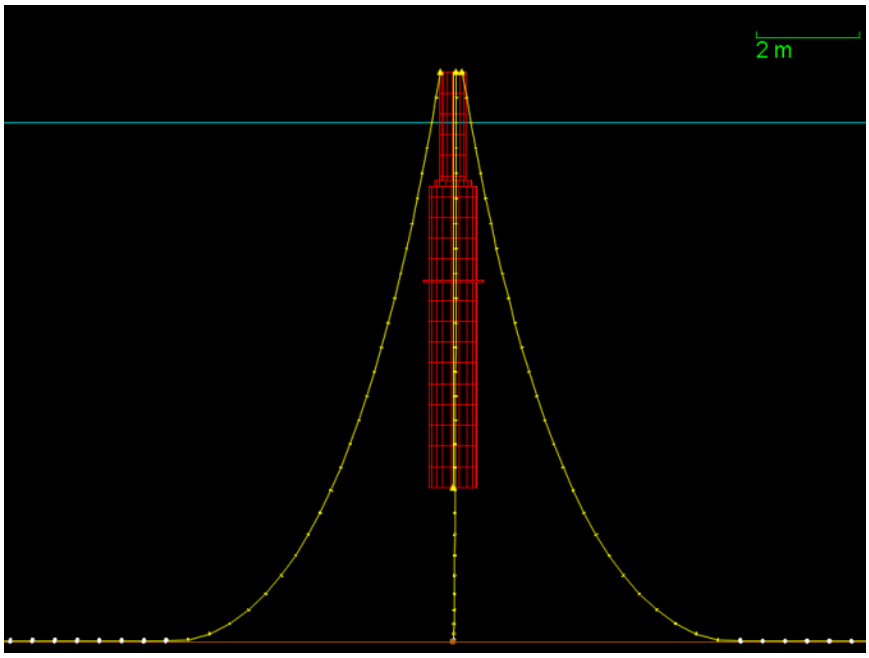

Figure 5: Mooring layout of the spar in OrcaFlex.

As an initial validation of the mooring system, the static tensions of the moorings at the fairleads were measured over the full range of tidal depths, from 10m to 12.5m. These tensions are plotted in Figure 6, along with field measurements reported by Utsunomiya et al. (2010). As seen in the figure, agreement is quite good, which lends credibility to the assumptions used to replicate the mooring model.

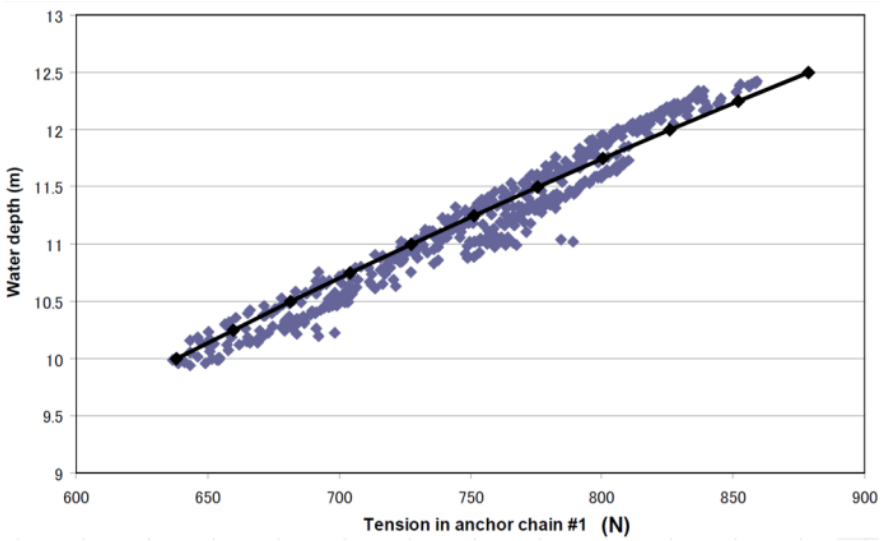

Figure 6: Relationship between water depth and mooring tension: comparison of field data with OrcaFlex model. OrcaFlex model is overlaid on Figure 12 from Utsunomiya et al. (2010).

Because of the simple shape of the spar, several quick checks of the added mass and natural periods may be done to ensure that the Aqwa model produces accurate results. For a cylinder moving in roll or pitch, the added mass is a function of the center of gravity, the center of buoyancy, and the radius and length of the cylinder (see Faltinsen, 1998, problem 3.4).

$$A_{44} = \rho A\left(\frac{d^3}{12} + d \times \overline{BG}\right) \quad (9)$$

Using this equation, the theoretical added mass of the two main cylindrical sections is A_{44} =1.36E4 kg-m^2. The result calculated in Aqwa-Line is 1.40E4 kg-m^2. These results are very similar. Differences may be attributed to slight variations caused by the smaller details in the model.

Similarly, the added mass in roll is checked against the predictions of Aqwa. The natural roll period T of a system is (Faltinsen, 1998):

$$T_{n4} = 2\pi\sqrt{\frac{Mr_{44}^2 + A_{44}}{\rho g V \overline{GM}}} \quad (10)$$

Using the expected displaced volume, V, added mass, A_{44}, and metacentric height, GM the calculated roll natural period is 7.31 seconds, which compares favorably to the predicted value in Aqwa of 7.29 seconds. A similar procedure may be done with the heave period, however the added mass is not known through any analytical formula, and therefore, although the results again compare favorably, there is little value in such a comparison.

The natural periods of the moored system were measured in heave, roll, surge, and yaw. These values are compared with predictions of both OrcaFlex models in Table 4.

Table 4: Field measurements of the natural periods of the moored system compared with predictions from OrcaFlex models.

	Field Measurement	OrcaFlex
Surge	58.8 s	54.6 s
Heave	8.93 s	8.7 s
Roll	8.47 s	9.2 s
Yaw	12.0 s	12.8 s

6.1.3 Simulation

Time domain simulations were performed to account for the mooring components and the wind turbine into the model. The moorings were modeled in OrcaFlex. As a preliminary model, the turbine thrust was modeled with a constant wind load applied at the location of the turbine hub. The wind load is modeled with an empirical thrust coefficient of C_T = 1.5 and a wind load equation (Utsunomiya et al., 2010):

$$F_{wind} = \frac{1}{8}C_T\rho\pi D^2 U|U| \quad (11)$$

Where D is the rotor diameter and U is the relative wind velocity with respect to the platform velocity. An additional wind load was incorporated to account for the load on the tower.

Field measurements of the platform response to wind and waves were reported. For the wind and wave conditions reported by Utsunomiya et al. (2010), the platform roll, pitch, yaw, and mooring tension performance was recorded. One hour of data was measured. To model this,

simulations were done in OrcaFlex using comparable wind and wave conditions. The wave spectrum was input into OrcaFlex as a user-defined spectrum. The wind spectrum was measured in OrcaFlex with an API wind spectrum of mean wind speed 4.5 m/s. The results are discussed in the next section.

6.1.3.1 Motion Results

Figure 7 and Figure 8 show the spar response in roll and pitch, respectively. The measured data (blue) is compared with the OrcaFlex (black) model. In both figures, two spectral peaks may be easily discerned in the measured data. The OrcaFlex model accurately predicts the response at lower frequencies, up to around 0.1 Hz. At higher frequencies the response is under predicted.

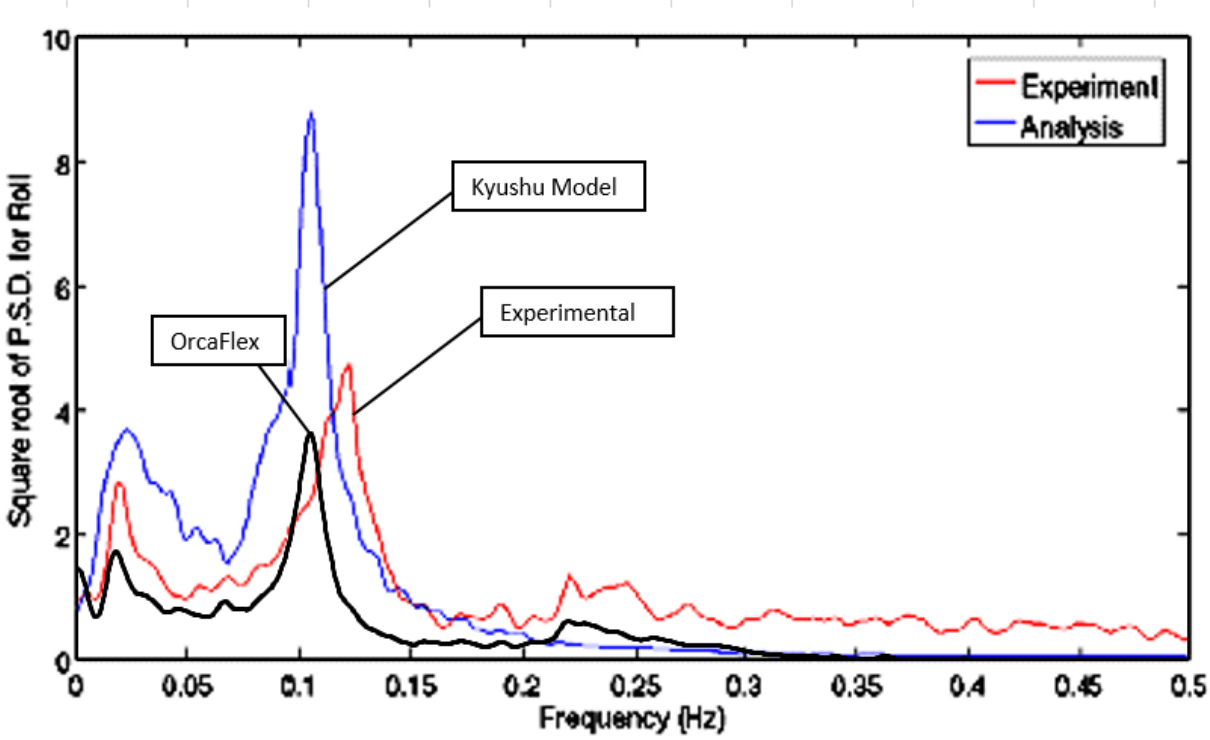

Figure 7: OrcaFlex spectral response in roll, overlaid on Figure 22 from Utsunomiya et al. (2010) showing the response of the Kabashima Island spar and the predicted response.

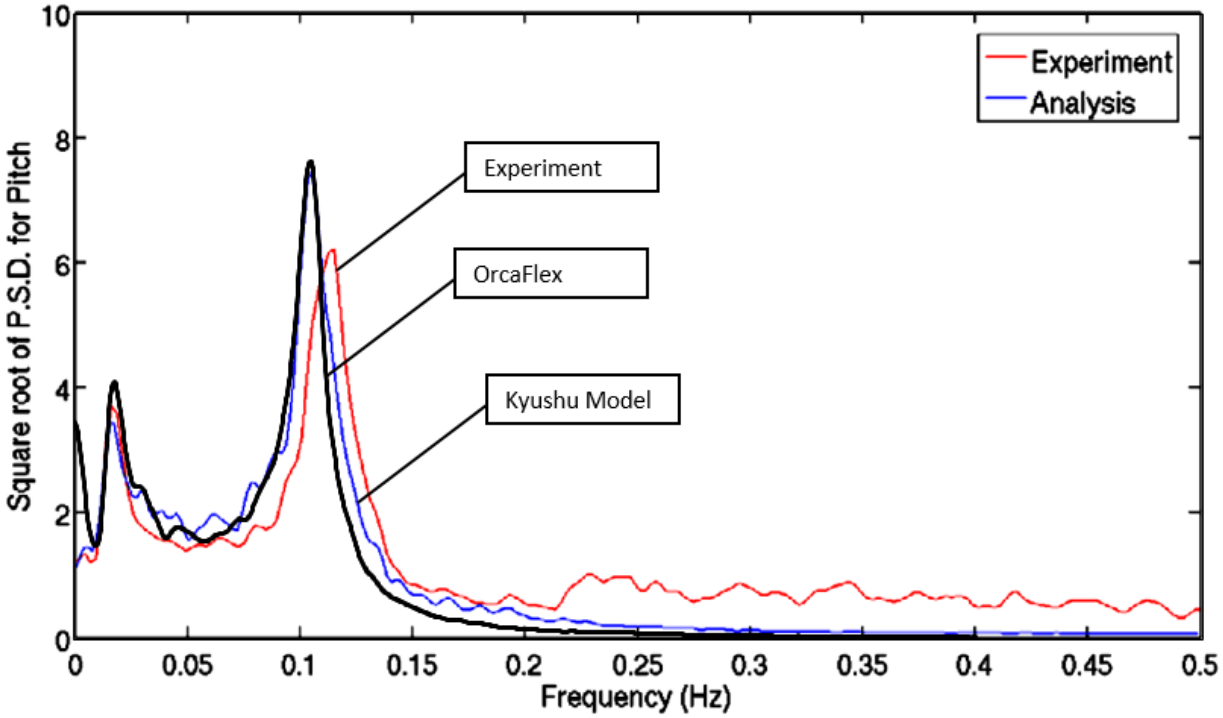

Figure 8: OrcaFlex spectral response in pitch, overlaid on Figure 23 from Utsunomiya et al. (2010) showing the response of the Kabashima Island spar and the predicted response.

A comparison of the yaw response in the system is not considered for this report. This is due to the fact that accurate information on the directional variability of the wind was not available, and therefore the wind direction was held constant. A brief sensitivity analysis was conducted which suggests that there is significant variation in the spectral response when the wind direction is altered.

Figure 9 shows the mooring response spectrum measured in the field and calculated with OrcaFlex. The significant response of the OrcaFlex model, calculated as the square root of the 0^{th} moment, compares favorably with the measured significant response (20.53 vs. 19.1).

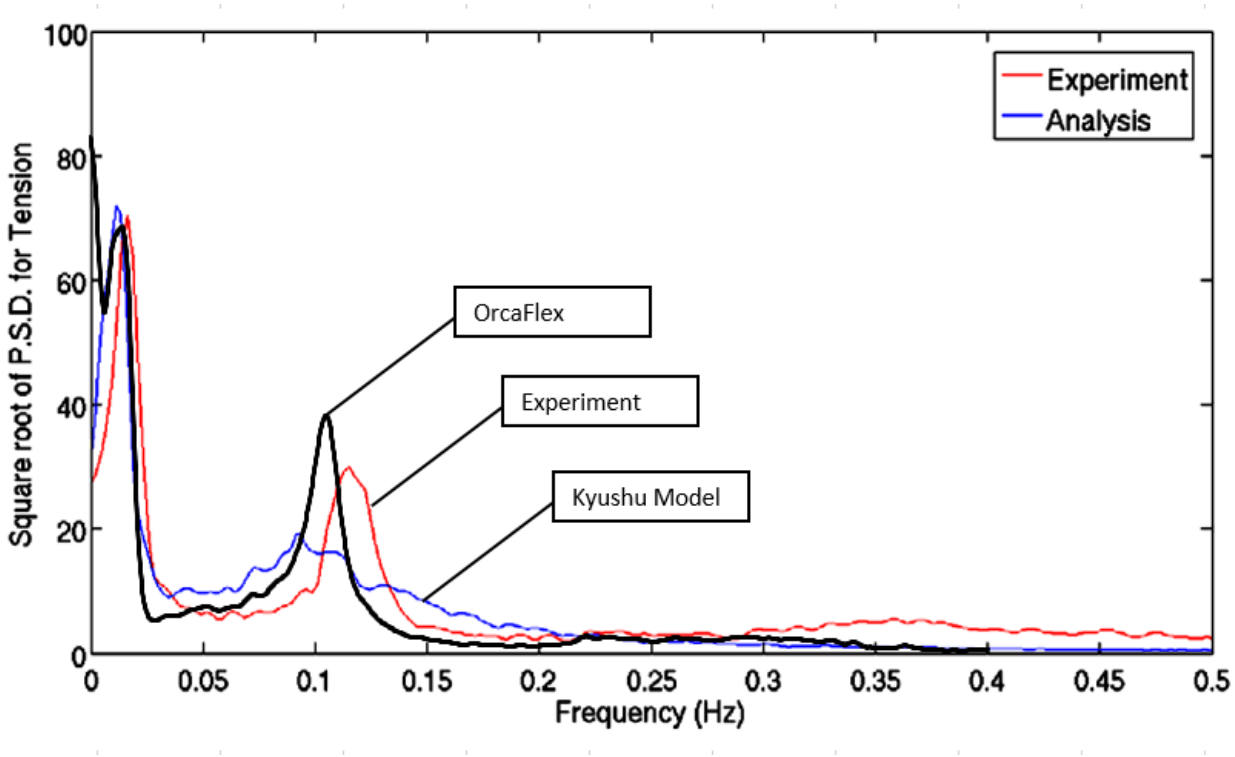

Figure 9: OrcaFlex mooring tension spectral response, overlaid on Figure 25 from Utsunomiya et al. (2010) showing the response from the Kabashima Island spar mooring and the predicted response.

6.1.4 Fatigue Study

Fatigue analysis was conducted using OrcaFlex's fatigue capabilities. The effects of chain deterioration due to corrosion are investigated in a conventional sense. Using a nominal corrosion rate of 0.4 mm/yr. over a hypothetical service lifetime of 20 years, the fatigue life was investigated for an uncorroded chain, a corroded chain at 50% of its design life (10 years), and a corroded chain at the end of its service life. These corrosion assumptions only affect fatigue in that they affect the T-N curve and therefore are assumed to reduce the predicted fatigue lifetime. Other effects of corrosion and abrasion are investigated in other case studies in this report and will constitute a significant portion of further research in this project. In this report, only the fatigue life of one mooring line is investigated.

The fatigue tools in OrcaFlex are discussed earlier in this report. Here the rainflow fatigue analysis tool and the regular wave fatigue analysis tool were used.

Environmental data at the site of the 1kW spar prototype was not available, so a suitable location in the Gulf of Maine was selected as a representative case. In the DeepCwind case study of this report, data was collected from the Northeastern Regional Association of Coastal and Ocean Observing Systems (NERACOOS) online database (www.neracoos.org). The buoy used in that analysis is NDBC Station 44032 Buoy E01, located near Monhegan Island off the coast of Maine. In this case study the same buoy is used for environmental data. However as the case study represents a 1:10 scale model, the environmental data is similarly scaled. According to the laws of Froude Scaling, the following relations are used (Viselli et al., 2014):

$$H_{s,scaled} = \frac{1}{10}H_s;\ T_{p,scaled} = \sqrt{\frac{1}{10}}T_p;\ U_{scaled} = \sqrt{\frac{1}{10}}U \quad (12)$$

The following data was collected for the Gulf of Maine test site:

- Significant wave height
- Peak wave period
- Wind speed

A wave scatter table of the dominant wave period and significant wave height is shown in Figure 10. A logarithmic relationship between the wind speed and the significant wave height was determined, which is used for the fatigue analysis (Figure 11).

		Wave Period (s)								
		0.32	0.95	1.58	2.21	2.85	3.48	4.11	4.74	5.38
Wave Height (m)	0.025	0%	5%	2%	2%	3%	1%	0%	0%	0%
	0.075	0%	7%	11%	5%	11%	6%	0%	0%	0%
	0.125	0%	1%	10%	5%	6%	4%	0%	0%	0%
	0.175	0%	0%	3%	4%	2%	3%	0%	0%	0%
	0.225	0%	0%	1%	2%	1%	1%	0%	0%	0%
	0.275	0%	0%	0%	1%	1%	0%	0%	0%	0%
	0.325	0%	0%	0%	0%	1%	0%	0%	0%	0%
	0.375	0%	0%	0%	0%	0%	0%	0%	0%	0%
	0.425	0%	0%	0%	0%	0%	0%	0%	0%	0%
	0.475	0%	0%	0%	0%	0%	0%	0%	0%	0%
	0.525	0%	0%	0%	0%	0%	0%	0%	0%	0%
	0.575	0%	0%	0%	0%	0%	0%	0%	0%	0%
	0.625	0%	0%	0%	0%	0%	0%	0%	0%	0%
	0.675	0%	0%	0%	0%	0%	0%	0%	0%	0%

Figure 10: Scaled wave scatter table for NDBC Station 44032 Buoy E01 for the past year.

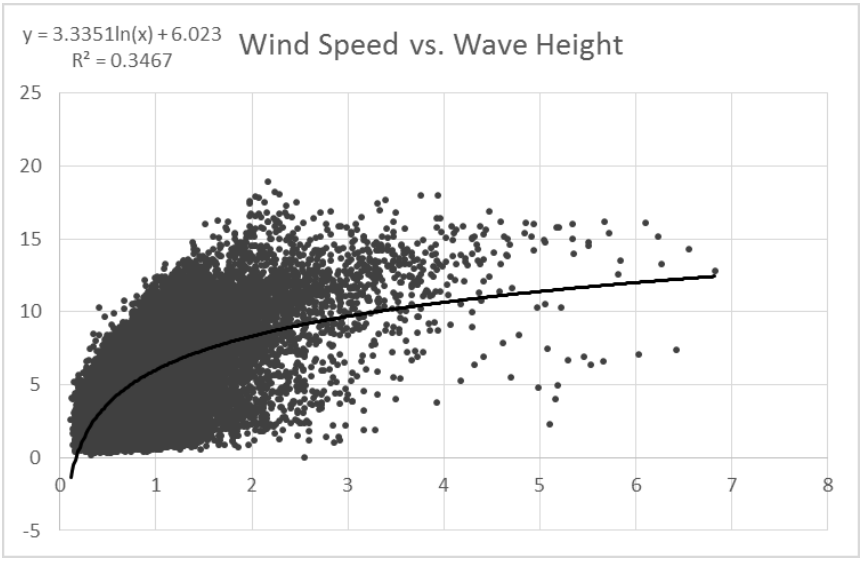

Figure 11: Relationship between wind speed and wave height for NDBC Station 44032 Buoy E01 for the past year. Equation for the logarithmic trend line is shown.

Relevant T-N curves were established from the recommendations for fatigue analysis in API-RP-2SK. The appropriate T-N parameters were obtained from API-RP-2SK, Section 6.2.1, page 25:

$$N = KR^{-M} \quad (13)$$

For studless chain, M = 3.0 and K = 316. The tensile strength of the chain is derived from the cross-sectional area of the chain. For purposes of this report, three values of cross-sectional area are considered: the nominal area of 16mm diameter chain, the area of chain that has corroded for 50% of its service live, and the area of chain that has corroded for 100% of its service life. A corrosion rate of 0.4mm/yr. is assumed (API-RP-2SK), as is a 20 year service life. For typical R3 chain the nominal, 10 year-corroded, and 20 year-corroded tensile strengths are 243.9 kN, 138.2 kN, and 61.9 kN, respectively (DNV-OS-E302). Rainflow fatigue was conducted with a 20 minute simulation as recommended by Orcina (Orcina, 2013).

Damage was calculated in OrcaFlex and is shown in Figure 12 for nominal 16 mm chain, 12 mm chain representing 10 years of corrosion, and 8 mm chain representing 20 years of corrosion. The expected lifetime for each size of chain is shown in Figure 13. The data shows very little expected fatigue damage for the mooring chain of the 1kW scale model turbine, which is due to small sea-states in a sheltered area.

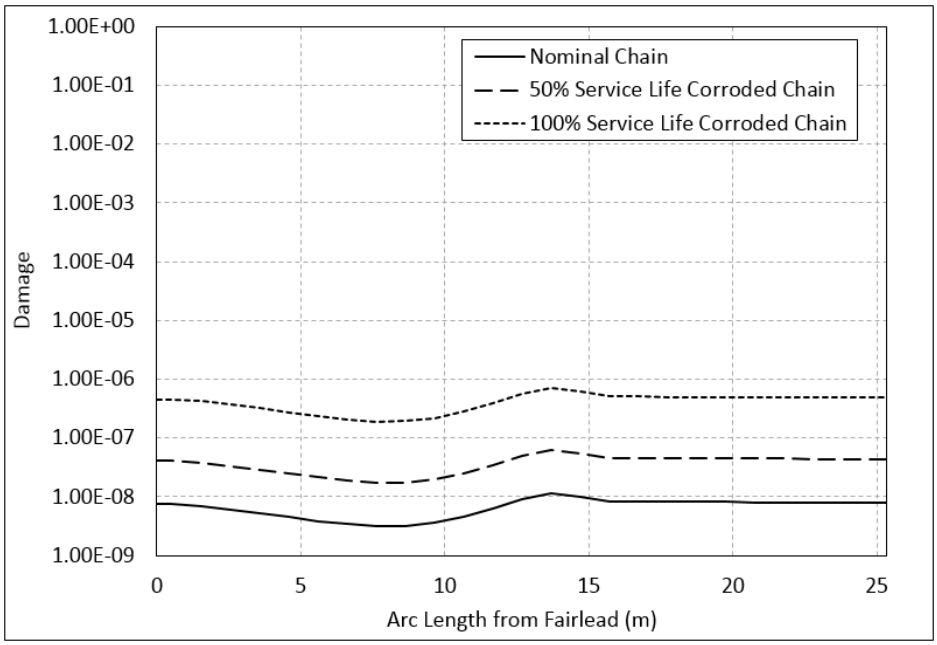

Figure 12: Calculated damage of uncorroded and corroded chain at each location on the chain.

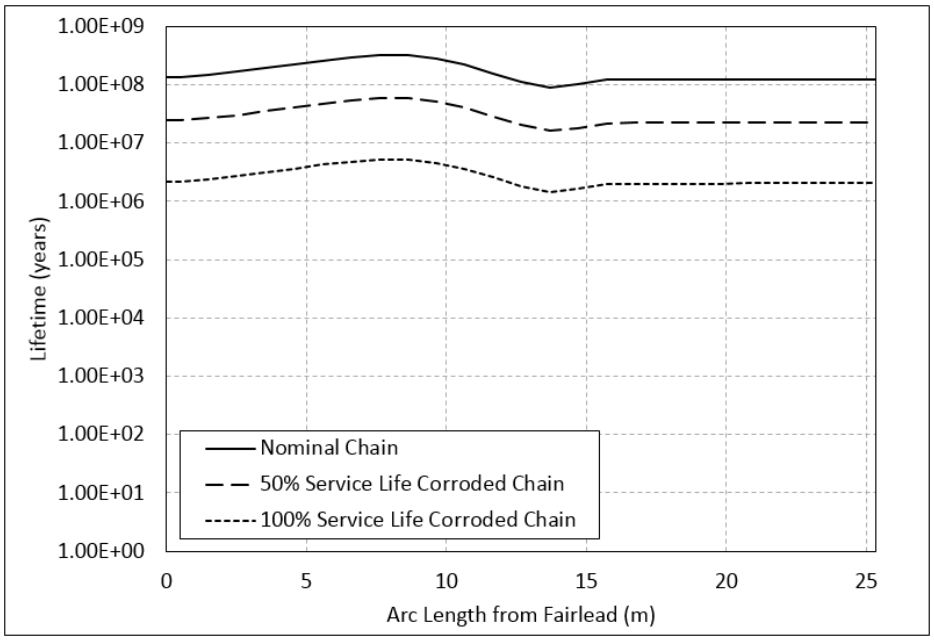

Figure 13: Calculated fatigue lifetime of uncorroded and corroded chain at each location on the chain.

6.1.5 Conclusions

ANSYS-Aqwa, NREL-FAST and OrcaFlex by Orcina were the primary tools used in the development of this case study. The basic model developed in each tool has been checked and validated where possible. As discussed in previous sections, the ANSYS-Aqwa model gives good agreement with expected natural periods. The NREL-FAST model matches the design power curve and gives a reasonable prediction for the rotor thrust loads, especially at higher wind speeds. The FAST model has the greatest amount of uncertainty when compared with the other models, owing to a significant amount of unavailable information regarding the turbine specifications. The mooring model developed in OrcaFlex similarly agrees well with predicted tension loads at various water depths.

The spar platform and mooring system models are based off of information and specifications reported by Utsunomiya et al. (2010). While the natural periods and mooring tensions match well with field measurements, there are some uncertainties about the inertia of the system and the scope of the mooring line.

1. Using published data, the project team was able to reproduce the published measured data with accuracy that approaches that reported by the Japanese design team. The natural periods were estimated accurately. The spectral response in roll and pitch were less accurate in that the predicted peak frequencies were close but the predicted magnitude of the response at those frequencies was low.
2. A hypothetical fatigue calculation showed that the mooring system is not expected to experience significant fatigue damage.
3. The results reported here have a great deal of uncertainty. If an engineering team were to use these results in a preliminary design, the team would be wise to apply a significant design margin.

4. The project team was unable to build a completely functional Charm3D model of the 1KW spar FOWT. We succeeded in building a model that reproduced measured heave/roll decay data with some accuracy, but the Charm3D model would not run in more complex time domain analyses.

6.2 USCG Aid to Navigation Buoys

6.2.1 Introduction

The absence of sufficient field data related to the performance of FOWT moorings prompted us to explore surrogate technologies for which sufficient long-term performance data is available. One alternative that emerged was the typical Aid to Navigation (ATON) used by the U.S. Coast Guard (USCG) to guide mariners. Floating ATONs are positioned in a variety of locations, seeing vastly different wave and current exposure levels depending on those locations, but the technology is largely the same regardless of that level of exposure and includes a concrete sinker connected to a floating buoy by a length of steel chain.

Floating ATONs employ heavy, studless buoy chain with a total length that is roughly twice the deployment depth. The specified chain size is based on the size of the buoy, the exposure level associated with the deployment location, and the USCG's experience in needing to replace chain. The buoy is therefore held in position within its "watch circle" with the precise location determined by the sum of forces it experiences from waves, wind, and current. Decades of service experience have resulted in an empirical data set on the steel loss in the "chafe zone" where most failures occur. This zone is the portion of the chain that is in early contact with the seabed and under constant motion due to the action of the waves and the tide on the system. While the elevation of the tide is a relatively long-period phenomenon typified by a 3.5m change in depth over approximately a six hour time span along mod-coast Maine, it means the chafe zone is distributed over a longer distance of chain compared to the same wave exposure absent tide.

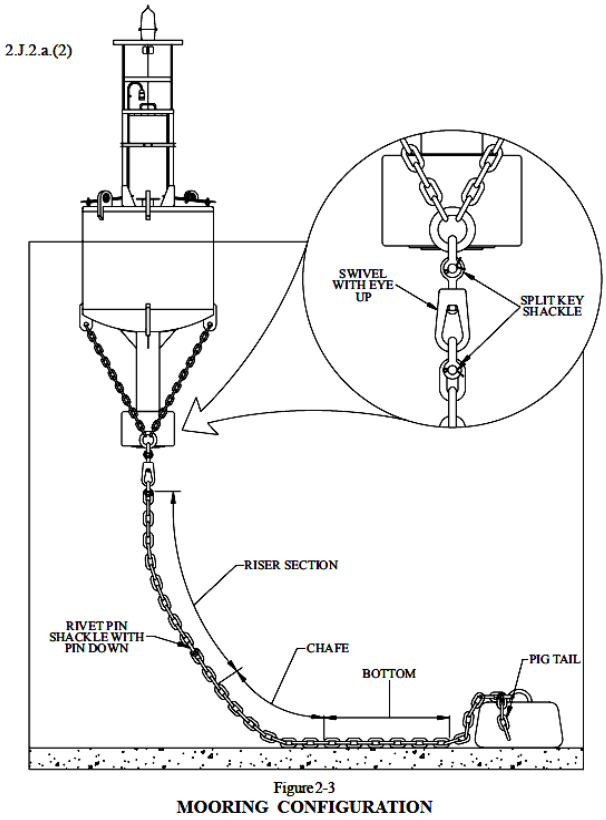

Figure 14 Typical mooring configuration for ATON buoys (reproduced from USCG, 2010). The chain bridle near the ATON buoy body is longer than shown here in order to avoid contact with the ballast.

The USCG delineates their buoy chain into three portions: 1) the suspended portion that hangs below the buoy but does not contact the seabed, 2) the chafe zone, and 3) the bottom chain that largely stays in contact with the seabed although may move around during the course of the tidal cycle or due to weather (refer to Figure 14).

In this study, the material loss in chain links was measured at ten different locations on each link as indicated in Figure 15. A sufficient number of links were measured to obtain representative results. Measurements were taken on new chain, sections of suspended chain, and chafe-zone links.

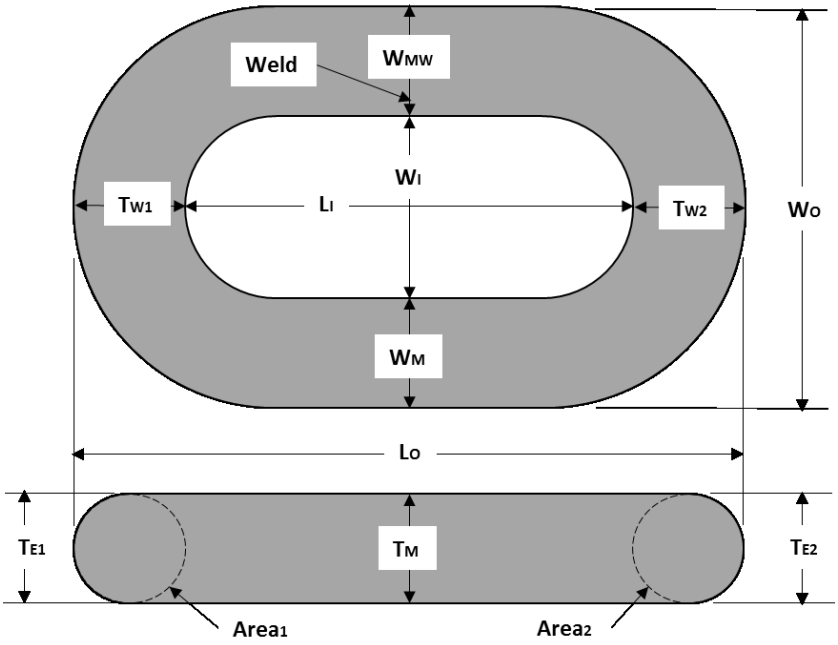

Figure 15: The ten chain link measurement locations.

6.2.2 Phase 1: ATON Buoys in Gulf of Maine

In cooperation with the South Portland, Maine Sector USCG, and the buoy tender USCG Abbie Burgess from Rockland, Maine, the project team collected data on the service performance of six buoys located within Penobscot Bay, Maine. The ATON buoys examined in this case study were selected due to ease of access to discarded chain and a to a long history of deployment, allowing for examination of historical trends. Service records collected by the USCG Abbie Burgess in the normal course of ATON maintenance included detailed measurements of chain thickness on deployed buoys as well of records of chain replacements. Detailed measurements were taken on samples of chain that had been taken out of service, and hardness measurements were taken on one of the chain links.

The utility of data collected by the USCG is variable depending on the time in which it was gathered. In general, buoys are serviced every two years to check for component condition and the buoy itself is changed out for overhaul every five years. At each visit, the entire system is brought on deck, conditions noted, connectors inspected, and the wire diameter of the links in the chafe zone is measured. From these periodic measurements, the wear rates of that portion of the chain can be estimated and projections made for chain replacement. Figure 16 shows the six locations within Penobscot Bay for which data was gathered from the ATON logs on the Abbie Burgess. Table 5 portrays that data along with their LAT/LON coordinates and the distanced-from-shore rubric used to determine the location's exposure to waves in the form of average fetch from shore or protective shoaling. This rubric is purely geometric and does not account for prevailing winds.

In Table 6, the bottom type, depth, exposure rating, and the logged measurement chafe-zone measurement data is presented. In this table, a 1.5-inch diameter value indicates that new chain was installed in the chafe portion of the system.

Figure 16: Penobscot Bay and the location of ATONs in Table 5.

Table 5: The location and distance from shore or shoal of six Penobscot Bay ATONs.

			Distance from shore/shoal (mi)								
Aid	Lat	Lon	N	NE	E	SE	S	SW	W	NW	Average
Foster Ledge	43 52 5.73	68 56 54.192	15	9	2.7	4.1	30	30	12	4.5	13.41
Old Horse	43 59 55.927	68 50 04.327	1.3	1.4	8	9	9	16	9.5	9.5	7.96
Marshall Point	43 55 18.298	69 10 52.161	3.2	4.7	8	3.7	9	15	1.5	1.5	5.83
Bay Ledge	43 57 57.257	68 51 45.340	4	6	15	8	7.2	19	9	8.5	9.59
Monroe Island	44 04 45.307	69 01 40.924	7.5	6	4.8	15	12	1.1	0.2	1.2	5.98
Moose Point	44 24 51.180	68 55 04.5	2.5	2.7	4.5	3	4.5	3	3.3	1.6	3.13

Table 6: Service data from ATON logs.

Aid	Bottom	Depth	Exposure	Date	Diameter	Days	Loss	Loss/year
Foster Ledge	rock	70	13.41	7/24/07	1.500			
				3/25/10	1.188	975	0.313	0.117
				4/11/12	0.781	748	0.406	0.198
Old Horse	rock	126	7.96	5/3/06	1.500			
				3/13/08	1.375	680	0.125	0.067
				6/9/10	1.188	818	0.188	0.084
Marshall Point	rock	111	5.83	5/22/06	1.500			
				10/17/07	1.375	513	0.125	0.089
				11/23/09	0.969	768	0.406	0.193
				11/23/09	1.500			
				10/24/10	1.250	335	0.250	0.272
Bay Ledge	mud	97	9.59	3/6/98	1.500			
				12/16/01	1.375	1381	0.125	0.033
				2/27/07	1.500	1899		
				2/16/09	1.375	720	0.125	0.063
				12/20/11	1.094	1037	0.281	0.099
Monroe Island	rock	99	5.98	7/3/07	1.500			
				7/11/09	1.406	739	0.094	0.046
Moose Point	mud	48	3.13	10/15/98	1.500			
				3/13/01	1.438	880	0.063	0.026
				3/19/02	1.375	371	0.063	0.061
				6/8/04	1.344	812	0.031	0.014
				6/1/05	1.188	358	0.156	0.159
				2/19/08	1.094	993	0.094	0.034
				12/20/10	0.938	1035	0.156	0.055

Wear rates were found to correlate with exposure and type of bottom and less so with water depth as shown in Figure 17 through Figure 19. Logically, increased exposure results in more buoy motions and therefore more movement in chafe-zone chain. Bottom type determines the abrasiveness of the movements along the seabed as well as the nature of the sediment grit that becomes involved in link-on-link wear activity.

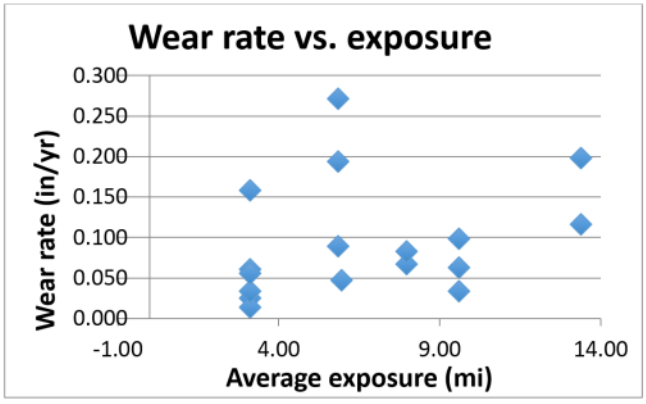

Figure 17: Chafe-zone wear rates vs. location exposure.

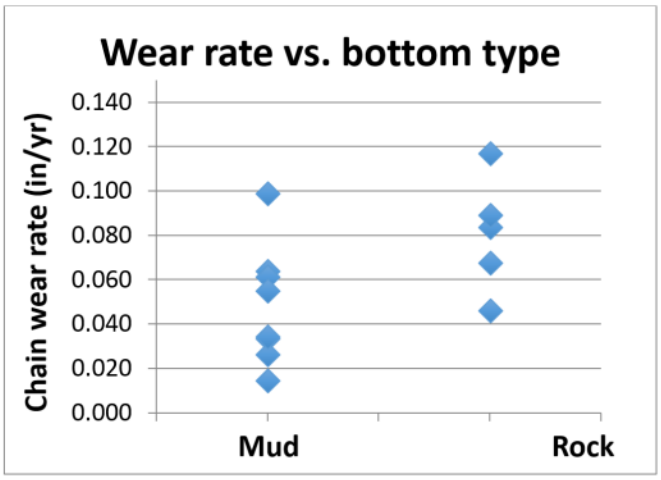

Figure 18: Chafe-zone wear rates vs. bottom type.

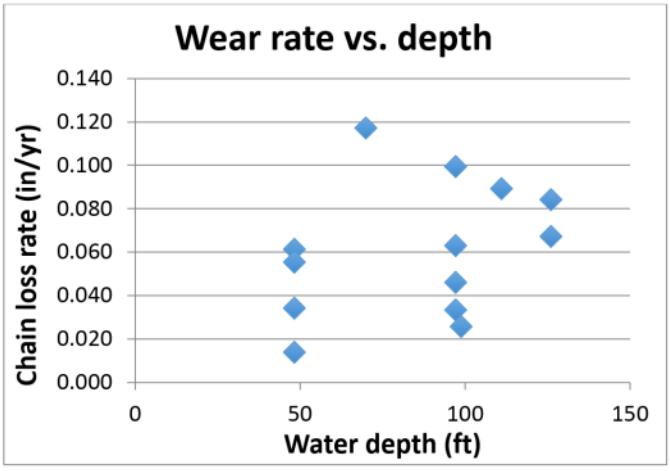

Figure 19: Chafe-zone wear rates vs. water depth.

6.2.3 Analysis of Marshall Point ATON Buoy

Given the clear importance of chain wear in the chafe zone, we requested samples of retired chain from the USCG in order to take more complete measurements of wear phenomena. The Abbie Burgess tended the Marshall Point buoy in early June of 2014. The shot of chain associated with the chafe zone was replaced and we were provided portions of that 90-foot length.

As indicated in Figure 16 and Figure 20, the Marshall Point buoy has significant exposure to the south and southwest, prevailing directions for waves coming in from the Gulf of Maine.

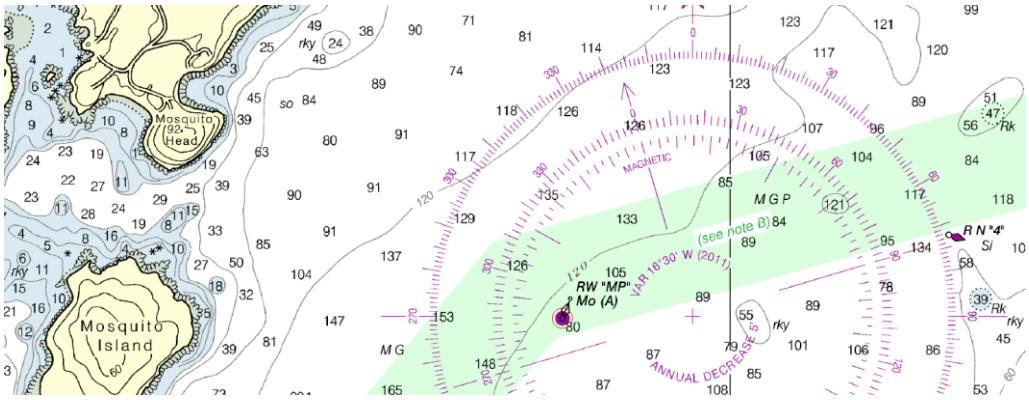

Figure 20: Location of Marshall Point buoy (source: National Oceanic and Atmospheric Administration, http://www.nauticalcharts.noaa.gov/mcd/NOAAChartViewer.html)

Chain segments removed from the chafe zone and the bottom region were been measured, and these measurements were compared with literature predictions of corrosion (refer to Table 7). The results were used to calibrate an OrcaFlex model of the chain motion over the seabed.

Figure 21: 1.5" chain samples from the Marshall Point buoy. The lower sample is from the chafe zone.

Portions of the retired chain supplied by the Coast Guard are shown in Figure 21. These are portions of the same length of removed chain with the chafe portion below and the bottom portion above. Detailed measurements of the links of these two portions of chain were taken as indicated in Figure 15. Using some measurements of some unused 1.5" chain as a baseline, the material losses in the suspended zone were slight, approximately 10% compared to approximately 45% losses in the chafe zone. The material loss in the chafe zone were quite uniform over the surface of the links with the internal length increasing only slightly more than the internal width (0.381" vs. 0.328") in comparison to the suspended measurements. The cross sectional area loss was uniform around the links but slightly higher at the link ends. The eccentricity at the link ends increases only slightly suggesting link-on-link wear was not particularly important.

Table 7 Chain link measurements (data in inches).

Suspended Chain																	
Link	L_o	L_i	W_o	W_i	T_{E1}	T_{W1}	$Area_1$	T_{E2}	T_{W2}	$Area_2$	W_M	T_M	$Area_M$	W_{MW}	T_{MW}	$Area_{MW}$	
1	8.833	6.056	5.415	2.462	1.422	1.395	1.558	1.430	1.382	1.552	1.451	1.409	1.606	1.502	1.468	1.732	
2	8.846	6.075	5.448	2.513	1.471	1.373	1.586	1.437	1.398	1.578	1.462	1.418	1.628	1.473	1.449	1.676	
3	8.862	6.131	5.414	2.445	1.453	1.359	1.551	1.438	1.372	1.550	1.473	1.421	1.644	1.496	1.485	1.745	
4	8.786	6.045	5.442	2.451	1.482	1.364	1.588	1.462	1.377	1.581	1.453	1.404	1.602	1.538	1.461	1.765	
5	8.828	6.076	5.416	2.469	1.425	1.379	1.543	1.474	1.373	1.589	1.454	1.418	1.619	1.493	1.443	1.692	
6	8.821	6.018	5.434	2.440	1.479	1.405	1.632	1.504	1.398	1.651	1.487	1.439	1.681	1.507	1.492	1.766	
7	8.723	5.933	5.454	2.485	1.501	1.419	1.673	1.502	1.371	1.617	1.457	1.423	1.628	1.512	1.457	1.730	Avg. Area
8	8.812	6.060	5.481	2.479	1.496	1.370	1.610	1.490	1.382	1.617	1.465	1.436	1.652	1.537	1.45	1.750	
Avg.	8.814	6.049	5.438	2.468	1.466	1.383	1.593	1.467	1.382	1.592	1.463	1.421	1.633	1.507	1.463	1.732	1.637
Max.	8.862	6.131	5.481	2.513	1.501	1.419	1.673	1.504	1.398	1.651	1.487	1.439	1.681	1.538	1.492	1.766	Centerline
Min.	8.723	5.933	5.414	2.440	1.422	1.359	1.543	1.430	1.371	1.550	1.451	1.404	1.602	1.473	1.443	1.676	length
S.D.	0.040	0.053	0.022	0.023	0.028	0.020	0.041	0.028	0.010	0.033	0.011	0.011	0.024	0.021	0.016	0.030	17.883

Chafe Zone																	
Link	L_o	L_i	W_o	W_i	T_{E1}	T_{W1}	$Area_1$	T_{E2}	T_{W2}	$Area_2$	W_M	T_M	$Area_M$	W_{MW}	T_{MW}	$Area_{MW}$	
1	8.576	6.469	5.195	2.796	1.166	1.042	0.954	1.194	1.065	0.999	1.198	1.226	1.154	1.201	1.238	1.168	
2	8.569	6.484	5.189	2.820	1.171	1.029	0.946	1.179	1.056	0.978	1.173	1.199	1.105	1.196	1.202	1.129	
3	8.600	6.499	5.123	2.781	1.161	1.039	0.947	1.183	1.062	0.987	1.158	1.208	1.099	1.184	1.168	1.086	
4	8.578	6.399	5.177	2.806	1.161	1.111	1.013	1.167	1.068	0.979	1.182	1.175	1.091	1.189	1.164	1.087	
5	8.587	6.470	5.157	2.858	1.150	1.068	0.965	1.151	1.049	0.948	1.154	1.166	1.057	1.145	1.192	1.072	
6	8.570	6.364	5.132	2.785	1.186	1.094	1.019	1.160	1.112	1.013	1.169	1.202	1.104	1.178	1.197	1.107	
7	8.644	6.428	5.209	2.756	1.191	1.091	1.021	1.196	1.125	1.057	1.193	1.195	1.120	1.260	1.219	1.206	Avg. Area
8	8.660	6.332	5.191	2.767	1.228	1.189	1.147	1.227	1.139	1.098	1.212	1.244	1.184	1.212	1.208	1.150	
Avg.	8.598	6.431	$ 5.17	2.796	1.177	1.083	1.002	1.182	1.085	1.007	1.180	1.202	1.114	1.196	1.199	1.126	1.062
Max.	8.660	6.499	5.209	2.858	1.228	1.189	1.147	1.227	1.139	1.098	1.212	1.244	1.184	1.260	1.238	1.206	Centerline
Min.	8.569	6.332	5.123	2.756	1.150	1.029	0.946	1.151	1.049	0.948	1.154	1.166	1.057	1.145	1.164	1.072	length
S.D.	0.033	0.057	0.029	0.030	0.023	0.049	0.063	0.022	0.033	0.045	0.019	0.024	0.037	0.031	0.023	0.044	18.061

Difference between suspended and chafe zones																	
	L_o	L_i	W_o	W_i	T_{E1}	T_{W1}	$Area_1$	T_{E2}	T_{W2}	$Area_2$	W_M	T_M	$Area_M$	W_{MW}	T_{MW}	$Area_{MW}$	Avg. Area
Avg.	0.216	-0.381	0.266	-0.328	0.289	0.300	0.591	0.285	0.297	0.585	0.283	0.219	0.519	0.312	0.265	0.606	0.575
Percent	2.51%	-5.93%	5.15%	-11.73%	24.59%	27.72%	37.11%	24.11%	27.40%	36.73%	23.97%	18.23%	31.77%	26.06%	22.08%	35.01%	35.13%

The dimensional variability of these measurements is portrayed below. The link cross-sectional-area calculations of the suspended portion of the chain are tabulated in Table 8 and plotted in Figure 22. The link measurements were taken from every fourth link, therefore we note that there is no evidence of material loss that is dependent on depth, at least over the portion examined.

Table 8: Suspended X-section areas.

Suspended Chain				
Link	$Area_1$	$Area_2$	$Area_M$	$Area_{MW}$
1	1.558	1.552	1.606	1.732
2	1.586	1.578	1.628	1.676
3	1.551	1.550	1.644	1.745
4	1.588	1.581	1.602	1.765
5	1.543	1.589	1.619	1.692
6	1.632	1.651	1.681	1.766
7	1.673	1.617	1.628	1.730
8	1.610	1.617	1.652	1.750
Avg.	1.593	1.592	1.633	1.732
Max.	1.673	1.651	1.681	1.766
Min.	1.543	1.550	1.602	1.676
S.D.	0.041	0.033	0.024	0.030

Logically, increased exposure results in more buoy motions and therefore more movement in chafe-zone chain. Bottom type determines the abrasiveness of the movements along the seabed as well as the nature of the sediment grit that becomes involved in link-on-link wear activity.

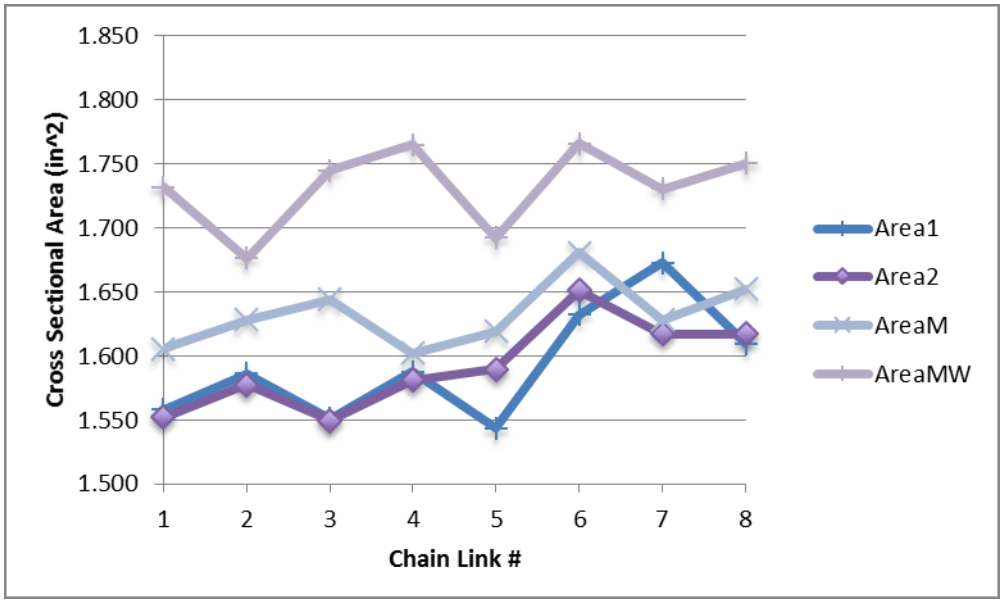

Figure 22: Suspended chain link area trends.

A similar comparison of the cross sectional area trends in the chafe zone conveys a different story. We see that material loss increases towards the middle of the sample indicate that the sample was indeed taken from the portion of chain experiencing the most loss. For the chafe-zone, measurements were taken every third link.

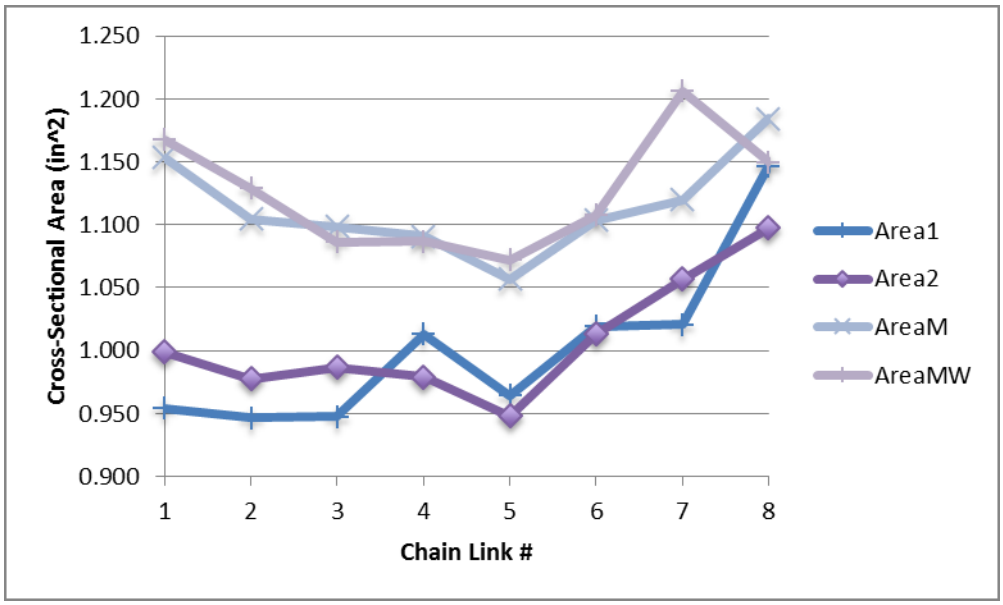

Figure 23 Chafe-zone chain link area trends.

6.2.3.1 Simulating Seafloor Abrasion

While several wear coefficients for interlink wear have been proposed in the literature (see Brown et al., 2010, and Shoup and Mueller, 1984), this project team is not aware of any equivalent wear coefficient for seabed abrasion. Therefore, the Marshall Point ATON buoy was used as a case study. The sliding distance is calculated by time-domain simulation using OrcaFlex, the hardness of a chain link was measured for chain from the Marshall Point location, and a wear coefficient has been calibrated for seafloor abrasion.

According to several sources, including Brown et al. (2010) and Shoup and Mueller (1984), abrasion between chain links may be modeled using Archard's Wear Equation. Archard's equation is derived by assuming that when two surfaces are in contact, wear occurs between surface asperities. By assuming that each asperity forms a differential contact area and summing over the entire surface, and further assuming that not all asperities are worn off during contact, Archard's Equation is reduced to:

$$\forall_{wear} = \frac{K}{H} F_n d \qquad (14)$$

Where $\forall_{wear}$ is the worn volume, H is the material hardness, F_n is the normal force between contacting surfaces, d is the relative sliding distance between contacting surfaces, and K is an empirical wear coefficient.

Because the wear between mooring links in the touchdown zone appears to be uniform and not restricted to the region between links, it is assumed that for this case study the ATON buoy primarily experiences wear due to contact with the seafloor. This wear mechanism has been observed previously for USCG buoys (Brown and Kohler, 1988). It is assumed that Archard's Equation may be used to model wear between the seafloor and chain links in the touchdown region. For a given bottom type and chain type, the material loss should be proportional to the distance travelled. If it were possible to estimate the distance travelled in year and if wear

coefficients were known, it would be possible to calculate the loss of material and thus the loss of strength in the chain during that year.

6.2.3.2 Chain Hardness

In order to determine the value of H for use in Archard's Equation, a link from the chafe zone was prepared into samples for hardness testing as shown in Figure 24. The ends of the cylindrical specimens were polished. All cutting, sanding, and polishing processes were done without any significant heating of the material.

Figure 24: Hardness specimens cut from a chafe-zone link.

Tests were done at Powder-Tech Associates, Inc a metallurgical testing laboratory located in North Andover, MA, using a Rockwell hardness tester. Under such tests, the depth of penetration of an indenter is measured. There are different indenter shapes and loads used depending on the hardness of the material. This is the industry standard for determining the hardness of metals and the machine was in calibration. Tests were done using the Rockwell B indenter and the results are shown in Table 9 Link hardness test results.. Measurements were taken on two of the specimens at various locations relative to the center and edge of the circular polished surface.

Table 9 Link hardness test results.

Specimen	Percent from edge	Rockwell B
1	90	79
1	50	79
1	10	80
2	100	79
2	80	80
2	50	80
2	10	80
Average		79.57
Tensile strength (psi)		72,500
Tensile strength (Pa)		5.0×10^8

The average hardness was found to be 79.57 on the Rockwell B scale with a corresponding tensile strength as indicated in Table 6. This suggests the composition is 1030 mild steel with approximately 0.3% carbon with a yield strength of 37,000 psi or 5.0×10^8 Pa.

6.2.3.3 Simulation Model

An OrcaFlex model of the ATON buoy was developed from the dimensions shown in Figure 25. Information regarding the draft and mass of the buoy was obtained from the Coast Guard. Inertia values of the buoy were estimated making reasonable assumptions about the material composition and geometries of each segment of the buoy. In OrcaFlex the buoy was modeled as a spar buoy element composed of three cylindrical segments of different diameters. This is shown in Figure 26. The loads on each segment are modeled according to Morison's Equation. Each segment has loading due to added mass and drag. These loads are a function of dimensionless added mass and drag coefficients, the dimensions of each segment, and the relative velocity and acceleration.

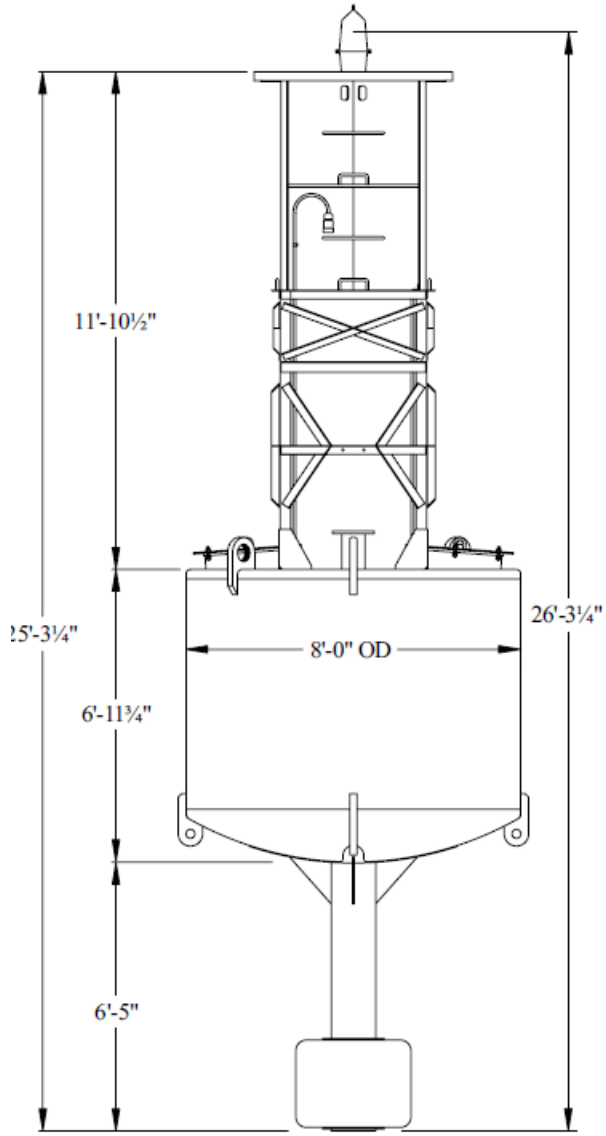

Figure 25: Dimensions for 8X26 buoy at Marshall Point location from the USCG ATON manual.

The mooring lines are modeled in OrcaFlex according to the specifications of USCG 1.25" and 1.5" chain. The mooring chain consists of one 55" shot of 1.25" chain from the buoy, and two 90" shots of 1.5" chain to the anchor. The mooring mass, equivalent diameter, stiffness, added mass, and drag coefficients are chosen from known values of chain of the specified diameter. The chain is assumed to have no bending or torsional stiffness. The mooring is anchored with a concrete block that is modeled as a shape in OrcaFlex that can interact with the mooring line.

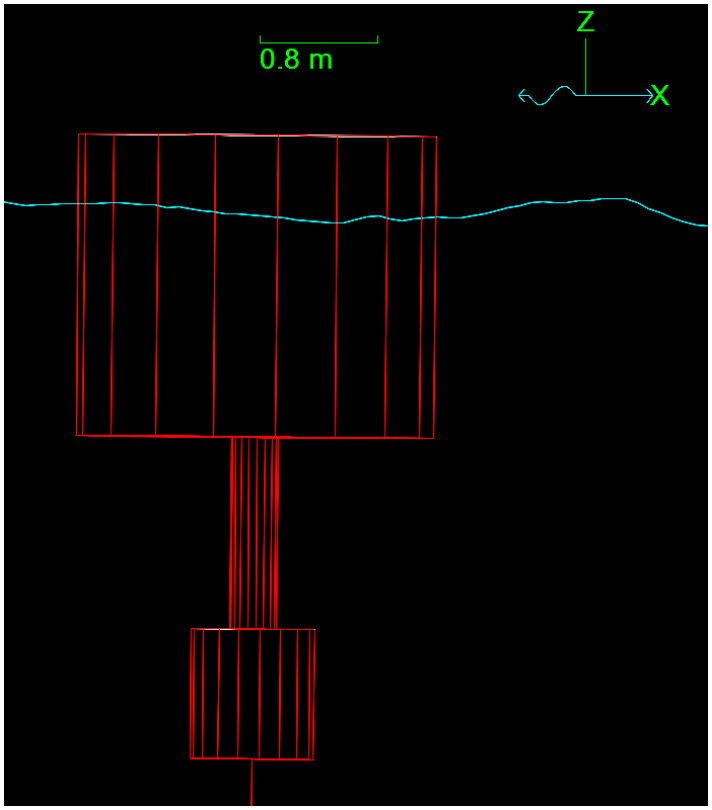

Figure 26: Buoy geometry used in OrcaFlex simulation. Cylindrical components and draft are shown. Mooring connection point is located at the base of the buoy.

The approximate shape of the seabed was estimated using the depths shown in Figure 20. From this point the locations of several nearby water depths were identified, and the seafloor surface was interpolated between them. The shape of the seafloor can be seen in Figure 27 and the final OrcaFlex model is shown in Figure 28.

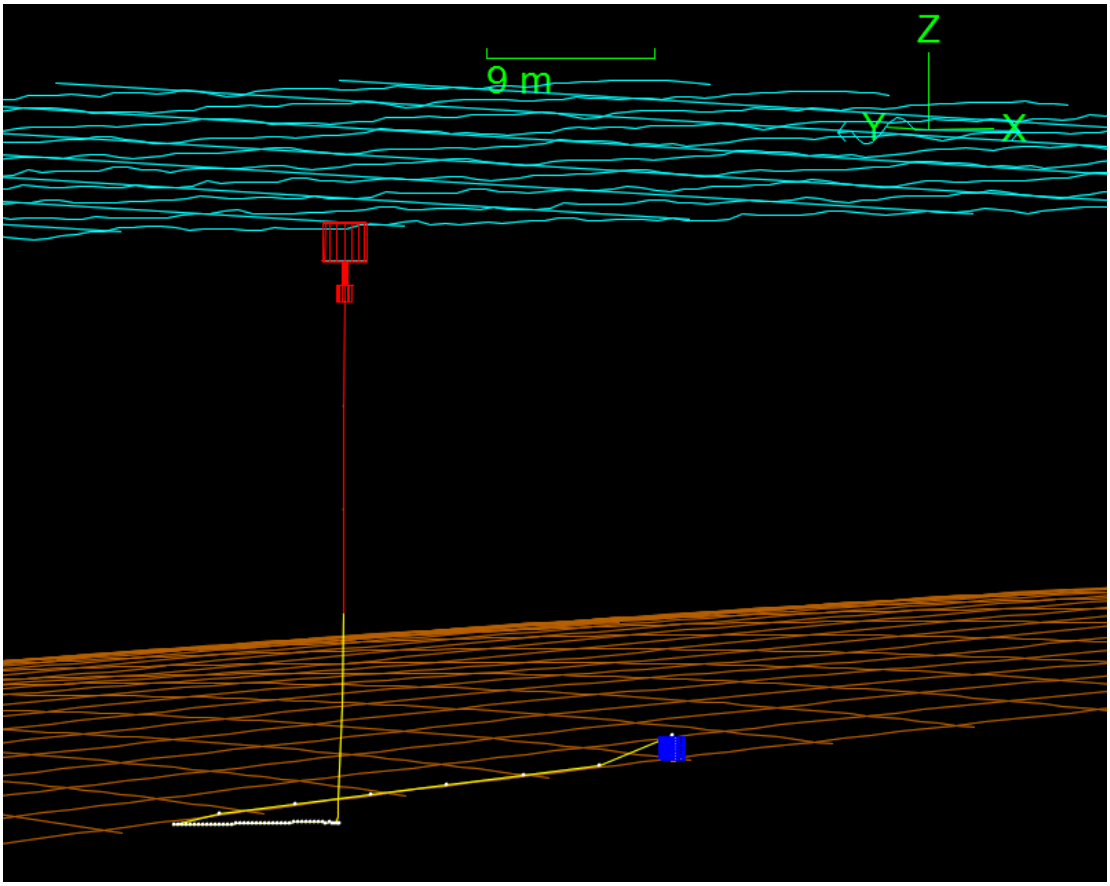

Figure 27: Layout of OrcaFlex model showing buoy, anchor block, 1.5" and 1.25" chain segments. Seabed geometry is estimated from nautical charts.

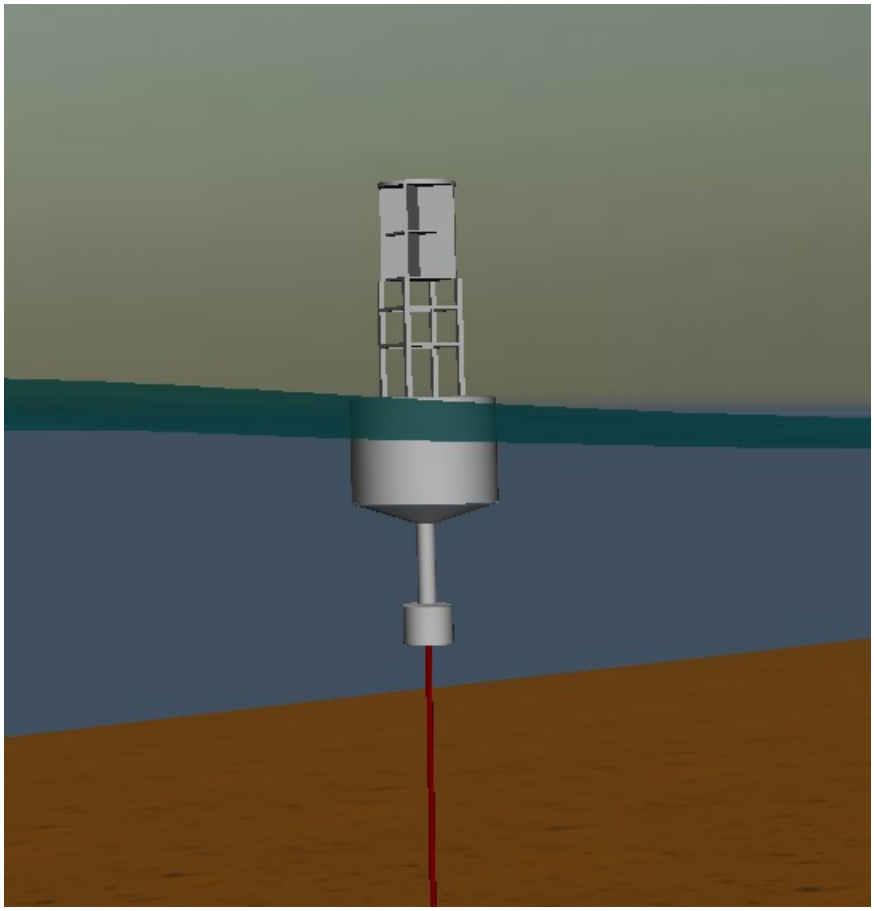

Figure 28: Final OrcaFlex model of ATON buoy at Marshall Point.

To determine the expected abrasion on mooring chain links located in the touchdown region, OrcaFlex simulations were conducted to model a full tidal cycle (12 hours) of buoy motion. The hypothesis is that the variation in current velocity and direction caused by tidal action, as well as the change in water depth, cause significant dragging of the chain along the seabed. This relative motion between the chain and the seafloor is assumed to be a primary driver in material abrasion.

Environmental data to be used in our simulations were collected from the National Oceanic and Atmospheric Administration (NOAA) National Data Buoy Center online database. Historical data were obtained from NOAA Station 44033 Buoy F01. This buoy is located in the Penobscot Bay, a relatively sheltered location in the Gulf of Maine near to the actual location of the Marshall Point ATON buoy. Data available from this buoy location included current velocity, direction, and depth gradient, significant wave height and wave period, and water temperature. The average water temperature over the past year is approximately 10^{o} C. For predicted corrosion calculations, the average water velocity is 0.2 m/s, neglecting wave velocity.

Due to long simulation times, only a single tidal cycle was simulated. The current velocity and direction are listed in Table 10. From the results of this simulation, the motion of the chain along the seafloor can be calculated. A trace of the x-y coordinates of a sample chain link is shown in Figure 29.

Table 10: Current velocity and direction for 12 hours of NOAA buoy data, used for OrcaFlex tidal simulation.

Time (hr.)	Water Depth (m)	Current Velocity (m/s)	Current Direction
1	26.9	0.28	SW
2	26.1	0.18	WNW
3	26.0	0.11	N
4	26.7	0.26	NNW
5	28.0	0.30	NNW
6	29.6	0.34	NNW
7	31.0	0.09	NNW
8	31.9	0.15	WNW
9	31.9	0.18	WNW
10	31.2	0.38	S
11	29.9	0.48	S
12	28.3	0.42	S

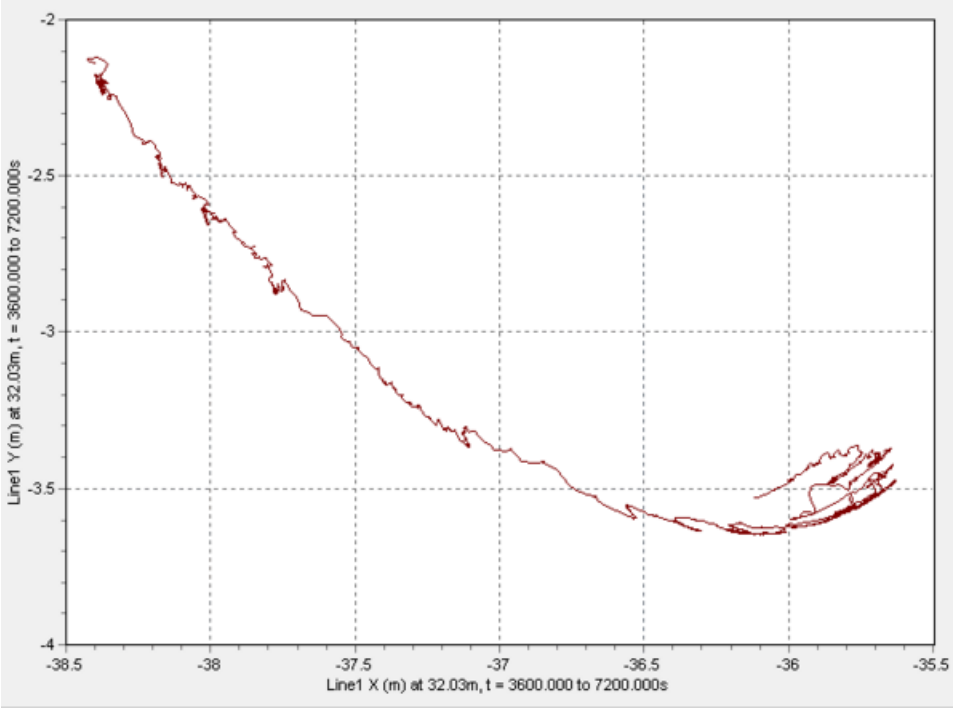

Figure 29: Plot of the motion of x-y coordinates of a chain link on the seafloor for a 1 hour OrcaFlex simulation.

The total motion of all links in the touchdown region was calculated. The eight links with the largest total motion were used to calibrate a value of the wear coefficient, *K*, such that the predicted wear + corrosion matched the measured material loss.

The corrosion predicted by the Melchers et al. (2007) model was compared to the measured material loss for chain links along the seafloor. Figure 30 shows a histogram of diameter loss rate from the nominal chain diameter of 1.5" at six points along the eight chain links. Also shown is a plot of the predicted corrosion, which is presented as a normally distributed variable with an average and standard deviation calculated according to Melchers et al. (2007). The values predicted by Melchers et al. (2007) model are:

Average = 0.371 mm/yr.

Standard Deviation = 0.066 mm/yr.

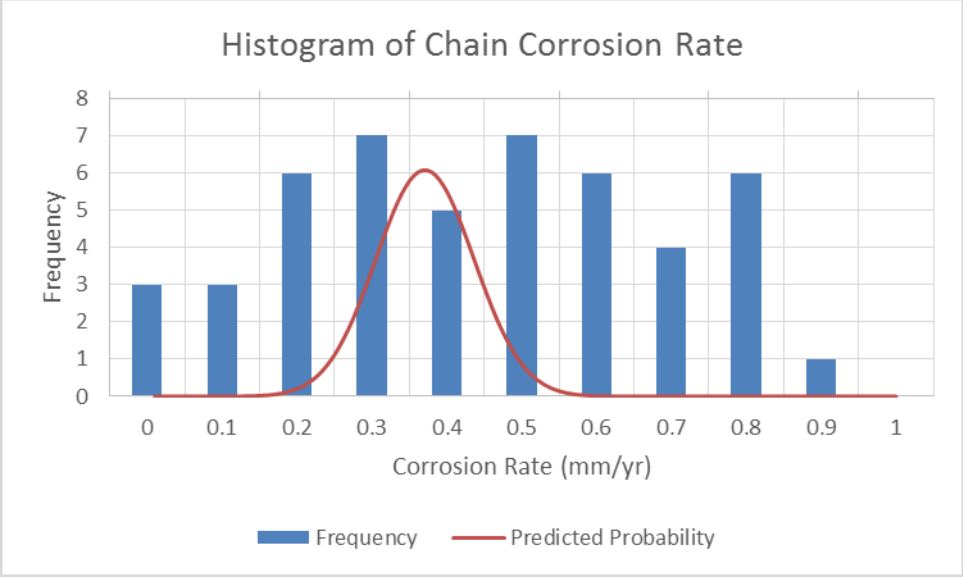

Figure 30: Histogram of corrosion rate in mm/yr. for six locations on the seafloor chain links. Measured rates are compared with predicted corrosion from Melchers et al. 2007 model.

As seen in Figure 30, the predicted corrosion falls close to the middle of the measured corrosion data points. However it is noted that there are many measurements significantly greater than the predicted value. An analysis of the field measurements indicates that all of the corrosion values above 0.7 mm/yr. occur at the crown of the link where interlink wear would be expected and may also occur (T_{w1} and T_{w2} from Figure 15). Figure 31 shows the result if the measurements at the crown of the links are not included and suggests that our methodology is usefully predictive.

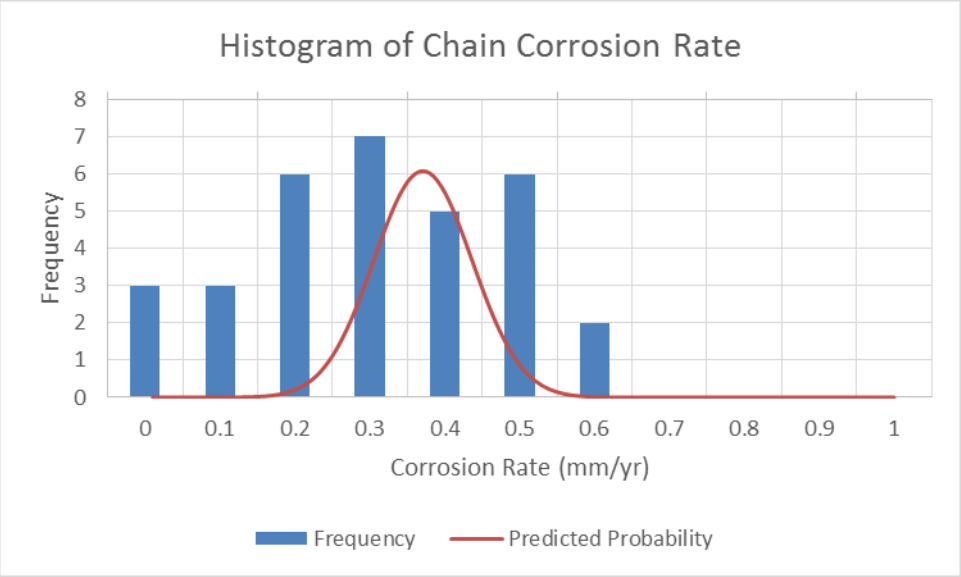

Figure 31: Histogram of corrosion rate in mm/yr. for four locations, neglecting interlink wear region, on the seafloor chain links. Measured rates are compared with predicted corrosion from Melchers et al. 2007 model.

6.2.4 Phase 2: ATON Buoys on US Coasts including AK and HI

During the analyses of buoys in Phase 1, it was determined that while data from six buoys were enough to identify trends, it was not enough to create a predictive model of chain material loss. Using public information from the USCG, a list of 54 ATON buoys was identified as being representative of the US coast including the coasts of Alaska and Hawaii. All of these are exposed buoys and represent a range of oceanic conditions. Unfortunately many of the buoys in the Gulf of Mexico, Caribbean, and Hawaii are privately maintained and little or no data is available for buoys in those regions. A complete list of the USCG ATON buoys selected for this study is included as APPENDIX 1 of this report. A total of 54 buoys were studied with a range of depths, bottom types, and hydrology conditions.

Maintenance records for ATON buoys are contained in notebooks on the responsible buoy tender and are copied into the Aids to Navigation Info System (I-ATONIS), a USCG database. Access to this database is restricted to USCG personnel, the National Oceanic and Atmospheric Administration (NOAA), and the National Geospatial-Intelligence Agency (NGA). Within the USCG access is restricted to local Aids to Navigation Teams, to personnel on the 65 foot icebreaking tug or on USCG buoy tenders.

USCG personnel in the First Coast Guard District, Aids to Navigation Office in Boston provided information from the I-ATONIS database on each one of the buoys. In some cases there were gaps in the field data, most often because measurements were not taken on removed chain - only chain that is inspected and left in service. A complete description of all of the buoys used in this study is included as Table 56 in Appendix 3. Maps showing the distribution of buoys selected for this study are shown below in Figure 32 and Figure 33. Slightly more buoys were selected in New England than other regions of the US because early stages of the study concentrated on buoys in New England waters.

Figure 32 Locations of USCG ATON Buoys used in this study

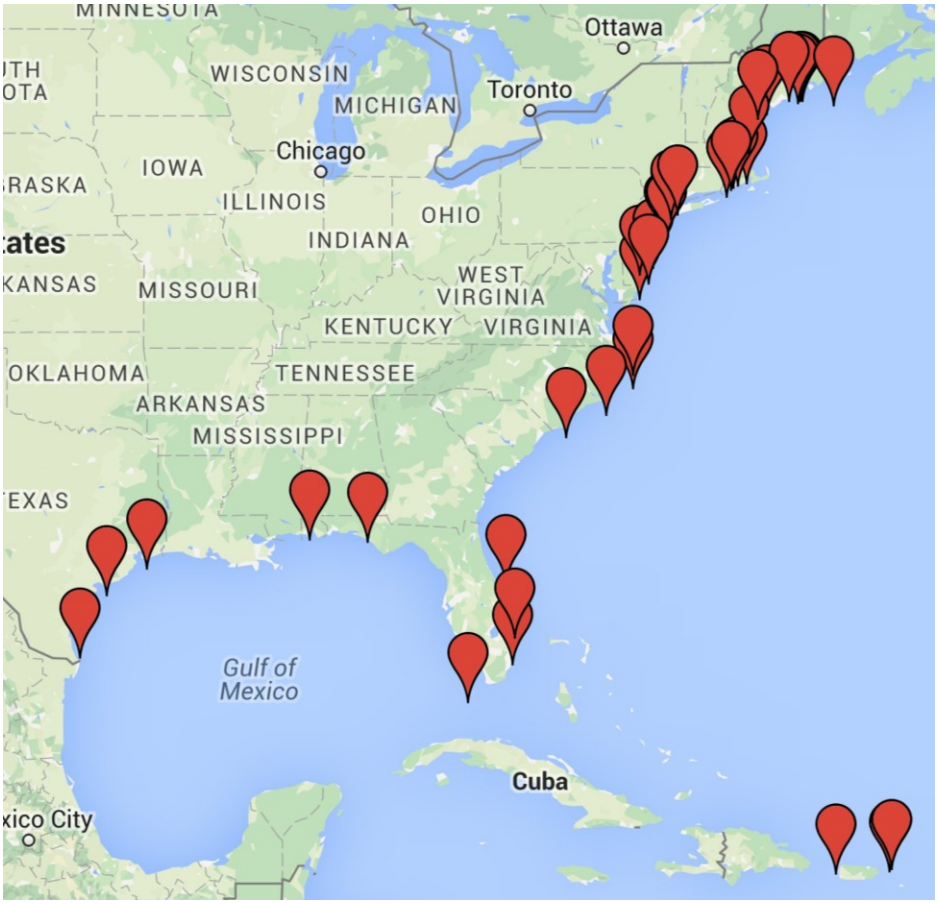

Figure 33 Distribution of USCG ATON Buoys selected from East Coast and South for use in this study

Table 11 summarizes the information collected from the USCG I-ATONIS database. The majority of the buoys are placed at sites with bottom types of mud, rock or sand.

Table 11 Maximum chain material loss rate was 0.81 inches per year

Bottom Type	# Samples	Material Loss (in/year)	
		Average	Maximum
coral	3	0.185	0.278
gravel	2	0.184	0.228
mud	17	0.167	0.383
rock	11	0.155	0.346
sand	18	0.161	0.281
shells	3	0.384	0.810
Total	***54***		

The USCG has defined a number of standard hull types to be used in its larger ATON buoys. Figure 34 is a set of drawings of the three types used across all 54 of the buoys in this study.

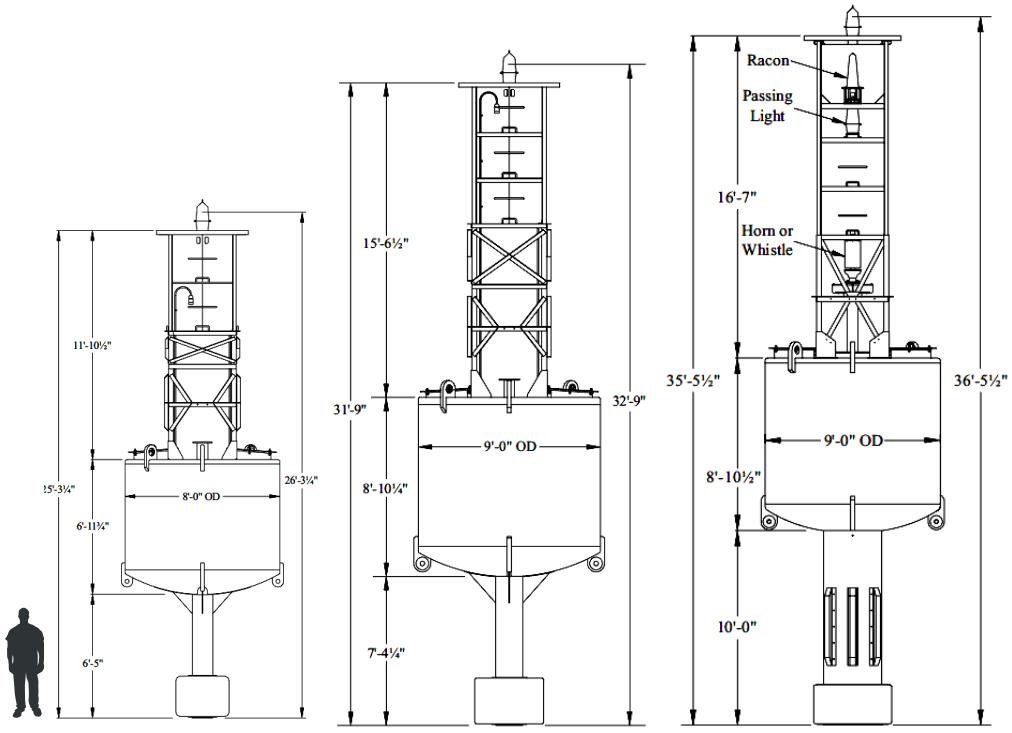

Figure 34: Dimensions for 8X26, 9x32 and 9x35 hulls used for USCG ATONs. Drawings are approximately to scale. (USCG, 2010)

Data from the more comprehensive data set was analyzed in two different ways. First a computer model was developed to estimate the annual energy applied to the chain, and the correlation between results from this model and measured chain-material loss was calculated. Second, data sources were identified that describe the ocean hydrology in the vicinity of each

ATON buoy. In this context, the term hydrology refers to the concentration of organic and inorganic materials in the water, and to the temperature and salinity of the water. The project team explored the correlation between the density of chemical components in the water and the loss of chain material.

6.2.4.1 Abrasion Analysis Using Chain Energy

From previous work on this project, it was concluded that the exposure of an ATON buoy has a strong correlation with material loss from the chain in the chafe zone. To refine this observation, an attempt was made to correlate the chain material loss with the annual energy applied to the chain. The hypothesis was that each cell in a wave scatter table can be converted to the energy applied to the buoy in surge and heave. By calculating these energies and by finding the weighted sum based on the probabilities of each cell, an energy index is created representing the total energy per year. By investigating the correlation between the energy index and the annual material loss in the abrasion zone, it should be possible to determine the ability of the energy index to predict future material loss.

The nearest ocean/weather buoy was identified for each ATON buoy considered in this project. Most of the ocean/weather buoys are operated by the National Data Buoy Center (NDBC) in the National Oceanographic and Atmospheric Administration (NOAA). The NDBC has been operating buoys for decades and offers current data for each buoy and in some cases historical data as well. Depending on the sensor package installed on a given buoy, it may be able to capture wave heights, periods, and headings, as well as ocean temperature and a variety of wind data. For many buoys the NDBC has post-processed years of data, creating quality-checked summaries of the data collected by each buoy. Some of this quality-checked historical data is provided in the form of wave scatter tables.

Wave Scatter Table. Table 12 is a wave scatter table created by the NDBC to describe the likelihood of various combinations of significant wave height and zero-crossing periods for NDBC Station 44007, which is located 12NM southeast of Portland, Maine. This table gives the probability of each metocean condition over a full year. For example, the cell at the intersection of "significant wave heights of 3.5 to 4.4m" and "wave periods of 10.0 to 12.9 seconds" shows a probability of 0.4%. This can be interpreted to mean that out of the entire year, there is a 0.4% likelihood of this storm condition. The sum of all of the probabilities in this table is 100% representing all of the likely conditions for a year.

ATON Buoy Response Amplitude Operator (RAO). A transfer function is a simple model of a process – the input value is multiplied by the transfer function to generate an output. An RAO is a frequency-domain transfer function for which each frequency component in the input spectrum is multiplied by the corresponding component in the RAO to produce a spectrum of output components. The RAO can be dimensional, converting amplitudes of input variables to amplitude of output variables. As a frequency-based transfer function can be represented by a scalar gain value and a scalar phase shift, the basic RAO is a complex variable function of frequency. Often the RAO is represented as a magnitude function in which each complex value is replaced by its equivalent magnitude, and the phase shift information is dropped.

The motion of the buoy can be described by six degrees of freedom, three linear and three rotational. The buoy is rather stable in design, moving up and down in heave, and fore and aft in surge or sway. Assuming that the energy can be represented by waves going in a single direction, arbitrarily the surge direction, it is possible to eliminate sway as a degree of freedom contributing to abrasion. Unless the fairlead attachment point to the buoy is significantly below

the center of gravity of the buoy, the small amount of pitch or roll motion will not be converted into any significant movement at the seafloor touchdown point. As the buoy is radially symmetric, any yaw motion in the buoy is lost as energy is applied to the mooring chain.

The motion of the buoy is a function of the wave heights and periods, the buoy's mass, damping and restoring forces, and the weight of the chain suspended below the buoy. ATON chain is heavy and plays a significant role in the motions of the buoy, so the ANSYS Aqwa Cable Dynamics module is used to calculate the surge and heave RAO for the buoy/chain ATON system.

By using a software tool such as the "ANSYS Aqwa with Cable Dynamics" it is possible to find the RAO to convert each component in a sea spectrum into each component in a heave or surge response spectrum. By selecting an input sea spectrum and multiplying it by the RAO, it is possible to predict the heave or surge response spectrum for the selected sea spectrum. The theory behind these calculations is described in the Aqwa Theory Manual (Aqwa, 2013).

Mooring Chain Energy from Spectral Density Function. Each cell in the wave scatter table represents a specific significant wave height Hsig and an average zero crossing period Tz. Assuming that the wave distribution follows a statistical distribution such as the Pierson-Moskowitz formulation for a fully-developed sea, it is possible to replace the (Hsig, Tz) value with the components of an actual sea spectrum.

For a given frequency the surge or heave velocity spectral response function is described by:

$$S_v^*(\omega) = \frac{\frac{1}{2} v(\omega)^2}{\partial \omega} \quad (15)$$

The asterisk on the S function signifies that the spectral response function is double sided for both positive and negative frequencies. The energy associated with a sinusoidal velocity function is:

$$E(\omega) = \frac{1}{2} m * v(\omega)^2 \quad (16)$$

Combining these equations yields:

$$E(\omega) = m * S_v^*(\omega) \partial \omega \quad (17)$$

The total energy associated with this degree of freedom is:

$$E_{TOTAL} = m * \int S_v^*(\omega) \partial \omega \quad (18)$$

This integral is calculated over the non-zero range of the spectral density function. This calculation is done numerically, so integration is replaced with weighted addition. The result of the integration is a scalar energy value representing the energy applied to the buoy/chain system for a unit length of time. This value is called the Energy Index in this report.

Mass in the Energy Equation. Equation (18) describes the kinetic energy related to the oscillatory motion of an object. To describe the energy in the buoy itself, the mass of the entire buoy could be used. However, this project is concerned with the velocity energy applied to the chain, which is independent of the energy in the buoy itself. Therefore it could be argued that the mass of the chain suspended in the water column below the buoy could be used, or the mass of a single link should be used. If the mass in Equation (18) is the mass of the entire buoy/chain system, then the Energy Index should be normalized by the mass of the chain/buoy system or by the mass of the suspended chain above the touchdown point. During this project it was found that a unit mass is the best value because the actual mass is that of a single chain link which is almost constant throughout the study.

Calculating the Velocity/Position Indices: The indices calculated in this report have been named the Velocity Index and the Position Index. The Velocity Index is defined in Equation (18), with the assumption that the mass is 1. Replacing the velocity response with the position response in Equation (19) yields the Position Index. As defined, both indices are dimensional. Since the dimensions/scale factors are constant throughout this report, it is acceptable to use a dimensionalized definition.

Figure 35 illustrates the steps in calculating the energy index. The process starts with a wave scatter diagram or table that describes the statistical distributions of sea-states at the ATON buoy site. Data in this table includes the storm statistics, Hsig/Tzero, and the probabilities of each set of storm conditions. An ANSYS Aqwa model and analysis are used to find the response spectrum for each individual Hsig/Tzero pair. The area under the response spectra are calculated as in Equation (18). The probabilities from the wave scatter table are used as weights to create a weighted sum of the velocity/position indices.

Velocity and position indices can be combined in multiple ways. In this report the sum of the heave velocity index and the surge velocity index are called the "total velocity index."

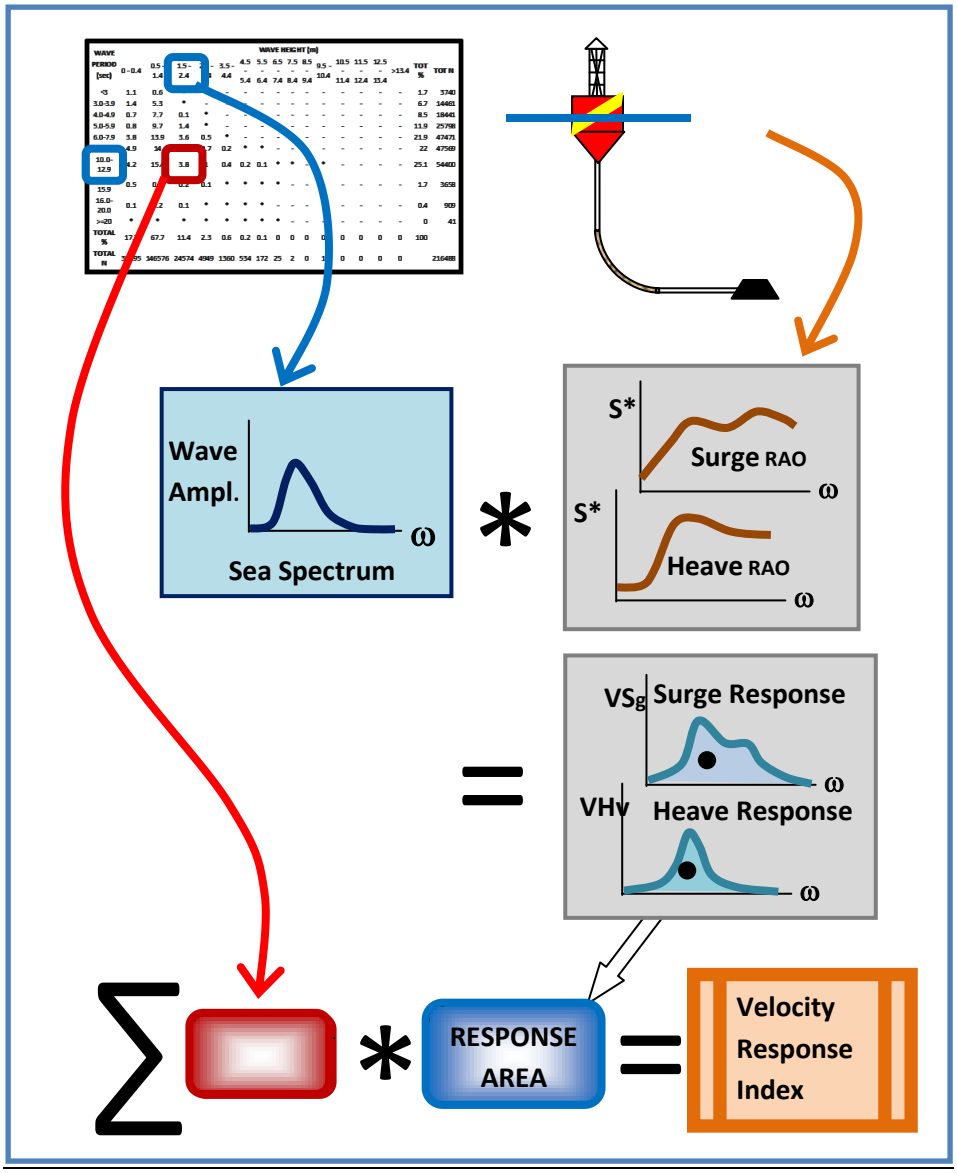

Figure 35 Calculating Velocity Response Index. Wave Scatter table in upper left supplies probability of storm type and Hsig/Tz. ANSYS Aqwa used to calculate RAOs. Custom MATLAB script adds weighted areas under response spectra to calculate Velocity Response Index.

Table 12 Annual Wave Scatter Table at NDBC Buoy 4407 (Portland, ME)

WAVE PERIOD (sec)	WAVE HEIGHT (m)																
	0 - 0.4	0.5 - 1.4	1.5 - 2.4	2.5 - 3.4	3.5 - 4.4	4.5 - 5.4	5.5 - 6.4	6.5 - 7.4	7.5 - 8.4	8.5 - 9.4	9.5 - 10.4	10.5 - 11.4	11.5 - 12.4	12.5 - 13.4	>13.4	**TOT %**	**TOT N**
<3	1.1	0.6	-	-	-	-	-	-	-	-	-	-	-	-	-	1.7	3740
3.0-3.9	1.4	5.3	*	-	-	-	-	-	-	-	-	-	-	-	-	6.7	14461
4.0-4.9	0.7	7.7	0.1	*	-	-	-	-	-	-	-	-	-	-	-	8.5	18441
5.0-5.9	0.8	9.7	1.4	*	-	-	-	-	-	-	-	-	-	-	-	11.9	25798
6.0-7.9	3.8	13.9	3.6	0.5	*	-	-	-	-	-	-	-	-	-	-	21.9	47471
8.0-9.9	4.9	14	2.1	0.7	0.2	*	*	-	-	-	-	-	-	-	-	22	47569
10.0-12.9	4.2	15.4	3.8	1	0.4	0.2	0.1	*	*	-	*	-	-	-	-	25.1	54400
13.0-15.9	0.5	0.9	0.2	0.1	*	*	*	*	-	-	-	-	-	-	-	1.7	3658
16.0-20.0	0.1	0.2	0.1	*	*	*	*	-	-	-	-	-	-	-	-	0.4	909
>=20	*	*	*	*	*	*	*	*	-	-	-	-	-	-	-	0	41
TOTAL %	17.7	67.7	11.4	2.3	0.6	0.2	0.1	0	0	0	0	0	0	0	0	100	
TOTAL N	38295	146576	24574	4949	1360	534	172	25	2	0	1	0	0	0	0		216488

Source: http://www.ndbc.noaa.gov/data/climatic/44007.txt

6.2.4.2 ANSYS Aqwa +Cable Dynamics Models

An Aqwa model of each ATON buoy and its chain was developed from the dimensions shown in Figure 34. Information regarding the draft and mass of the buoy hull was obtained from the Coast Guard. Inertia values of the buoy were estimated making reasonable assumptions about the material composition and geometries of each segment of the buoy. The buoy was modeled as a solid floating element composed of three cylindrical segments of different diameters.

The mooring lines are modeled in Aqwa according to the specifications of USCG 1.25" and 1.5" chain. The mooring mass, equivalent diameter, stiffness, added mass, and drag coefficients are chosen from catalog values describing chain of the proper diameter. The chain is assumed to have no bending or torsional stiffness. The mooring is anchored with a concrete block that is modeled as a fixed point on the seafloor.

Three different buoy hull models were created and RAOs were calculated for the chain type and depth for each of the 54 buoys. The results of this effort are two RAOs (surge and heave) for each one of the 54 ATON buoys.

An issue for future research is whether or not current should be used in the Aqwa model. The presence of current will stretch the anchor chain, changing its effective axial stiffness due to the increased suspended chain length. For this study the anchor chain was assumed to be slack; no current was modeled.

6.2.4.3 Results and Discussion

Of the 54 buoys studied in this project, 18 are deployed over a sandy bottom. As can be seen in Figure 36, there is a great deal of scatter in the data relating material loss (abrasion) with the total velocity index (TVI).

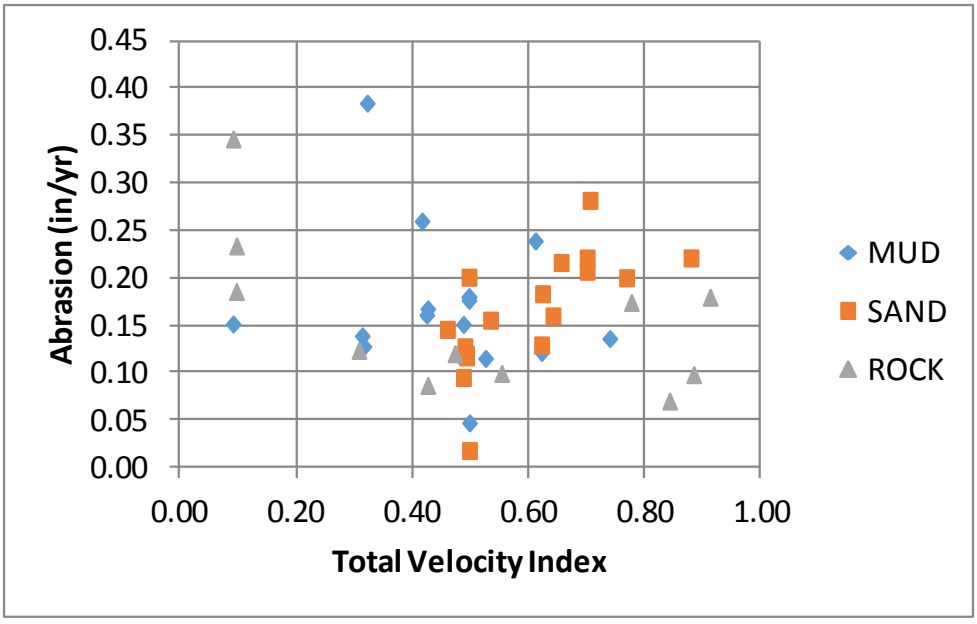

Figure 36 Mean Abrasion Rate vs. Sum of Surge and Heave Velocity Indices (Total Velocity Index, TVI)

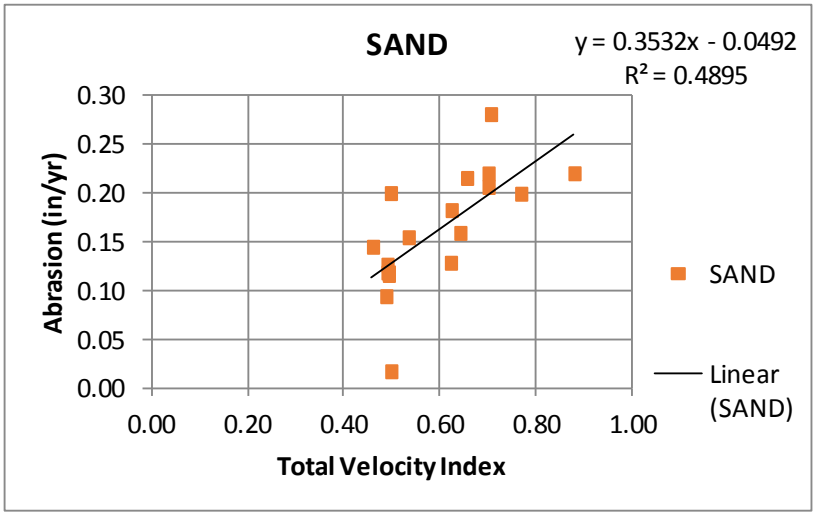

Figure 37 Mean Abrasion Rate vs. Sum of Surge and Heave Velocity Indices (Sand bottom only)

Another motion index called the "Position Index" can be defined by assuming a unit mass and replacing the velocity response spectrum with the position response spectrum in Equation 4. The Position Index is defined as in Equation (19). The "Total Position Index" is defined as the sum of the surge and heave position indices.

$$PI = \int S_p^*(\omega)\partial\omega \qquad (19)$$

Figure 38 is a chart showing the relationship between the annual material loss and the Total Position Index (TPI). There appear to be three outlier points at TPI values of 0.7 and 1.0. These three points correspond to the Columbia River, Honolulu, and San Francisco ATON buoys. Removing these points leads to the relationship shown in Figure 39. The R^2 values go from only 0.1878 using all of the data to 0.3589 after the high-motion outlier points are removed.

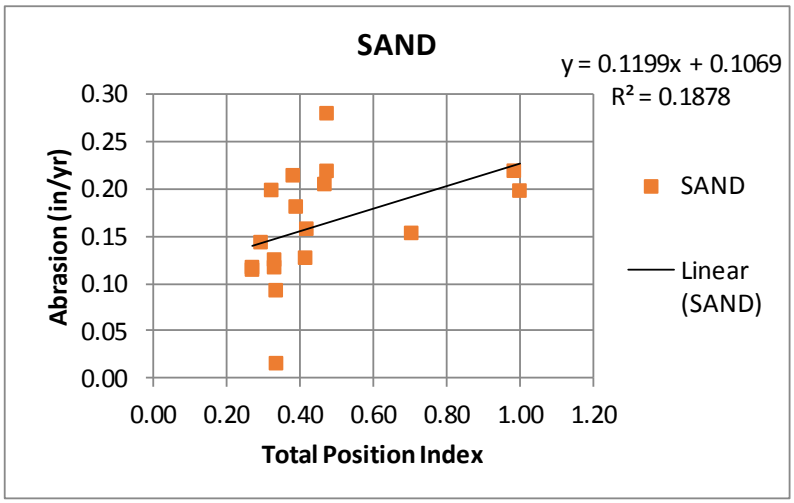

Figure 38 Mean Abrasion Rate vs. Sum of Surge and Heave Position Indices (Sand bottom only)

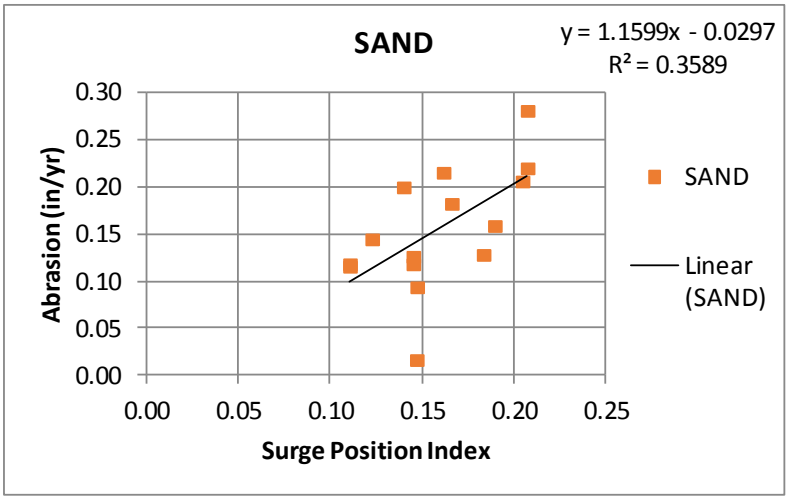

Figure 39 Mean Abrasion Rate vs. Surge Position Index (Sand bottom only, outliers removed)

Although the status of these three buoys as outliers was not as pronounced in the TVI vs. Material Loss Rate (Figure 37), after these points were removed the quality of the fit between TVI and material loss improved only slightly (Figure 40).

From all of the charts above, it can be concluded that the TVI is a better predictor of chain abrasion than is the TPI and that removing some outlier points based on the TPI makes little difference to the TVI.

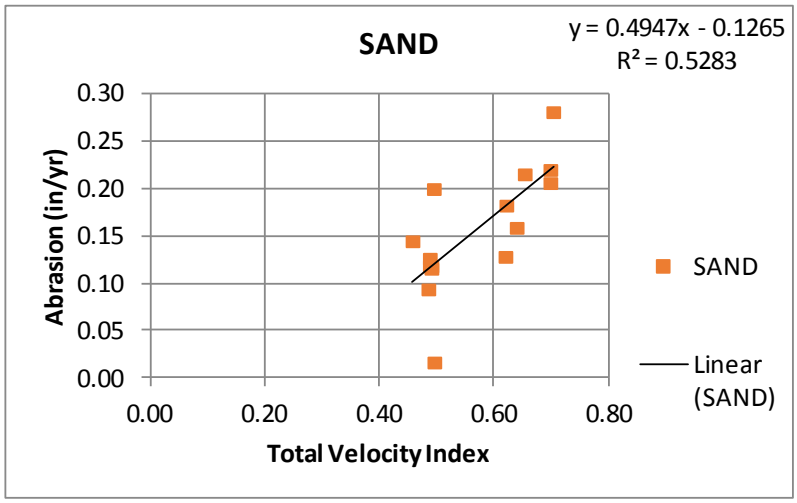

Figure 40 Mean Abrasion Rate vs. Sum of Surge and Heave Velocity Indices (Sand bottom only, outliers removed)

Additional analyses were performed investigating the link between the TVI and material loss for buoys located in rocky sea bottoms (Figure 41). The best fit between material loss and TVI came from fitting a curve to data relating material loss to the log of the TVI. As seen in this figure, the relationship is tenuous; more data would be required to validate the model.

Qualitatively Figure 41 indicates a negative relationship between the TVI and material loss for those buoys deployed over a rocky seafloor. This may be a defect of the data set, or it may

indicate some other abrasion mechanism such as active motion reducing contact with the seafloor and thus reducing abrasion.

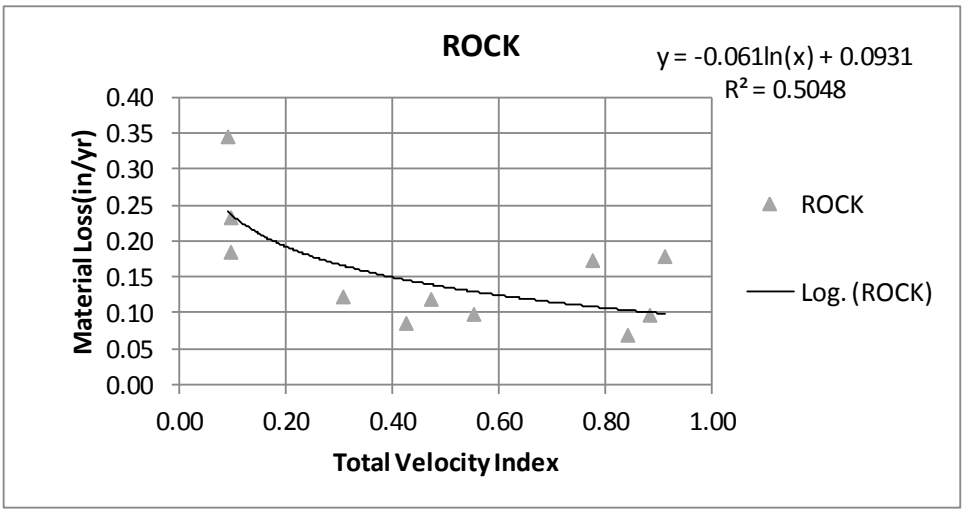

Figure 41 On rocky seafloor, there is a negative logarithmic correlation between material loss and the velocity index.

6.2.4.4 Conclusions Regarding Material Loss from Abrasion:

- Abrasion rates of ATON buoys anchored over sand bottoms appear to be correlated to buoy motion.
- The Velocity Spectrum Index is a better indicator of abrasion rate than Position Spectrum Index.
- The Total Velocity Index (TVI, Surge Velocity Index + Heave Velocity Index) is a slightly better indicator of abrasion rate than either heave or surge independently.
- Abrasion rates of ATON buoy mooring systems over rock or mud bottoms do not appear to be strongly correlated to buoy motion.
    - This may be because these categories are too broad (flat bedrock, boulders, and craggy bottoms are all rock but may have different abrasion rates).
    - This may be because the primary abrasion mechanism in a rocky environment is different from that in a sandy environment and is not related to buoy motion.

6.2.5 Predicting Corrosion

6.2.5.1 Corrosion

An empirical model for corrosion rate on submerged mooring chain was proposed by Melchers et al. (2007). This model assumes that the mooring chain is always fully submerged and is subjected to enough interlink motion that rust build-up is prevented by abrasion, or is removed within 3-4 months. A typical diagram of corrosion vs. time for submerged steel is shown in Figure 42. The proposed model is applicable to the unshaded Region 1. The requirement that abrasion prevents or removes rust build-up every 3-4 months assures that corrosion does not enter Region 2.

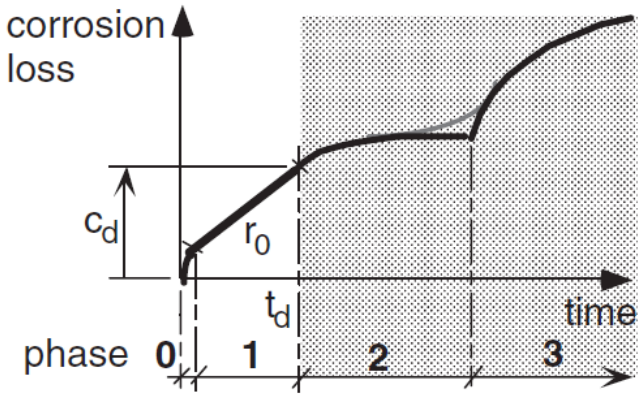

Figure 42: Typical curve of corrosion vs. time. Source: Melchers et al. (2007).

The empirical model assumes that corrosion is a function of average water temperature, average water velocity, and dissolved oxygen content. As shown in Figure 43, corrosion is exponentially related to water temperature. Corrosion is further linearly related to water velocity and dissolved oxygen. The empirical model may be reduced to two equations, for average corrosion rate and coefficient of variation (Melchers et al., 2007):

$$Avg.Corrosion = 0.056e^{0.065T}(DO\%)(1 + 4.6V) \quad (20)$$

$$Coef.of\ Variaton = (0.085 + 0.005T)^2 + \left(\frac{5\%}{DO\%}\right)^2 + 0.1^2 \quad (21)$$

Where *T* is water temperature, *DO%* is dissolved oxygen percent, and *V* is water velocity.

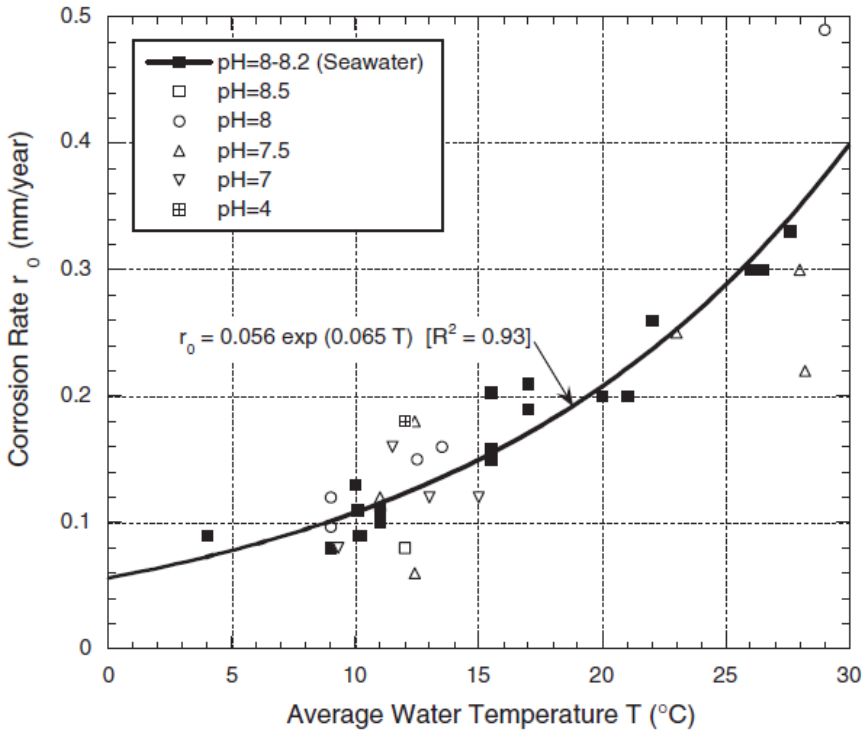

Figure 43: Relationship between rate of corrosion and average water temperature. Source: Melchers et al. (2007).

6.2.5.1.1 Environmental Data

Table 13 is a list of parameters that are known to affect the corrosivity of seawater. To investigate the correlation between these factors and the corrosion of mooring chains a source of hydrology data describing factors in this figure must be found.

Table 13 Corrosivity parameters in Seawater, reproduced from *Microbiologically Influenced Corrosion, p. 167* (Little, 2007)

TABLE 8-4 Parameters that Can Affect the Corrosivity of Seawater

- Biochemical oxygen demand during 5 days (BOD_5)
- Chemical oxygen demand (COD)
- Total organic carbon (TOC)
- Total aromatic compounds (TAC)
- Polycyclic aromatic hydrocarbons (PAH)
- Inorganic compounds (i.e., PO_4^{2-} NO_3^-, SO_4^{2-}, S_2^-, CN^-, and NH_4^+)
- Heavy metal ions (i.e., Fe, Cr, Cu, Ni, Hg, Zn, and Sn)
- Bacteriological analysis[15]
  - Most probable number (MPN) for SRB
  - MPN for sulfur-oxidizing bacteria (SOB)
  - MPN for chemoorganotrophic bacteria (COT)
  - Total bacterial count

Source: Gubner and Beech (1999a. © NACE International).

6.2.5.2 Environmental Data

This case study requires one or more sources of environmental/hydrological data. One source has been described, historical data from the nearest NDBC buoy or the equivalent. Unfortunately this data is confined to wind and wave statistics, water temperature, and possibly salinity. An additional source is required that describes the concentration of organic and inorganic compounds in the vicinity of each ATON buoy.

Oceanographers have been collecting hydrology data on the world's oceans for hundreds of years. Typically a research vessel executes a cruise with the objective of collecting a specific type of data such as oxygen percentages in the water, descriptions of microbiology populations along the way, or current gradients in the water column. Thousands of cruises have been completed and a number of attempts have been made to organize the data from all of these cruises into databases for additional research work.

Two other potential hydrological databases were evaluated for this study, the Hydrobase3 project from Woods Hole Oceanographic Institution (WHOI), and the Global Hydrographic Climatology Dataset from the World Ocean Circulation Experiment (WOCE). Ultimately the latter was chosen for this project, primarily due to the relatively complete dataset in this database.

6.2.5.2.1 WHOI Hydrobase3

Hydrobase3 is an effort by researchers at WHOI to combine climatology and hydrology datasets into a single database. The project was built on a more general database system netCDF. NetCDF is a set of self-describing, machine-independent data formats implemented as software libraries. The software system was developed by the Unidata program at the University Corporation for Atmospheric Research (UCAR) to support creation, access, and sharing of array-oriented scientific data. The Hydrobase3 team created a specialized set netCDF-data definitions and dozens of command line programs to access this data. The data definitions and programs are all designed to support grid-based hydrological data captured primarily from research cruises.

> "HydroBase3, developed by Woods Hole Oceanographic Institution, is a tool for climatological analysis of oceanographic properties. The package is comprised of software and database products that together provide a flexible means of constructing and analyzing datasets customized to investigators' research needs."
> *[Statement on http://www.whoi.edu/science/PO/hydrobase/php/index.php. June 2015]*

The Hydrobase3 system supports gridded climatology and topography data in netCDF format. The climatology data includes monthly and annual objectively mapped fields of pressure, temperature, salinity. The topography data includes seafloor topography (depth) at a 1 minute-arc resolution. Further, the system supports observed profile data on individual cruises. The goal of the Hydrobase3 software system is to enable users to use these databases for further analysis to create such things as property plots, vertical sections, horizontal maps, and time-series plots of ocean components.

The set of observed profile data were collated from the World Ocean Database, WOCE Hydrographic Programme (WHPO), CLIVAR Carbon and Hydrographic Data Office (CCHDO), Argo, and also from individual scientists and oceanographers. The profiles include original observations of pressure, temperature, salinity, oxygen, nutrients, and tracers, and they look to be of value to this project.

WHOI distributes gridded climatology products are as netCDF files organized by ocean basin (e.g. a single file covering the Indian Ocean). Also distributed by WHOI is a 1 arc-minute and 0.1

degree global relief model of the Earth and ice surface integrating land topography and ocean bathymetry.

Experiences and Observations with Hydrobase3. The project team acquired the Hydrobase3 source files and built a working version of the Hydrobase3 system for Window 7. At that point this project team investigated the distribution datasets and determined that the WHOI data does not include the oxygen, nutrients and tracer data components, and that this team would have to find other public sources of data to populate the database. Although other sources of data for the Hydrobase3 system were identified, the team was unable to construct a robust Hydrobase3-based database for use in this project.

6.2.5.2.2 WOCE Global Hydrographic Climatology Dataset

During the search for additional hydrological datasets for Hydrobase3 described in the previous section, the Global Hydrographic Climatology Dataset (WGHC) from the World Ocean Circulation Experiment (WOCE) was identified as a possible alternative source of environmental and hydrological data. The WGHC gridded data set on 45 depth levels with a 0.5-degree resolution. The following quotations are taken from the WGHC page at the Bundesamt für Seeschifffahrt und Hydrographie website (BSH, 2015):

> "High quality hydrographic observations from the WOCE one-time and repeat hydrographic cruises with ca. 9000 stations for the period 1990- 1998 are the modern basis.
>
> "The reference observed data set, comprising WOCE and high quality cruises occupied after 1970 (a total of 19867 profiles distributed over 384 cruises) is used to quality control a historical data set of older cruises occupied mostly before 1970 and profiles not included in the high–quality subset (a total of 1 039 668 profiles distributed over ca. 42 000 cruises).
>
> "… the original profile data have been [averaged at a constant data density] using optimal interpolation. Seven parameters subjected to a strict quality control are given: temperature, potential temperature, salinity, oxygen, silicate, nitrate, phosphate."

The actual WGHC data was found on a mirror website hosted by the Institute of Atmospheric Physics, Chinese Academy of Sciences at:

- CD-1: ftp://ds1.iap.ac.cn/ftp/ds022_WOCE-CD1_0_0_ascii/
- CD-2: ftp://ds1.iap.ac.cn/ftp/ds023_WOCE-CD2_0.5_0_ascii/

The gridded data is in the folder labeled CD-2. Parameters in the WGHC database are listed in Table 14. The database includes quantitative levels of chemical contaminants, but does not address microbiological contaminants directly. This study investigated correlations between material loss and each of the following factors from the WGHC database:

- Surface Temperature
- Salinity (g/kg)
- Oxygen (ml/l)
- Silicate (umol/kg)
- Nitrate (umol/kg)
- Phosphate (umol/kg)

For many buoys the source data was incomplete so a number of buoys were omitted from this portion of the study. Table 58 in APPENDIX 1lists the data extracted from the WGHC for this study. Any fields in this table marked "Unknown" represent missing data in the gridded database.

Table 14 Data Members in WOCE Profile

PARAMETER	DEFINITION
NBRLEV	Number of gridded levels
RADBUB	Radius of the influence bubble (km)
RADCOR	Decorrelation length scale (km)
DEPTHML	Mixed layer depth (m), defined as depth where vertical density gradient >= 0.005 kg/m4
XGRID	Grid-node longitude (from 0 to 359.5e)
YGRID	Grid-node latitude (from -80s to 90n)
ETDEP	Grid-node etopo5 depth (m)
PAR(1,K)	Depth (m) of the k-th level
PAR(2,K)	Pressure (dbar)
PAR(3,K)	Temperature_in-situ (degr. C)
PAR(4,K)	Potential temperature (degr. C)
PAR(5,K)	Salinity (g/kg)
PAR(6,K)	Oxygen (ml/l)
PAR(7,K)	Silicate (umol/kg)
PAR(8,K)	Nitrate (umol/kg)
PAR(9,K)	Phosphate (umol/kg)
PAR(10,K)	Gamma-n
PAR(11,K)	Sig-0 (kg/m3)
PAR(12,K)	Sig-2 (kg/m3)
PAR(13,K)	Sig-4 (kg/m3)
ERROR(1,K)	Relative optimum interpolation error for t, theta & s
ERROR(2,K)	Relative optimum interpolation error for oxygen
ERROR(3,K)	Relative optimum interpolation error for silicate
ERROR(4,K)	Relative optimum interpolation error for nitrate
ERROR(5,K)	Relative optimum interpolation error for phosphate
LEVELS(1,K)	Actual number of observations used for the optimal interpolation of t, theta & s
LEVELS(2,K)	Actual number of observations used for the optimal interpolation of oxygen
LEVELS(3,K)	Actual number of observations used for the optimal interpolation of silicate
LEVELS(4,K)	Actual number of observations used for the optimal interpolation of nitrate
LEVELS(5,K)	Actual number of observations used for the optimal interpolation of phosphate

PARAMETER	DEFINITION
VAR(1,K)	Temperature standard deviation from the mean (within the influence radius = radcor)
VAR(2,K)	Salinity standard deviation from the mean (within the influence radius = radcor)
VAR(3,K)	Oxygen standard deviation from the mean (within the influence radius = radcor)
VAR(4,K)	Silicate standard deviation from the mean (within the influence radius = radcor)
VAR(5,K)	Nitrate standard deviation from the mean (within the influence radius = radcor)
VAR(6,K)	Phosphate standard deviation from the mean (within the influence radius = radcor)

6.2.5.3 Correlation between Hydrology Data and Chain Material Loss

Data from the NDBC buoys includes 50-percentile temperatures. The WGHC database includes mean temperatures at various depths for all of the buoys except two. Mean temperature values from the NDBC buoys were used to replace the missing data in the WGHC database.

Figure 44 shows the relationships between mooring line material loss and the mean temperature, with the data segregated by bottom type. As can be seen in this figure, the relationship is weak, at least for the ATON buoys used in this study.

The goal of this work was to identify predictor variables and relationships to calculate the material abrasion rate, with a high degree of accuracy. To accomplish this, the candidate predictor variables must be independent, or at least have low cross-correlation values. Figure 45 shows the very strong linear correlation between temperature and phosphate and oxygen levels. The correlation is slightly weaker between temperature and silicate and nitrate levels. The cross-correlation between impurity levels is evident as well. From this data it can be concluded that only one of the variables is sufficient to represent all of them. In this study the Phosphate level was selected to be the independent or predictor variable.

When all of the data points were considered in the aggregate, the correlations between the individual contaminants and material loss are low. Noticing that the relationships between material loss and phosphate levels seemed to fall into several clusters, the ATON buoys were split into geographic groups to be considered separately: Northeast, Southeast, Gulf of Mexico, and West.

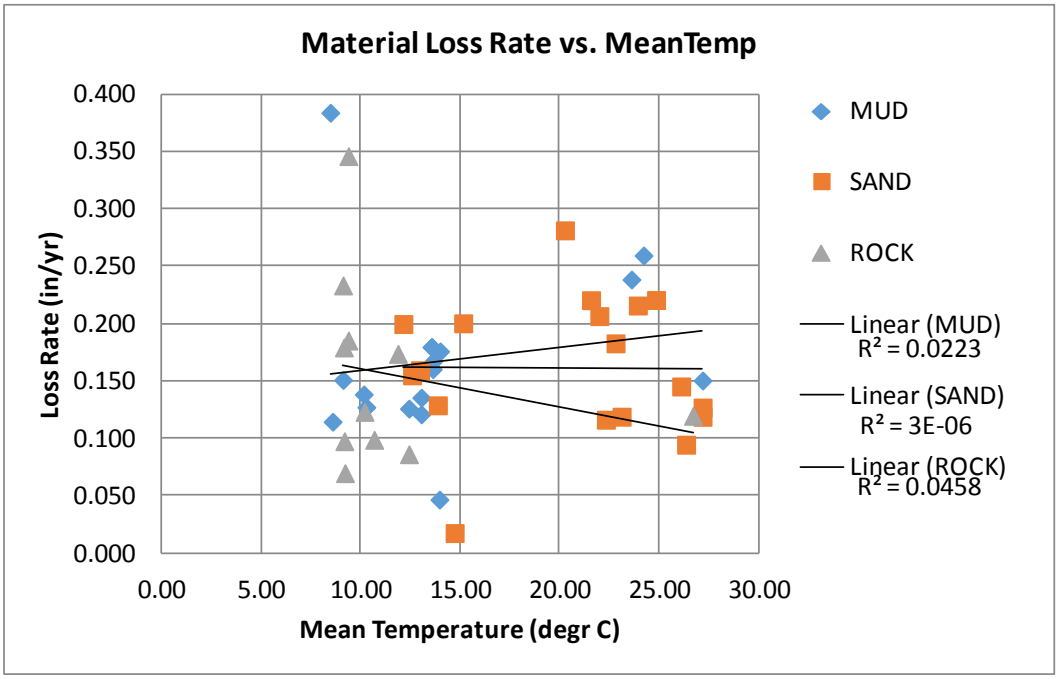

Figure 44 Mean Material Loss vs. Mean Water Temperature, by Bottom Type

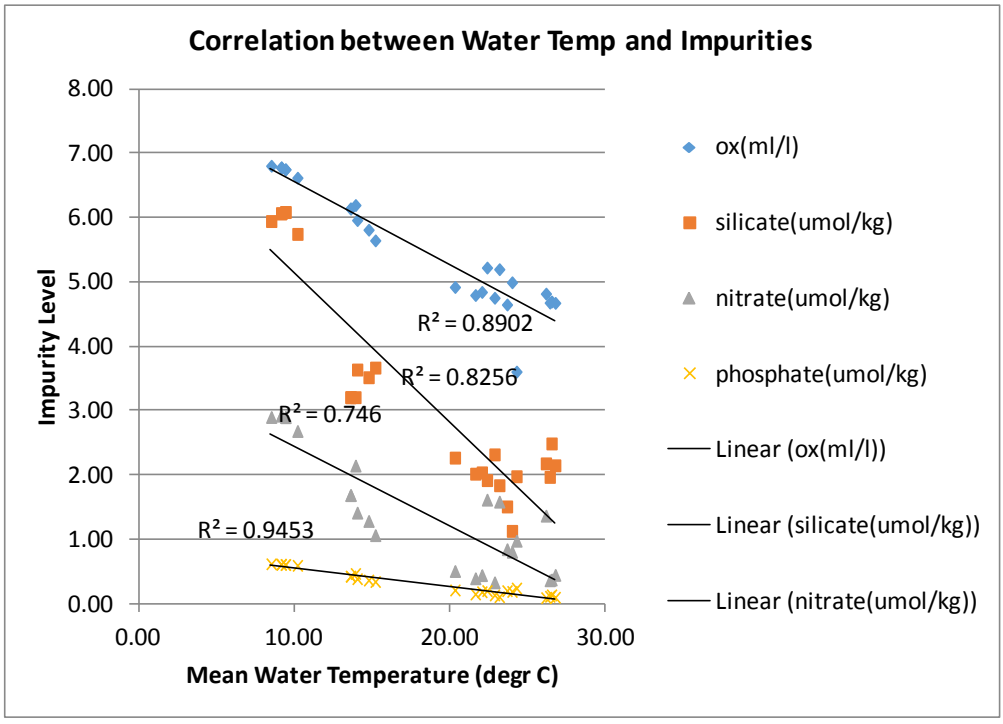

Figure 45 Correlation between water temperature and impurities. There is a strong linear correlation between temperature and phosphate and oxygen levels. The correlation is slightly weaker between temperature and silicate and nitrate levels.

Table 15 Correlation between chemical contaminates in sea water.

	Oxygen (ml/l)	*Silicate (umol/kg)*	*Nitrate (umol/kg)*	*Phosphate (umol/kg)*
Oxygen	1			
Silicate	0.6352	1		
Nitrate	0.7133	0.9633	1	
Phosphate	0.8518	0.8879	0.931	1

As seen in Table 13 the correlation between the levels of contaminants in sea water is high, probably due to a combination of common sources between the various chemicals. More data would be required to distinguish between the chemical contaminants. Given the high level of correlation, a single chemical contaminant can be chosen to represent the entire group. In this report the phosphate level was chosen for further correlation studies.

Figure 46 shows the results of considering clusters of buoys. The correlation between material loss and phosphate levels is strong for buoys in the southeast region, roughly stretching from Nags Head, NC to Miami, FL, as is the correlation associated with buoys in the Gulf of Mexico. The correlation between material loss and phosphate levels in buoys in the Northeast is less apparent, although there is a positive correlation. Finally there is no obvious correlation between material loss and phosphate levels for West Coast buoys, probably because the sample size is small and other factors dominate corrosion mechanisms.

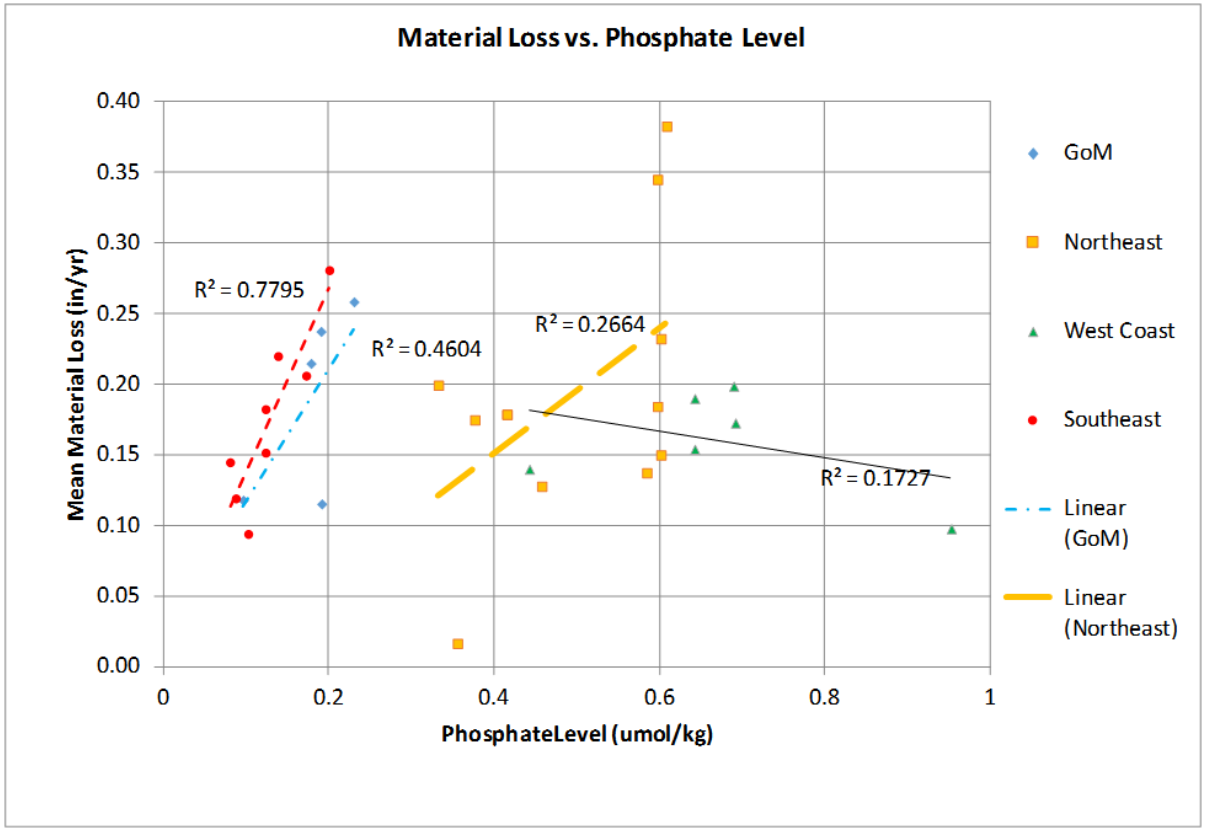

Figure 46 On a regional basis there is a strong correlation between measured material loss and phosphate levels.

This report has considered buoy motion, temperature and water impurities as predictors of material loss. A question that should be considered is whether or not the level of chemical contaminants is a function of the velocity index, essentially whether the level of chemicals in the water is a function of wave action. Figure 47 shows that at least for this data set there is significant correlation between buoy motion and water impurities. Further research with more complete data sets is indicated to determine what the actual predictor variables are for chain abrasion and corrosion.

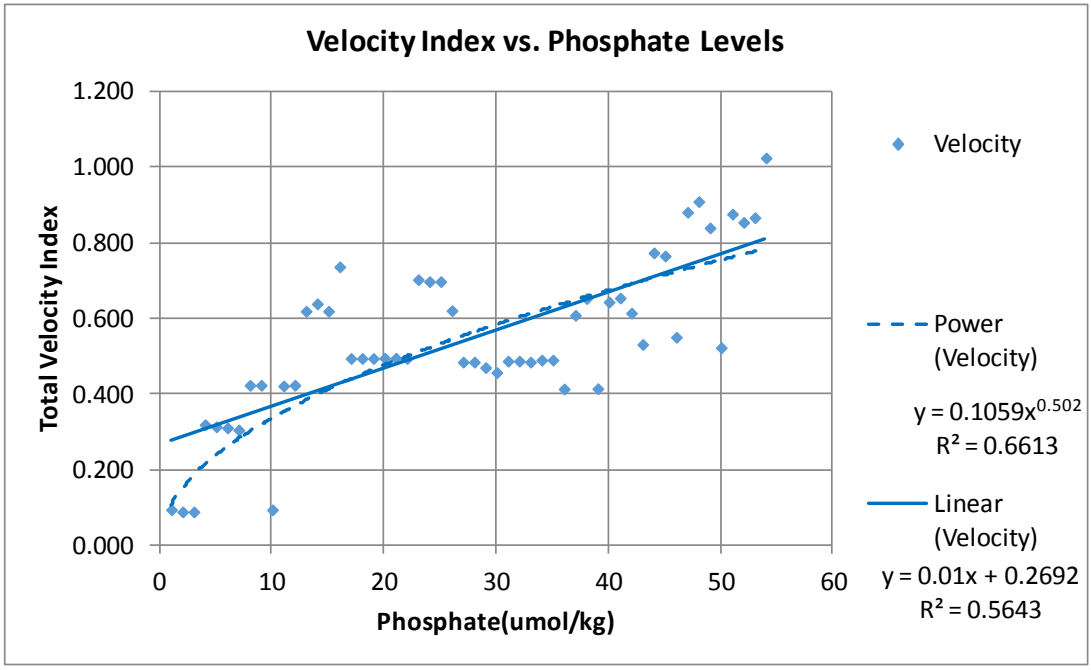

Figure 47 Relationship between Total Velocity Index (TVI) and Phosphate levels.

6.2.5.4 Conclusions and Discussion

- Looking at the entire data set as a whole, temperature is not a good predictor of material loss/corrosion.
    - Categorizing the data by bottom type (rock, sand, etc.) does not improve the correlation between temperature and corrosion significantly.
    - The correlation between mean ocean temperature and contaminants such as silicate, oxygen, nitrates, and phosphates is high.
- It is unlikely that any of the contaminants will be good predictor of the corrosion levels of the data set as a whole.
- Categorizing the data set by geographic region improves the correlation between phosphate levels and corrosion significantly.
- There is a significant correlation between the Total Velocity Index, a mechanical predictor, and the chemical contaminant levels, e.g. phosphate. More research is required to determine whether the variables are independent of each other, or if the TVI and the chemical contaminant levels are equivalent as material loss predictors.

6.2.6 Future Plans

The ATON buoys examined in this case study were selected as exemplars for floating offshore wind turbines. Mooring chains on ATON buoys are often in place for multiple years and sometimes for decades, so the time scales are equivalent. Mooring chains on the buoys are much smaller than on FOWTs and the motions are expected to be much higher so any corrosion and abrasion effects should be magnified on ATON buoys. The data provided by the USCG was valuable for this study, but additional data is needed to gain a better understanding of the

relationship between bottom types, energy levels, the chemical makeup of the sea, and material loss in mooring chains:

- Better knowledge of the bottom characteristics for each buoy deployment would be very useful to the study. Correlation studies show that categorizing the data by bottom type improves the correlation between other factors and material loss.
- While useful, the WOCE WGHC database has significant gaps in coverage. The NOAA World Ocean Database looks like a promising source of new hydrological information. Possibly this database can be accessed with the Hydrobase3 programs.
- The size of the dataset can be increased by adding buoys from other bureaus and from other countries.

One of the goals of this case study is to assess methods of predicting corrosion and abrasion and to compare them against current industry practice recommended in API-RP 2SK and DNV-OS-E301, for example. As has been discussed in detail in previous phases of this project, there is a growing body of evidence to suggest that current industry practice for predicting corrosion and abrasion on mooring lines is inadequate and under predictive. Therefore, more sophisticated models may be necessary for predicting degradation of mooring chain on FOWTs.

6.3 DeepCwind 50Th Scale Model

The DeepCwind Joint Industry Project was conducted from 2009 – 13, headed by the University of Maine with the financial support of the Department of Energy, and technical support of several organizations. As part of this research, three generic FOWT concepts were tested at 1/50th scale at the Maritime Research Institute Netherlands (MARIN) wave basin facility and reported in earlier works of MARIN (2011), Martin et al. (2012), Kimball et al. (2012) and Koo et al. (2012). The floater concepts included 1:50 scaled models of a spar buoy (Spar), a tension leg platform (TLP), and a semi-submersible (Semi). Data from the semi-submersible model was selected for this case study.

Figure 48 and Figure 49 respectively show the side and top views of the model. Figure 50 and Table 18 show the semi-submersible model and model tests with wind turbine installed on the Semi. Table 16shows the main properties of the semi-submersible platform. The prototype water depth was 200m and the draft was 20m. This wind turbine model was based on the NREL 5MW wind turbine, whose main properties are shown in Table 17. Table 18 and Table 19 show the major properties of hub and nacelle and blade respectively.

Figure 52 shows the semi wind turbine model set-up in the basin. The prototype mooring system includes three catenary lines oriented at 180, 60 and 300 degrees with respect to x axis. The lines were studless chains with properties as shown in Table 5. The mooring system used in the model experiments were made up of inextensible lines attached to linear springs located at the anchors to provide a close match to the prototype stiffness values.

Among various measurements made during the experiment, the platform motions and mooring line tensions were made available for this study. All results presented in this report are in full scale units.

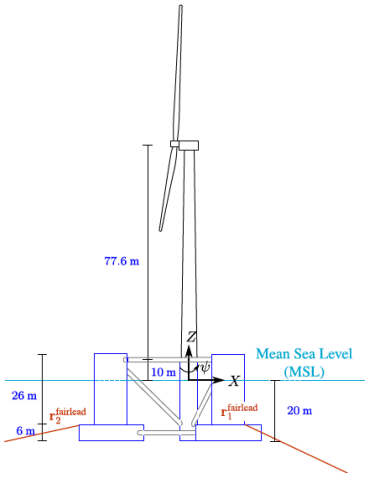

Figure 48 Side view of Semi wind turbine model (MARIN, 2011)

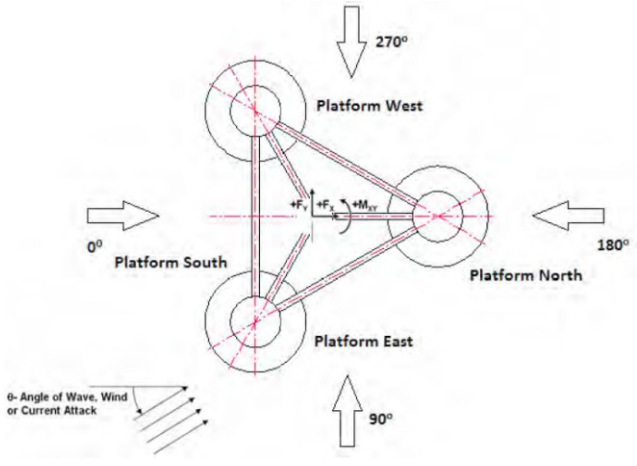

Figure 49 Top view of Semi wind turbine model (MARIN, 2011)

Figure 50 Semi model.

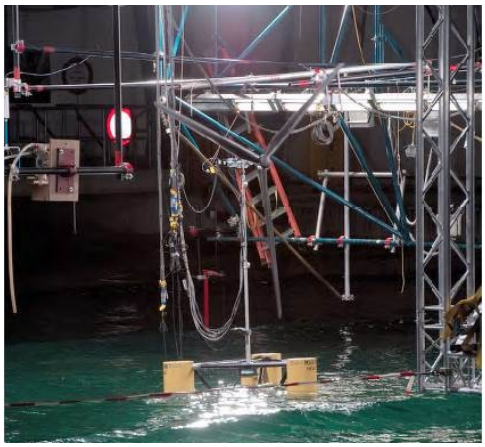

Figure 51 Model tests with wind turbine and Semi (MARIN, 2011)

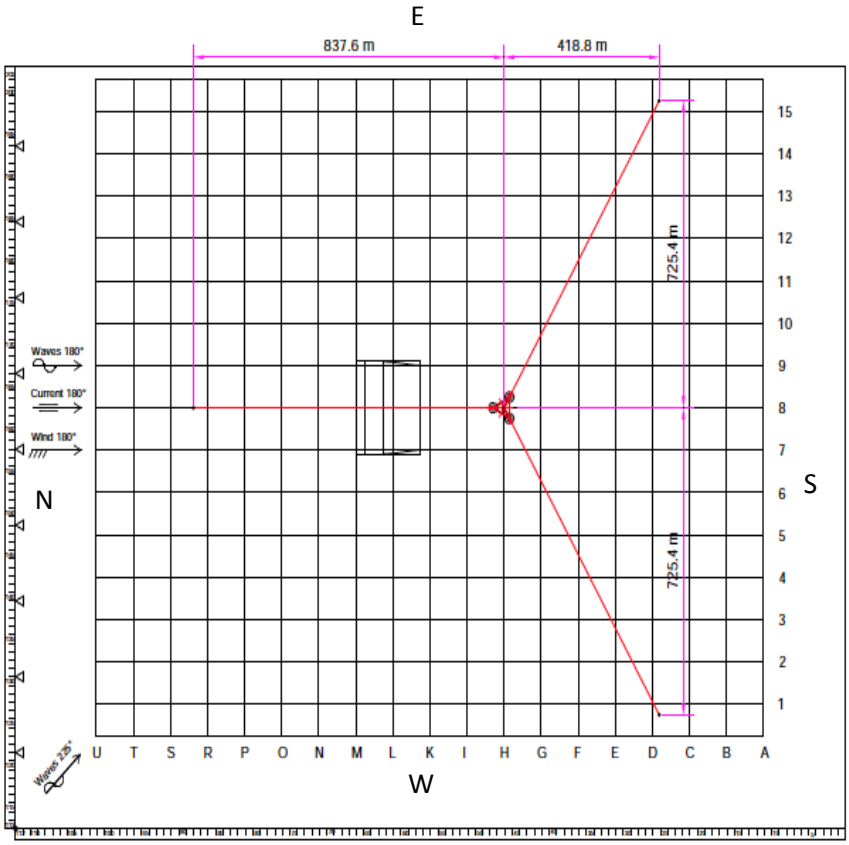

Figure 52 *Semi wind turbine model set-up in the basin (MARIN, 2011)*

Table 16 *Main properties of the semi-submersible*

Designation	Symbol	Unit	Magnitude
Mass	M	ton	13,444
Displacement	Δ	ton	14,265
Centre of Gravity below SWL	KG	m	14.4
Roll radius of gyration in air	K_{xx}	m	23.91
Pitch radius of gyration in air	K_{yy}	m	24.90
Yaw radius of gyration in air	K_{zz}	m	32.17

Table 17 Main properties of the wind turbine

Designation	Unit	Magnitude
Rotor orientation, configuration	Upwind,	3 blades
Rotor diameter	m	126.0
Hub diameter	m	3.0
Hub height above SWL	m	90.0
Height of tower-top flange above SWL	m	87.6
Total tower-top mass	kg	397,160

Table 18 Main properties of hub and nacelle

Designation	Unit	Magnitude
Nacelle mass	kg	274,940
Nacelle center of mass (above tower)	m	2.4
Nacelle center of mass (downwind)	m	4.56
Nacelle roll inertia	kg* m^2	298,100
Nacelle pitch inertia	kg* m^2	22,440,000
Nacelle yaw inertia	kg* m^2	22,440,000
Hub mass	kg	72,870
Hub inertia about rotor axis	kg* m^2	Negligible (0)

Table 19 Main properties of blade

Designation	Unit	Magnitude
Blade length	m	61.5
Blade mass	kg	16,450
Location of blade center of mass (measured from blade root)	m	23.4
Blade first mass moment of inertia	kg* m	385,150
Blade second mass moment of inertia	kg* m^2	13,940,000

Table 20 Main properties of mooring line

Designation	Unit	Magnitude
Number of mooring lines	3	
Angle between adjacent lines	degree	120
Depth to anchors below SWL	m	200
Depth to fairleads below SWL	m	14
Radius to anchors from platform centerline	m	837.6
Un-stretched length	m	835.5
equivalent diameter	m	0.077
mass density in air	Kg/m	113.35
mass density in water	Kg/m	108.63
Extensional stiffness	kN	$753.6*10^3$

6.3.1 Simulation Model

The DeepCwind semi-submersible was modeled and its motion properties simulated using the Aqwa-OrcaFlex-FAST package, and with Charm3D successively. The input to these programs is the model geometry, which was developed using ANSYS Aqwa and Rhino3D respectively. Figures 5 and 6 show the geometry and the panel models of the semi-submersible. The panel model for Charm3D is shown up to the water line only. There is little difference between the model without braces and the model with braces replaced by Morison elements. In this case study, the braces are not included in the Charm3D panel model to simplify the simulation. Other inputs to the program include model mass properties, as given in Table 1, and wind turbine properties given in Tables 2 – 5. Following validation tests were performed with each software tool:

- Static offset tests
- White noise tests and response amplitude operators (RAO)

- Natural period, damping and free decay tests

The simulation results compared with experimental data provide the necessary validation of the simulation, prior to further simulation runs for different sea-state conditions. Details are provided in Appendix 1.

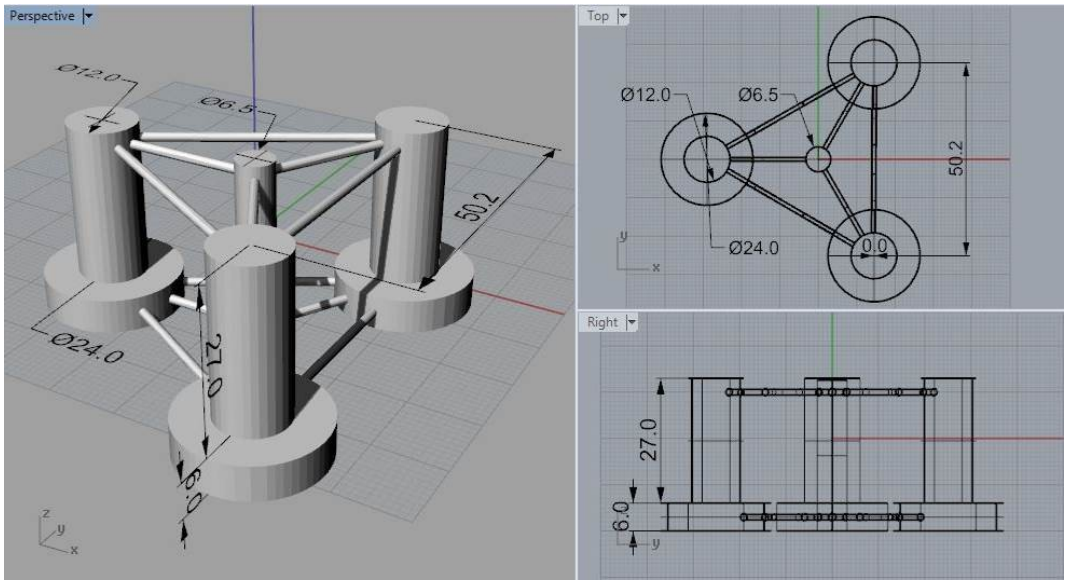

Figure 53 Geometry Model

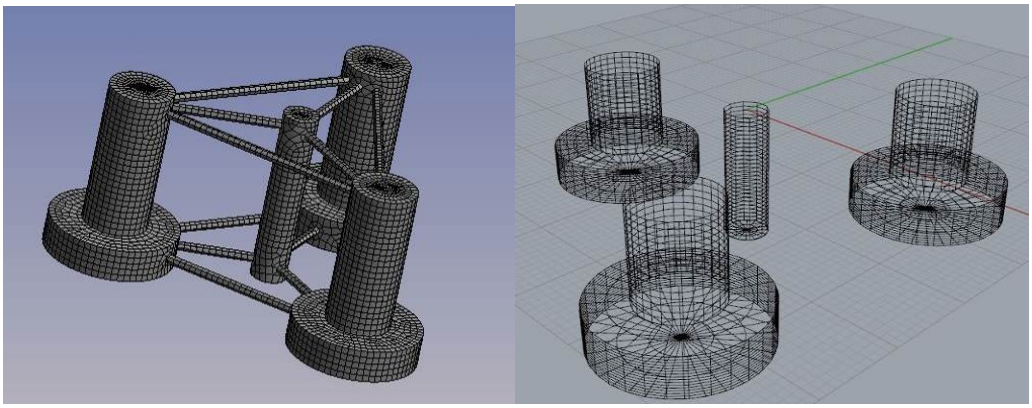

Figure 54 Panel model used in Aqwa (left) and Charm3D+FAST (right)

To further understand the capability of OrcaFlex+FAST and Charm3D+FAST, two case studies are considered. They are operational wave case and survival sea-state case. For Charm3D+FAST comparison, the operational wave case is used combined with steady wind speed of 0 m/s and 11.4 m/s. For OrcaFlex+FAST comparison, the survival sea-state combined with steady wind of 21.8 m/s was considered.

A typical sea-state is described by a spectrum model (e.g. JONSWAP), that depends on characteristic parameters like significant wave height (Hs) and spectral peak period (Tp). In experiments, a typical sea spectrum is used to generate a random time series signal, which is

input into the wave maker. The generated waves are measured by a wave probe at the location of the structure model (without the structure being physically present), and analyzed to reveal the measured spectrum. The wave maker transfer function is adjusted to obtain good agreement between measured and desired spectral conditions. The time series of the wave as output by the probe is a good indicator of the wave field "seen" by the model.

In both case studies, the time series of the wave elevation as obtained from the model tests were used as input to the simulation models. This method was chosen over the conventional way of using a wave spectrum to create a random time series input because it allows for very realistic comparisons to be made with experimental measurements. For Charm3D+FAST, The chosen time series corresponds to a survival sea-state described by a JONSWAP spectrum with $H_s = 7.1m, T_p = 12.1\ s.$, while for OrcaFlex+FAST, the chosen time series corresponds to a survival sea-state described by a JONSWAP spectrum with $H_s = 10.5m, T_p = 14.3\ s.$

6.3.2 Simulation of Operating Load Condition

The operational wave case is used combined with steady wind speeds of 0m/s and 11.4m/s, as shown in Table 21. These values correspond to the conditions used in our experiments. The sea-state is described by a JONSWAP spectrum where the significant wave height (H_s) is 7.1m, and the peak wave period (T_p) is 12.1s. The considered steady wind speed (V_w) is 11.4m/s and the rotor speed (Ω) is 7.78rpm. The simulation duration and the integration time step of both cases are 3 hours and 0.02s respectively. The wave, motion and mooring tension data calculated from Charm3D + FAST model are compared with the test results.

Table 21 Wave and Wind Conditions

Case	Wave Conditions			Wind Conditions	
	H_s (m)	T_p (s)	Γ	V_w (m/s)	Ω (rpm)
1	7.1	12.1	2.2	0	0
2	7.1	12.1	2.2	11.4	7.78

This case study investigates the global performance of the Semi FOWT and compares the results between numerical modeling and test data. The global performance includes motions in surge, heave and pitch, mooring line tensions of three mooring lines and rotor torque. The time series, power spectral density (PSD) and statistical analysis are presented. The Parzen window function (Simonoff, 1996) is applied to the power spectral density analysis. The wind effect on the Semi FOWT is discussed as well.

Wave and Platform Motions Comparison: Figure 55 through Figure 58 show the time series and PSD comparisons for wave, surge, heave and pitch, respectively, between experiments and Charm3D+FAST under no wind and steady wind conditions. The wave elevation time history and spectra agreement is fairly close, as would be expected. The surge motion time history shows higher absolute mean value under steady wind conditions than the absolute mean value under no wind conditions. The comparison for surge PSD is fairly good in the wave-energy range (0.05 to 0.2 Hz), while the simulation results are significantly lower at the low frequency range corresponding to the surge natural period of 0.0092 Hz. The differences are 47% and 63% for no

wind and steady wind condition respectively. Moreover, the surge PSD of no wind conditions are slightly higher at the low frequency range than the surge PSD under steady wind speed of 11.4 m/s.

The heave motion time histories have a common mean value and overall behavior under steady wind conditions and under no wind conditions. The PSD calculated through simulations at the wave frequency range of 0.7 to 0.9 Hz are 22% lower than that of experiments, while the simulations at the heave natural frequency of 0.056Hz are 12% lower than that of experiments. This could be attributed to the heave RAO difference between experiment data and simulation in the wave frequency range.

The pitch motion time histories show a higher absolute mean value under steady wind conditions than under no wind conditions. The pitch PSDs of coupled Charm3D-FAST model are in good agreement at wave frequency range with test data and are much lower at frequency of 0.035Hz than test data. The differences are 83% and 90% for no wind and steady wind condition respectively.

The discrepancy of surge and pitch PSDs in the low frequency range between Charm3D+FAST model and test model could be due to second-order hydrodynamic effects that are not captured in the numerical model (Coulling et al., 2013; Masciola et al., 2013).

Table 6 shows a comparison of statistics in wave height, surge, heave and pitch motion. In the three motions of both Case 1 and Case 2, the standard deviations of test data are all slightly larger than the standard deviations of Charm3D+FAST simulations. For Case 1, the standard deviation difference of surge, heave and pitch are 24.21%, 14.29% and 31.13% respectively. For Case 2, the standard deviation difference of surge, heave and pitch are 27.64%, 12.93% and 26.24% respectively. In addition, the mean three motions under both Case 1 and Case 2 differ below 25% instead of mean surge motion of Case 1, which has up to 50% difference.

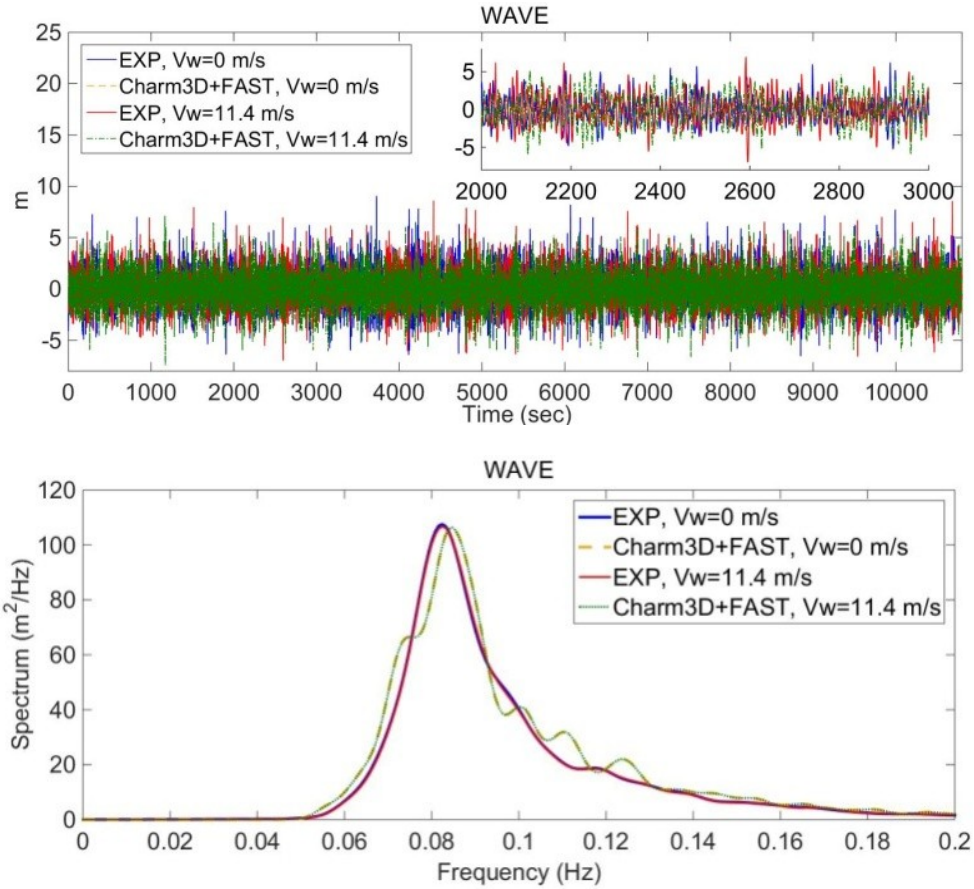

Figure 55 Comparison of wave time series (top) and PSD (bottom) of coupled Charm3D-FAST with test data under Case 1 and Case 2

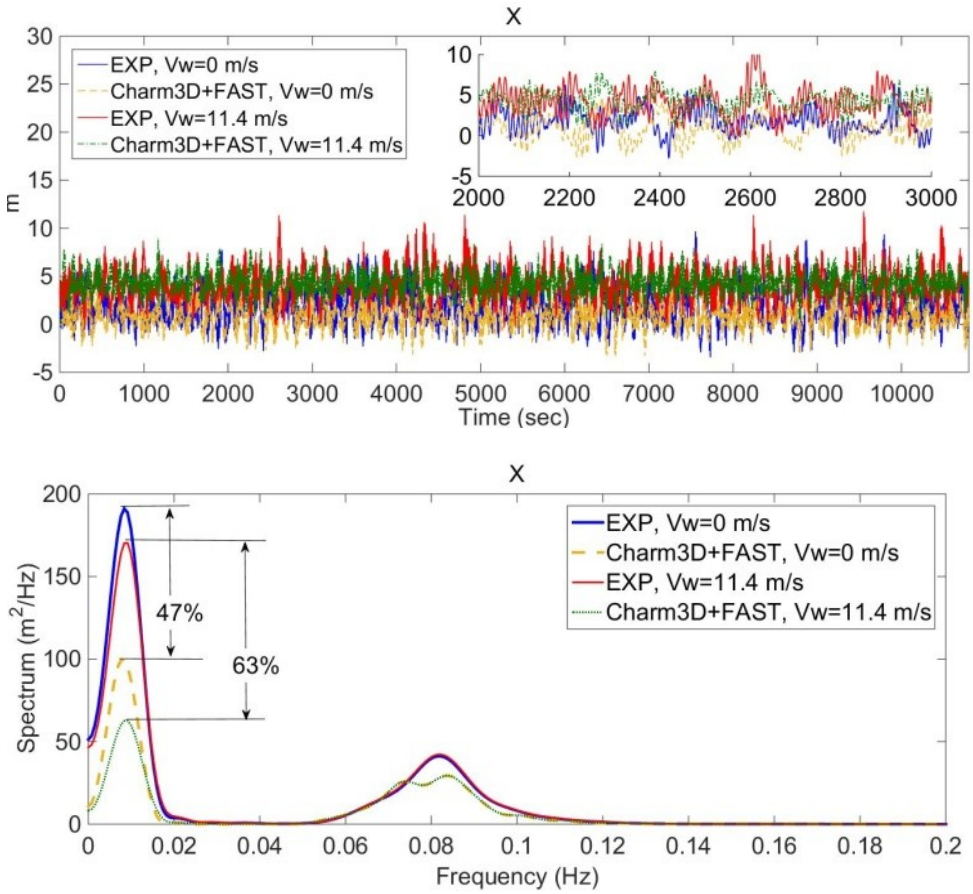

Figure 56 Comparison of surge time series (top) and PSD (bottom) of coupled Charm3D-FAST with test data under Case 1 and Case 2

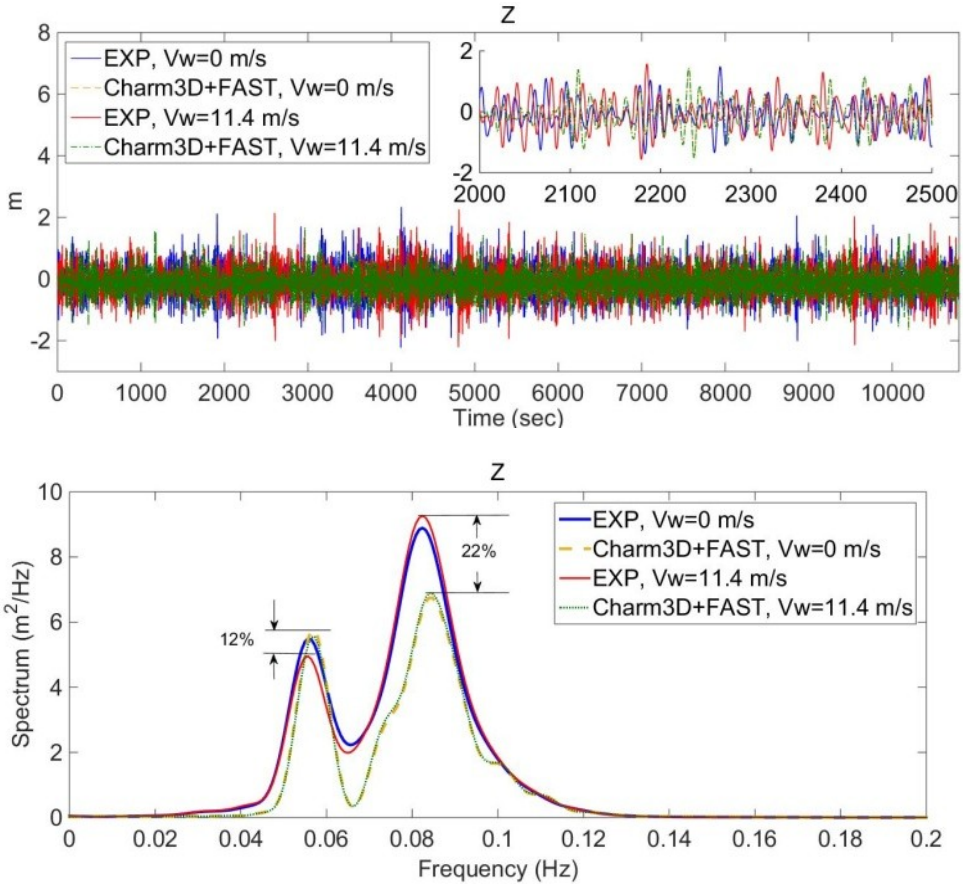

Figure 57 Comparison of heave time series (top) and PSD (bottom) of coupled Charm3D-FAST with test data under Case 1 and Case 2

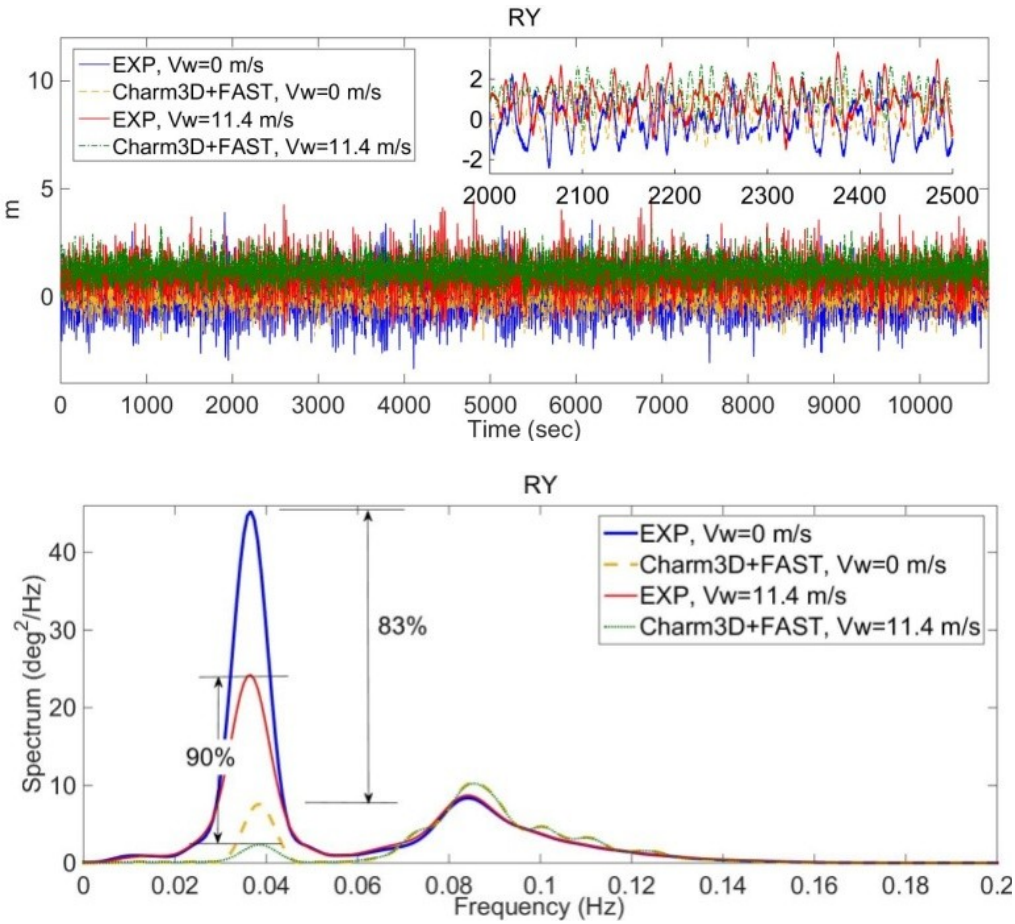

Figure 58 Comparison of pitch time series (top) and PSD (bottom) of coupled Charm3D-FAST with test data under Case 1 and Case 2

Table 22 Comparison of coupled Charm3D-FAST prediction and test data statistics of wave, surge, heave and pitch under Case 1 and Case 2

		Case1			Case2		
		Exp.	Sim.	Diff (%)	Exp.	Sim.	Diff (%)
Mean	Wave	1.46	1.53	4.66	1.43	1.53	6.74
	Surge	1.81	0.88	51.60	4.12	4.32	4.89
	Heave	-0.10	-0.11	7.76	-0.09	-0.11	22.90
	Pitch	-0.06	0.07	16.67	1.01	1.26	24.32
Std. Dev.	Wave	1.11	1.15	3.13	1.10	1.15	4.08
	Surge	1.71	1.29	24.21	1.63	1.18	27.64
	Heave	0.51	0.44	14.29	0.51	0.44	12.93
	Pitch	0.86	0.60	31.13	0.76	0.56	26.24

Note: Wave height, surge and heave are m. Pitch is in degrees.

Mooring Tension Comparison: In this section, mooring line tensions at the fairlead are presented. Time series, PSDs and statistical analyses from both simulation exercises are presented successively. Certain common trends are evident. As in the motion simulation results, Charm3D+FAST results are lower than experiments form mooring line tensions, because of the decreased motion of the FOWT in Charm3D+FAST model.

Fig. 12, Fig. 13 and Fig. 14 respectively show the time series and PSD comparisons for line 1, line 2 and line 3 between experiments and Charm3D+FAST under no wind and steady wind conditions. The mooring line tension history of line 1 shows lower mean values under no wind conditions than the values under steady wind while the mooring tension history of line 2 and 3 shows higher mean values under no wind conditions than the values under steady wind. The distribution of loads across the lines appears to differ between the static offset tests and the simulation, which possibly could be due to some differences in experimental set up and arrangement. The surge mean value increases from 1.81m to 4.12m under steady wind condition, thus the line 1 tension increases and line 2 and 3 tension decrease. The wave force effects on mooring lines are significant which are observed on both test model and coupled Charm3D-FAST model, because PSDs at wave frequency range of 0.05 to 0.2 are higher or slightly smaller than the PSDs at low frequency range. For line 1, the tension PSDs of test data and under steady wind conditions are higher than the PSDs of simulation results and under no wind conditions respectively. Moreover, the tension dynamic of line 1 are under predicted by numerical modeling which is possible with higher drag coefficient, higher stiffness of mooring chain or extra damping system in coupled Charm3D-FAST. Both line 2 and 3 have similar experiment and simulation results of tension time history and tension PSDs in wave frequency ranges which differ by below 6.5%. Moreover, the tension PSDs of line 2 and 3 are larger under no wind conditions than the PSDs under steady wind. This is expected since line 2 and 3 are downwind and therefore loose more tension loads under steady wind conditions. The differences at the low frequency range of tensions in line 1, 2 and 3 could be possible because

the second-order hydrodynamic effects not captured in Charm3D+FAST model (Coulling et al., 2013; Masciola et al., 2013).

Statistics seen in Table 7 show that Charm3D+FAST overall does fairly well in predicting mean tensions which differ by below 4%. For line 1, standard deviations differ by 32.5% and 26.9% under no wind and steady wind conditions respectively. For both line 2 and 3, standard deviation differ by below 6.5% and 0.3% under Case 1 and Case 2 respectively. The underestimation of line 1 stiffness could cause the standard deviation difference between test data and simulation results. Max and min values, being non-statistical, can differ considerably between experiments and simulations.

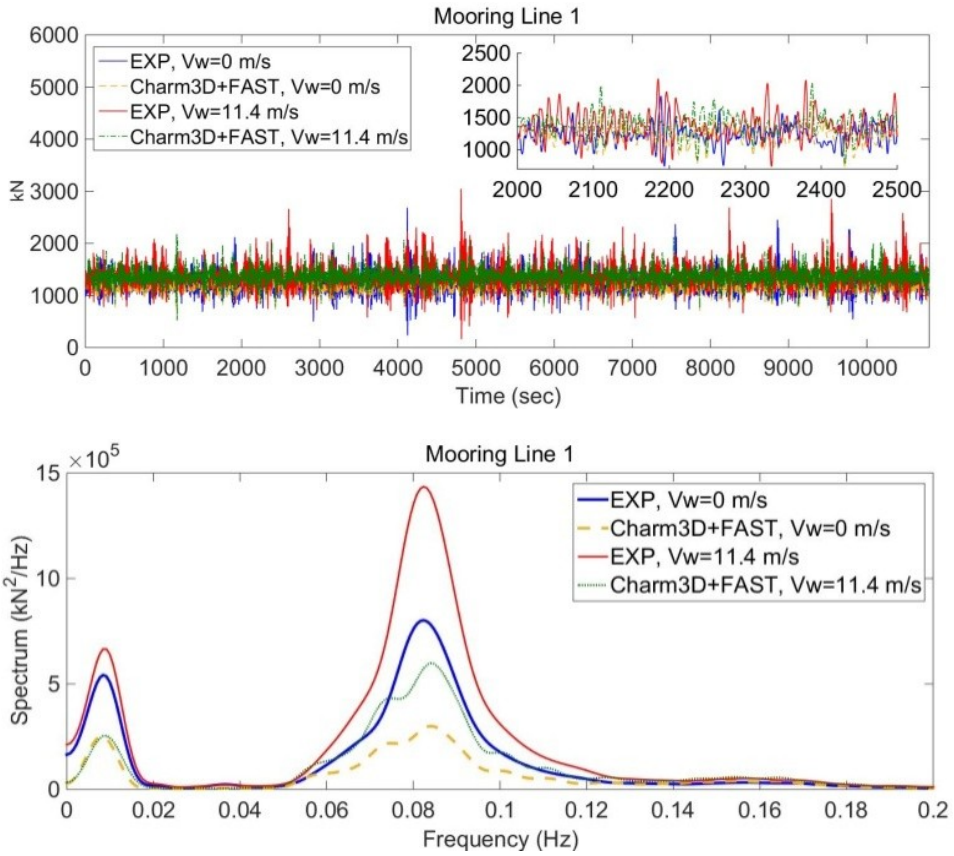

Figure 59 Comparison of mooring line (#1) tension time series (top) and PSD (bottom) of coupled Charm3D-FAST with test data under Case 1 and Case 2

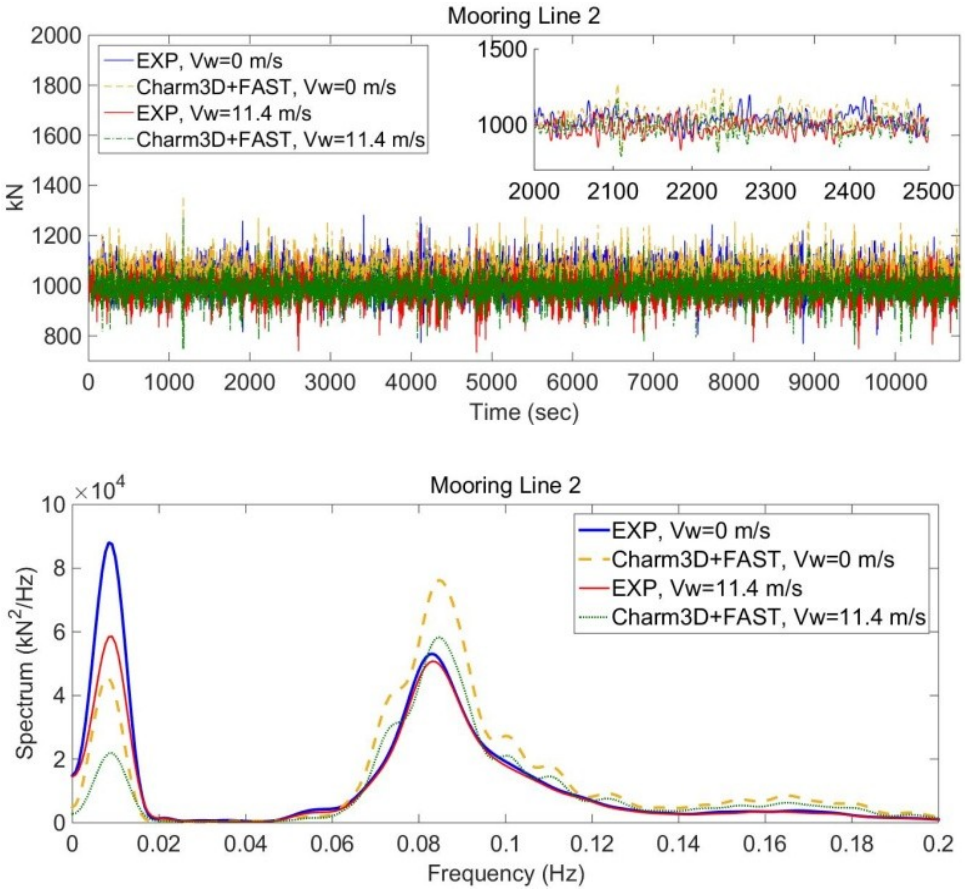

Figure 60 Comparison of mooring line (#2) tension time series (top) and PSD (bottom) of coupled Charm3D-FAST with test data under Case 1 and Case 2

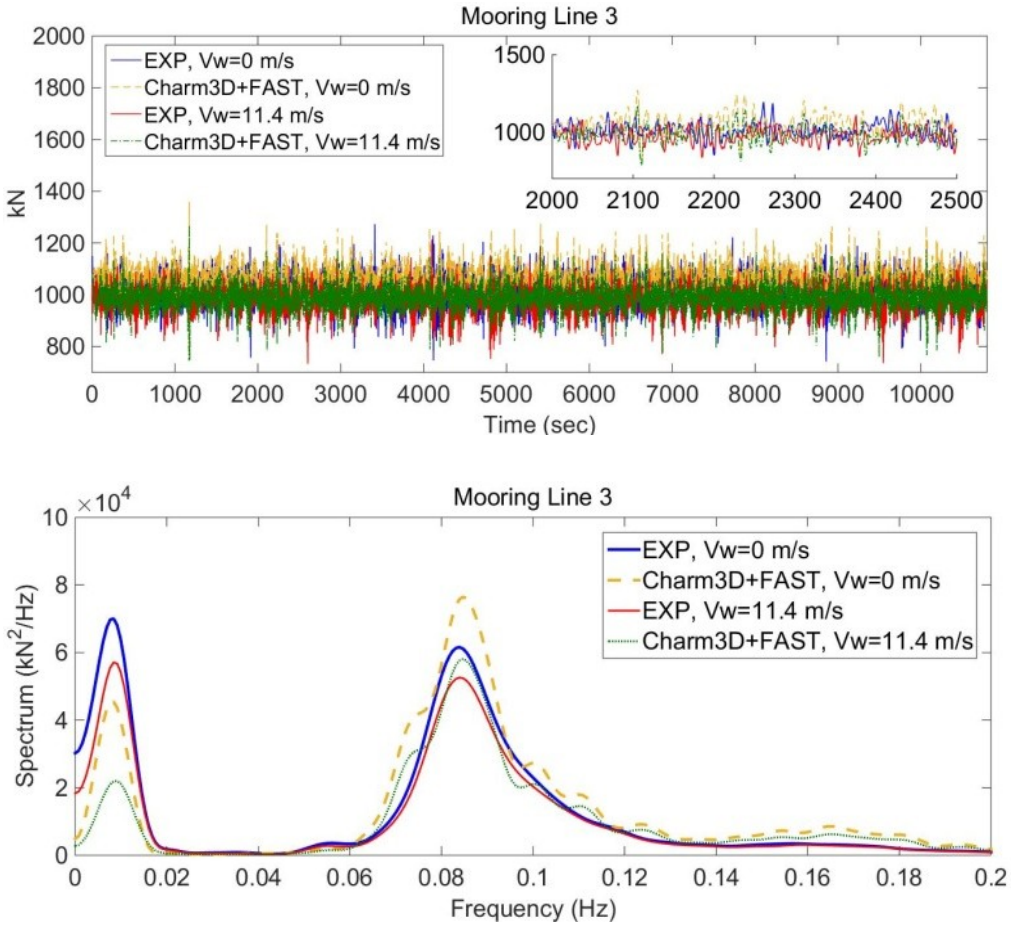

Figure 61 Comparison of mooring line (#3) tension time series (top) and PSD (bottom) of coupled Charm3D-FAST with test data under Case 1 and Case 2

Table 23 Comparison of coupled Charm3D-FAST prediction and test data statistics of mooring line (#1-3) tension under Case 1 and Case 2

	Line	Case1			Case2		
		Exp.	Sim.	Diff (%)	Exp.	Sim.	Diff (%)
Mean	1	1219.97	1176.81	3.54	1373.12	1366.85	0.46
	2	1040.19	1055.62	1.48	980.52	988.73	0.84
	3	1016.94	1056.36	3.88	974.90	987.15	1.26
Std. Dev.	1	166.05	112.06	32.52	207.12	151.36	26.92
	2	50.38	53.61	6.41	46.06	46.17	0.23
	3	50.93	53.65	5.34	46.18	46.07	0.22
Max.	1	2682.34	1825.71	31.94	3044.95	2189.77	28.09
	2	1283.27	1340.05	4.42	1214.35	1254.65	3.32
	3	1273.03	1341.10	5.35	1214.09	1252.22	3.14
Min.	1	231.65	552.25	138.40	158.22	520.05	228.68
	2	767.69	782.34	1.91	732.91	757.26	3.32
	3	742.31	782.73	5.45	732.65	755.86	3.17

Note: Mooring line tensions are in kN

6.3.3 Simulation of Survival Load Condition

In this case study, the survival sea-state is used combined with a steady wind speed. The sea-state is described by a JONSWAP spectrum where the significant wave height (H_s) is 10.5m, and the peak wave period (T_p) is 14.3s. The considered steady wind speed (V_w) is 21.8m/s and the rotor speed (Ω) is 12.73rpm. The simulation duration and the integration time step are 3 hours and 0.0125s respectively. The wave, motion and mooring tension data calculated from OrcaFlex+FAST model are compared with the test results.

Wave and Platform Motion Comparison: Figure 14 shows the time series and PSD comparisons for wave, surge, heave and pitch between experiments and OrcaFlex+FAST respectively. The wave elevation time history and spectra agreement is fairly close as would be expected. The comparison for surge PSD is fairly good in the wave-energy range (0.05 to 0.2 Hz), while the simulation results are significantly lower at the low frequency range corresponding to the surge natural period of 0.0095 Hz. The experimental spectrum do not show the large peak due to the non-zero mean value as frequency approaches zero. The heave motion time history show common mean value and overall behavior, however, the PSD of simulations are lower than that of experiments. The largest discrepancy occurs with the pitch motion. We believe that pitch motions are actually affected strongly by the turbine aerodynamics, and hence simulation results often show discrepancies.

Table 6 shows a comparison of statistics in surge, heave and pitch motion. In these three motions, standard deviations of test data are all larger than the standard deviations of OrcaFlex+FAST simulations. The standard deviation difference of surge, heave and pitch are 17.611%, 28.263% and 46.672% respectively.

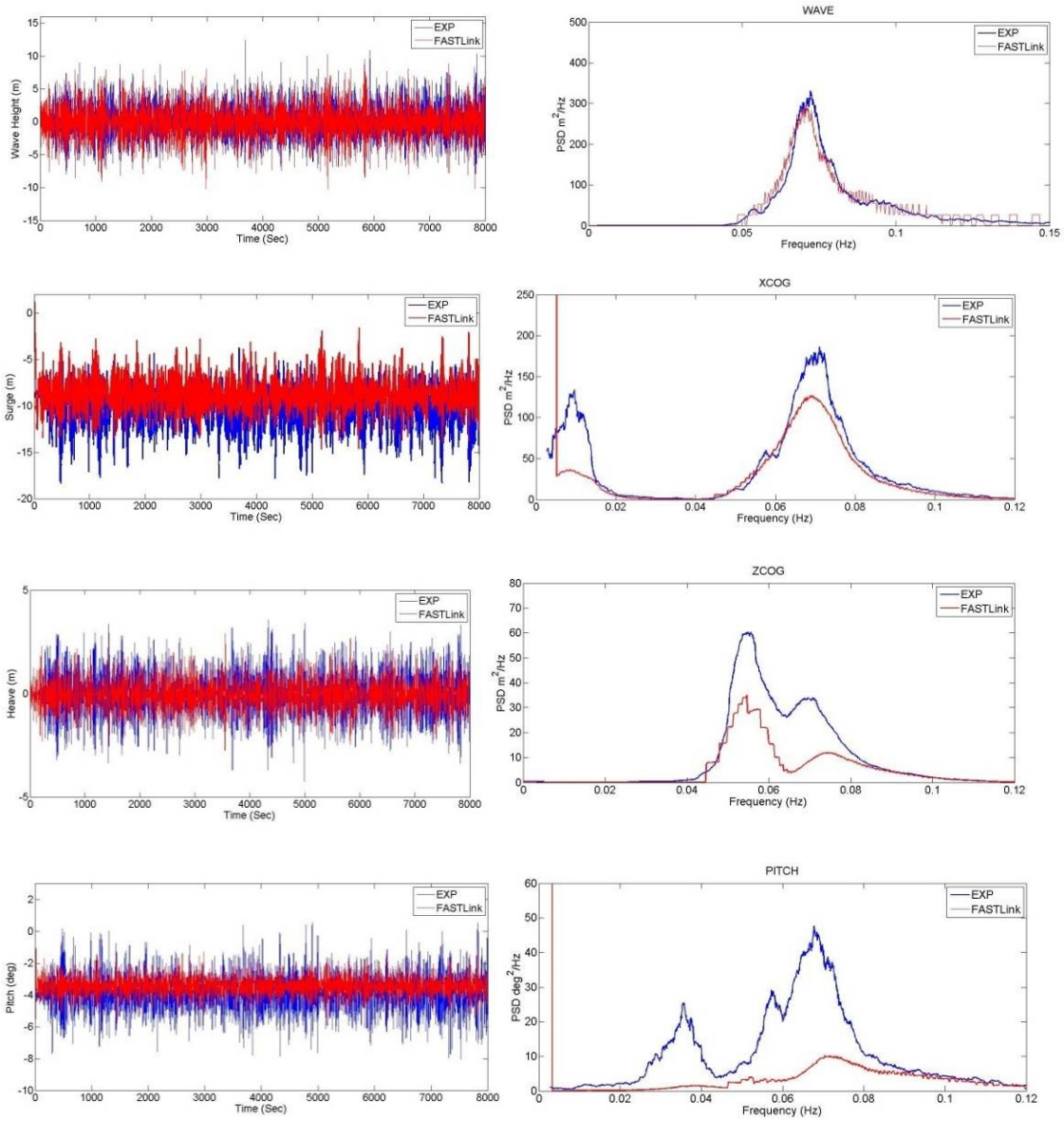

Figure 62 Comparison of time series (left) and power spectral density (right) of OrcaFlex+FAST with experimental data. Rows describe surge, heave and pitch respectively.

Table 24 Comparison of OrcaFlex+FAST predictions and test data statistics

	Experiments		OrcaFlex+FAST		Diff (%)	
	Mean	St. Dev.	Mean	St. Dev.	Mean	St. Dev.
Wave	2.0324	1.568	2.0581	1.6043	1.265	2.315
Surge	-10.442	2.1617	-8.7833	1.781	15.885	17.611
Heave	-0.03	1.1085	-0.0499	0.7952	66.33	28.263
Pitch	-3.8924	1.1418	-1.917	0.6089	50.75	46.672

Mooring Tension Comparisons: In this section, mooring line tensions at the fairlead are presented. Time series, PSDs and statistics analyses from both simulation exercises are presented successively. Certain common trends are evident. Contrary to the motion simulation results, OrcaFlex+FAST results are higher than experiments form mooring line tensions. Snap load events (large tension spikes) are observed for the upstream mooring line (#1) in the test data and OrcaFlex+FAST simulation output, however the characteristics are quite different. The magnitude of the spikes is smaller in the simulations and occurs at different times. The downstream lines (#2 and #3) do not see any snap load events.

Statistics seen in Table 7 show that OrcaFlex+FAST overall does a fairly good job of predicting mean tensions, while max, min and STD values can be predicted to within 50%.

Probability of snap load occurrence. For extreme events such as snap loading in moorings, it is useful to study the exceedance probability of occurrence, in line with extreme value theory. An analysis of exceedance probability may reveal trends and allow for prediction of expected behavior over given return periods. Exceedance probability of the mooring line tension is defined as:

$$EP(x) = \frac{n(x)}{N+1} \quad (22)$$

where $\mathrm{EP(x)}$ is the exceedance probability of the specified reference tension amplitude. x is the ranked mooring line tension amplitude from greatest to least, n(x) is the number of the reference tension amplitude exceedance events. In this analysis, the time series of mooring line tension (simulated or experimental) is examined and local maximum values are identified and cataloged. The trend of exceedance probability is used to compare the local maxima (LM) with snap loads and without (LMwoSN) to understand the importance of snap events. Figure 68 shows the comparison of exceedance probability of LM, LMwoSN and SN of test data and OrcaFlex+FAST for the case of interest. The normalized tension is defined as:

$$T_{norm} = \frac{T}{T_{mean}} \quad (23)$$

where $\mathbf{T_{norm}}$ is the normalized tension, T represents the tension of interest (LM, LMwoSN or SN), and $\mathbf{T_{mean}}$ is the mean of all LM data sets for each case.

It is apparent that the larger tension values are dominated by snap type events. Generally speaking, the exceedance probability of LM follows the exceedance probability distribution of SN beyond the large tension range. The local maxima excluding snap (LMwoSN) appear to follow a Weibull distribution, while snap events are well represented by a GEV distribution (Hsu et al. 2015). Consequences of snap loads on mooring fatigue are discussed later in this report.

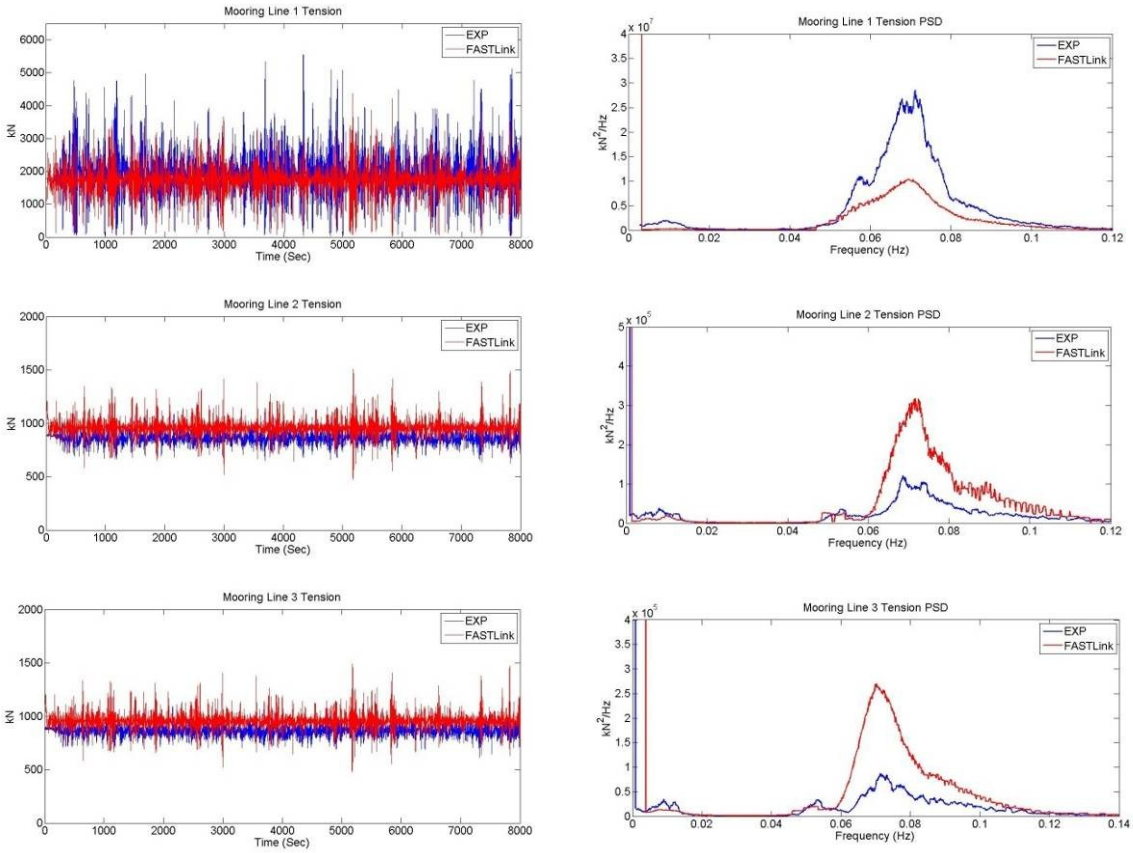

Figure 63 Comparison of time series (left) and power spectral density (right) of OrcaFlex+FAST with experimental data. Rows describe mooring line 1tension, mooring line 2 tension and mooring line 3 tension respectively.

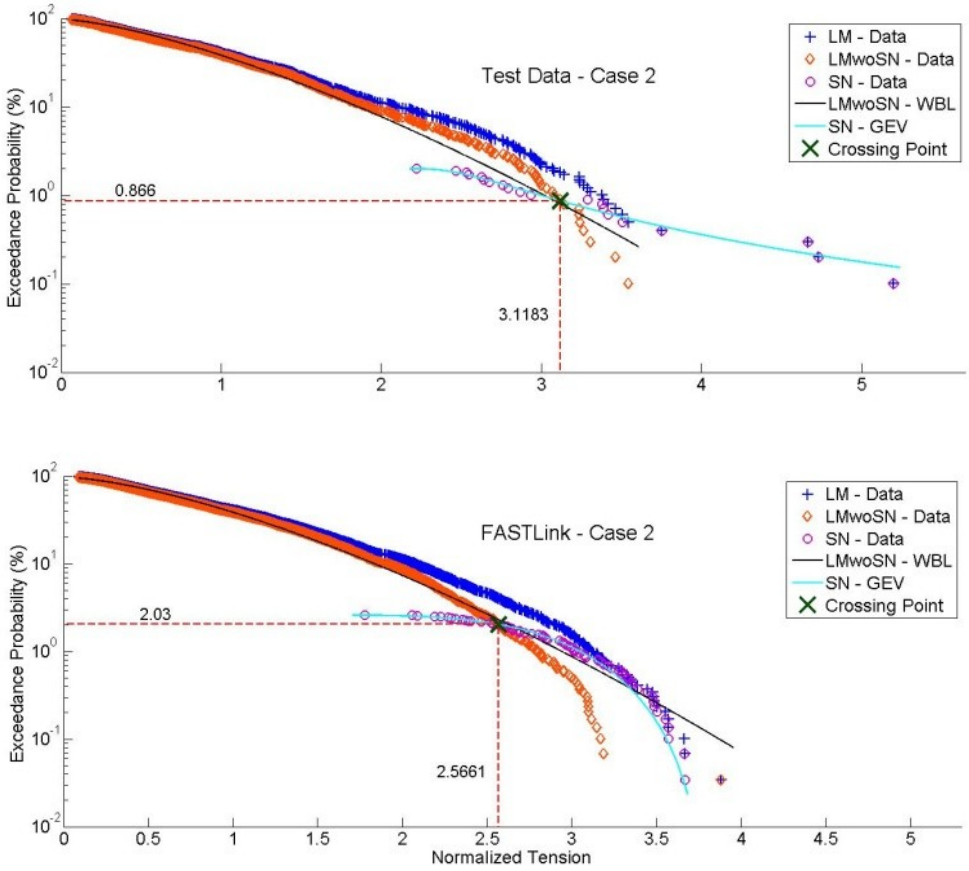

Figure 64 Comparison of exceedance probability of LM, LMwoSN and SN. Statistics from measure data and from simulation results using OrcaFlex+FAST under Case 2 are shown.

Table 25Comparison of OrcaFlex+FAST predictions and test data statistics

		EXP	Simulation	Diff (%)
Line 1	Mean	1938.9	1737.3	10.398
	Standard Deviation	742.306	498.84	32.799
	Maximum	7835.2	4364.644	42.2944
	Minimum	33.9177	23.215	31.555
Line 2	Mean	859.6382	958.37	11.485
	Standard Deviation	53.487	79.892	49.367
	Maximum	1171.2	1503.1	28.338
	Minimum	517.143	474.61	8.225
Line 3	Mean	860.4478	954.84	10.97
	Standard Deviation	49.986	78.867	57.778
	Maximum	1119.4	1491.6	33.25
	Minimum	561.326	478.13	14.821

6.3.3.1 Fatigue Analysis

A fatigue analysis of the DeepCwind mooring system was conducted using OrcaFlex's fatigue analysis capabilities. Time domain simulations were done using FAST+OrcaFlex. For the purpose of this study, only one mooring line was examined. Several of OrcaFlex's fatigue analysis tools were tested to compare both the quality of the results and the computation time needed.

The DeepCwind model is as described in previous sections of this report. Realistic environmental data was obtained using NOAA buoy information. Nominal fatigue parameters, including T-N curve coefficients, corrosion allowances, and typical chain breaking strength, were obtained from the standards, including API-RP 2SK, DNV-OS-E301, and DNV-OS-E302.

6.3.3.1.1 Environmental Conditions

The fatigue analysis of the DeepCwind mooring system was conducted using environmental conditions obtained from NOAA buoy data. The buoy used in the analysis is NDBC Station 44032 Buoy E01, located in the Gulf of Maine near Monhegan Island. The buoy was selected due to its proximity to the proposed University of Maine FOWT site near Monhegan Island. Hourly data was collected for the past year, including:

- Significant wave height
- Wave period
- Wind speed

A wave scatter table was developed from the hourly data, and is shown in Figure 65. For purposes of this study, a logarithmic relationship between wind speed and wave height was

established, as shown in Figure 66. It was assumed that wind and wave directions were the same in all analyses.

		Wave Period (s)								
		1	3	5	7	9	11	13	15	17
Wave Height (m)	0.25	0%	5%	2%	2%	3%	1%	0%	0%	0%
	0.75	0%	7%	11%	5%	11%	6%	0%	0%	0%
	1.25	0%	1%	10%	5%	6%	4%	0%	0%	0%
	1.75	0%	0%	3%	4%	2%	3%	0%	0%	0%
	2.25	0%	0%	1%	2%	1%	1%	0%	0%	0%
	2.75	0%	0%	0%	1%	1%	0%	0%	0%	0%
	3.25	0%	0%	0%	0%	1%	0%	0%	0%	0%
	3.75	0%	0%	0%	0%	0%	0%	0%	0%	0%
	4.25	0%	0%	0%	0%	0%	0%	0%	0%	0%
	4.75	0%	0%	0%	0%	0%	0%	0%	0%	0%
	5.25	0%	0%	0%	0%	0%	0%	0%	0%	0%
	5.75	0%	0%	0%	0%	0%	0%	0%	0%	0%
	6.25	0%	0%	0%	0%	0%	0%	0%	0%	0%
	6.75	0%	0%	0%	0%	0%	0%	0%	0%	0%

Figure 65: Wave scatter table for NDBC Station 44032 Buoy E01 for the past year.

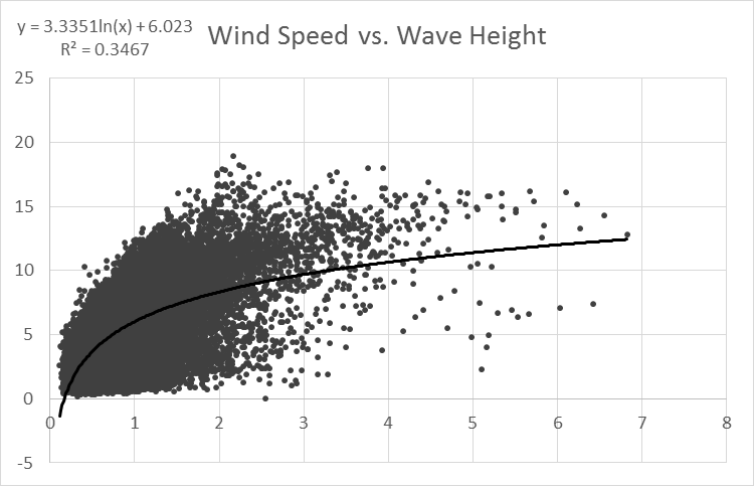

Figure 66: Relationship between wind speed and wave height for NDBC Station 44032 Buoy E01 for the past year. Equation for the logarithmic trend line is shown.

6.3.3.1.2 OrcaFlex Fatigue Analysis

OrcaFlex offers three types of fatigue analyses (see Orcina, 2013 for additional detail):

6.3.3.1.2.1 Rainflow Fatigue

Rainflow fatigue analysis requires time domain simulations be carried out for each cell of the irregular wave scatter table. OrcaFlex conducts rainflow counting of the mooring tension time history. From these rainflow cycles, Miner's Rule is used to estimate the total damage and expected lifetime of the mooring component under consideration. Miner's Rule states that:

$$damage = \sum_{i=1}^{k} \frac{n_i}{N_i} \quad (24)$$

In this equation, n_i is the number of cycles counted at a given stress or tension range, N_i is the number of cycles to failure at that stress or tension range (determined in OrcaFlex from a user-specified S-N or T-N curve), and i and k are indices for the tension bins in the analysis.

Typically it is assumed that if the damage exceeds unity, then the system will fail (although appropriate thresholds may be specified in OrcaFlex to account for safety factors, etc.). If damage is calculated for a year, then the expected lifetime until failure can be determined by inverting the damage (i.e. lifetime=1/damage).

Rainflow fatigue is the most computationally expensive fatigue analysis method, but also the most accurate. Orcina recommends that each irregular wave simulation have a duration of at least 20 minutes.

6.3.3.1.2.2 Regular Wave Fatigue

For regular wave fatigue analysis, an irregular wave scatter table may be converted to a regular wave scatter table. OrcaFlex includes capabilities to do this conversion and to calculate the number of encounters for each wave condition in the scatter table (see Orcina, 2013 for discussion).

Simulations are conducted in OrcaFlex or FAST+OrcaFlex for each wave condition in the scatter table to determine the steady state response of the system. In the fatigue calculation only the response for the final wave period of the simulation is used.

Fatigue damage and lifetime expectation are calculated using the same methodology as before. A key parameter in accurate regular wave fatigue analysis is determining the number of wave periods required to establish a steady state response.

6.3.3.1.2.3 Spectral Fatigue

OrcaFlex includes functionality to conduct spectral fatigue analysis. For several reasons, computation speed being primary among them, the makers of OrcaFlex no longer recommend this method for mooring fatigue analysis in OrcaFlex. According to the User Manual (Orcina, 2013):

> "The advent of multi-core processors and the wave scatter conversion facility mean that regular wave fatigue is often just as fast as spectral fatigue analysis, as well as giving much more reliable and accurate answers. Because of this we no longer recommend the use of spectral fatigue analysis in OrcaFlex."

For this reason, spectral fatigue analysis was not conducted for the current project.

6.3.3.1.2.4 T-N Curve

Each fatigue analysis method applies a T-N curve to the response history, and uses the Palmgren-Miner Rule to determine damage and expected lifetime for the mooring. For this analysis an appropriate T-N curve was obtained from API RP 2SK, section 6.2.1, page 25:

$$N = KR^{-M} \quad (25)$$

The T-N curve is a function of empirical parameters *M* and *K*, as well as the ratio of tension to mean breaking load (MBL), *R*. For stud-less, grade R3S chain, *M=3.0*, and *K=316*. Three values of MBL were analyzed: the MBL at the nominal chain size, the MBL assuming 50% lifetime

corrosion, and the MBL assuming 100% lifetime corrosion. The API MBL of the nominal chain diameter of 77 mm is 5586.4 kN. If the chain is assumed to corrode at 0.4 mm/yr. (recommended design value in API RP 2SK), then the diameter will be 69 mm after a 20 year lifetime. The MBL of 69 mm chain is 4561.8 kN. Finally, if the corroded chain size at 50% of the lifetime is assumed (recommended by DNV OS-E301), then the chain diameter is 73 mm and the MBL is 5063.5 kN.

6.3.3.1.2.5 Results

Two rainflow fatigue analyses and two regular wave fatigue analyses were conducted to study the computation time and the similarity of the results. Regular wave simulations were run with six wave periods (one ramp-up period and five more to establish steady state), as well as 51 wave periods. Six wave periods are the minimum recommended by Orcina.

Irregular wave simulations were also conducted over both a 20 minute and a 60 minute duration. As before, 20 minutes corresponds to the recommended minimum duration by Orcina for rainflow fatigue analysis.

Table 26 shows the computation time and number of simulations run in FAST+OrcaFlex for each of the cases considered.

Table 26: Comparison of computation time for two Regular Wave Fatigue durations and two Rainflow Fatigue durations.

Type of Fatigue	# Simulations	Simulation Duration	Computation Time	Damage at Fairlead
Regular Wave	95	6 Wave Cycles	10 minutes	3.20×10^{-2}
Regular Wave	95	51 Wave Cycles	85 minutes	3.15×10^{-2}
Rainflow	26	20 Minutes	75 minutes	6.79×10^{-3}
Rainflow	26	60 Minutes	97 minutes[1]	6.34×10^{-3}

Unsurprisingly, regular wave fatigue has significantly lower computation time than a comparable rainflow (irregular) simulation, even though the rainflow fatigue cases have significantly few required simulations.

The fatigue damage and lifetimes for each set of fatigue calculations are shown in Figure 67 and Figure 68. Expected lifetime is calculated over the entire arc length of the mooring line. As seen in the figures, the tension-fatigue lifetime is lowest at the fairlead and highest near the anchor, where the mooring system experiences little or no uplift. It must be noted that OrcaFlex only considers tension fatigue for mooring systems. Another option in OrcaFlex is to calculate fatigue based on "stress factors," which accounts for both tension and bending in fatigue calculations. This fatigue option is intended for umbilicals but may be tailored to model fatigue of rope mooring systems. It has not been studied for this report as each of the case studies employ all-chain mooring systems.

[1] Due to time constraints, the 60-minute rainflow fatigue analysis was done on a different machine than the other three analyses.

It is also observed that in the cases considered in this analysis, the regular wave fatigue produces more conservative results than rainflow fatigue. It is unknown whether this would be the case for all mooring fatigue analyses, but if so then regular wave fatigue may safely be used in preliminary analysis and design, where its reduced computation time is beneficial. A rainflow fatigue analysis is clearly necessary for final results, however, as there is a substantial difference between the two methods.

Finally, it may be observed that while there is substantial difference between the regular wave fatigue and rainflow fatigue results, there is little difference between the two regular wave fatigue analyses and the two rainflow fatigue analyses. This lends credibility to Orcina's recommended simulation durations for fatigue study.

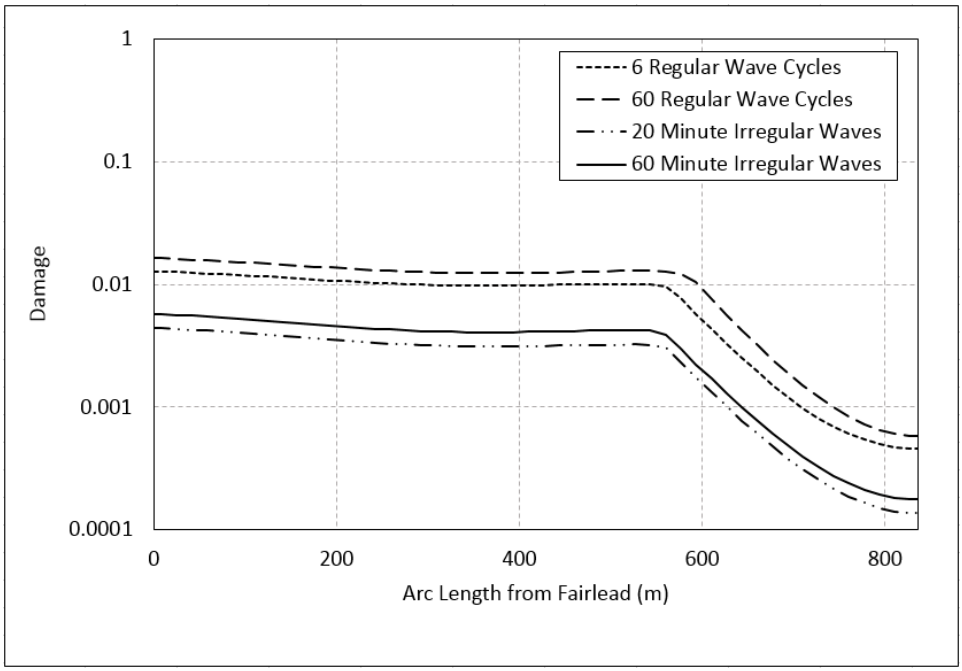

Figure 67: Fatigue damage calculated by Regular Wave and Rainflow fatigue in OrcaFlex. Damage is calculated over the entire mooring. The fairlead is at x=0.

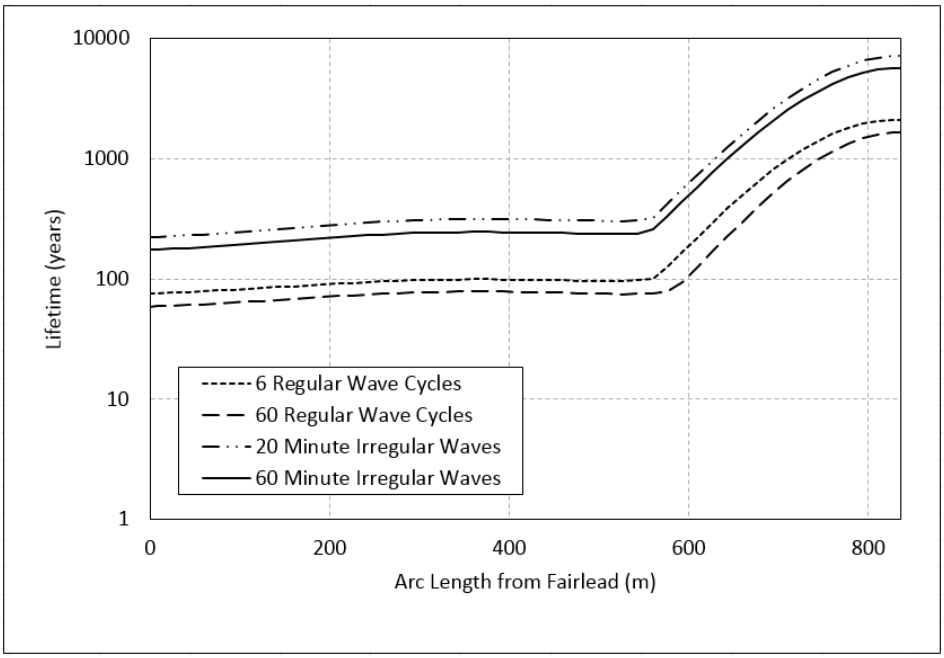

Figure 68: Fatigue lifetime calculated by Regular Wave and Rainflow fatigue in OrcaFlex. Lifetime is calculated over the entire mooring. The fairlead is at x=0.

The effect of corrosion on the fatigue damage and lifetime of the mooring system are shown in Figure 69 and Figure 70. The fairlead damage and expected lifetimes are shown in

Table 27. In this analysis the parameters of the T-N curve are adjusted to assume that the mooring chain has decreased in diameter at a rate of 0.4 mm/yr. (nominal value recommended in API RP-2SK) over a lifetime of 20 years. The expected lifetime is shown for uncorroded chain, fully corroded chain, and chain that has corroded over 50% of its lifetime (10 years). All T-N curves are applied to the 20 minute rainflow fatigue simulations.

Table 27: Chain damage and expected lifetime at the fairlead under various corrosion assumptions.

	Fatigue Damage	**Fatigue Lifetime**
Nominal Chain Diameter	5.75×10^{-3}	174 years
Corroded Chain Diameter at 50% Service Life	7.72×10^{-3}	130 years
Corroded Chain Diameter at 100% Service Life	1.06×10^{-2}	95 years

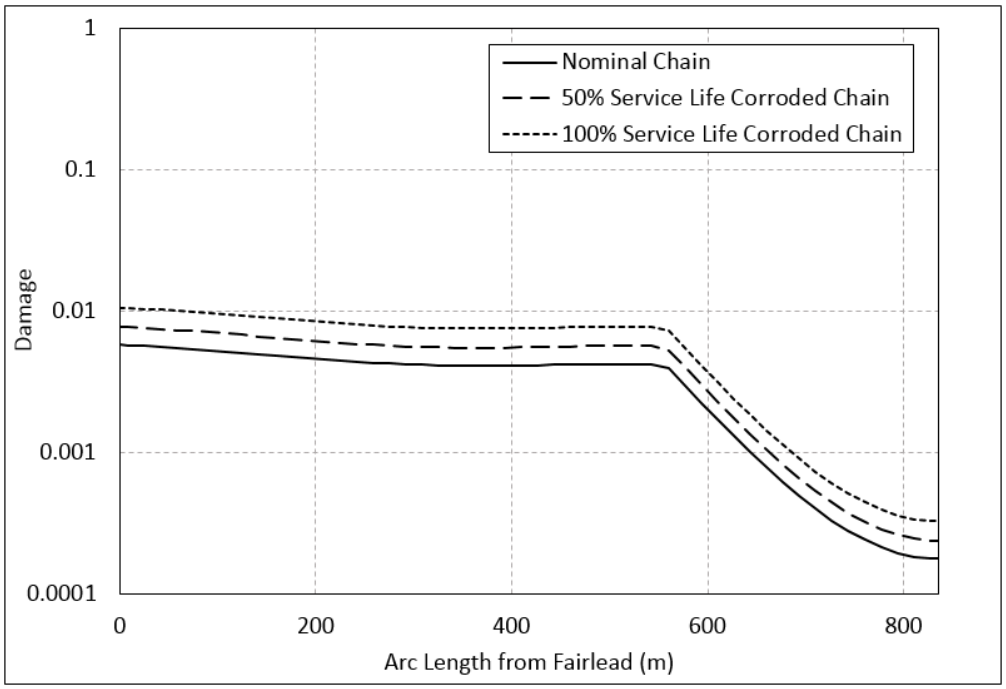

Figure 69: Fatigue damage calculated in OrcaFlex under various corrosion allowance assumptions. 20 minute rainflow fatigue analysis is used. Damage is calculated over the entire mooring. The fairlead is at x=0.

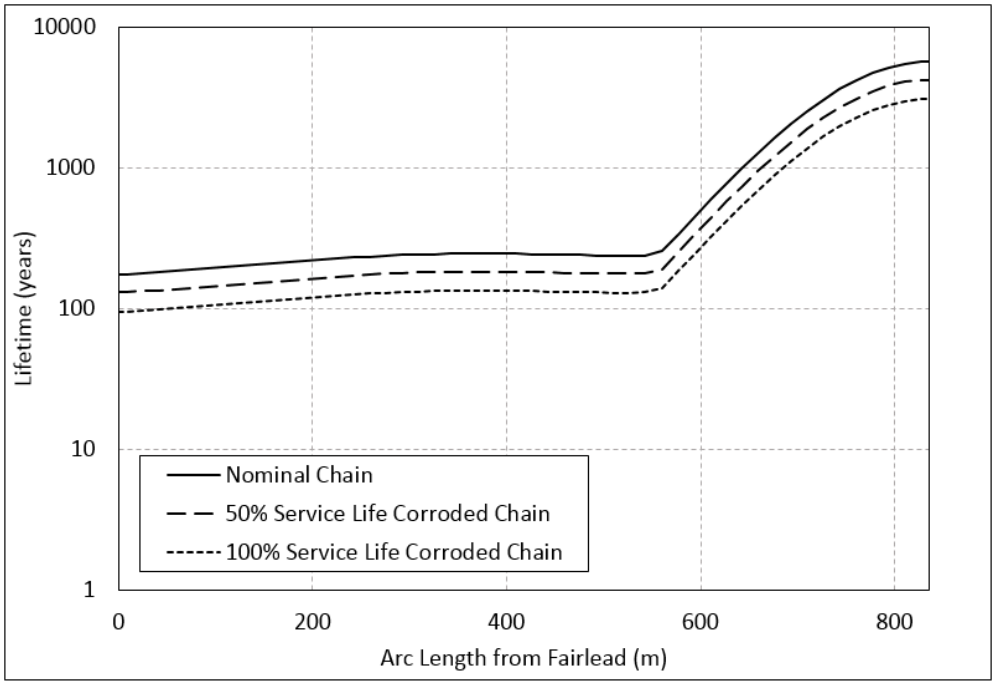

Figure 70: Fatigue lifetime calculated in OrcaFlex under various corrosion allowance assumptions. 20 minute rainflow fatigue analysis is used. Lifetime is calculated over the entire mooring. The fairlead is at x=0.

6.3.3.1.3 Fatigue Analysis with Charm3D

In this section, damage of mooring lines is estimated from the simulations performed in Charm3D. API RP 2SK suggests three approaches of fatigue analysis. Three methods are:

1. Simple summation method: low-frequency fatigue damage of mooring line tension and wave frequency fatigue damage of mooring line tension are calculated separately. The total damage is the sum of the two.
2. Combined spectrum: First, low-frequency and wave frequency spectra are calculated. Second, fatigue damage is calculated by the combined root mean square tension range.
3. Time domain cycle counting. This approach is generally considered to be more precise. The Rainflow counting algorithm is applied to the time series of mooring line tension, which is used to estimate the number of tension cycles and the tension range for each time interval. A T-N curve of the expected mooring line is used. Finally, Miner's rule is applied for cumulative fatigue damage.

In this study, the third approach is used to calculate the damage of mooring line tensions from Charm3D simulations. The wave scatter table for NDBC station 44032 Buoy E01 for the past year (Figure 65) and specific wind speeds corresponding to different wave heights (Figure 66) are applied. The estimation of fatigue damage was done in Matlab using a Rainflow counting algorithm from Matlab file exchange center. The procedure for calculating damage from Charm3D simulation results is:

i. Simulate DeepCwind Semi-submersible model with 26 different environment conditions in Charm3D. Each simulation period is 20 minutes.

ii. Time series of three mooring line tensions are output for each case.

iii. The T-N curve of 3RS grade stud-less chain is defined according to parameters found in API-RP-2SK and an estimated breaking load was listed in DNV OS-E302. The parameters are the same as in the OrcaFlex fatigue analysis and are provided in Section 6.3.3.1.2.4.

iv. The rainflow counting algorithm is applied to each mooring line tension time history. The number of cycles (n_i) and tension ranges are estimated for each time interval (i). In this study, 2000 to 11000 intervals are applied to each of the 20 minute simulations.

iv. The wave scatter of the past year is applied to convert number of tension cycles in the 20 minute episode to cycles in a 1 year episode. The following equation describes the conversion method.

$$n_{ij}^{1\,year} = n_{ij}^{20\,minutes} * \frac{60\,\frac{mins}{hour} * 24\,\frac{hours}{day} * 365\,\frac{days}{year}}{20\,min} * p_{ij} \qquad (26)$$

$$i = 1,2,3\ldots m;\ j = 1,2,\ldots,26.$$

———

where i is the time interval, m is the total number of intervals and j is case number. p_{ij} corresponds to the probability as given by the scatter diagram.

vi. Once the tension range in each time interval is obtained, the number of cycles to failure in 1 year ($N_{ij}^{1\,year}$) can be calculated with the T-N curve.

vii. Finally, Miner's rule is applied for cumulative annual fatigue damage.

$$D_{annual} = \sum_{j=1}^{26} \sum_{i=1}^{m} \frac{n_{ij}}{N_{ij}} \quad (27)$$

A Rainflow counting algorithm, T-N curve determination and Miner's rule were implemented as Matlab code.

6.3.3.1.4 Discussion and Comparison of Fatigue Results

One of the primary challenges in implementing a full fatigue analysis is processing all of the required data. With this in mind it is important for purposes of this report to include a discussion of the batch processing facilities available in OrcaFlex and FAST+OrcaFlex.

For regular wave fatigue OrcaFlex has a Wave Scatter Conversion facility that pre-processes and creates OrcaFlex files for all regular waves that must be simulated.

Pre-processing the necessary FAST input files was done by modifying the input files manually. A set of template FAST files were created containing all data fields that need not be modified for each simulation (turbine geometry, simulation details such as time step, etc.). The input fields that were modified include the wind speed, total simulation time, and calls to the proper AeroDyn and wind files. FAST+OrcaFlex requires that the input fast file (with extension .fst) have the same name as the OrcaFlex file (with extension .dat). All pre-processing of FAST files was done using batch files in the command line.

For irregular wave scatter analyses there are several options for pre-processing the files. The simplest option is to use OrcaFlex's Microsoft Excel spreadsheet module. This module allows the user to create batch files for pre-processing and to post-process results using Microsoft Excel as a user interface.

Another option is to create the necessary OrcaFlex simulation files using Python. OrcaFlex includes a Python module called OrcFxAPI that has functionality to modify OrcaFlex files, run simulations, post-process results, and develop external functions that can coupled with OrcaFlex during simulation.

Damage and lifetime calculations are done in OrcaFlex's Fatigue Analysis post-processor. For Regular Wave Fatigue, the number of cycles must be specified for each wave condition. For Rainflow Fatigue, the annual duration must be specified. T-N curves are also specified with the parameters discussed above.

6.3.3.1.5 Comparison of Fatigue Predictions from OrcaFlex and Charm3D

The fatigue damage and lifetime for Charm3D and OrcaFlex results are compared in Table 28. For Charm3D simulation results with Matlab fatigue analysis, the damage on mooring line 1 is 47.92 and 47.74 times larger than the damage on mooring line 2 and mooring line 3 respectively. This is not surprising, since the wave and wind are applied to the positive x-axis and the orientation of mooring line 1 is 180 degrees. Mooring line 1 experiences most of the wave load and wind load. There is a 44% difference in damage estimates on mooring line 1 between results obtained using the Matlab code and OrcaFlex's built-in tool. This possibly is because the result of a time domain simulation in OrcaFlex would not be expected to be identically equal to a time domain simulation in Charm3D under the same environmental conditions, due to

differences in model development, integration/time-stepping algorithms, intrinsic assumptions of each software, etc. The post-processing of fatigue calculations could be different as well. The fatigue damage calculated using OrcaFlex's simulation results are also shown.

Table 28 Comparison of the fatigue damage and lifetime for Charm3D and OrcaFlex simulation results

	Charm3D Simulation results with Matlab code fatigue analysis		OrcaFlex Simulation results with OrcaFlex built-in fatigue analysis	
	Fatigue Damage	Fatigue Lifetime	Fatigue Damage	Fatigue Lifetime
Mooring Line 1	3.8×10^{-3}	264 yrs.	5.75×10^{-3}	174 yrs.
Mooring Line 2	7.93×10^{-5}	12613 yrs.	Results not calculated (minimal damage expected)	
Mooring Line 3	7.96×10^{-5}	12561 yrs.		

6.3.4 Conclusions and Observations

Both Charm3D+FAST and OrcaFlex+FAST (FASTLink) can predict the global performance of DeepCwind under operational wave and survival sea-state conditions. The reason for using operational wave and survival data is to understand the software's capability of predicting different sea-states. Moreover, we also want to investigate the software's capability of predicting snap events under survival sea-states. For operational wave cases, we investigated the Charm3D-FAST coupler performance, and proposed a comparison of test data and Charm3D-FAST coupler results. Overall, the dynamic motions in surge, heave and pitch, and the dynamic tension (line #2 and #3) have good agreement with the test data in wave frequency ranges. However, the dynamic mooring line (#1) tensions are underestimated by Charm3D+FAST. For survival wave case, we investigated the Orcaflex+FAST coupler (FASTLink) performance. Overall, the PSDs of surge and heave have good agreement with the test data in wave ranges. However, the dynamic mooring line tension on line #1 is underestimated and the dynamic mooring tensions on line #2 and #3 are overestimated by Orcaflex+FAST coupler. Moreover, snap load events observed in test data are predicted by OrcaFlex+FAST as well. However the characteristics are quite different. The magnitude of the spikes is smaller in the simulations and occurs at different times.

In both Charm3D+FAST and OrcaFlex+FAST, dynamic mooring line (#1) tension is underestimated. It is possible to tune the system with the higher drag coefficient, higher stiffness or the extra damping system in Charm3D+FAST and OrcaFlex+FAST, which is not considered in the case studies. In addition, various stiffness and drag coefficients of mooring lines are applied to different simulations and results are investigated for this case study. The noticeable discrepancy in pitch motions in the low frequency range are observed by Charm3D+FAST and OrcaFlex+FAST as well. It is affected by second-order hydrodynamic effects not captured in Charm3D+FAST or OrcaFlex+FAST mode.

The fatigue lifetime of the mooring system was examined using time domain simulations with rainflow counting. The purpose of this study was to examine both the tools available in the software and the recommended methodologies in the offshore standards.

- The software tools are well equipped to calculate fatigue damage in accordance with the assumptions of Miner's Rule.
- Recommended practice for fatigue damage calculation is highly sensitive to choice of inputs, and susceptible to large scatter. The influence of (a) material loss due to corrosion and abrasion, and (b) high intensity events such as snap loads, may not be adequately addressed in the offshore standards for FOWTs.
- Sensitivity studies were conducted to compare (1) regular wave vs. irregular wave fatigue, and (2) length of simulation. Difference in simulation time was found to change the calculated lifetime by only 7%. Comparing regular wave fatigue vs. irregular wave fatigue, the regular wave fatigue damage was found to be nearly 5x higher than irregular wave fatigue.

6.4 VolturnUS 1/8-Scale Semi-Submersible Prototype

6.4.1 Background

The VolturnUS 1:8 is an eighth scale of a 6 MW prototype floating wind turbine (Figure 71) that was deployed in Castine, Maine, USA in May 2013, and decommissioned in Sept 2014, for an 18-month autonomous offshore deployment. The goal of the testing was to de-risk the deployment of a full-scale system. Some features of the VolturnUS System full-scale system include:

- Pre-stressed concrete semi-submersible floating foundation design.
- Complete assembly quayside in 10m water depth.
- low-cost tug boat for tow-out.
- Drag anchors and chains for mooring system.
- Light-weight composite tower.

Froude scaling for floating offshore wind turbines (Chakrabarti, 1994; Martin, 2014; Goupee, 2012) demonstrated that the motions of the prototype at the Castine site were representative of the full-scale unit in an open site installed farther offshore. During the course of its deployment, the unit experienced representative operational and extreme scaled design load cases as specified in the American Bureau of Shipping Guide for Building and Classing Floating Offshore Wind Turbines (ABS, 2013).

Figure 71 *VolturnUS 1:8 installed off Castine, Maine, USA (Thiagarajan, 2015).*

The project site is shown in Figure 72. An instrumented metocean buoy collected wind, wave, and current data at the test site. An Acoustic Doppler Current Profiler (ADCP) mounted on the sea floor was also present. The turbine is connected to the power grid via a subsea cable east of the prototype on the shoreline. Three catenary chain moorings connected to drag embedment anchors make up the station-keeping system. The anchors are labeled Anchor North East, West, and South East. A comprehensive instrumentation package monitored key performance characteristics of the system, including turbine power, thrust, hull motions, and metocean conditions. Figure 73 shows the key instrumentation on the VolturnUS 1:8. The anchor segments are shown in Figure 95.

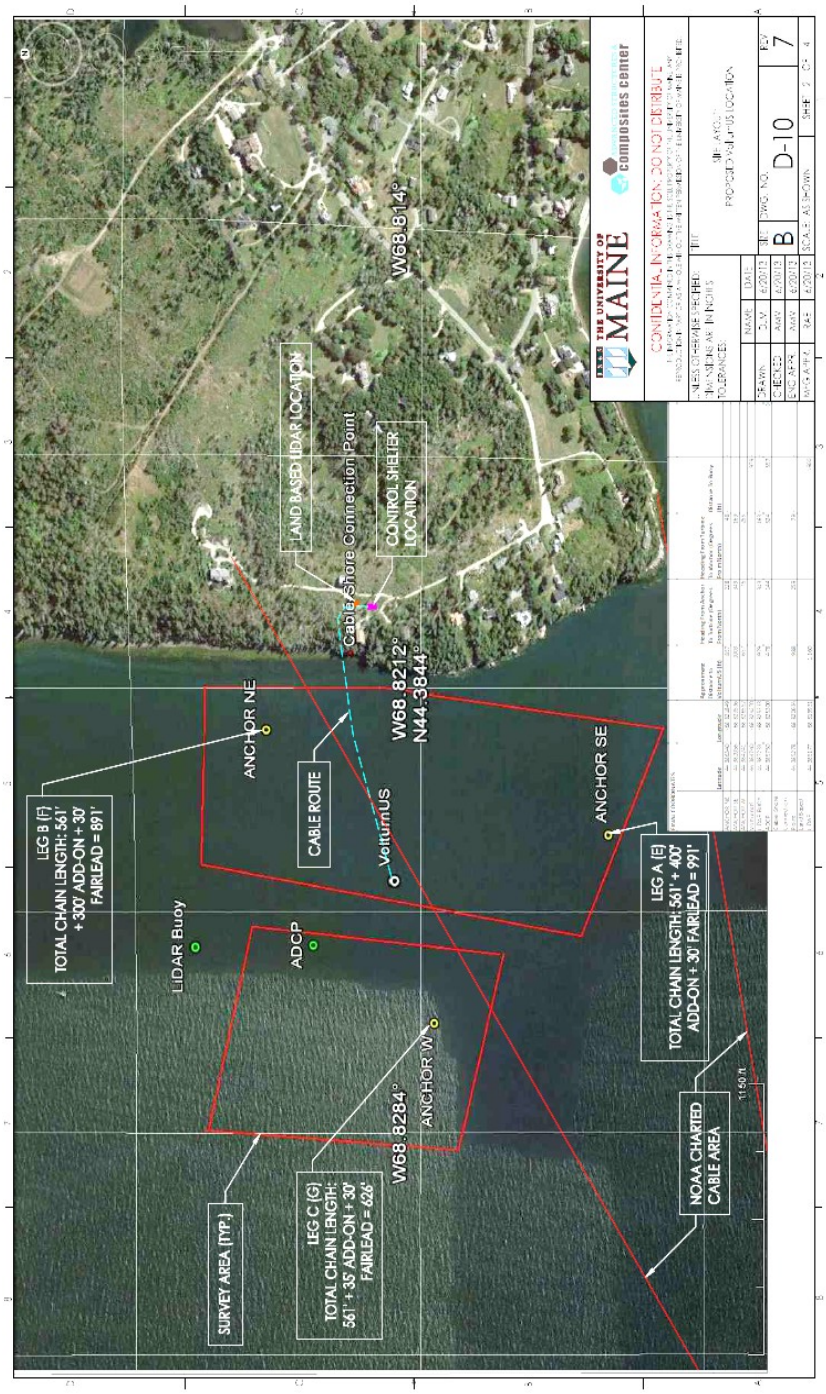

Figure 72 ***VolturnUS 1:8 project test site with showing mooring line details (DeepCwind, 2013).***

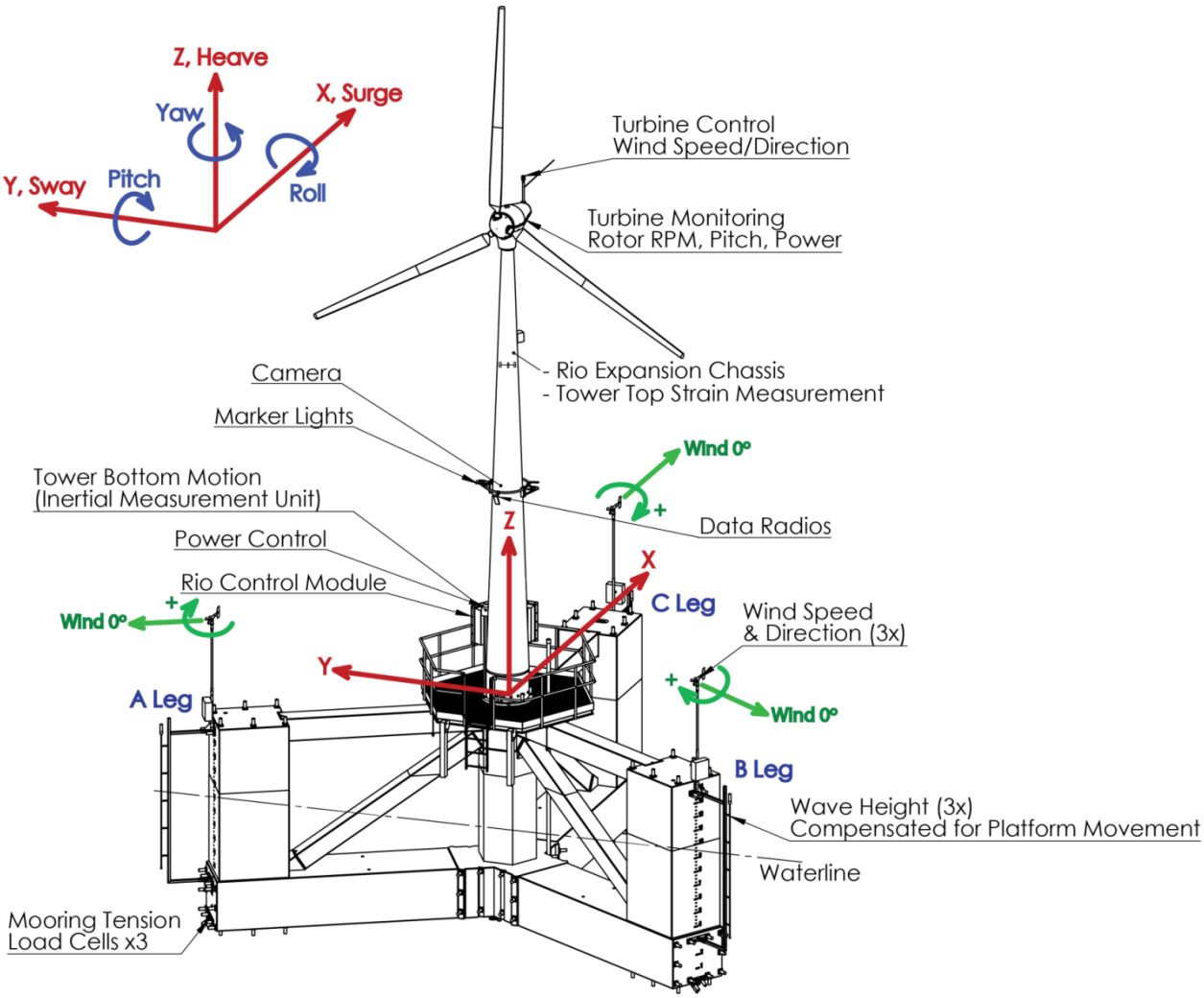

Figure 73 *Instrumentation systems onboard the VolturnUS 1:8 (Thiagarajan, et al. 2015)*

Sample design conditions discussed in the paper by Viselli et al. (2014) were used to validate the simulations. These cases were one-hour measurements corresponding to the following design load cases:

- Scaled ABS Design Load Case 1.2: November 9th, 2013, 6:53:04 AM – 7:53-04 AM
- Scaled ABS Design Load Case 1.6: November 1st, 2013, 5:14:49 AM – 6:14:49 AM
- Scaled ABS Survival Load Case: November 27th, 2013, 12:51:54 PM – 1:01:54 PM

Time histories of the following channels were provided:

- Environmental information
  - Wave direction and height
  - Current speed and direction
  - Wind speed and direction
- Platform Motion information in all 6 degrees of freedom (surge, sway, heave, roll, pitch, yaw)
- Mooring load cell time history measurements for all three mooring lines.

    - Locations of the load cells in the mooring lines (load varies along mooring line length)
- Turbine information
    - Thrust
    - Torque
    - Rotor RPM
    - Power generation
    - Tower base accelerations

6.4.2 Field Data

For validation of the computer simulation tools with the present case study, system response information was provided for three one-hour time periods. These time periods were selected by members of the University of Maine Advanced Structures and Composites Center (ASCC) to correspond to three key design storm conditions, if the system were scaled from its 1:8 scale to the full scale. This method is outlined by Viselli et al (AWEA, 2014). Two design load conditions (DLC 1.2 and DLC 1.6) and a survival load condition (SLC) were studied. While the design load cases are titled to correspond to the full scale system, all analysis is done on the 1:8 scale system.

Each of the three one-hour durations for which field data was available was simulated with FAST/OrcaFlex, and Charm3D/FAST to validate the respective software tools. Time series field data included the following:

- Wind velocity
- Wind heading (only available for DLC 1.6 and SLC time periods)
- Wave elevation
- Platform acceleration in all six degrees of freedom
- Fairlead tension on all three mooring lines
- Generator power and energy

Mean values of the following were also provided:

- Wave heading
- Current velocity and heading
- Wind heading (only mean value was provided for DLC 1.2 time period)

6.4.2.1 Data Source

Wave and wind measurements were taken on each leg of the platform, as well as on a LiDAR buoy located near the VolturnUS. Current measurements were only taken on the LiDAR buoy. The location of this buoy in relation to the platform and anchor locations is shown in Figure 74. The buoy is located approximately as far from the platform as the anchors, and it is impossible to say how well the current measurements at this location represent the current profile at the platform location.

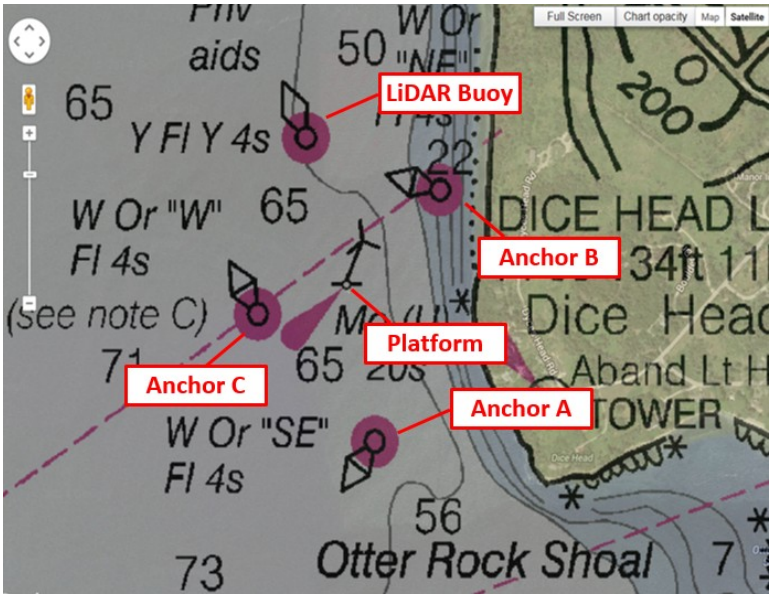

Figure 74: Approximate location of VolturnUS 1:8 platform, mooring anchors, and LiDAR buoy. Source: http://me.usharbors.com/harbor-guide/castine.

For the analysis undertaken in this report, wind and wave measurements on Leg C of the platform were used. A relative comparison of measurements taken here and at other locations is presented in Table 29, Table 30, Table 31, and Table 32. As seen in these tables, there are variations in data measurements in several cases, which again may influence simulation results.

Table 29: Significant wave height measurements in meters, taken at each leg of the platform (Leg A, Leg B, Leg C), and on the LiDAR buoy (Triaxys, Acc., Microstrain).

	DLC 1.2	DLC 1.6	SLC
Leg A	0.18	0.92	1.71
Leg B	0.11	0.52	3.24
Leg C	0.13	0.86	1.48
Buoy Triaxys	0.16	0.82	1.32
Buoy Accelerometer	0.17	0.87	1.16
Buoy Microstrain	0.01	0.57	0.50

Table 30: Dominant wave period measurements in seconds, taken at each leg of the platform (Leg A, Leg B, Leg C), and on the LiDAR buoy (Triaxys, Acc., Microstrain).

	DLC 1.2	DLC 1.6	SLC
Leg A	8.00	4.26	5.16
Leg B	8.00	6.80	17.06
Leg C	8.00	4.26	5.16
Buoy Triaxys	1.90	4.70	5.30
Buoy Acc.	2.13	4.57	4.00
Buoy Microstrain	2.47	3.57	3.70

Table 31: Mean wave heading measurements in degrees, taken at the platform location and on the LiDAR buoy.

	DLC 1.2	DLC 1.6	SLC
Platform	113	265	263
Buoy Triaxys	347	194	197
Buoy Microstrain	343	161	77

Table 32: Mean wind speed measurements in meters/second, taken at each leg of the platform (Leg A, Leg B, Leg C), at the turbine controller, and on the LiDAR buoy (anemometer 2).

	DLC 1.2	DLC 1.6	SLC
Leg A	N/A	8.90	13.53
Leg B	4.87	N/A	13.87
Leg C	4.92	8.61	14.11
Turbine Controller	4.49	8.78	14.73
Buoy Anemometer 2	5.30	8.82	13.77

6.4.2.2 Design Load Condition 1.2: Feb. 9, 2014

Design Load Condition 1.2 is classified as a fatigue design condition, in which the wind speed is within operating conditions, with a corresponding wave sea-state. Figure 5 shows the relative heading of the environmental forces, and sample plots of the field data are shown in Figure 76 through Figure 78. The wave spectrum shown in Figure 78 indicates a likely bimodal spectrum comprising of a wind driven sea superposed on a long period swell.

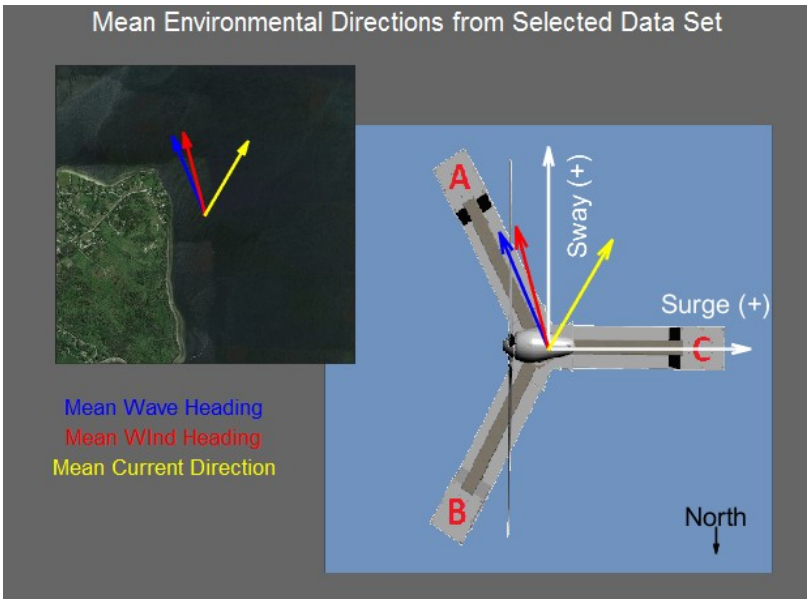

Figure 75: Coordinate system and wind, wave, and current headings for Design Load Case 1.2 (DLC 1.2)

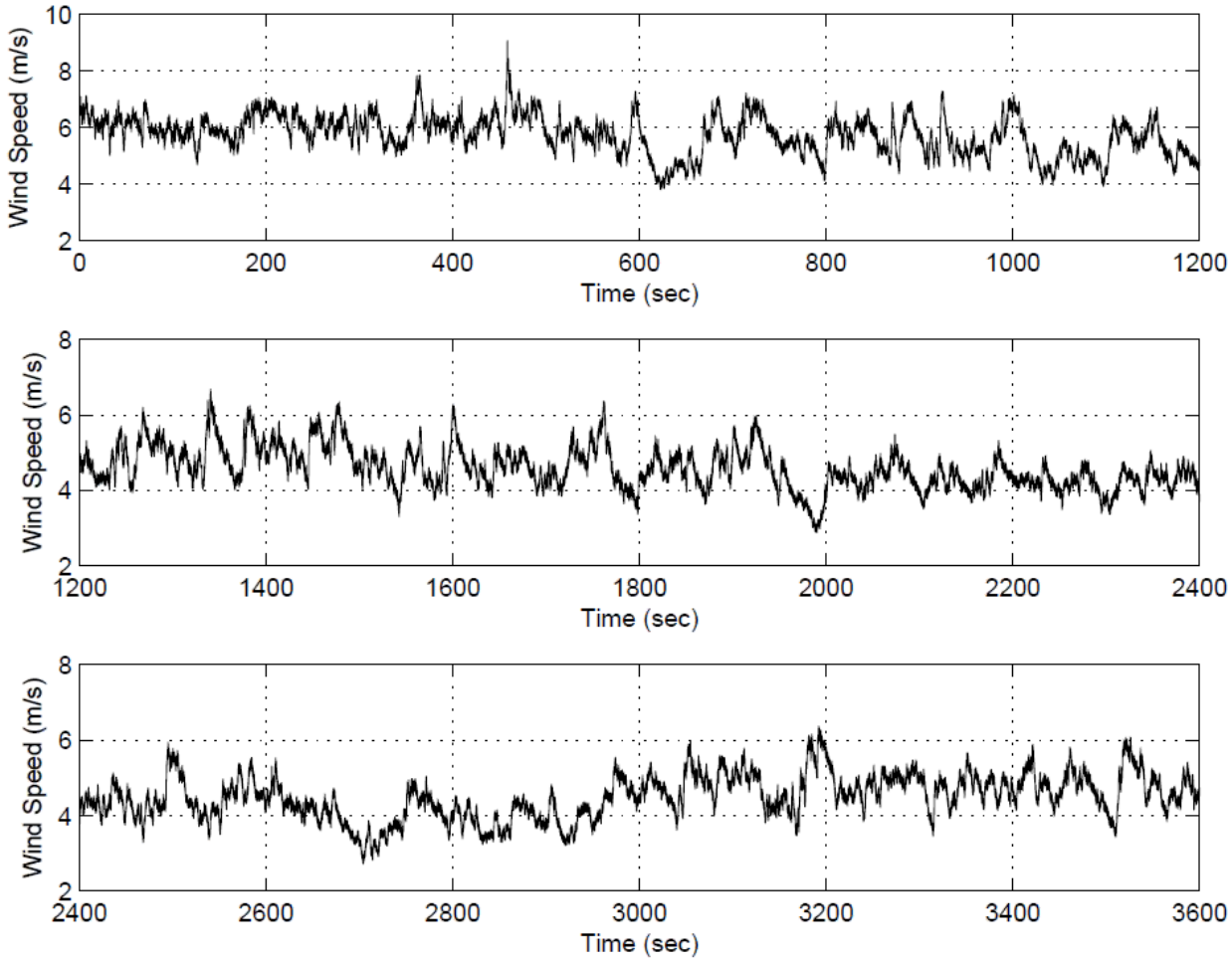

Figure 76: Wind speed time history for DLC 1.2. The one-hour time series is split into three segments of 1200 s each.

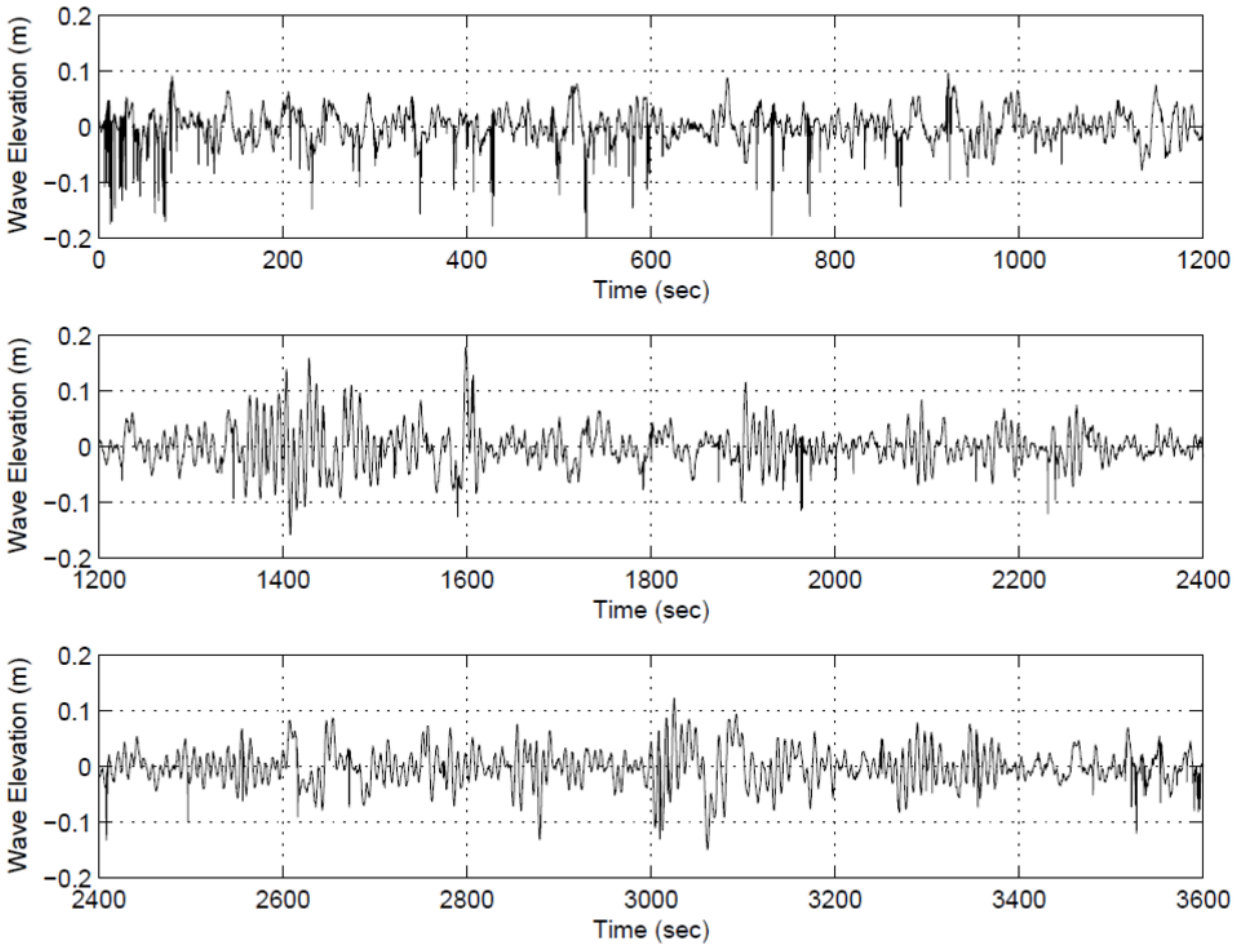

Figure 77: Wave height time history for DLC 1.2. . The one-hour time series is split into three segments of 1200 s each.

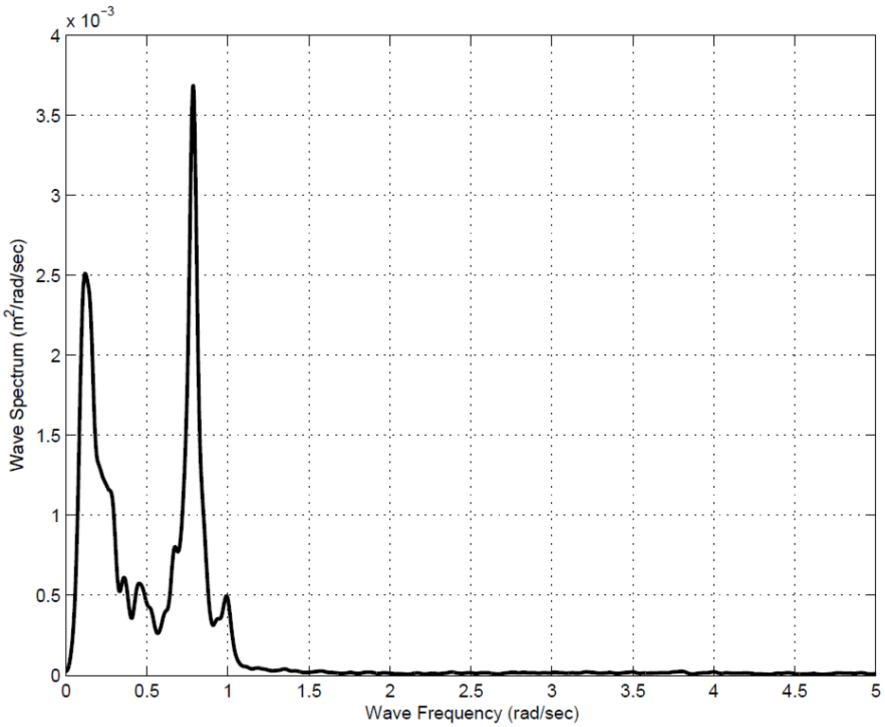

Figure 78: Wave spectrum for DLC 1.2.

6.4.2.3 Design Load Condition 1.6: Jan. 19, 2014

Design Load Condition 1.6 is classified as a survival design condition, in which the wind speed is within operating conditions, and the significant wave height is one with a 50-year return period. Figure 79 shows the directions, and Figure 80 through Figure 83 show plots of the environment.

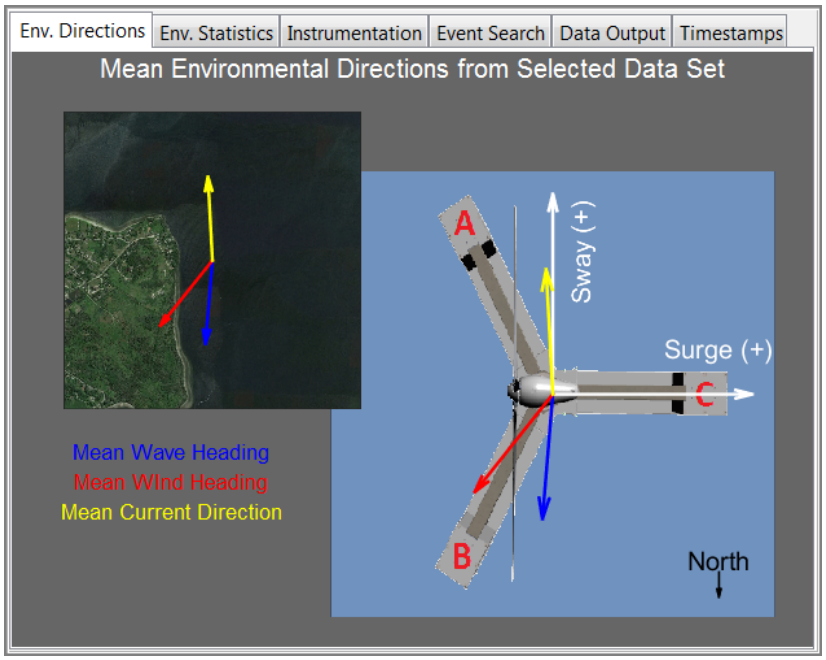

Figure 79: Coordinate system and wind, wave, and current headings for Design Load Case 1.6 (DLC 1.6)

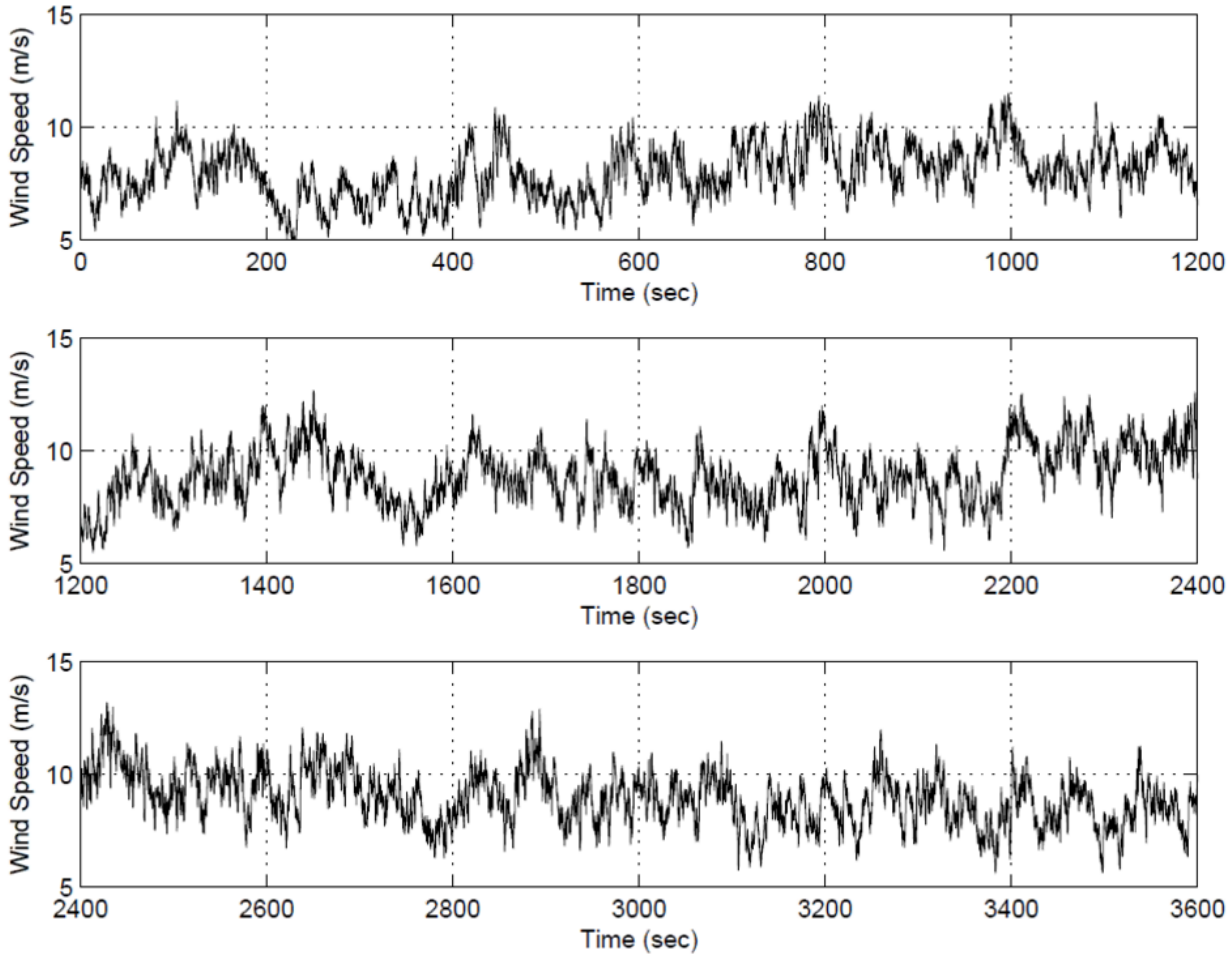

Figure 80: Wind speed time history for DLC 1.6. The one-hour time series is split into three segments of 1200 s each.

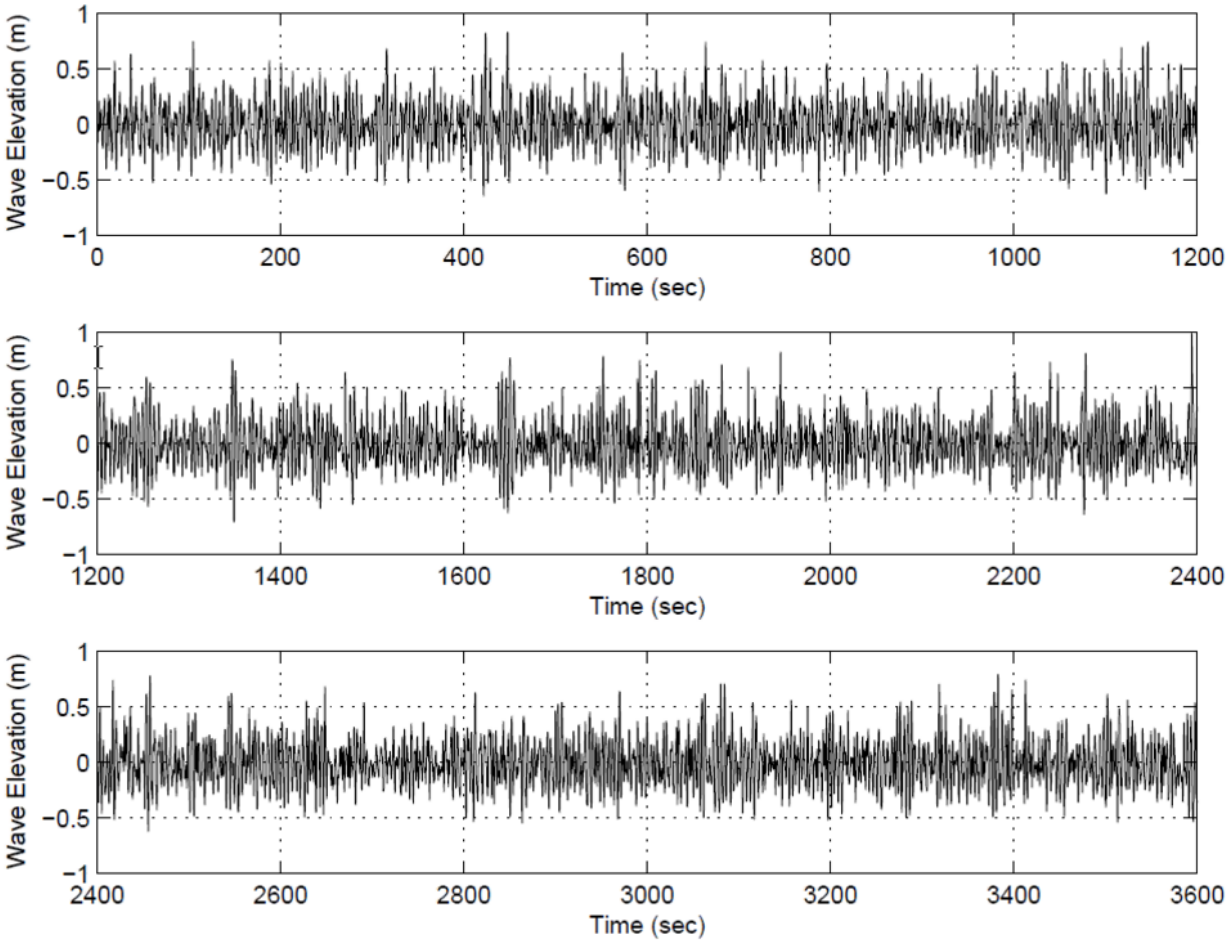

Figure 81: Wave elevation time history for DLC 1.6. The one-hour time series is split into three segments of 1200 s each.

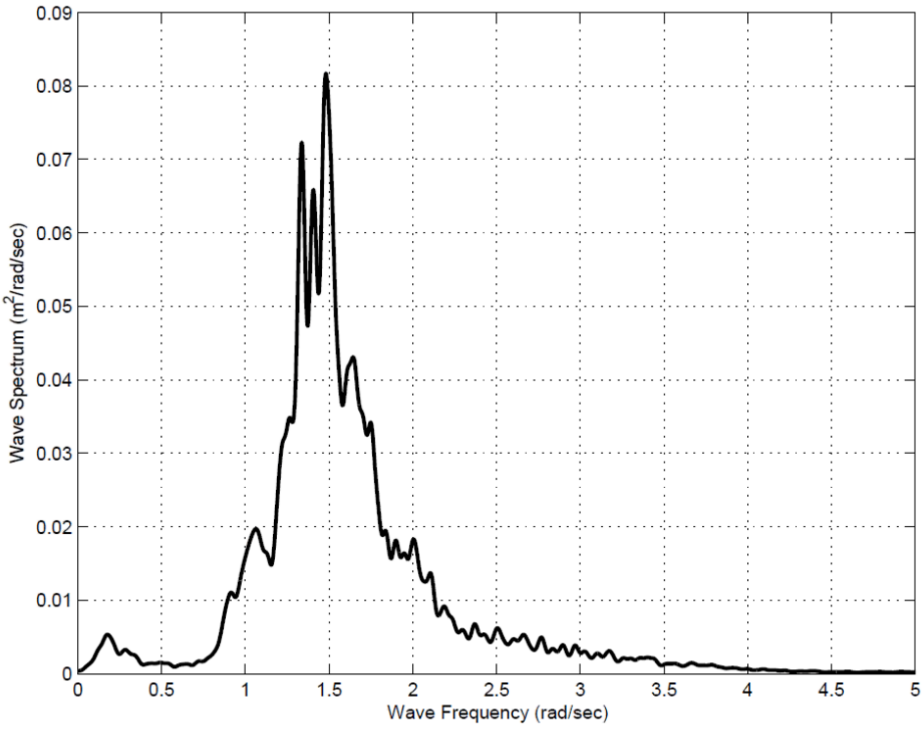

Figure 82: Wave spectrum for DLC 1.6.

6.4.2.4 Survival Load Condition: Jan. 25, 2014

The survival load condition is one in which the turbine is parked (wind speed is above cut-out speed) and the environmental conditions include a 500-yr return period wave height, with corresponding wind and current. Figure 83 through Figure 86 show directions and plots of the environment.

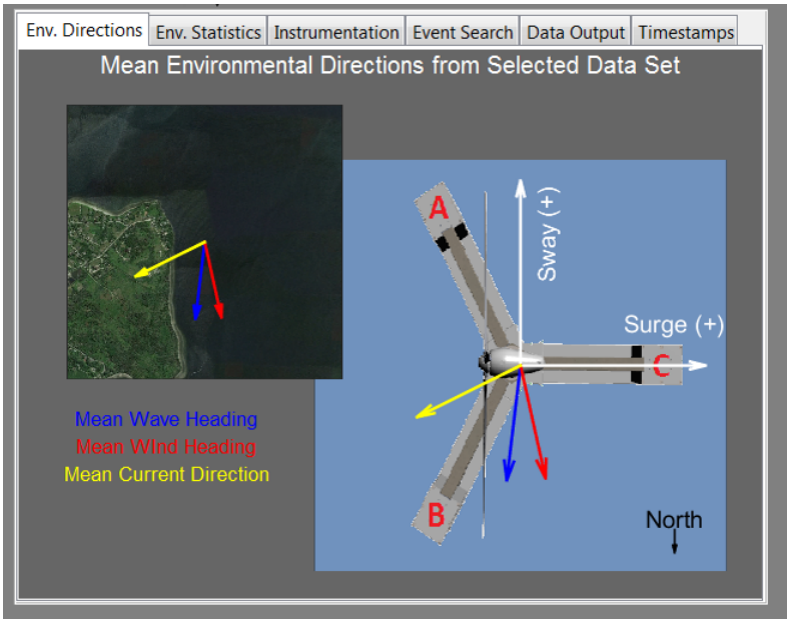

Figure 83: Coordinate system and wind, wave, and current headings for Survival Load Case (SLC)

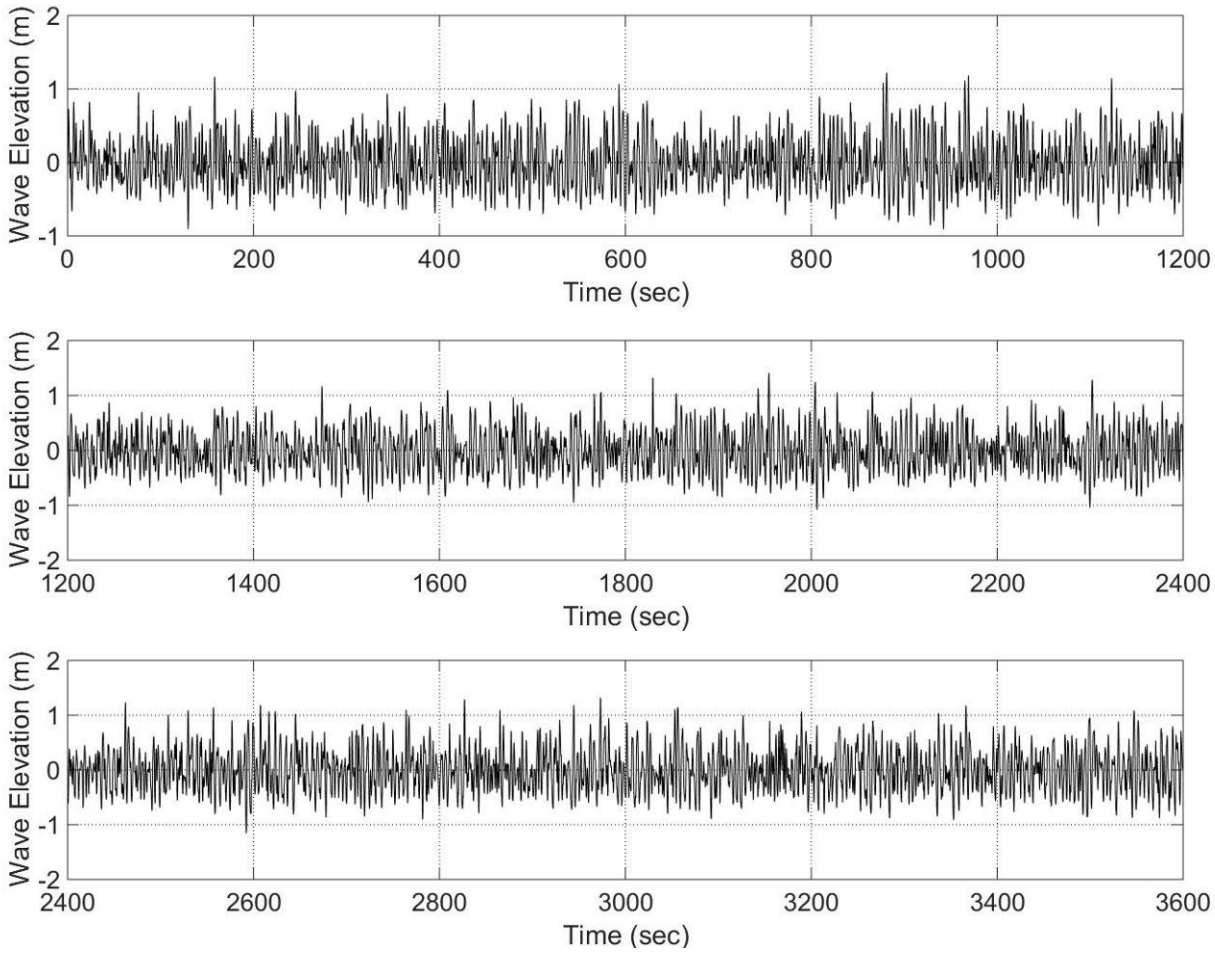

Figure 84 Wave elevation time history for SLC

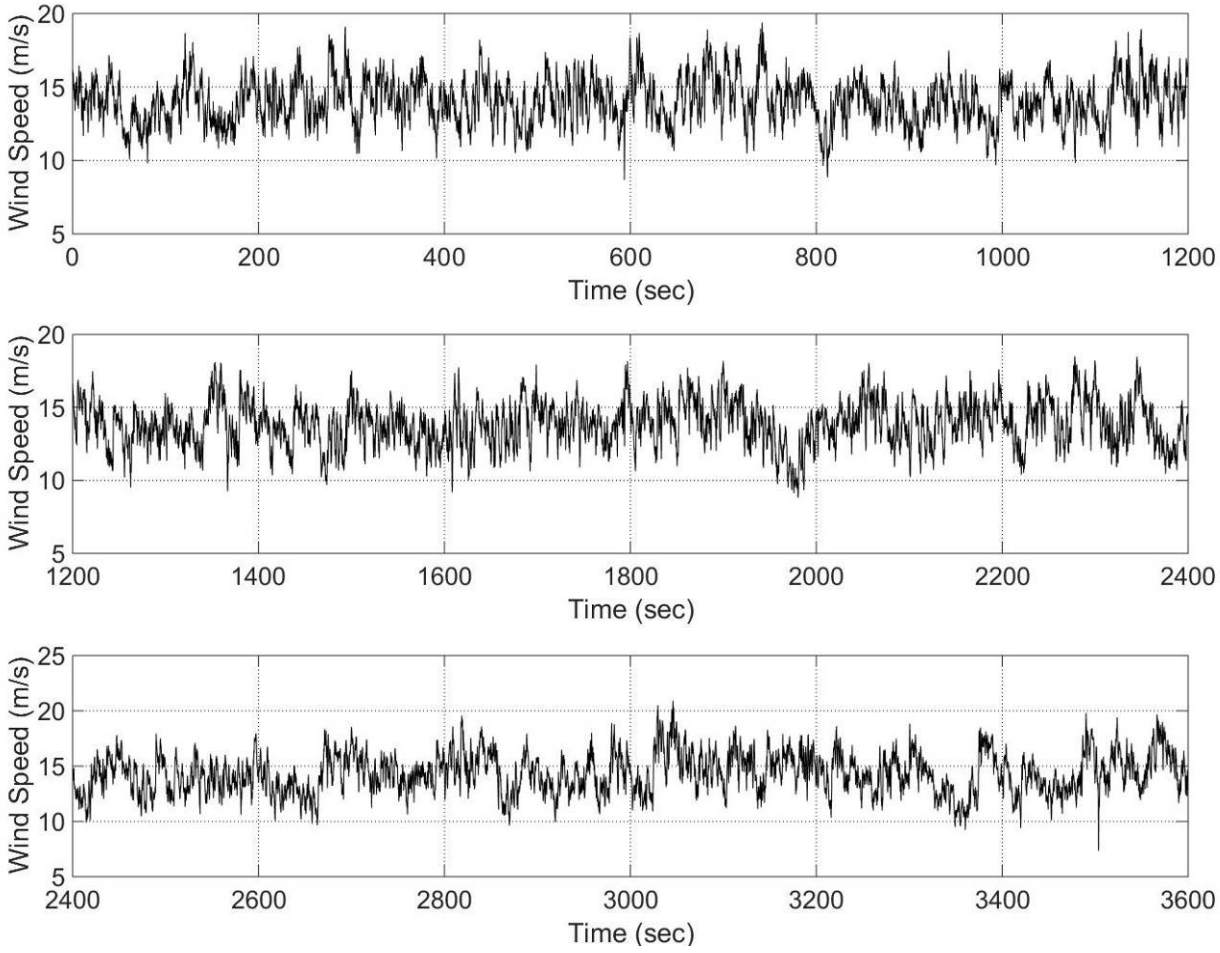

Figure 85 Wind speed time history for SLC

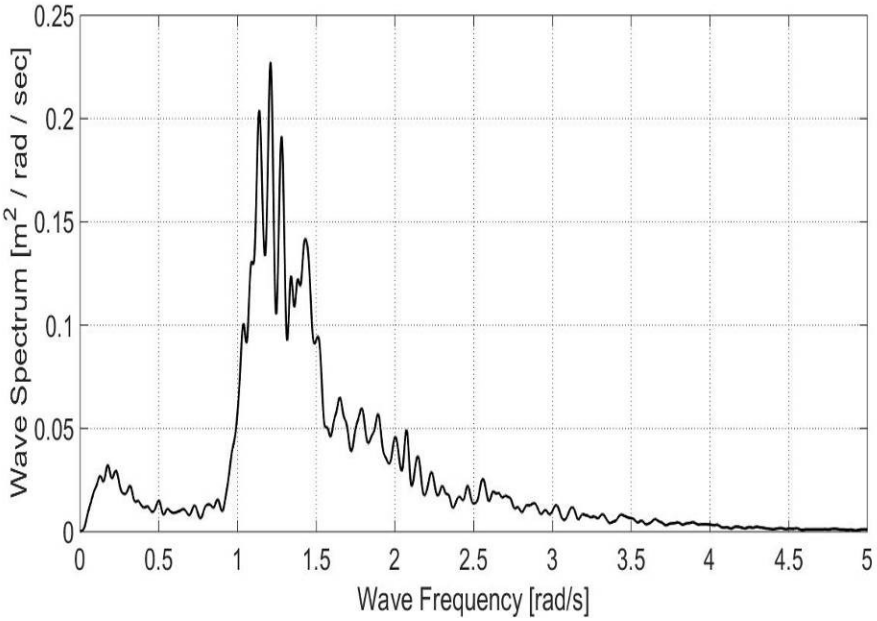

Figure 86 Wave spectrum for SLC

6.4.3 Simulation using FAST+OrcaFlex

6.4.3.1 FAST

The performance of the wind turbine is modeled using NREL's FAST software. For the present study, FAST's hydrodynamics module, HydroDyn, was not used to model the floating platform and mooring dynamics. Instead, both OrcaFlex and Charm3d were implemented. As reported by Viselli et al (AWEA, 2014), FAST alone was found to be insufficient for predicting the mooring line dynamics of the VolturnUS.

A blade pitch control algorithm is implemented. The blade pitch angle is increased when the wind speed exceeds the design wind speed, which reduces rotor thrust and keeps rotor torque and power generation constant. This blade pitch algorithm is implemented in the FAST model, and the results as a function of wind speed are shown in Figure 87, Figure 88, Figure 89, and Figure 90.

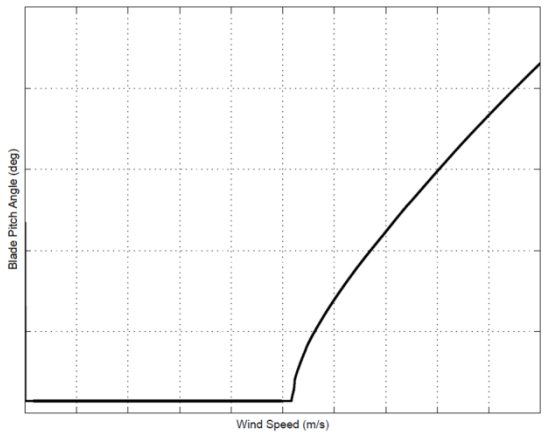

Figure 87: Blade pitch angle as a function of wind speed, according to FAST model.

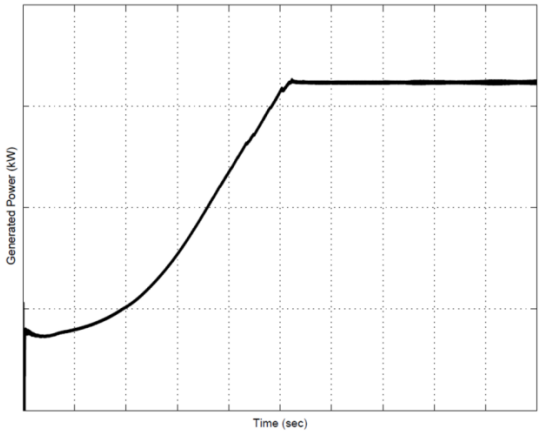

Figure 88: Generated power as a function of wind speed, according to FAST model.

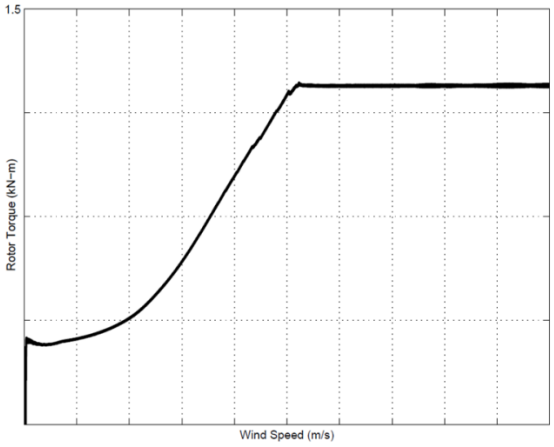

Figure 89: Rotor torque as a function of wind speed, according to FAST model.

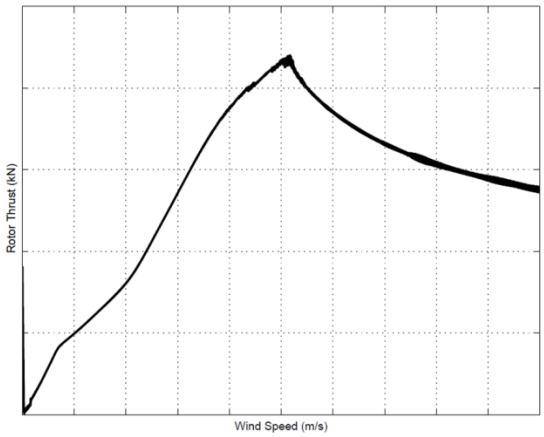

Figure 90: Rotor thrust as a function of wind speed, according to FAST model.

6.4.3.2 Geometry

The first step in creation of a hydrodynamic model of the VolturnUS is development of a CAD geometry that will be used for diffraction analysis. An initial model was developed from available dimensions of the platform. The VolturnUS is a semi-submersible with three pontoons and columns. These pontoons are connected to a center column. The side columns and pontoons are rectangular in cross-section. The center column is hexagonal. Rectangular cross trusses connect the base of the side columns to the center column above the waterline. The geometry is shown in Figure 91.

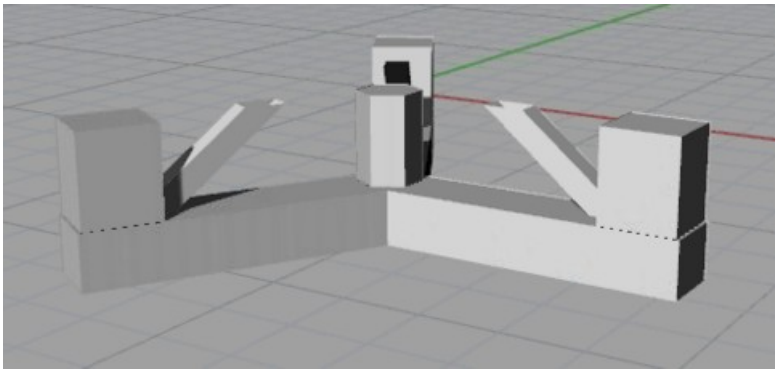

Figure 91: Geometry of VolturnUS 1:8 scale platform.

6.4.3.3 ANSYS Aqwa

The VolturnUS geometry was imported into ANSYS Aqwa for hydrodynamic diffraction analysis. As a validation, the hydrodynamic database, including wave forces (Froude-Krylov and Diffraction forces), added mass, and damping coefficients were compared with the values included in the original FAST model. A comparison of wave forces is shown in Figure 92. Good agreement is observed. This model was extended to include cross truss elements, shown in Figure 91. As expected, the results, shown in Figure 93, are similar but show higher wave loading in the surge and pitch directions.

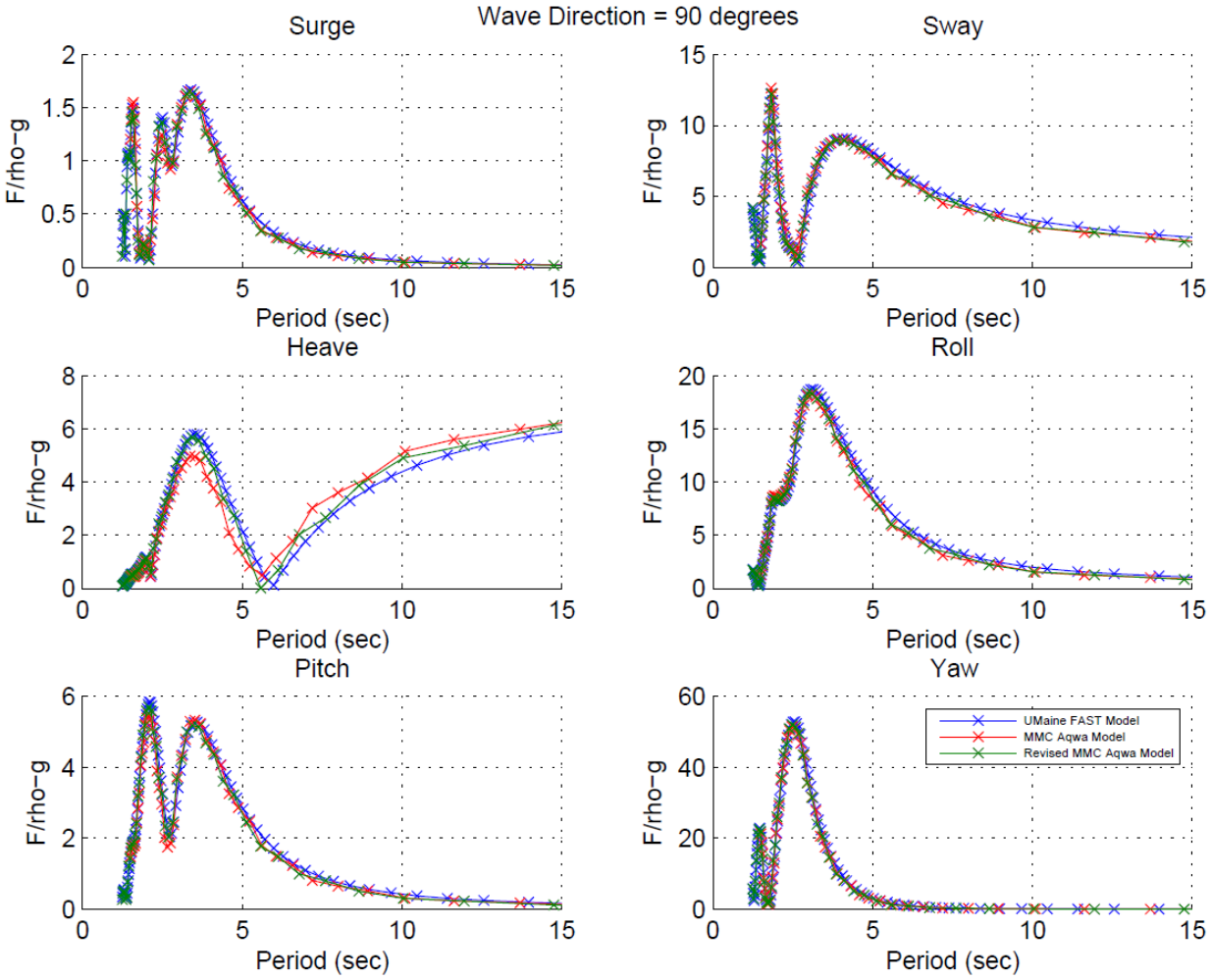

Figure 92: Wave loading in each degree of freedom, wave heading = 90°. Y-axis units are in m^3 for Surge, Sway, and Heave plots, and m^4 for Roll, Pitch, and Yaw plots.

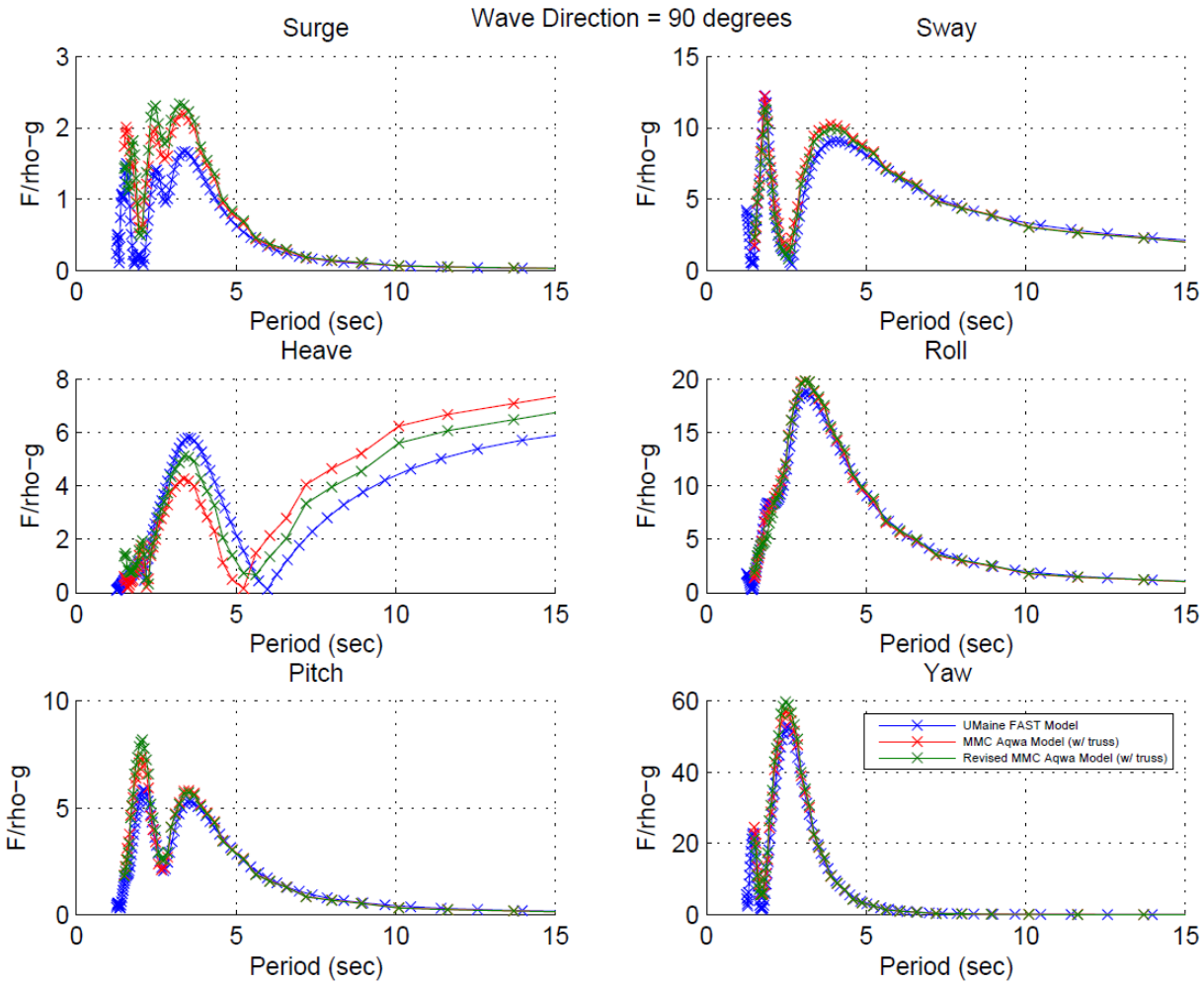

Figure 93: Wave loading in each degree of freedom, wave heading = 90°, with truss added to model. Y-axis units are in m^3 for Surge, Sway, and Heave plots, and m^4 for Roll, Pitch, and Yaw plots.

6.4.3.4 OrcaFlex

The completed hydrodynamic database of the platform was used in OrcaFlex, where the mooring line effects are considered in the time domain. The arrangement of the mooring lines, including the anchor locations and line lengths, were not readily available. After numerous discussions with members of the University of Maine ASCC, a mooring arrangement was agreed upon. This arrangement is shown in Figure 95.

It is observed that the scope of these mooring lines was extremely long in relation to the water depth. This long scope has a number of consequences.

- The long scope of the mooring lines eliminates the risk of snap loading. While this is ideal, it is rarely economical in deeper water, commercial applications.
- The long scope also ensures that it will often be the case that one of the mooring lines is completely slack. This typically will correspond to the downwind mooring line.
- Finally, the long scope creates the potential for a large radius of motion of the platform as it responds to changing tides, wind headings, etc.

All of these phenomena discussed above were observed in the modeling of the VolturnUS.

The VolturnUS was decommissioned on November 4th, 2014, being towed offsite fully intact with a single tugboat. From the loads measured on the towline (Viselli et al, 2014), it was possible to calculate the steady drag coefficient on the platform. A steady drag coefficient of 1.48 was calculated using this method, compared with a value of 1.5 calculated using empirical methods outline in DNV RP C205.

Morison viscous drag was calculated using a stick approach, with coefficients derived using a method in Faltinsen (1990).

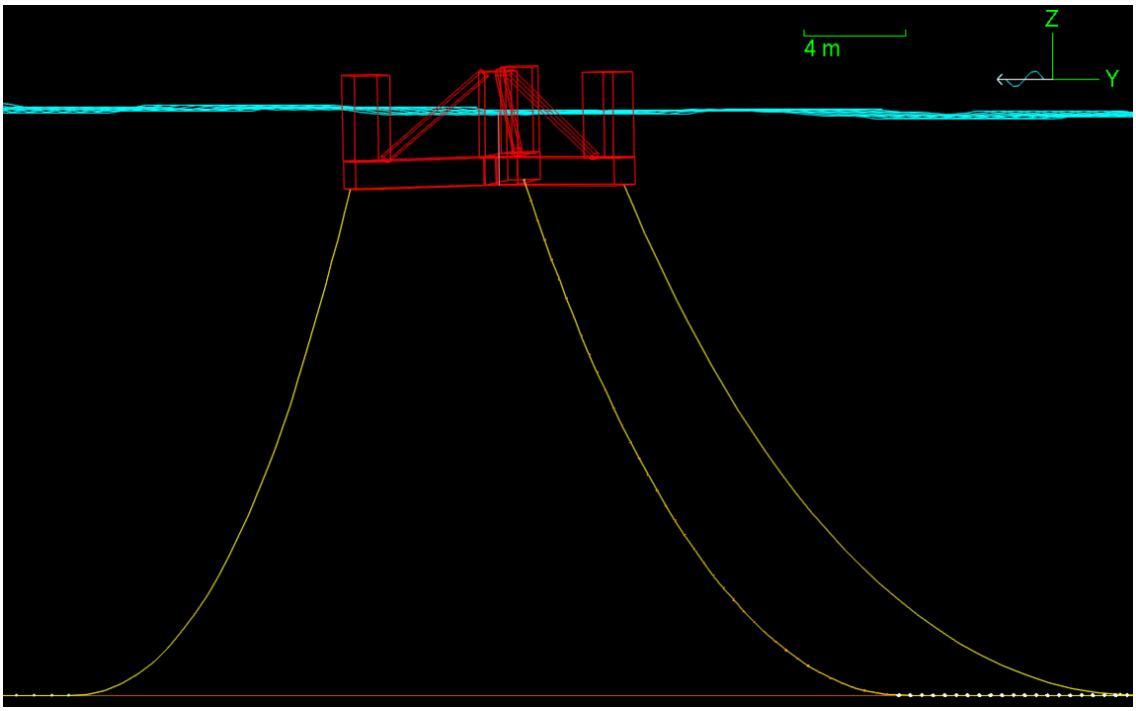

Figure 94: OrcaFlex model of platform and mooring arrangement.

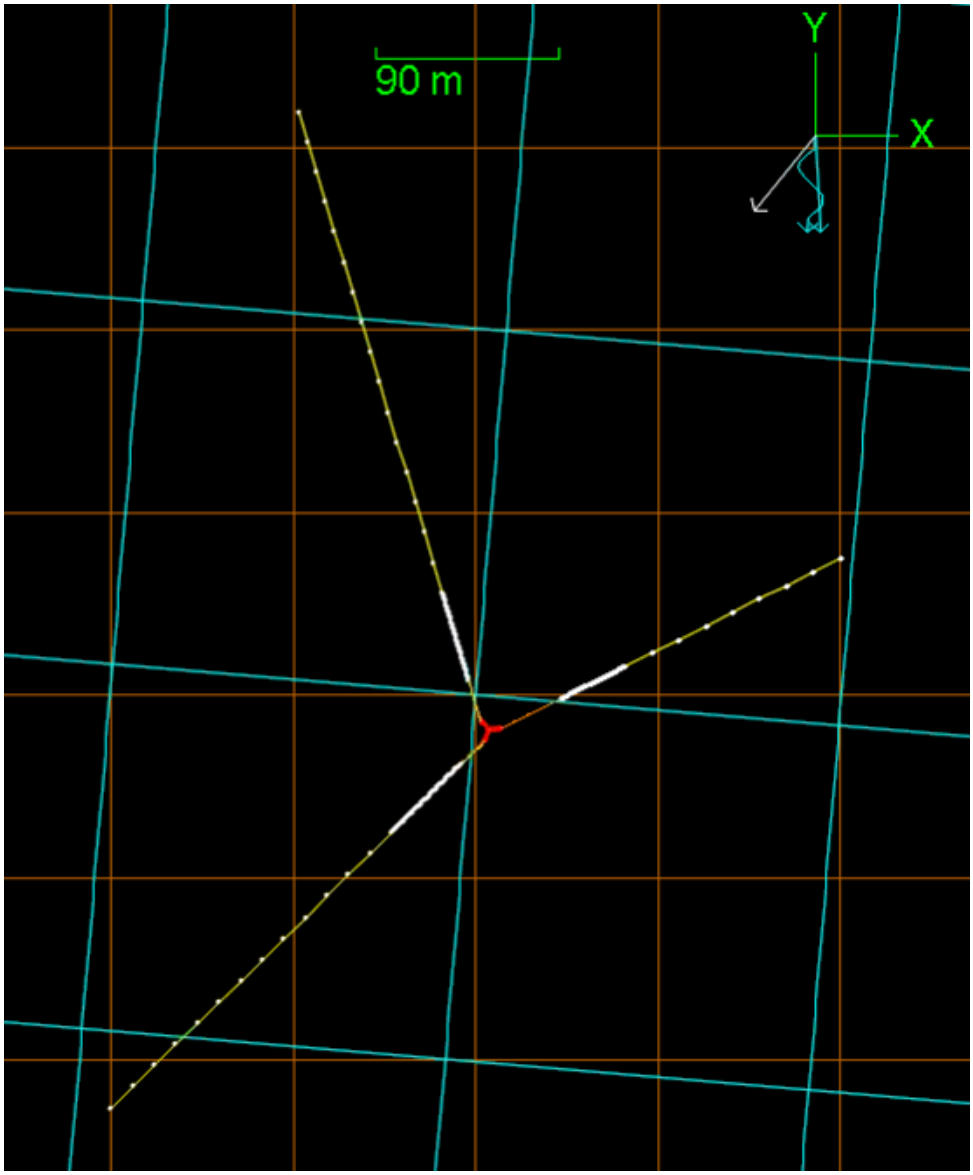

Figure 95: Plan view of OrcaFlex model, showing mooring arrangement.

To test that the mass, inertia, and platform hydrostatics were properly understood, a static offset test was performed in OrcaFlex. This test replicates a heave and pitch static offset test that was done on the VolturnUS dockside, and reported by Viselli et al (AWEA, 2014). The results are shown in Figure 96 and Figure 97, where the OrcaFlex results are overlaid in red over Figure 5 from Viselli et al (AWEA, 2014). Good agreement is observed, indicating that the platform hydrostatics, mass and inertia are well understood.

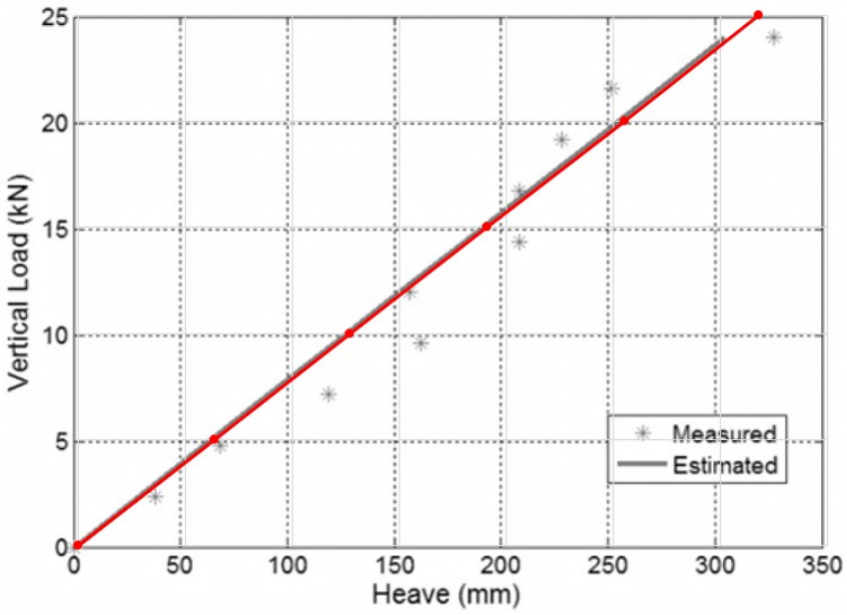

Figure 96: Static heave offset test. OrcaFlex result shown in red, measured and estimated values shown in gray (Viselli, 2014).

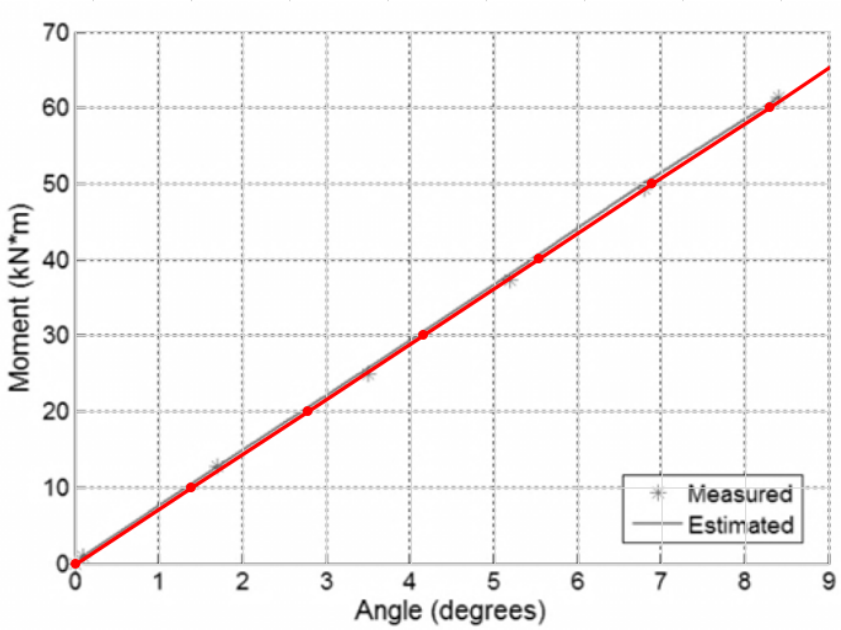

Figure 97: Static pitch offset test. OrcaFlex result shown in red, measured and estimated values shown in gray (Viselli, 2014).

Two separate models were run using FAST and OrcaFlex.

1. Decoupled FAST and OrcaFlex model

In the initial model, FAST and OrcaFlex were fully decoupled. FAST simulations were run assuming that the tower is on a fixed platform. No assumptions about the dynamics of the

platform are made, and the turbine is modeled as though it was fixed to the ground. The forces and moments experienced at the base of the tower were computed from this model.

An OrcaFlex simulation was conducted based off of the results of the fixed-tower FAST model. The tower base forces and moments were input as time-dependent Applied Loads and Applied Moments. This model does not account for the interaction between the dynamics of the rotor and the dynamics of the platform/moorings.

The decoupled FAST and OrcaFlex model was used for initial development of the computer models. Results in many cases were found to be similar to the coupled OrcaFlex+FAST model, and are not reported herein.

2. Fully coupled OrcaFlex+FAST model

A more sophisticated solution, in which FAST and OrcaFlex were fully coupled, was also examined. This coupled model used the open source FASTLink software, which fully couples FAST and OrcaFlex. The coupling calculates platform motion in FAST, and is called as an External Function in OrcaFlex. Mooring dynamics and positions are calculated in OrcaFlex. The External Function which drives platform motion accounts for both rotor dynamics in FAST, and wave, current, and mooring dynamics in OrcaFlex.

6.4.4 Simulation using Charm3D+FAST

6.4.4.1 FAST

The pitch control algorithm provided by the University of Maine's ASCC was used to create a custom DLL for Charm3D-FAST. The file DISCON.DLL was compiled and built using Intel Composer XE 2015.

Figure 98 and Figure 99 compare the rotor behavior predicted by a FAST model provided by ASCC and the Charm3D+FAST model developed by this project team. The results are identical as expected because the FAST pitch source file used by ASCC and this project team are the same.

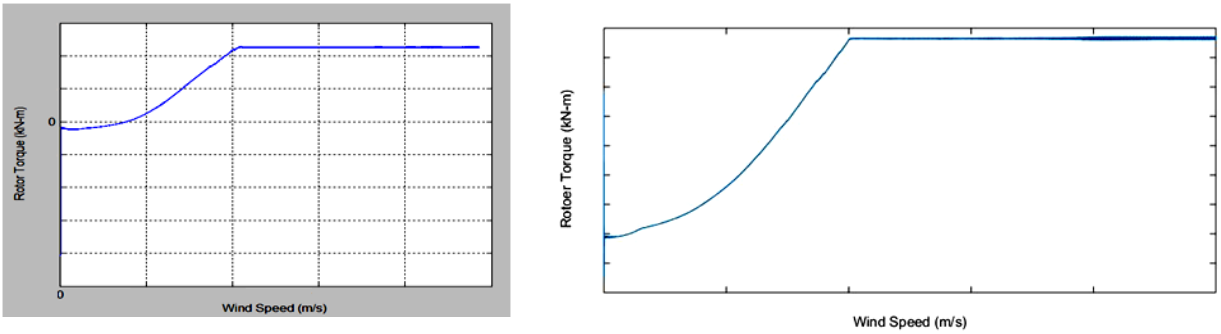

Figure 98 Rotor Torque vs. Wind Speed. (L) Simulation results provided by Univ. of Maine. (R) Simulation results from Charm3D+FAST model

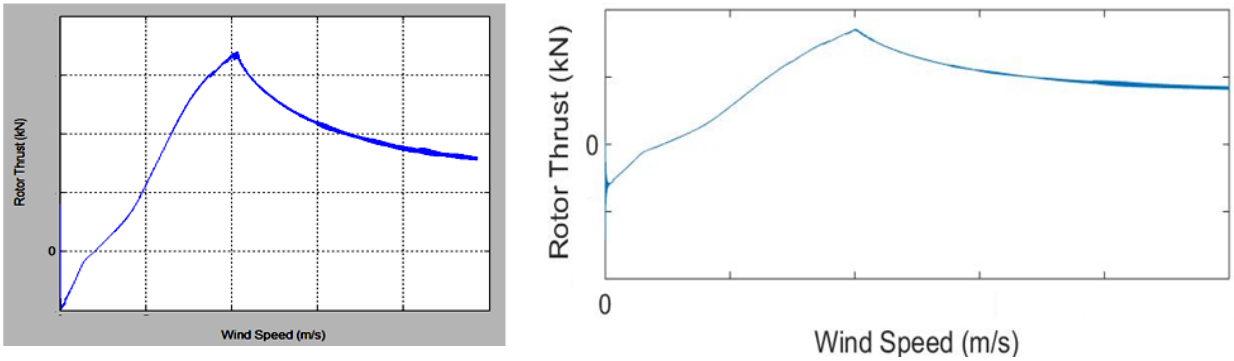

Figure 99 Rotor Thrust vs. Wind Speed. (L) Simulation results provided by Univ. of Maine. (R) Simulation results from Charm3D+FAST model

6.4.4.2 Geometry and Panel Model

The 1/8th scale VolturnUS geometry and panel model were built in Rhino-3D. It is common in panel methods to get spurious results at the so-called irregular frequencies (e.g. Faltinsen, 1990; Ohmatsu, 1975). To remove irregular frequencies, internal lids are added at each of the columns of the platform. Such a procedure does not compromise the accuracy of the external flow (Lee, 1995, 2004; WAMIT, 2013). Since the VolturnUS is symmetric about the y-axis, in order to reduce numerical calculation time, panel model is one half of VolturnUS with a total of 9680 elements. The panel model is imported into HARP/Charm3D pre-processor WAMIT. Figure 100 through Figure 102 shows the half panel model, panel model and panel model in Charm3D respectively.

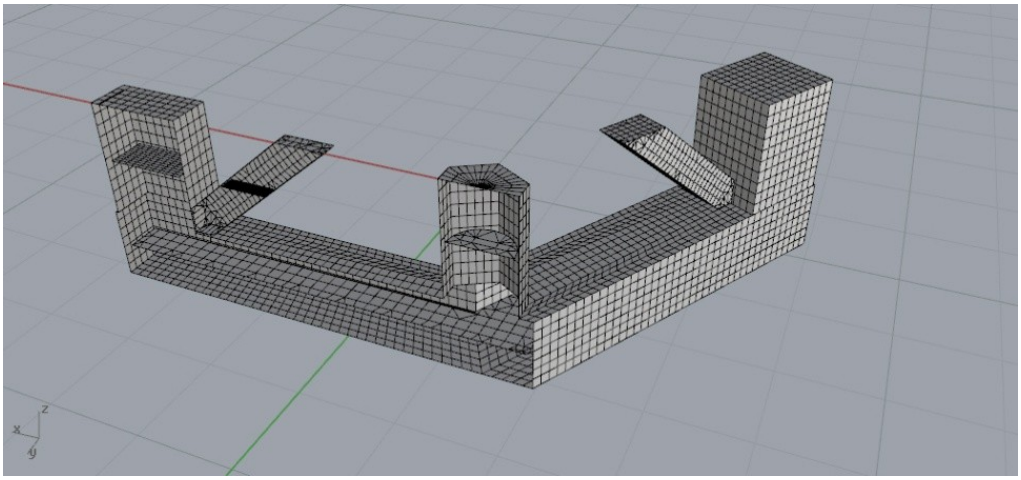

Figure 100 Half Panel Model of VolturnUS

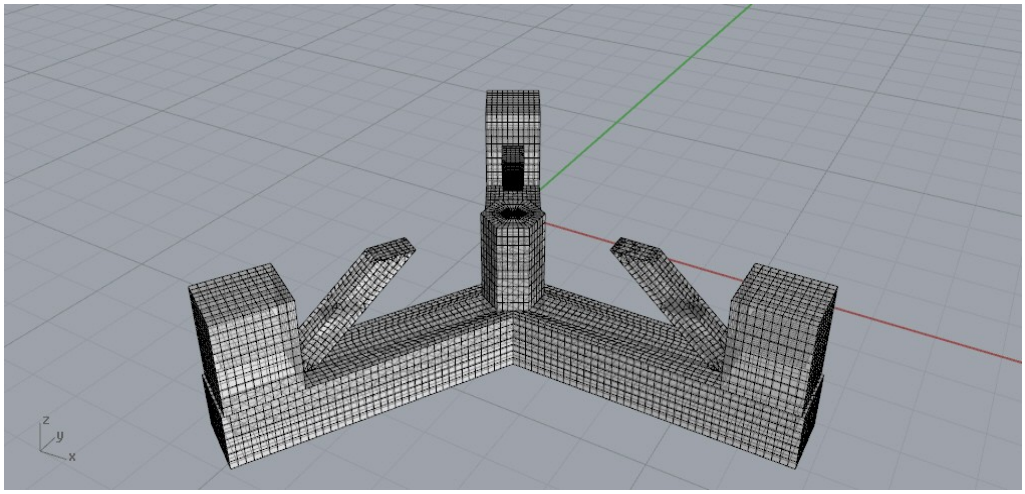

Figure 101 Panel Model of VolturnUS

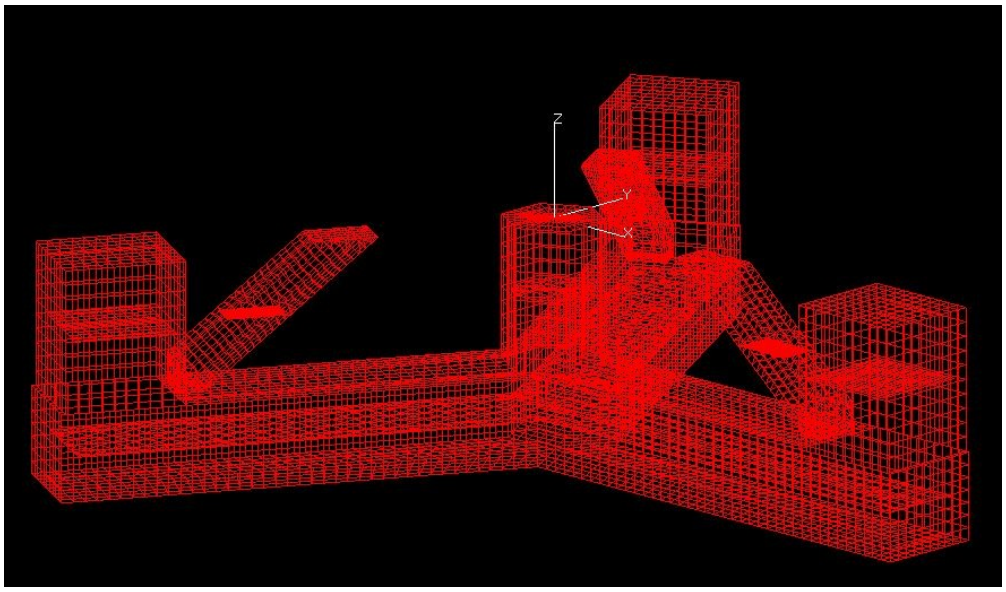

Figure 102 Panel Model in Charm3D

6.4.4.3 HARP/Charm3D pre-processor WAMIT

The center of gravity and moments of inertia of the VolturnUS FOWT were calculated based on the platform, nacelle, tower, and rotor properties provided by ASCC, and then entered into the Charm3D model. The buoyancy force, draft, center of buoyancy, water-plane area and stiffness matrix are calculated based on the panel model.

The first- and second-order hydrodynamic coefficients of the VolturnUS are calculated in the frequency domain using a panel-based 3D diffraction and radiation program (HARP/Charm3D pre-processor WAMIT). Figure 103 shows the 6DOF forces with respect to frequency, for the beam sea condition (wave approach angle = 90 deg). The blue line (x markers) shows results predicted by ASCC's FAST model (using WAMIT for hydrodynamic pre-processing) for coupled analysis. The black line (o markers) shows the results predicted by WAMIT and imported into

Charm3D model for coupled analysis. Unlike the present model, ASCC's FAST model does not include three cross trusses. As noted in the previous section, the difference in surge, heave and pitch could be due to this reason. Since the wave condition is beam seas, the magnitudes of surge and pitch forces are small. The Charm3D model predicts higher peak wave forces in surge and pitch, and higher heave wave force in for long wave periods than does ASCC FAST model. This is explained by the wave forces on the cross trusses in the MOOR Charm3D model.

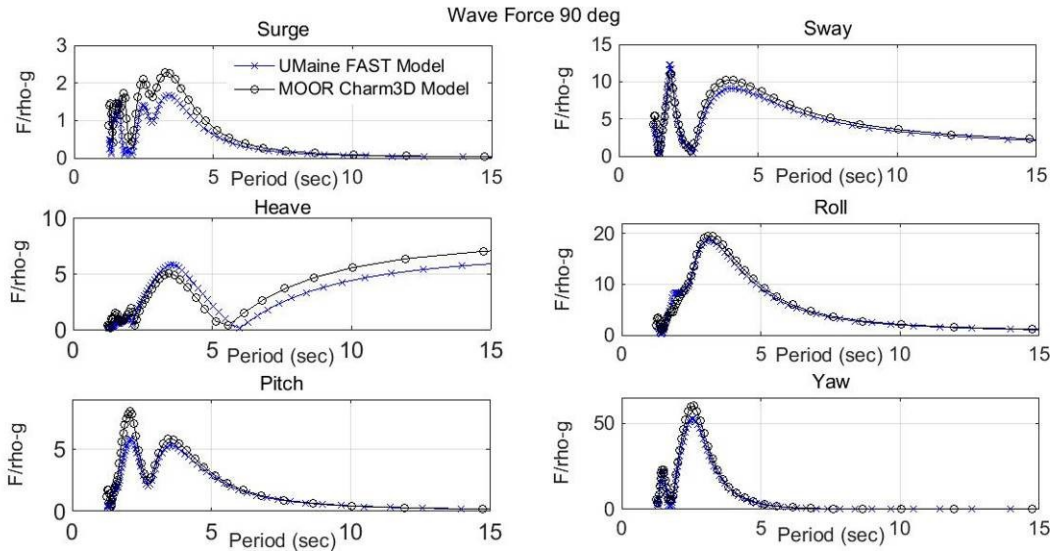

Figure 103 Comparison of 90 degree Wave Force between UMaine FAST Model and MOOR Charm3D Model. Y-axis units are in m^3 for Surge, Sway, and Heave plots, and m^4 for Roll, Pitch, and Yaw plots.

6.4.5 HARP/Charm3D

6.4.5.1 Drag Coefficients

The drag coefficients of the platform are modeled using Morison elements. M1, M2, M3 and M4 are the Morison elements of the columns shown in Figure 104. The drag coefficient for each column is shown in Table 33. The value is selected based on the DNV-RP-C205 Table D-2 and Figure 7.9 of Faltinsen (1999).

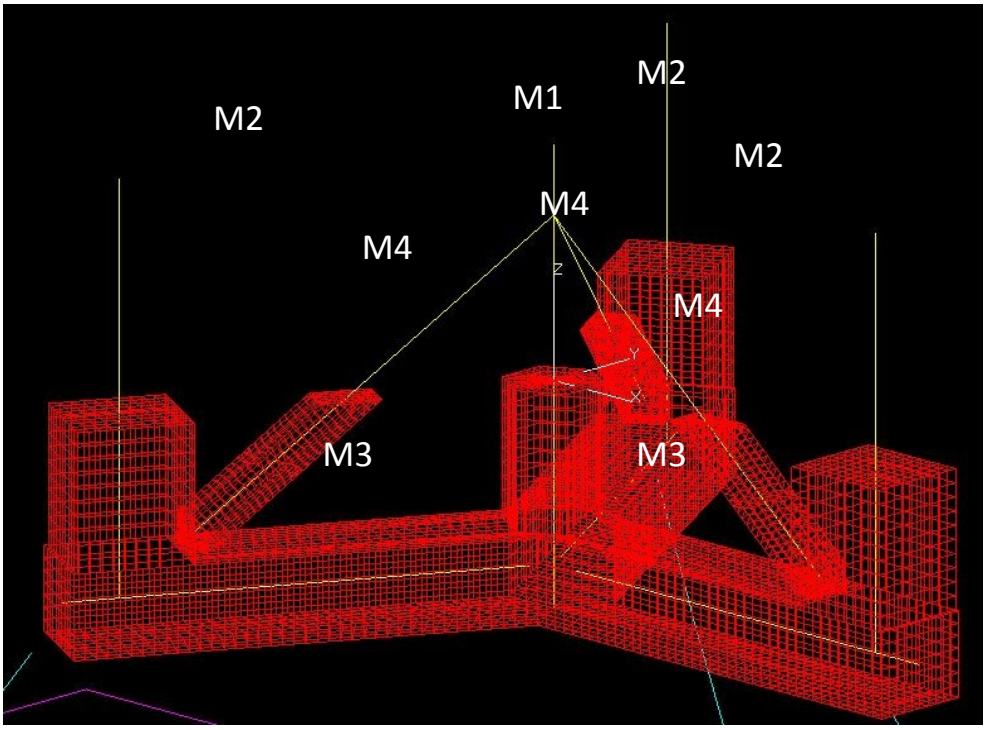

Figure 104 Morison Elements of the Charm3D model

Table 33 Drag Coefficient of the Morison elements

Morison Element in Figure 104	Drag Coefficient
M1	0.8
M2	0.8
M3	0.95
M4	0.8

6.4.5.2 Natural Period

A free decay test of the freely floating platform was performed on the 1/8-scale VolturnUS FOWT dockside, and reported by Viselli et al (2014). To predict the freely floating natural period using Charm3D, the free-decay simulations were done in heave and pitch motions. Since Charm3D cannot model the free-decay test without including a mooring system, the structure is modeled with an artificially low weight and low stiffness mooring system so that damping effects from the mooring system do not affect the simulation results. The heave natural period and pitch period are compared with the test data. Good agreement is observed. Figure 105 and Figure 107 show the heave and pitch free decay test of Charm3D respectively. Figure 106 and Figure 108 show the heave power spectrum of the free decay field tests. The heave natural period of simulation and test data are 6.45 sec and 6.25 sec respectively. The pitch natural period predicted by Charm3D and observed in the test data are 8.65 sec and 8.33 seconds respectively.

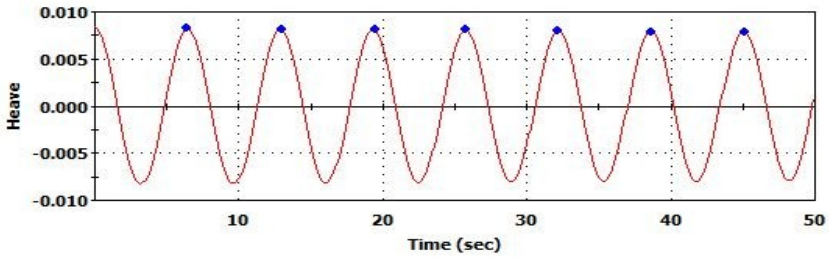

Tp=6.45 sec

Figure 105 Heave Free Decay Test of Charm3D

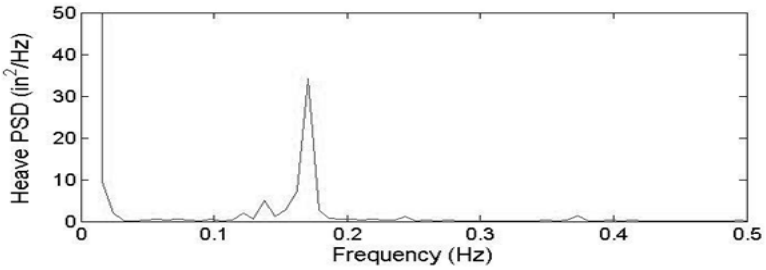

Tp =6.25 sec

Figure 106 Heave Power Spectrum of Free Decay Field Test

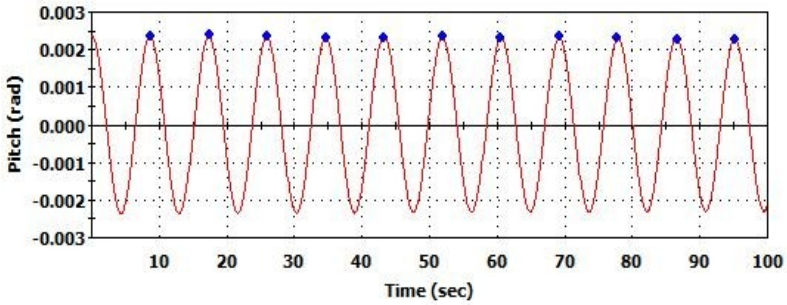

Tp=8.65 sec

Figure 107 Pitch Free Decay Test of Charm3D

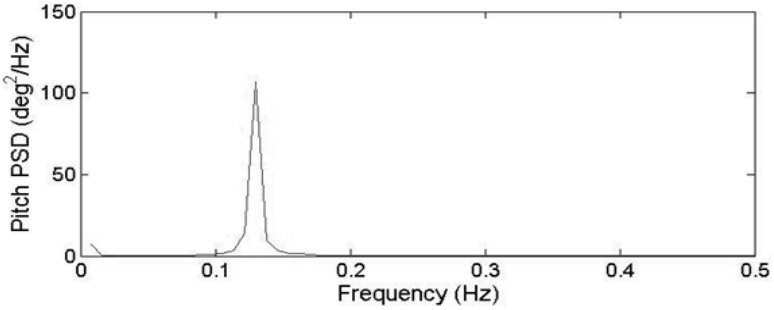

Tp =8.33 sec

Figure 108 Pitch Power Spectrum of Free Decay Field Test

6.4.5.3 Platform Vertical Plane Offset

Vertical plane offset tests were performed on the VolturnUS platform when the latter was near a dock. The platform was systematically moved in the vertical (heave) and rotational (pitch) direction by ballast/deballast operations. Figure 109 and Figure 110 show the comparison of the

heave and pitch static offset, between measured data, OrcaFlex (also discussed in the previous section) and Charm3D respectively. The black dot shows the measurement of test data, solid line in red shows the OrcaFlex results and solid in blue shows the Charm3D results. In the high force range, Charm3D shows higher and lower displacement respectively in heave and pitch motion than field data.

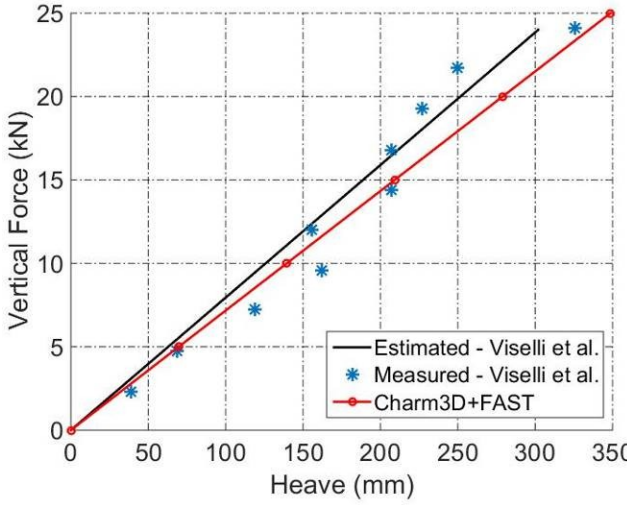

Figure 109 Comparison of heave static offset between test data, OrcaFlex and Charm3D

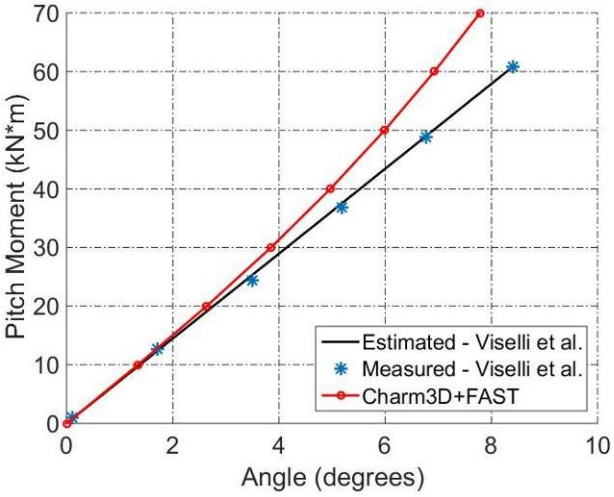

Figure 110 Comparison of pitch static offset between test data, OrcaFlex and Charm3D

6.4.5.4 Mooring Line Model

The structural analysis module of HARP/Charm3D includes Mooring/SCR configuration and analysis program, as well as top tensioned riser/tendon configuration and analysis program. Here we focus on the mooring lines only and ignore the riser modeling capabilities. A nonlinear large displacement flexible finite element analysis solver is used in the mooring system design and analysis. The upper ends of the mooring lines are connected to the fairleads through generalized elastic connection conditions.

The mooring system includes three catenary lines oriented at 20.5, 106.9 and 228.5 degrees with respect to the x-axis as defined in Figure 111. The lines are stud-less chains with properties shown in Table. A mooring line drag coefficient, 2.4, recommended by DNV (2010) for stud-less chain is applied to the Charm3D+FAST model.

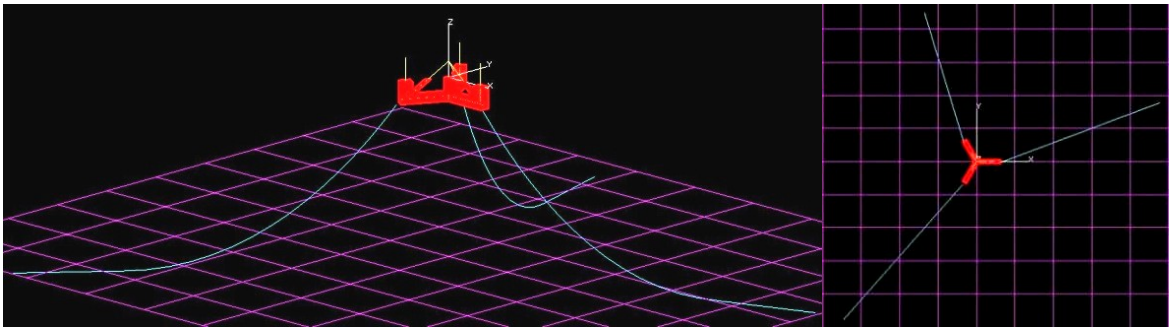

Figure 111 Mooring Line Layout

Table 34 Mooring Line Properties

Mooring Leg	A	B	C
Anchor Angular Position	106.9°	228.5°	20.5°
Depth to Anchor Below MWL	23.0 m	22.1 m	23.0 m
Radius to Anchors from Platform Centerline	300.3 m	271.7 m	191.6 m
Fairlead Angular Position	120°	240 °	0 °
Depth to Fairleads Below MWL	2.9 m	2.9 m	2.9 m
Radius to Fairleads from Platform Centerline	6.32 m	6.32 m	6.32 m
Unstretched Mooring Line Length	308.9 m	277.1 m	198.5 m
Wet Weight	67.6 N/m	67.6 N/m	67.6 N/m
Equivalent Mooring Line Extensional Stiffness	8.0×10^7 N	8.0×10^7 N	8.0×10^7 N

6.4.5.5 Pre-tension

Charm3D describes a mooring system by a combination of fairlead position, line length, stiffness, wet weight, pretension, diameter, inertia coefficient and drag coefficient for each mooring line. A key parameter is mooring line pre-tension, which was not documented and provided by the ASCC. In the absence of accurate measurements of mooring line pretensions in the field data, pretension estimates from the ASCC were used. The ASCC used ANSYS Aqwa software to predict the pretension of each mooring line based on the given fairlead and anchor positions.

6.4.5.6 Environmental Conditions Set-up

The wave elevation measurement time history is imported into Charm3D, and a wave-component input file, WCOMP.IN, is created to be used in the time-domain analysis in Charm3D+FAST. WCOMP.IN contains wave direction, wave spectrum distribution and their phases.

6.4.6 Simulation Results

6.4.6.1 Turbine Generator Power

For each time series, the generator power, as measured in the field, was compared to both the OrcaFlex+FAST model and the Charm3D+FAST model. This comparison is plotted for DLC 1.2 in Figure 112. Agreement between both models and measured field data is very good. Similarly, results for DLC 1.6 are plotted in Figure 113, and Figure 114 for the SLC, again showing good agreement.

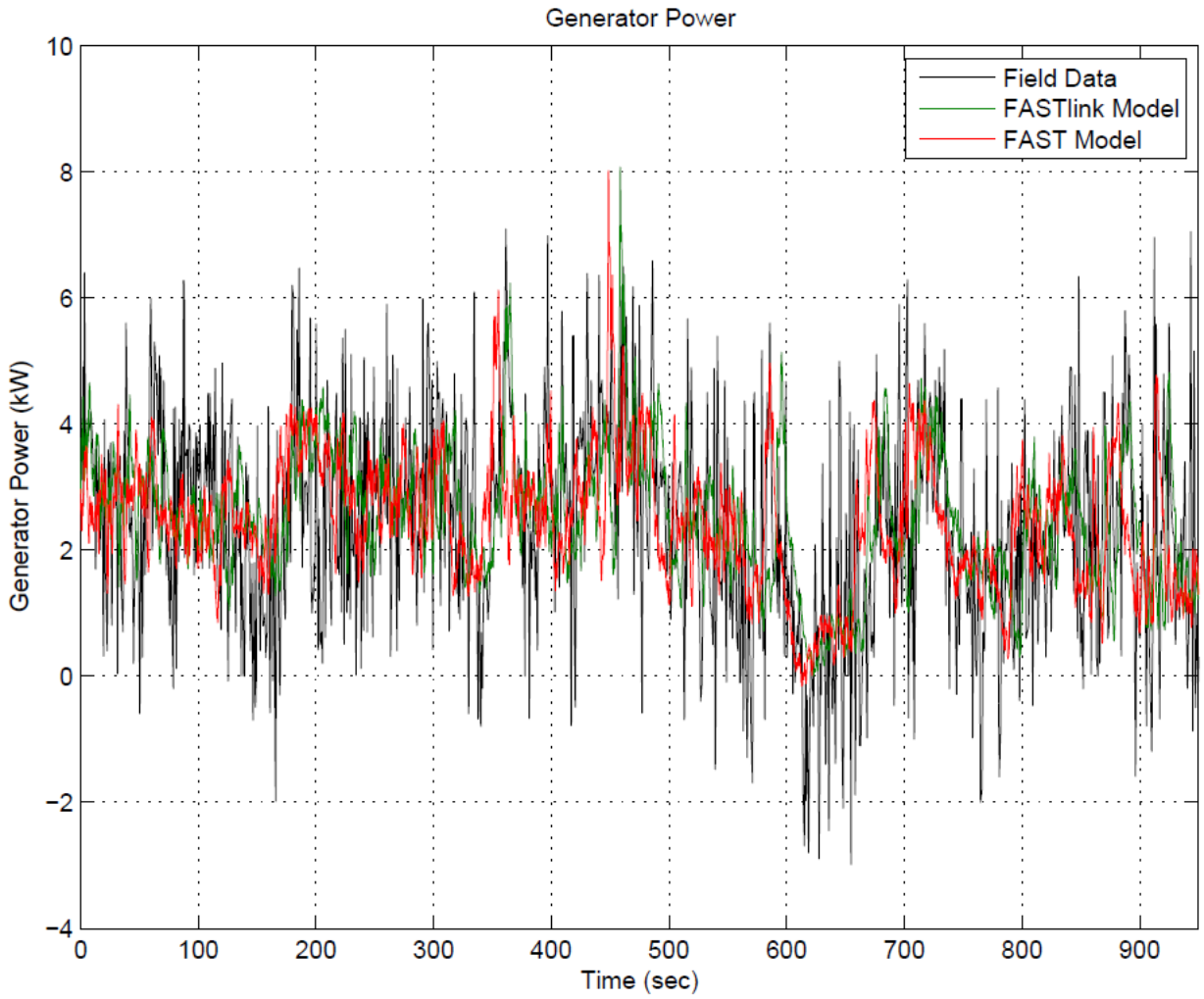

Figure 112: Comparison of generator power between field data (black), OrcaFlex+FAST simulation (green), and Charm3D+FAST simulation (red) for DLC 1.2.

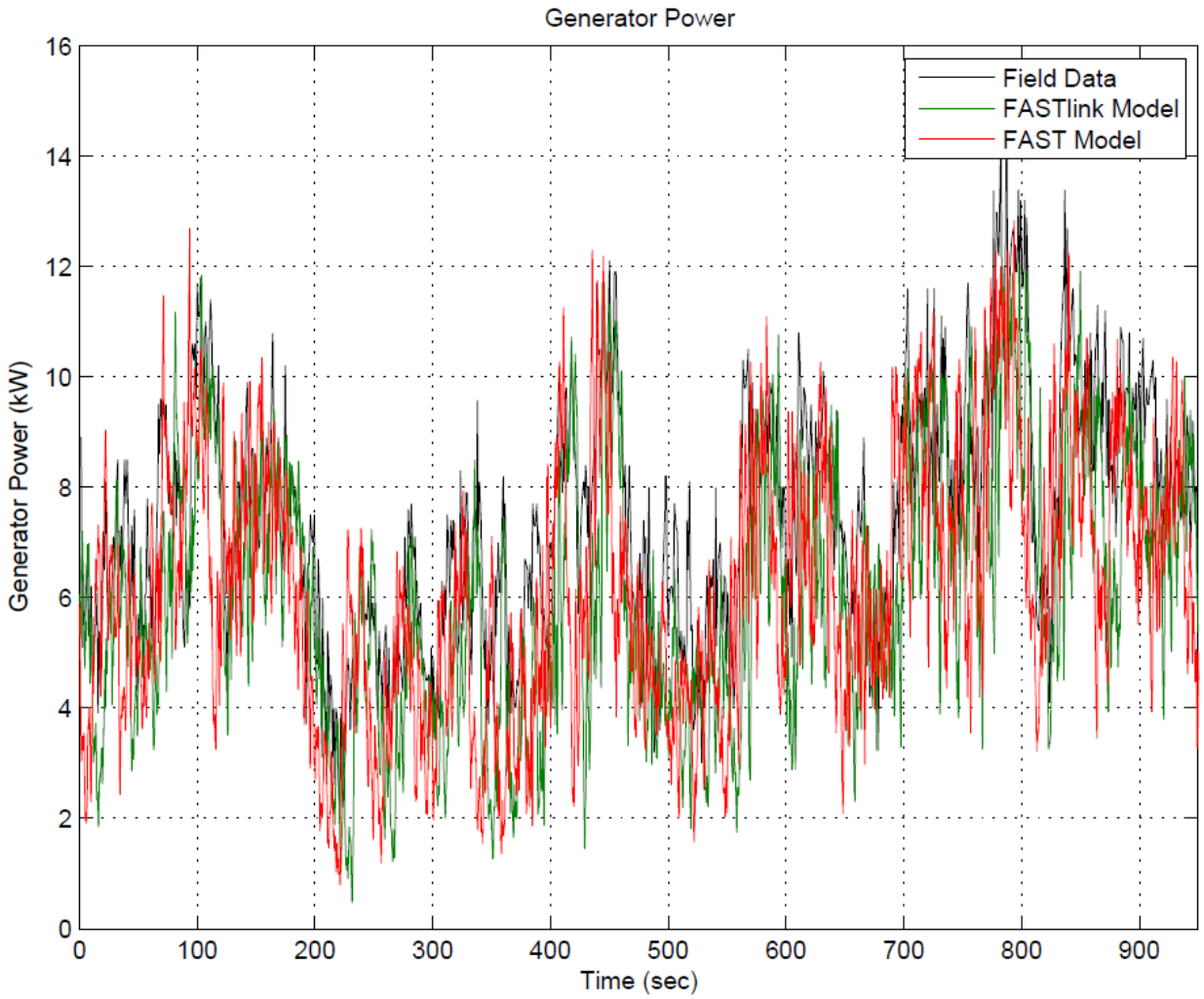

Figure 113: Comparison of generator power between field data (black), OrcaFlex+FAST simulation (green), and Charm3D+FAST simulation (red) for DLC 1.6.

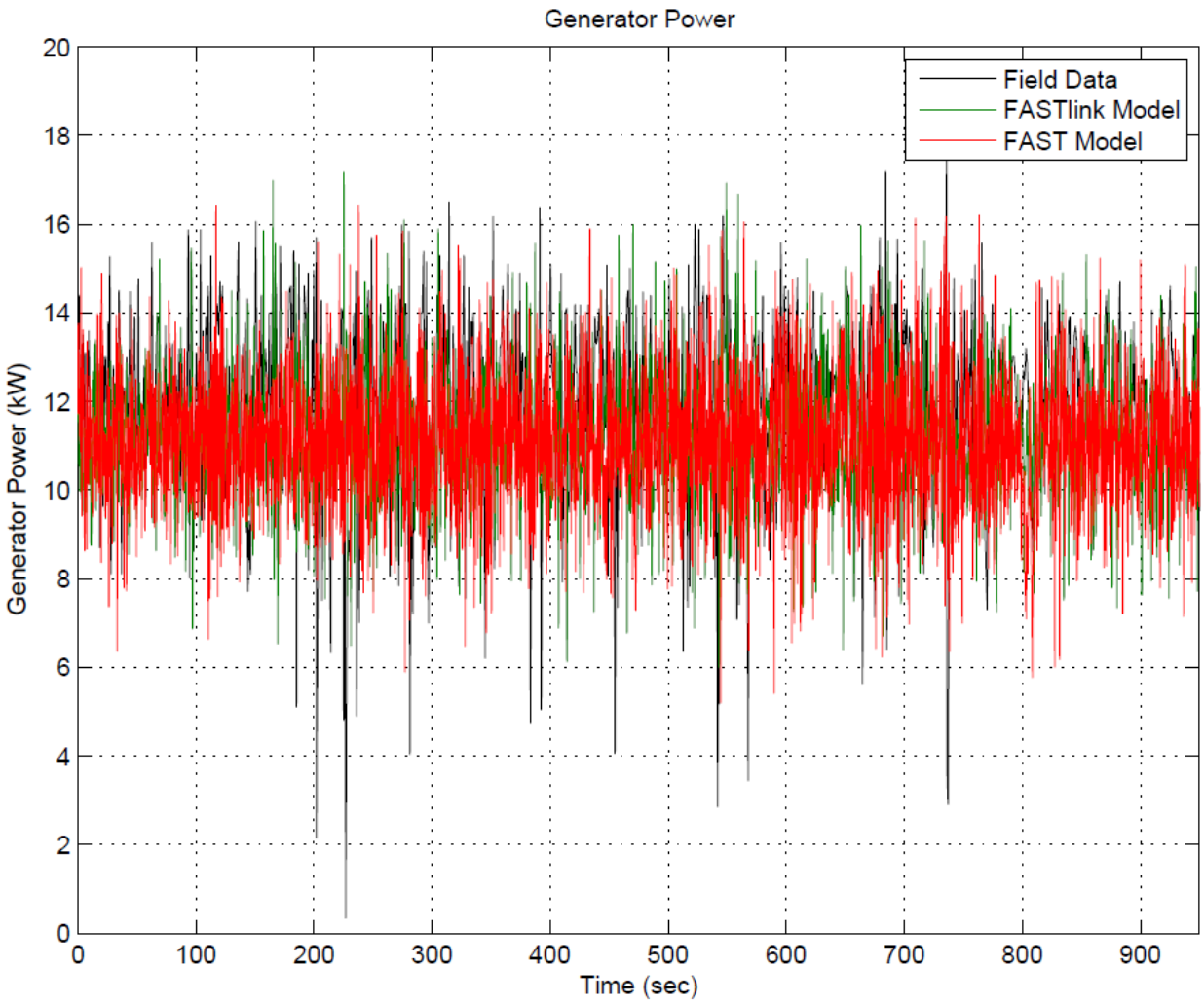

Figure 114: Comparison of generator power between field data (black), OrcaFlex+FAST simulation (green), and Charm3D+FAST simulation (red) for SLC.

6.4.6.2 Platform Motions

Platform accelerations are presented in the section for each of the three load conditions, along with simulation results from both Charm3D+FAST and OrcaFlex+FAST models.

6.4.6.2.1 DLC 1.2

Root mean square (RMS) accelerations are shown in Table 35 for Design Load Case 1.2. Platform motion accelerations were calculated in each degree of freedom for the three time series, and were compared with field measurements.

For DLC 1.2, the simulation models under-predict linear accelerations, while they are able to accurately predict roll and pitch acceleration. Yaw acceleration is also under-predicted, which may be due to the fact that the variation of wind heading with time was not provided. This variation in wind heading is likely the primary driving force in causing the platform to yaw.

Table 35: RMS values of acceleration for field data, Charm3D+FAST model, and OrcaFlex+FAST model; DLC 1.2.

	Field Measurement RMS	Charm3D+FAST		FAST+OrcaFlex	
		RMS	Difference (%)	RMS	Difference (%)
Surge (m/s^2)	0.04	0.01	-80%	0.01	-67%
Sway (m/s^2)	0.06	0.02	-72%	0.02	-63%
Heave (m/s^2)	0.03	0.04	30%	0.03	-1%
Roll (deg/s^2)	0.21	0.21	-1%	0.21	-2%
Pitch (deg/s^2)	0.18	0.12	-36%	0.14	-21%
Yaw (deg/s^2)	0.34	0.01	-96%	0.06	-84%

Time history and spectral responses in each degree of freedom are shown in Figure 115 - Figure 120. Figure 115 and Figure 116 show that both models under-predict surge and sway accelerations, however, models reflect spikes in response at the wave frequency (approx. 1 rad/sec) and the rotor frequency (approx. 11 rad/sec) that occur in field data. Most of the under-prediction occurs around 3-4 rad/sec, which may be attributed to instrumentation or other behavior not captured by the simulations (such as time-dependence of wind heading).

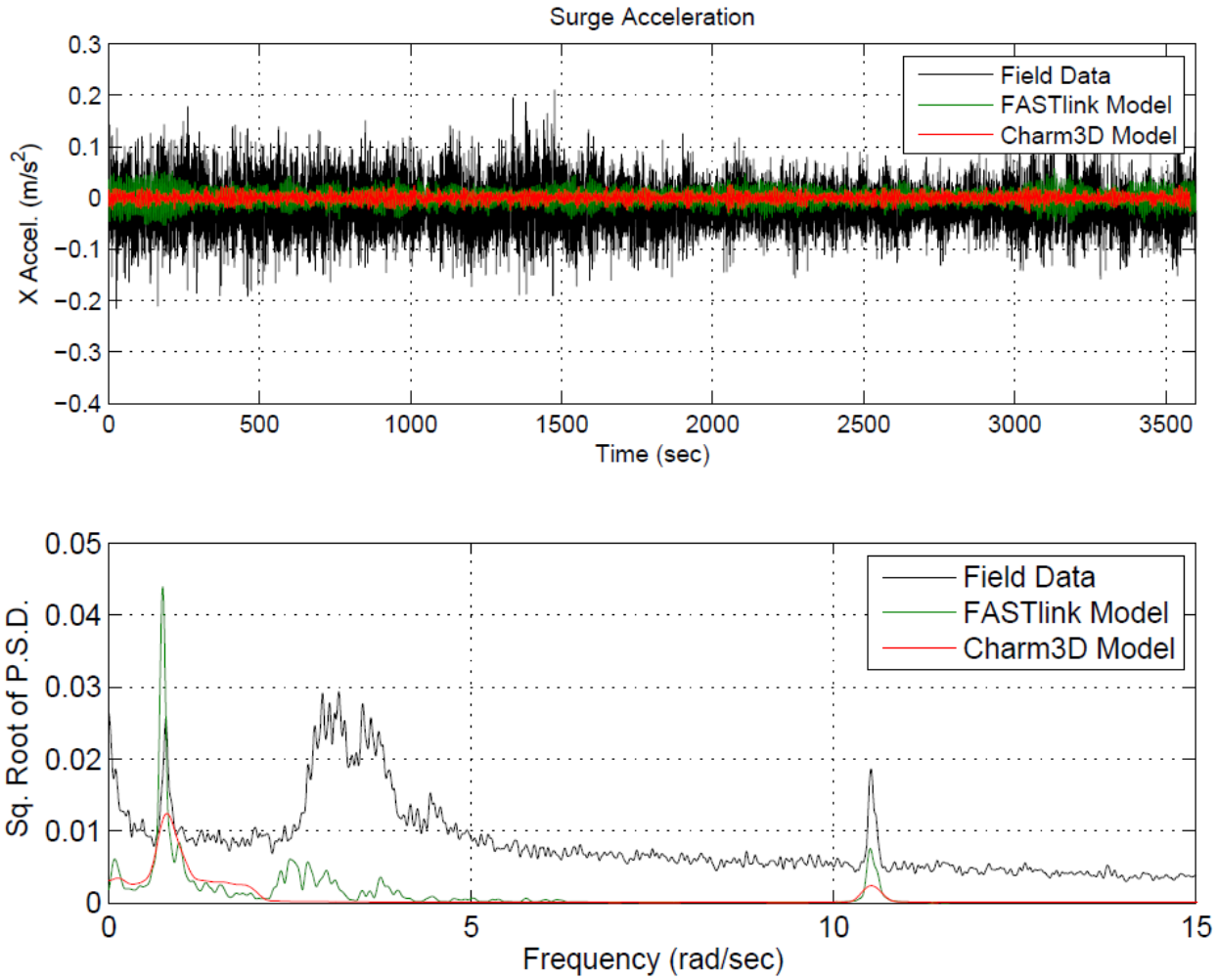

Figure 115: Surge acceleration time history (top) and square root of Power Spectral Density (bottom).

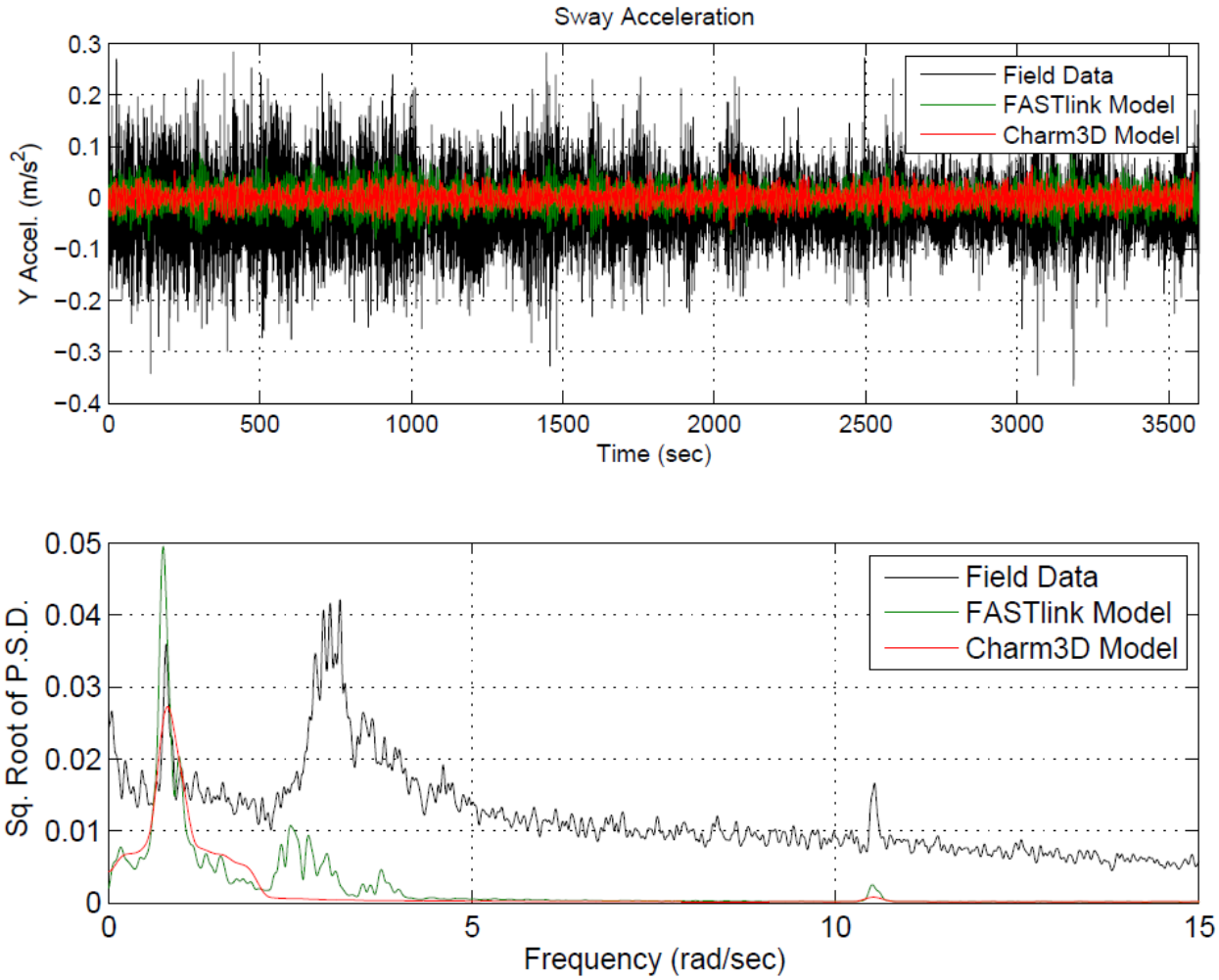

Figure 116: Sway acceleration time history (top) and square root of Power Spectral Density (bottom).

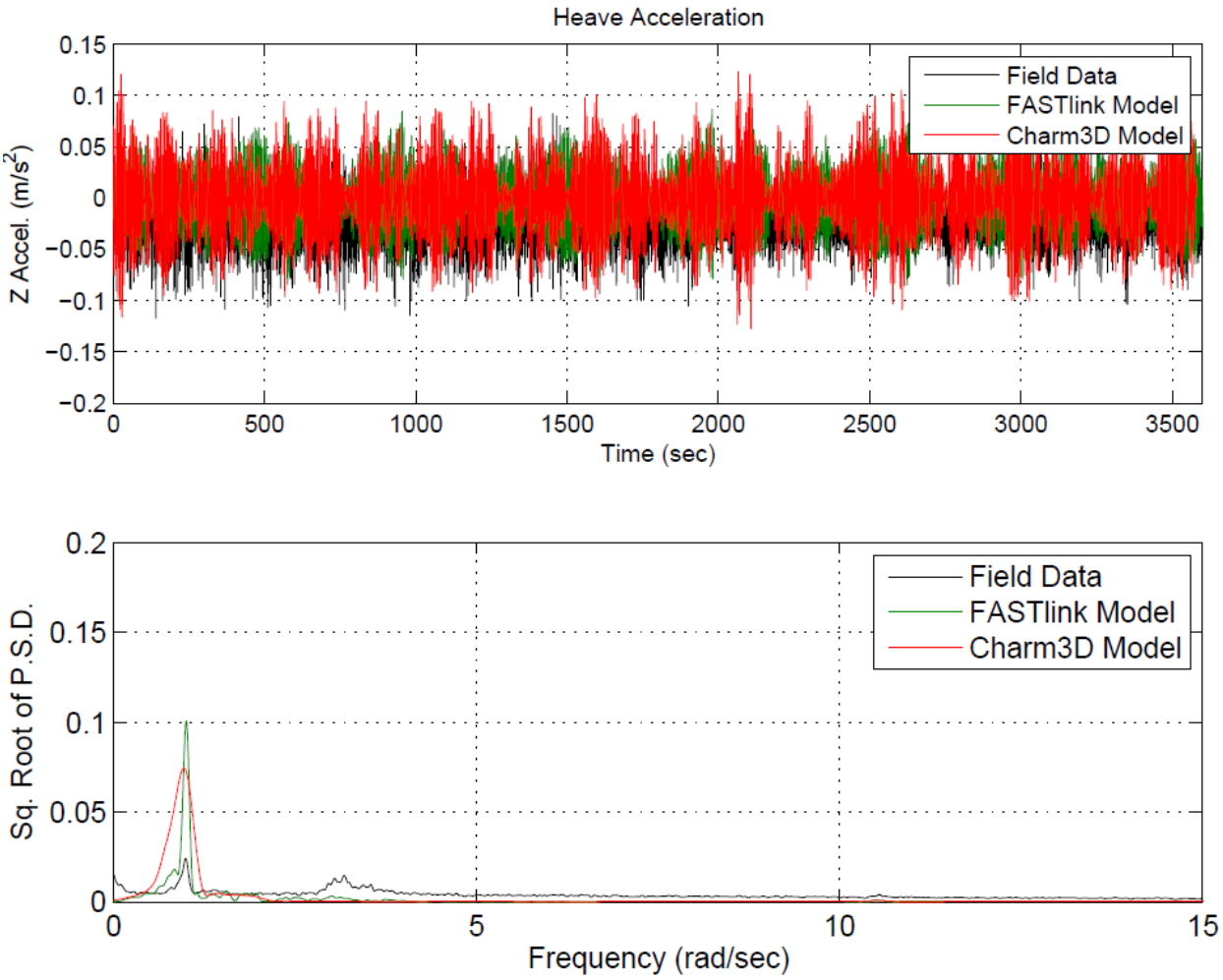

Figure 117: Heave acceleration time history (top) and square root of Power Spectral Density (bottom).

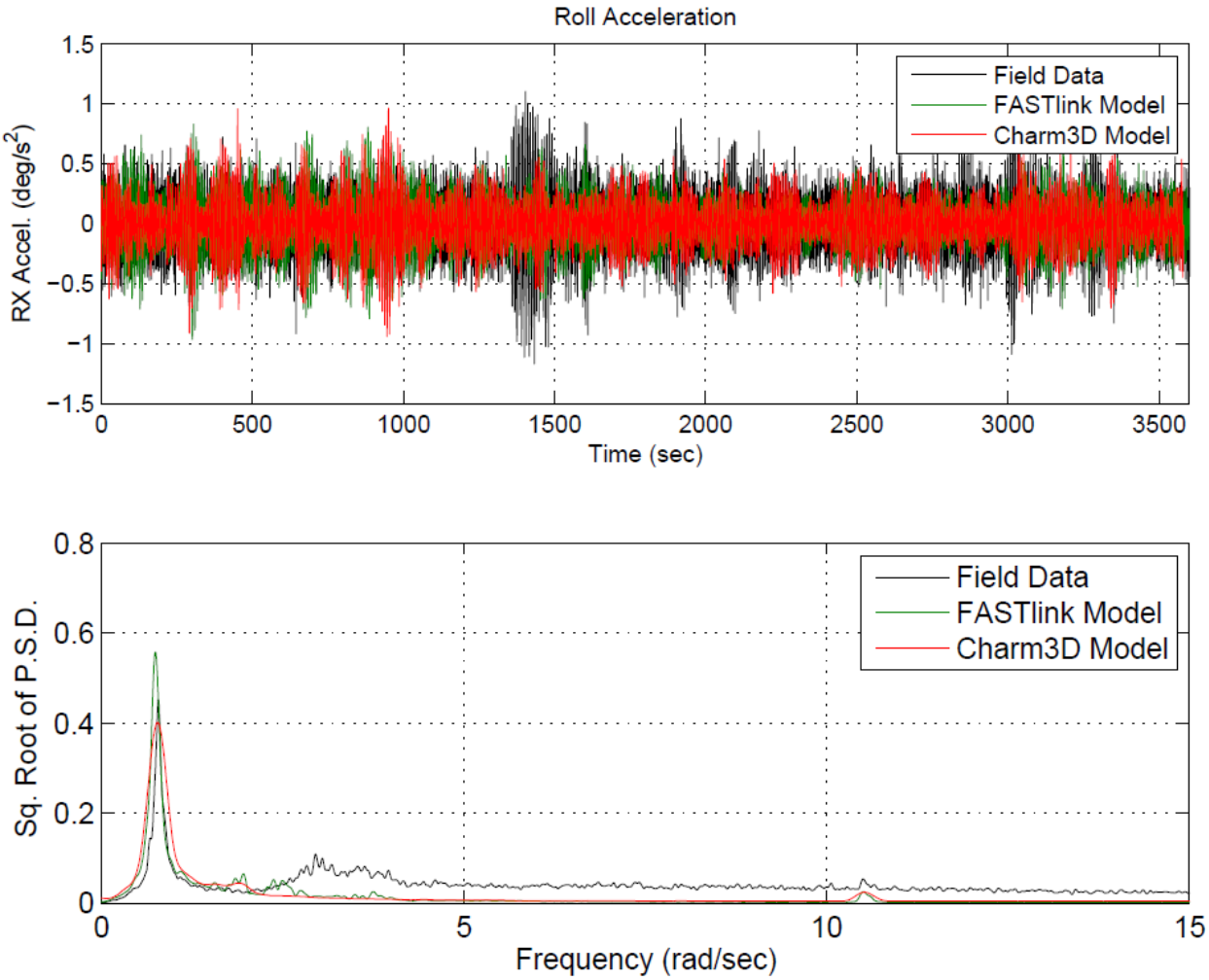

Figure 118: Roll acceleration time history (top) and square root of Power Spectral Density (bottom).

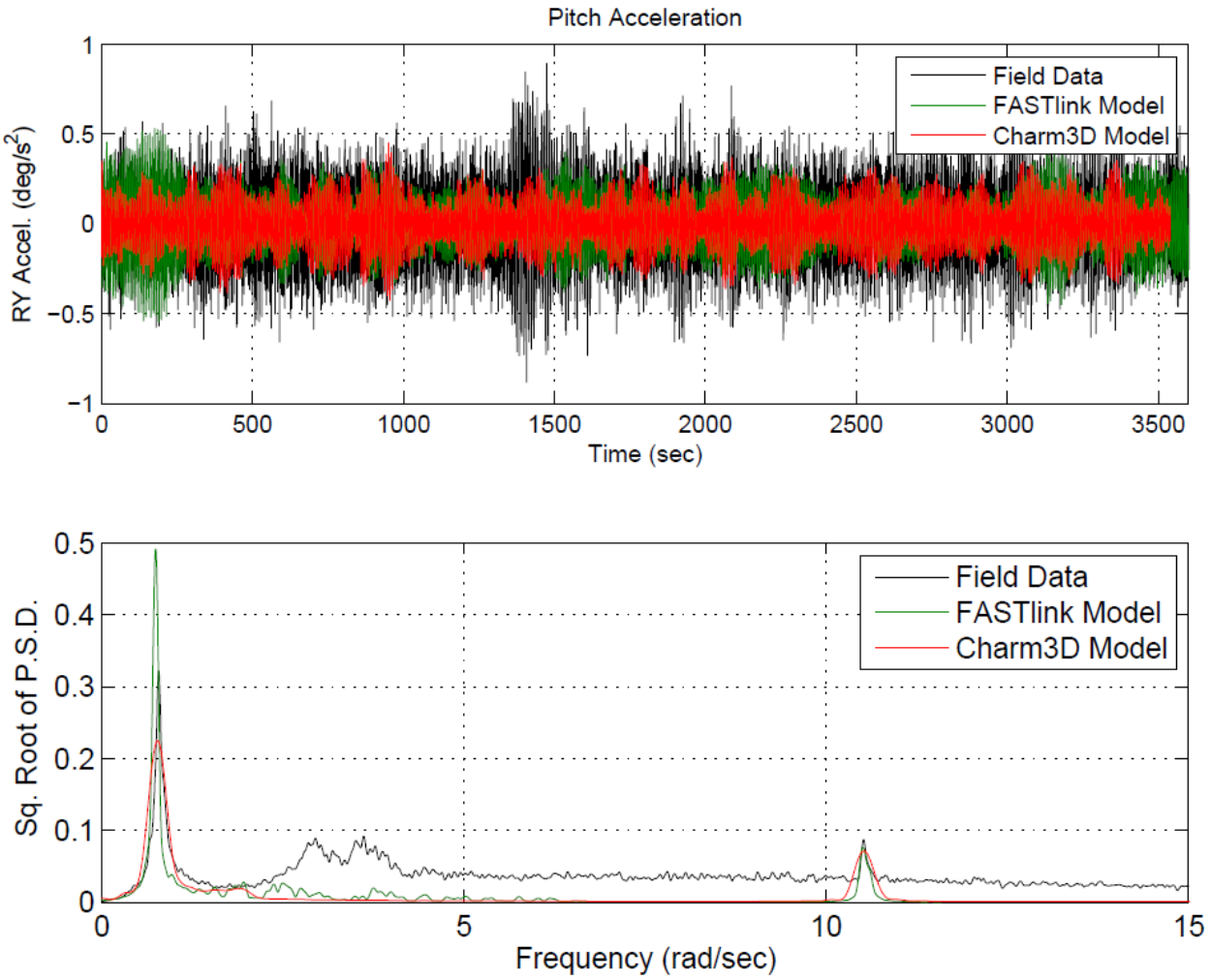

Figure 119: Pitch acceleration time history (top) and square root of Power Spectral Density (bottom).

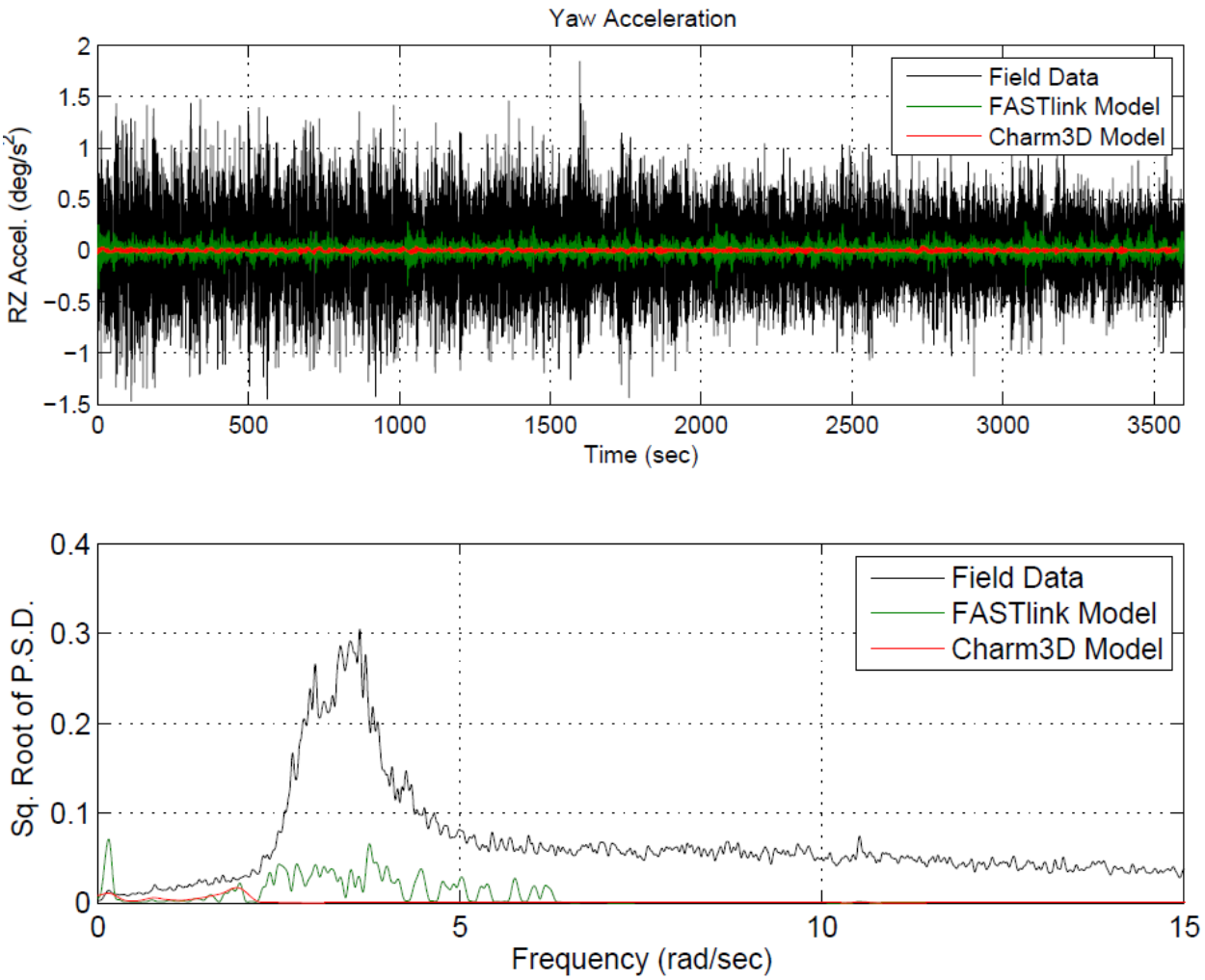

Figure 120: Yaw acceleration time history (top) and square root of Power Spectral Density (bottom).

6.4.6.2.2 DLC 1.6

Table 36 shows RMS values calculated from field measurements, Charm3D+FAST simulation, and OrcaFlex+FAST simulations for Design Load Case 1.6. There is generally good agreement between simulation results and field measurements in this case.

Table 36: RMS values of acceleration for field data, Charm3D+FAST model, and OrcaFlex+FAST model; DLC 1.6.

	Field Measurement RMS	Charm3D+FAST RMS	Charm3D+FAST Difference (%)	FAST+OrcaFlex RMS	FAST+OrcaFlex Difference (%)
Surge (m/s^2)	0.09	0.05	-47%	0.05	-42%
Sway (m/s^2)	0.18	0.26	43%	0.18	0%
Heave (m/s^2)	0.18	0.18	-4%	0.16	-13%
Roll (deg/s^2)	1.17	1.22	5%	1.35	15%
Pitch (deg/s^2)	0.58	0.61	5%	0.66	14%
Yaw (deg/s^2)	1.09	1.92	76%	1.41	29%

Time response and spectral density plots are shown in Figure 121 - Figure 126. Overall, agreement is good between simulation models and field measurements. The greatest response occurs at the frequencies corresponding to peak wave energy. Some response is observed at higher frequencies, corresponding to turbine rotor excitation.

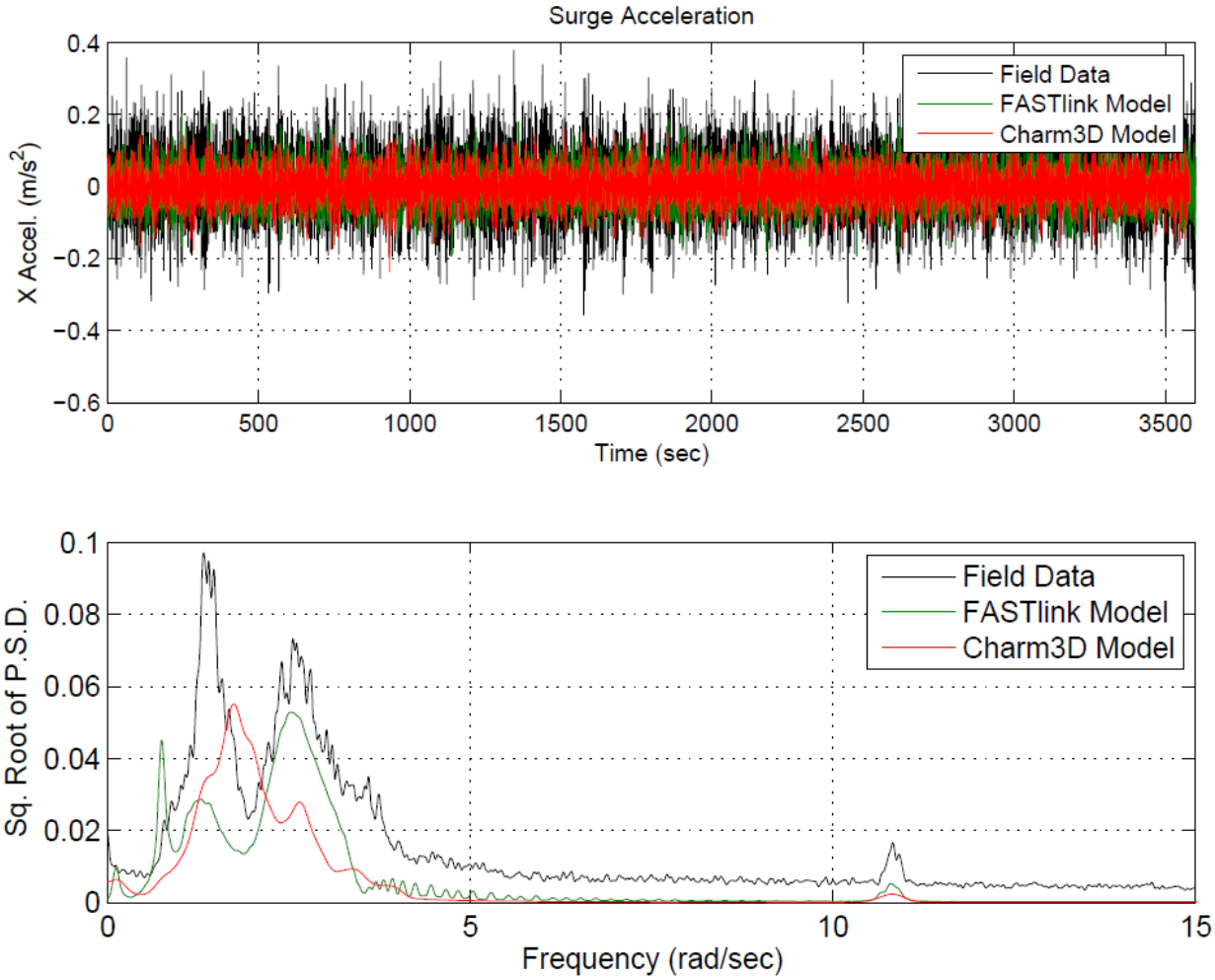

Figure 121: Surge acceleration time history (top) and square root of Power Spectral Density (bottom).

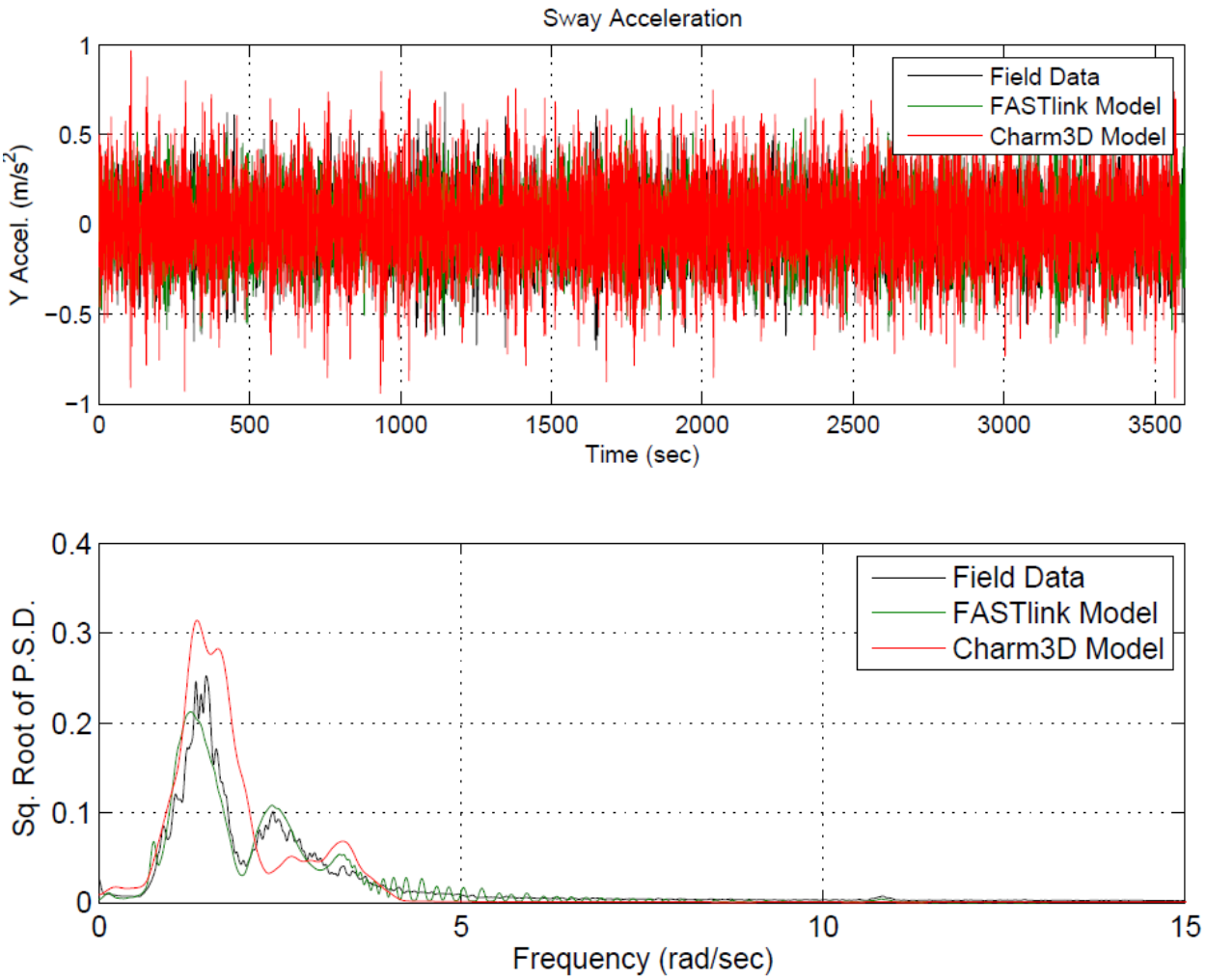

Figure 122: Sway acceleration time history (top) and square root of Power Spectral Density (bottom).

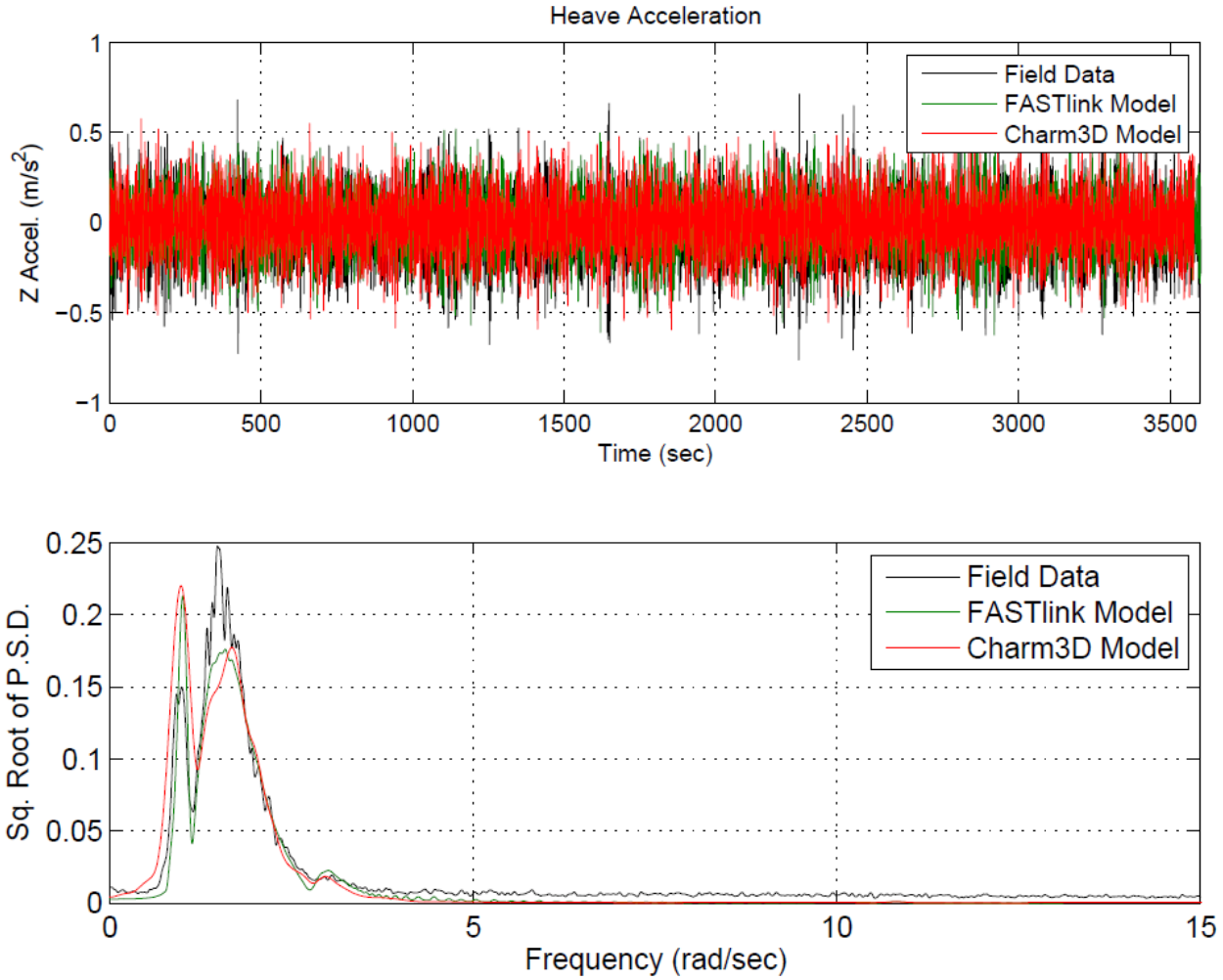

Figure 123: Heave acceleration time history (top) and square root of Power Spectral Density (bottom).

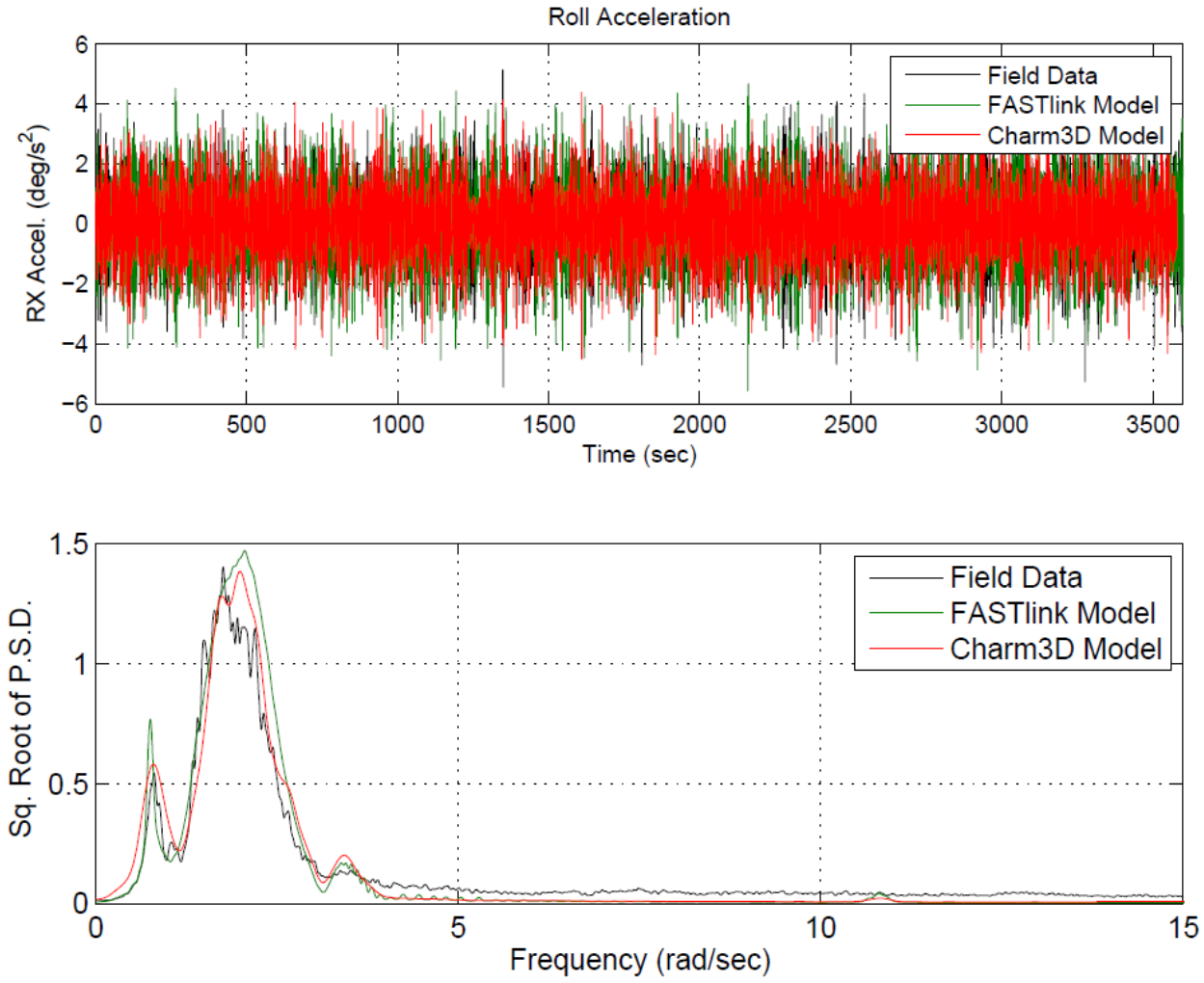

Figure 124: Roll acceleration time history (top) and square root of Power Spectral Density (bottom).

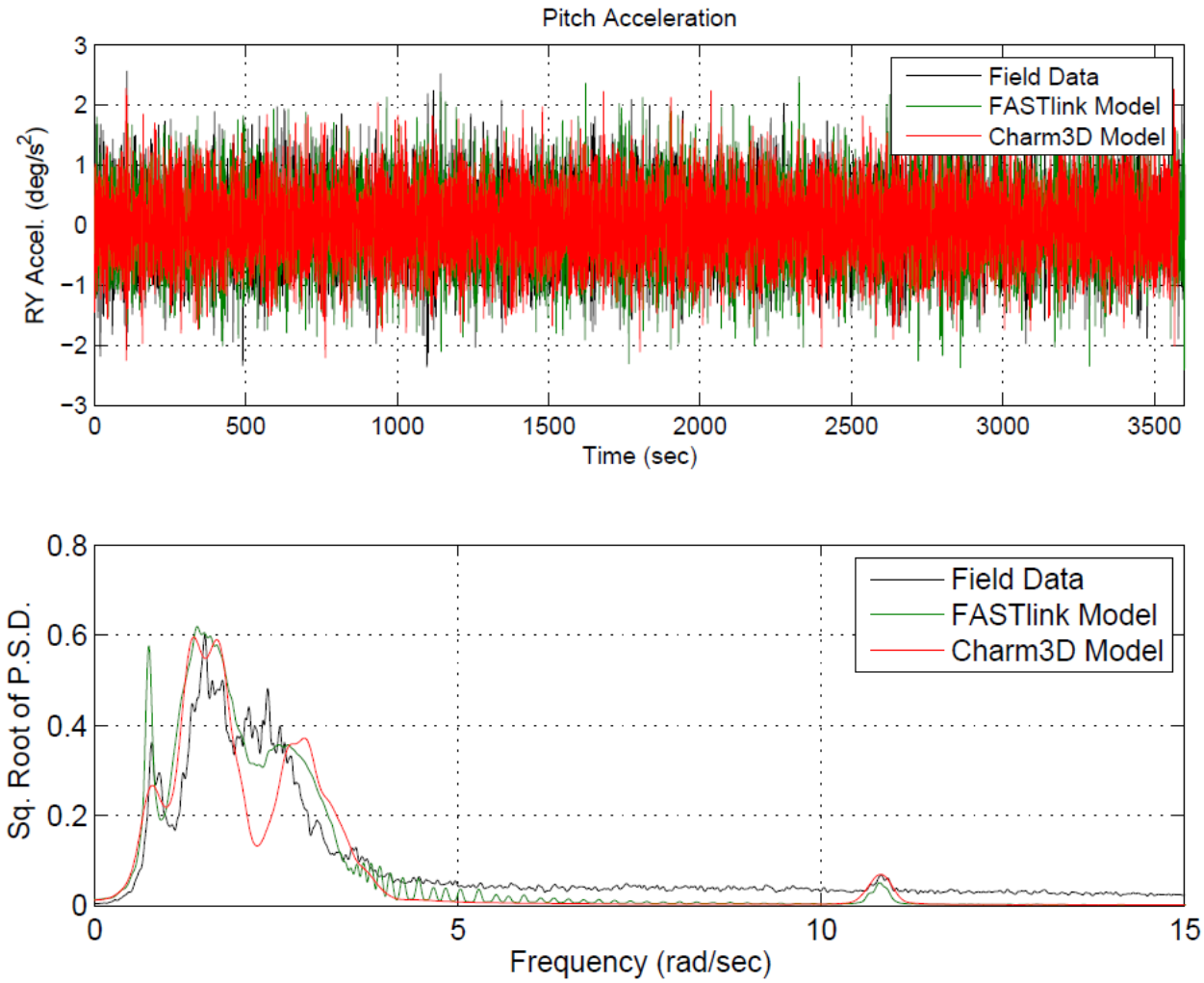

Figure 125: Pitch acceleration time history (top) and square root of Power Spectral Density (bottom).

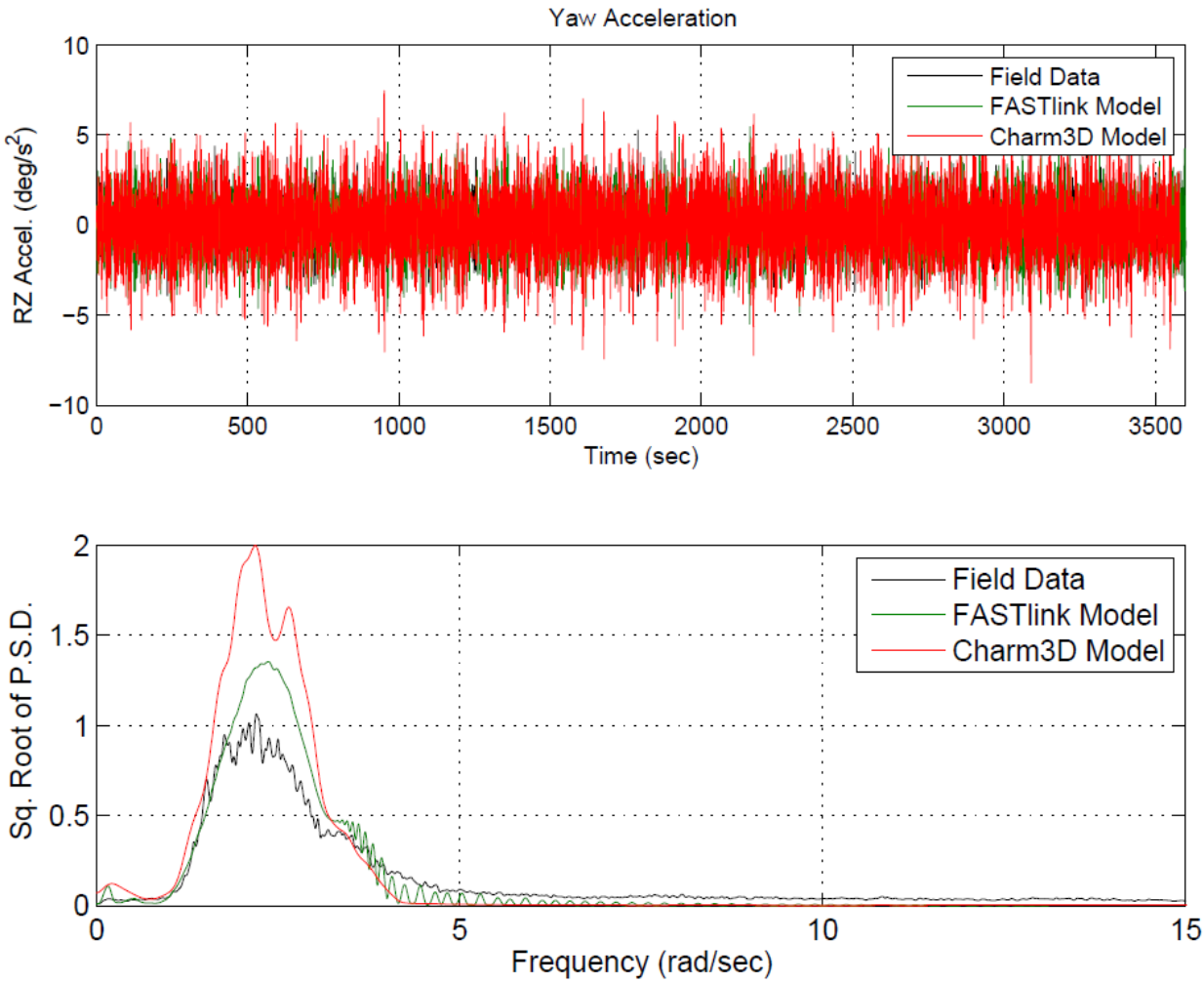

Figure 126: Yaw acceleration time history (top) and square root of Power Spectral Density (bottom).

6.4.6.2.3 SLC

For the Survival Load Case, RMS platform accelerations are shown in Table 37. Simulation models tend to over-predict the angular accelerations, while producing good agreement in the linear degrees of freedom. Qualitatively, this is shown in Figure 127 through Figure 132.

Table 37: RMS values of acceleration for field data, Charm3D+FAST model, and OrcaFlex+FAST model; SLC.

	Field Measurement RMS	Charm3D+FAST		FAST+OrcaFlex	
		RMS	Difference (%)	RMS	Difference (%)
Surge (m/s^2)	0.11	0.13	26%	0.10	-4%
Sway (m/s^2)	0.24	0.40	63%	0.29	18%
Heave (m/s^2)	0.22	0.25	14%	0.26	17%
Roll (deg/s^2)	1.40	1.86	33%	2.32	65%
Pitch (deg/s^2)	0.74	1.27	71%	1.13	51%
Yaw (deg/s^2)	1.46	3.26	122%	2.53	73%

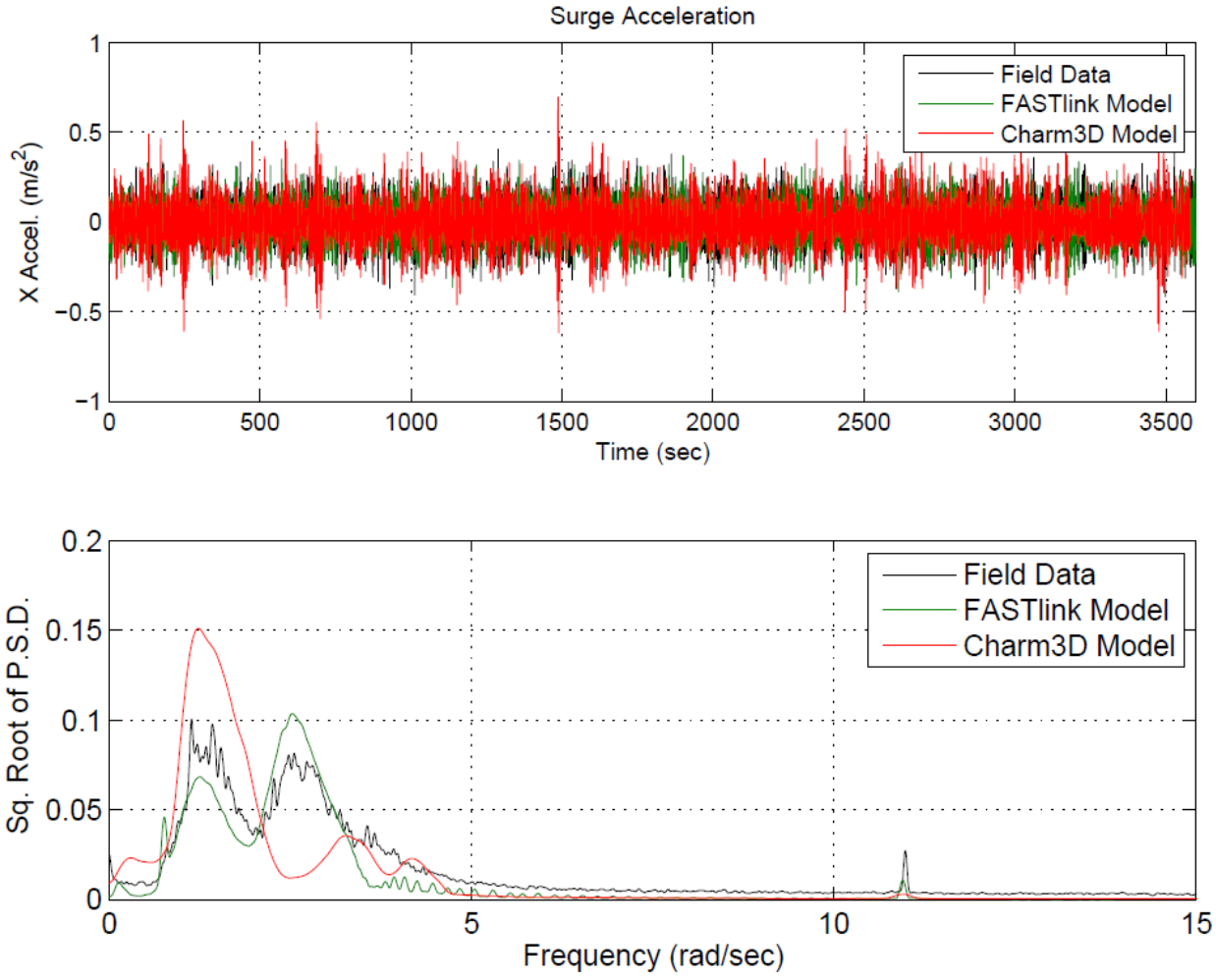

Figure 127: Surge acceleration time history (top) and square root of Power Spectral Density (bottom).

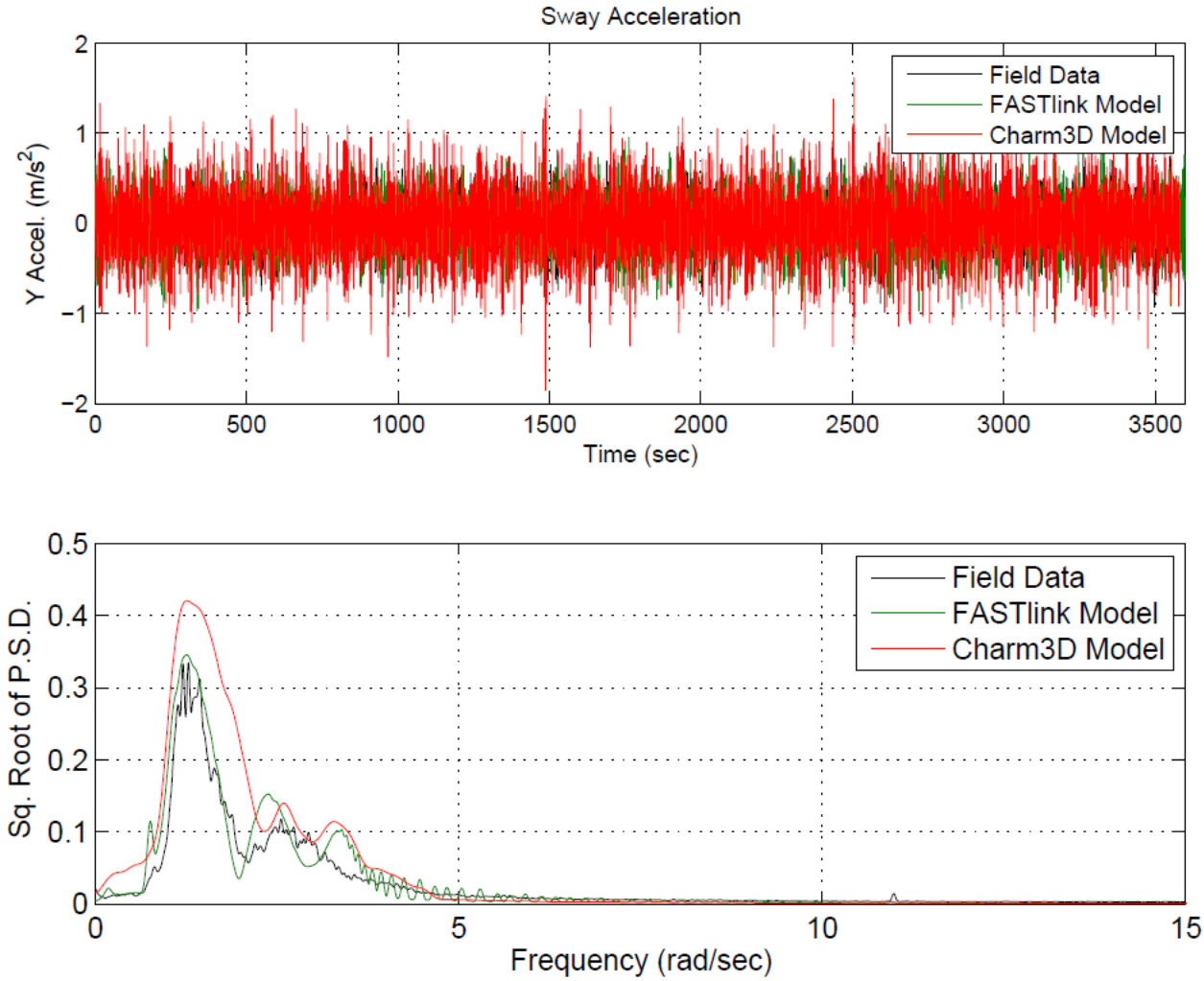

Figure 128: Sway acceleration time history (top) and square root of Power Spectral Density (bottom).

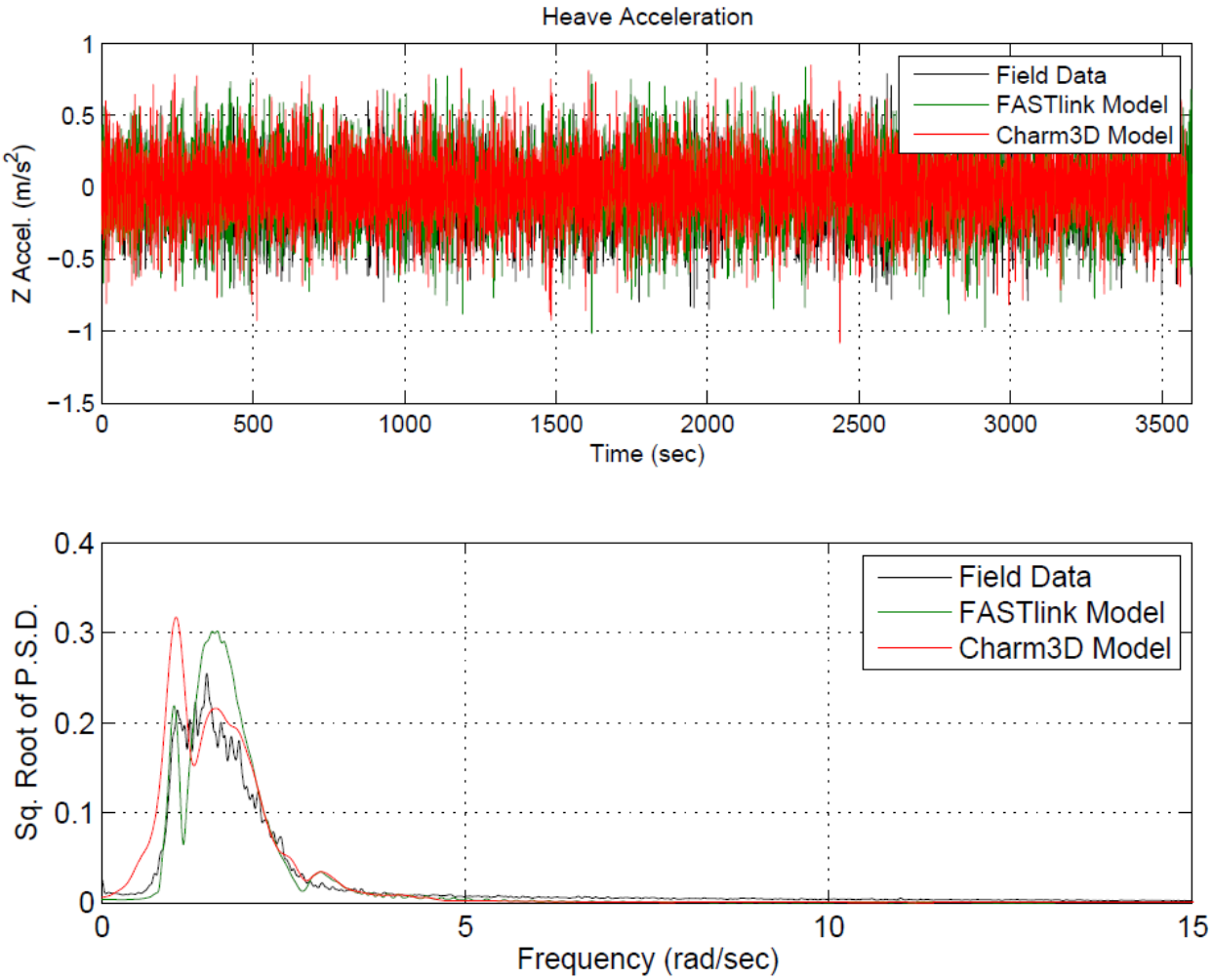

Figure 129: Heave acceleration time history (top) and square root of Power Spectral Density (bottom).

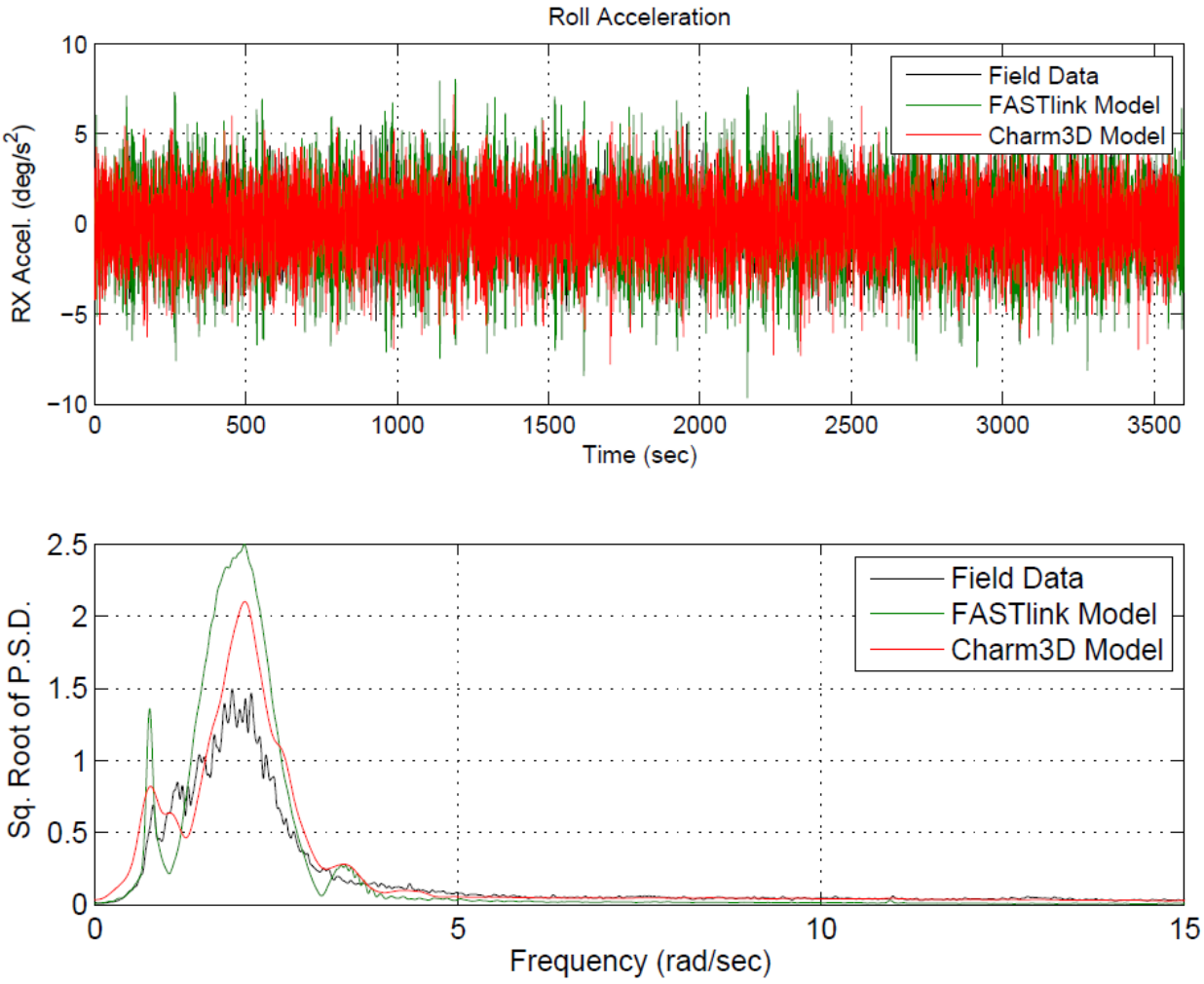

Figure 130: Roll acceleration time history (top) and square root of Power Spectral Density (bottom).

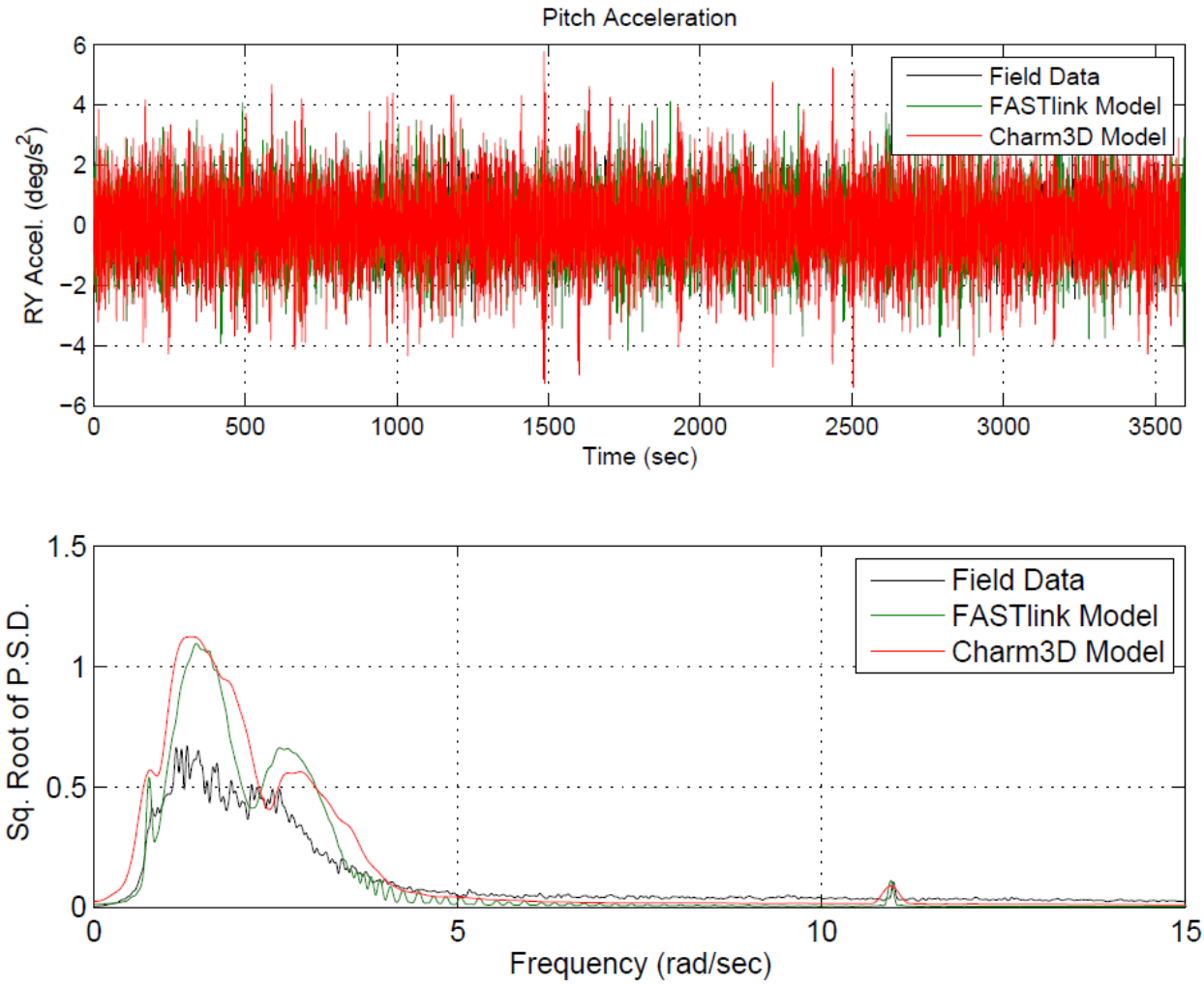

Figure 131: Pitch acceleration time history (top) and square root of Power Spectral Density (bottom).

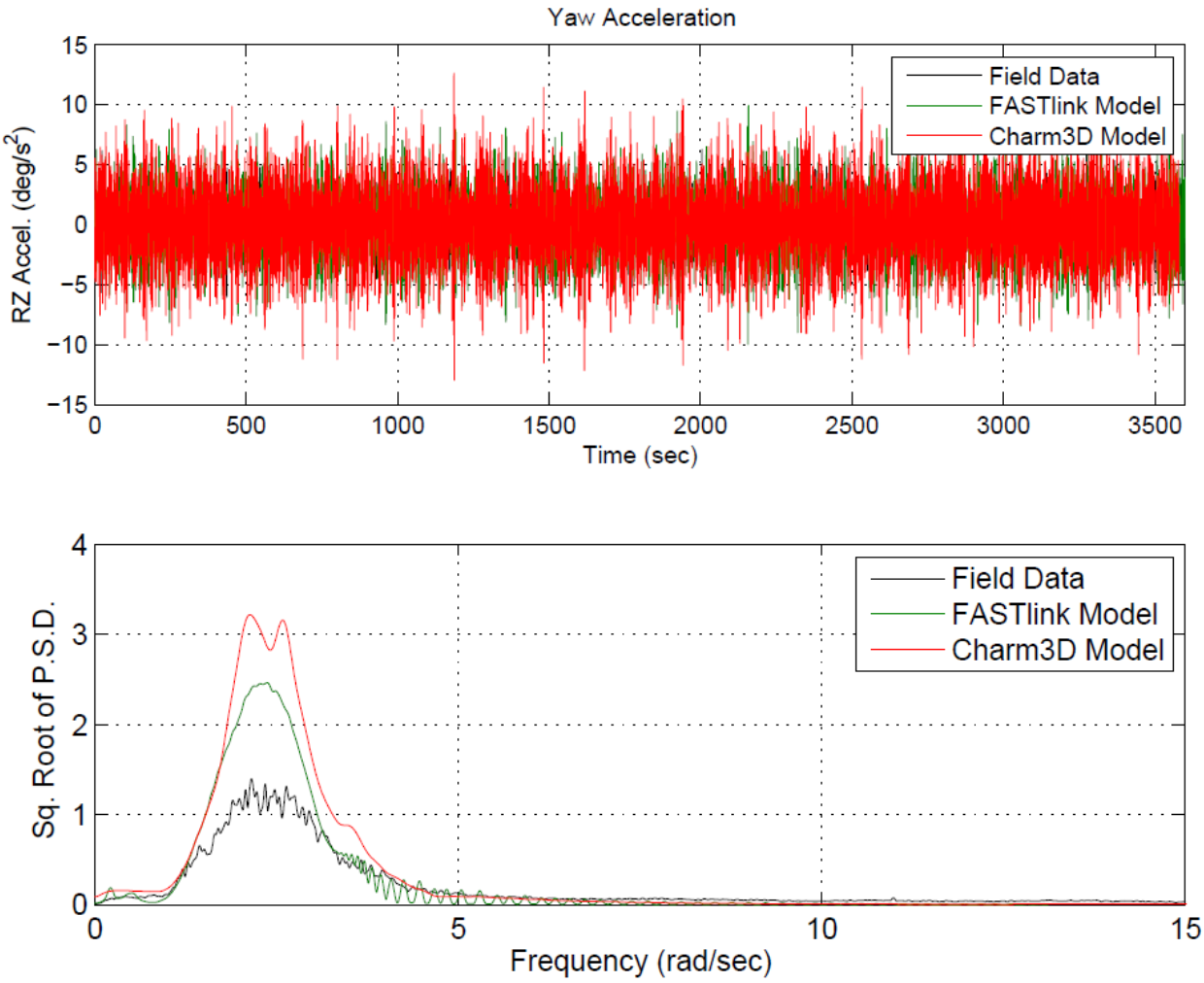

Figure 132: Yaw acceleration time history (top) and square root of Power Spectral Density (bottom).

6.4.6.3 Mooring Loads

The mooring response was calculated for each design condition using Charm3D+FAST and OrcaFlex+FAST, and compared with field measurements. In both DLC conditions, the response history suggests that one of the mooring lines was generally very slack, with a tension nearly equal to the suspended weight of the chain.

Wind loading on the tower and unsubmerged platform is not accounted for in FAST v7. At high wind speeds, these loads could contribute an additional 1-2 kN of load not accounted for by OrcaFlex+FAST (As a sample calculation, assume a wind area of 14 m^2, a drag coefficient of 0.5, and a wind speed of 15 m/s. The load would be roughly $F_{wind} = \frac{1}{2} C_D \rho A v |v| = 0.945\ kN$.). Because the VolturnUS is a small scale FOWT, this load is significant. As the system is scaled up to full-scale, it may become negligible. The platform and tower wind loads were added to the OrcaFlex model as applied loads. Wind drag coefficients were estimated from Halkyard (2013).

6.4.6.3.1 DLC 1.2

For Design Load Case 1.2, RMS mooring tensions are shown in Table 38. There is generally good agreement between simulated mooring response and field measurements. Time histories and spectral plots are shown in Figure 133, Figure 134, and Figure 135 for each of the three mooring legs (refer to Figure 75 for mooring line labels). As seen in the spectral plots, there is virtually no response of note beyond low frequency drift response, which is a function of the low wave heights for this time period. No tension response is observed at rotor frequencies.

Table 38: RMS of fairlead tension for field data, Charm3D+FAST model, and OrcaFlex+FAST model; DLC 1.2.

	Field Measurement RMS	Charm3D+FAST		FAST+OrcaFlex	
		RMS	Difference (%)	RMS	Difference (%)
Leg A (kN)	1.45	1.49	3%	1.53	5%
Leg B (kN)	3.59	3.70	3%	3.59	0%
Leg C (kN)	3.16	2.87	-9%	2.85	-10%

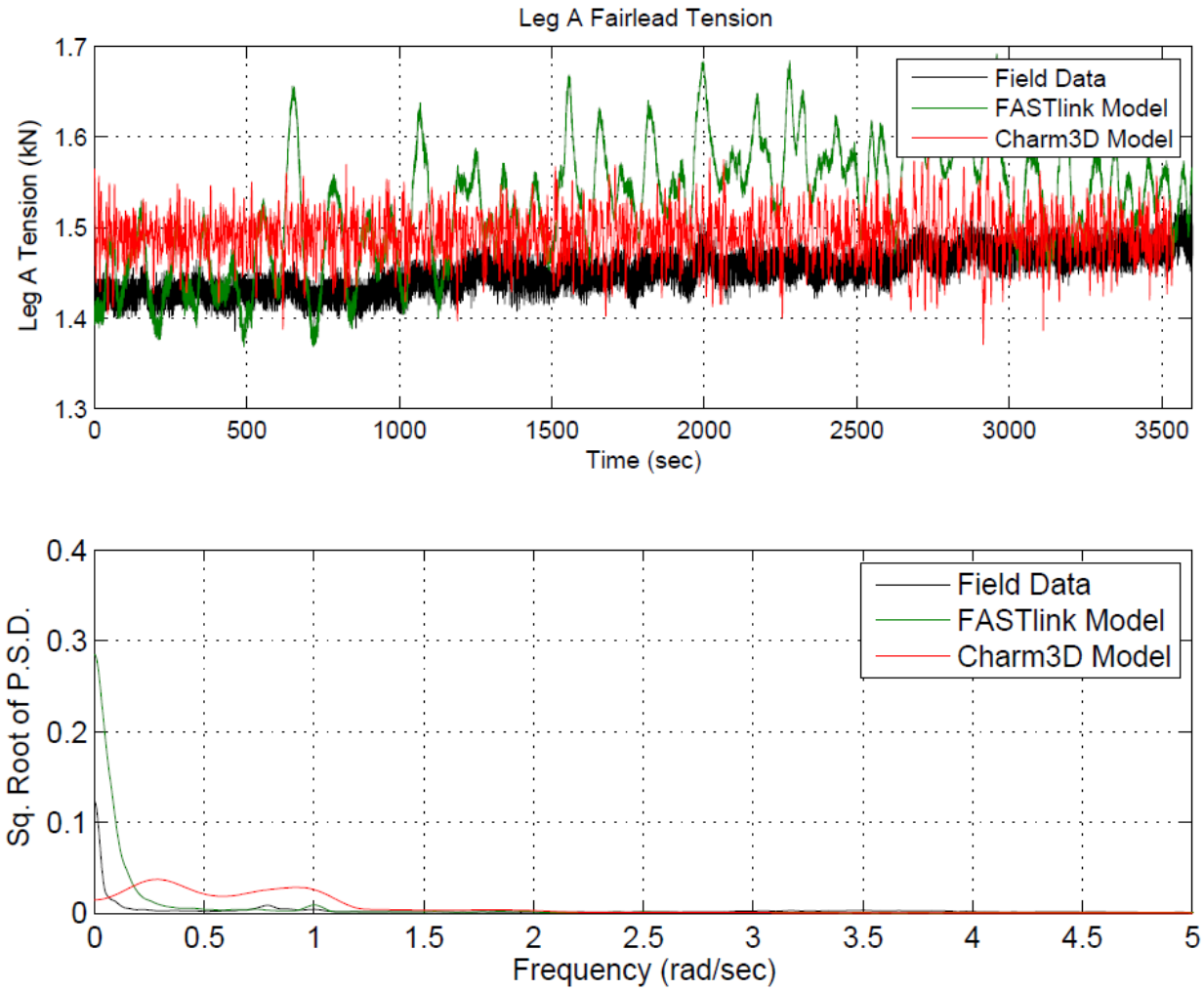

Figure 133: Leg A Tension. Time history (top) and power spectral density (bottom) shown for DLC 1.2.

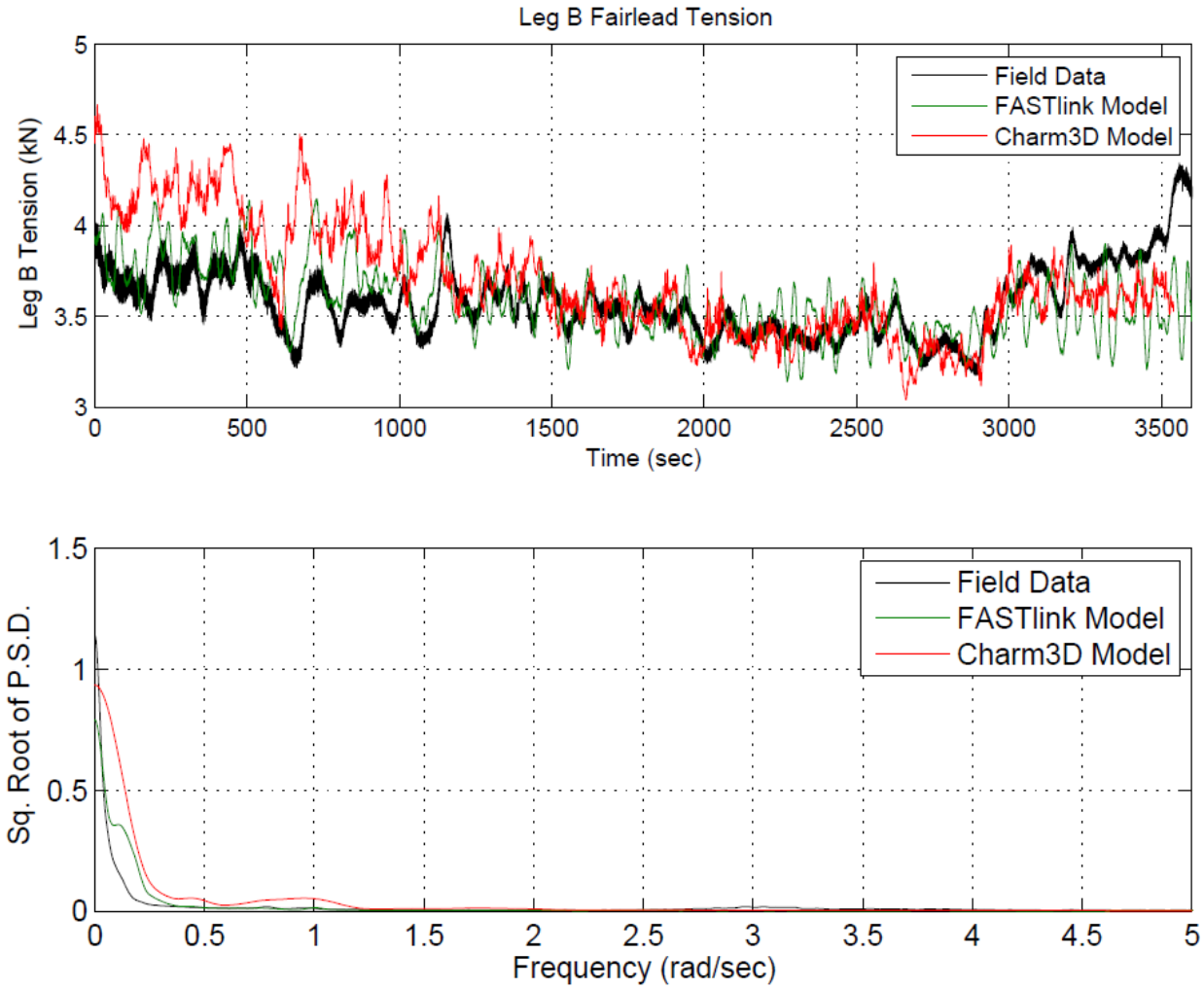

Figure 134: Leg B Tension. Time history (top) and power spectral density (bottom) shown for DLC 1.2.

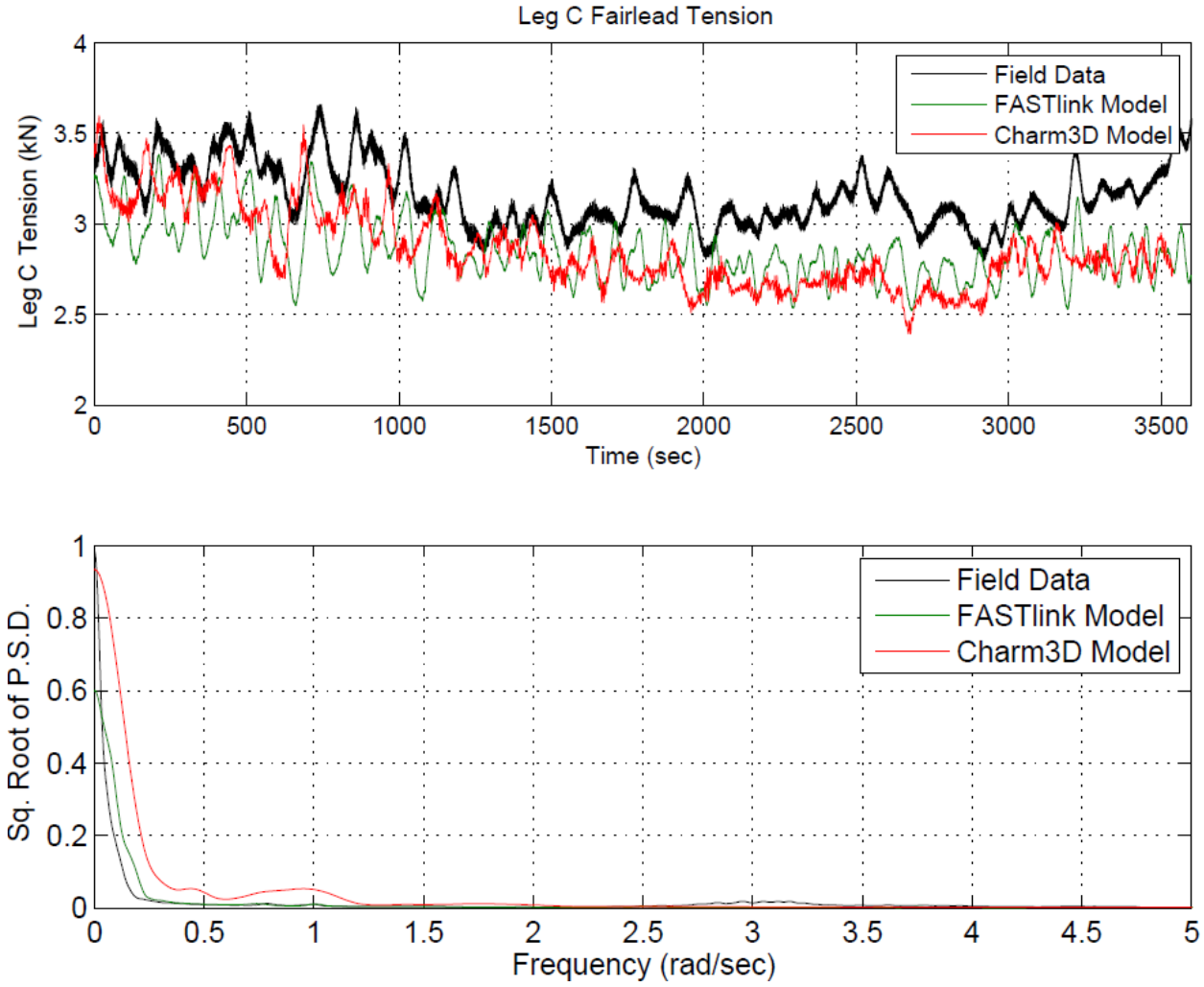

Figure 135: Leg C Tension. Time history (top) and power spectral density (bottom) shown for DLC 1.2.

6.4.6.3.2 DLC 1.6

For Design Load Case 1.6, RMS responses are shown in Table 39, and results are plotted in Figure 136, Figure 137, and Figure 138, for Leg A, Leg B, and Leg C, respectively. From the figures it is clear that OrcaFlex+FAST better predicts the response of Leg A, while both models over-predict the response of Leg B. For Leg B, the spectral response of OrcaFlex+FAST is in better agreement. Both models slightly mis-represent the mean tension for Leg C, while Charm3D better predicts the spectral response.

Table 39: RMS of fairlead tension for field data, Charm3D+FAST model, and OrcaFlex+FAST model; DLC1.6.

	Field Measurement RMS	Charm3D+FAST		FAST+OrcaFlex	
		RMS	Difference (%)	RMS	Difference (%)
Leg A (kN)	3.04	2.17	-28%	2.93	-3%
Leg B (kN)	1.52	2.10	38%	2.54	67%
Leg C (kN)	3.25	2.77	-15%	3.98	23%

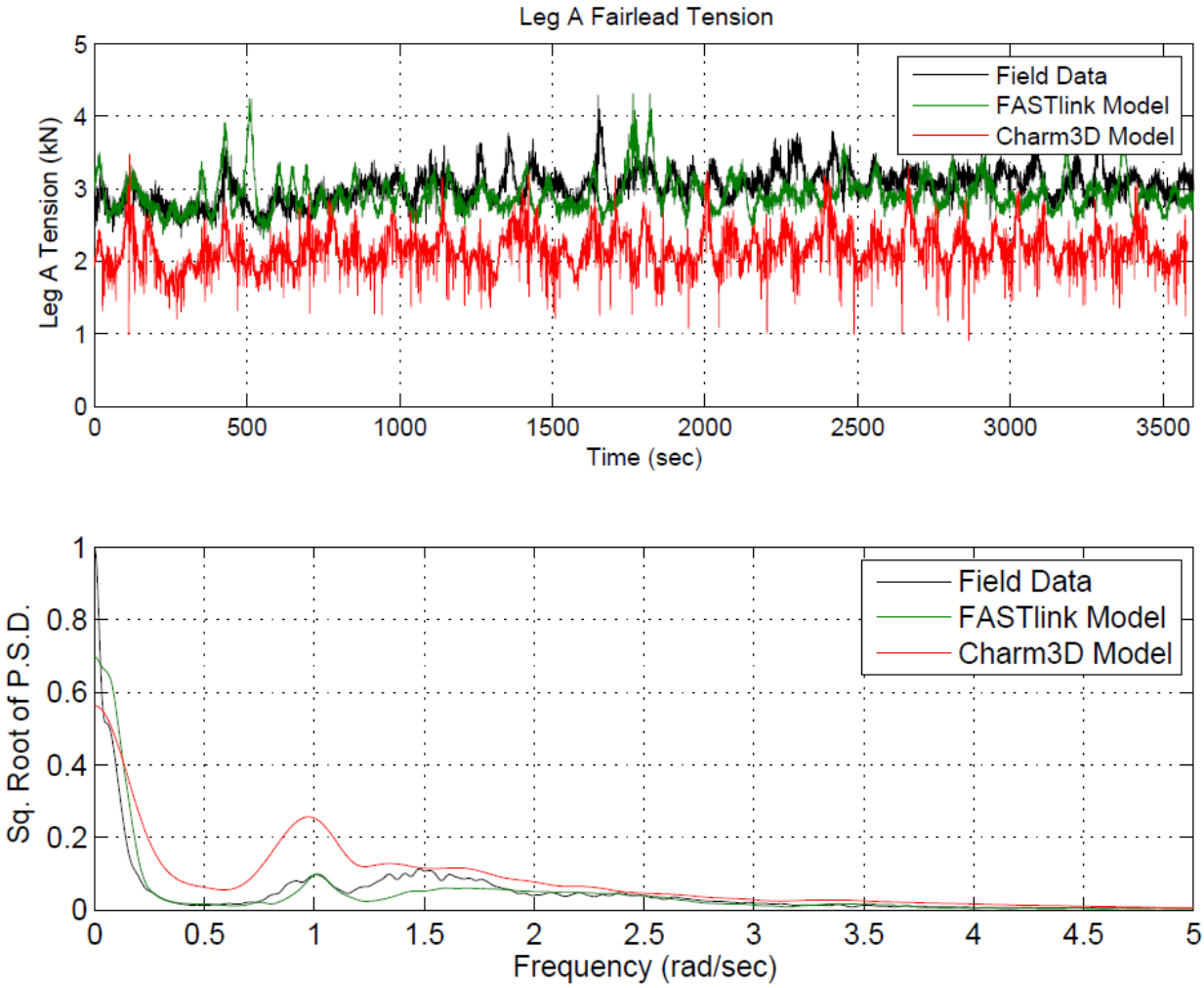

Figure 136: Leg A Tension. Time history (top) and power spectral density (bottom) shown for DLC 1.6.

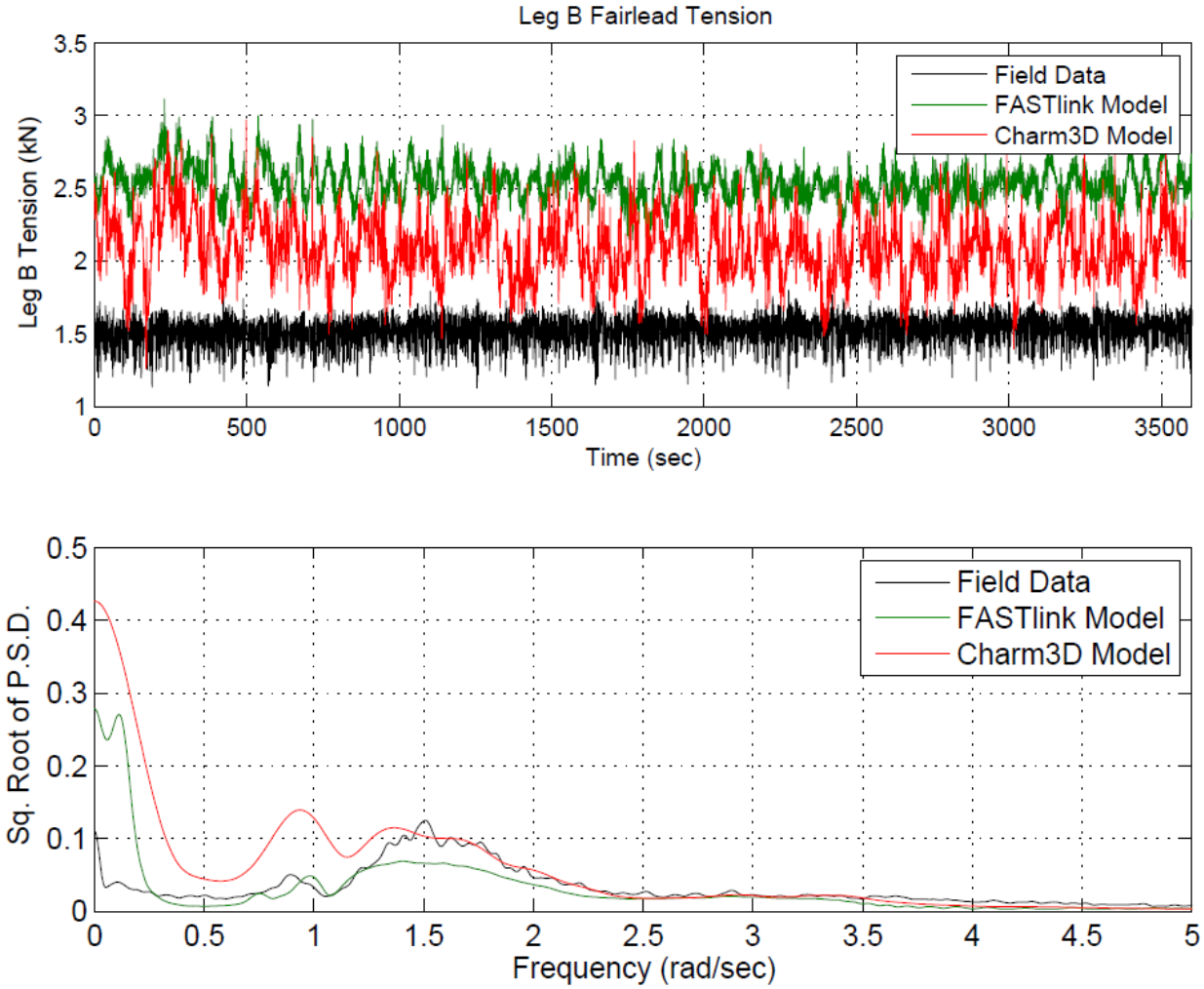

Figure 137: Leg B Tension. Time history (top) and power spectral density (bottom) shown for DLC 1.6.

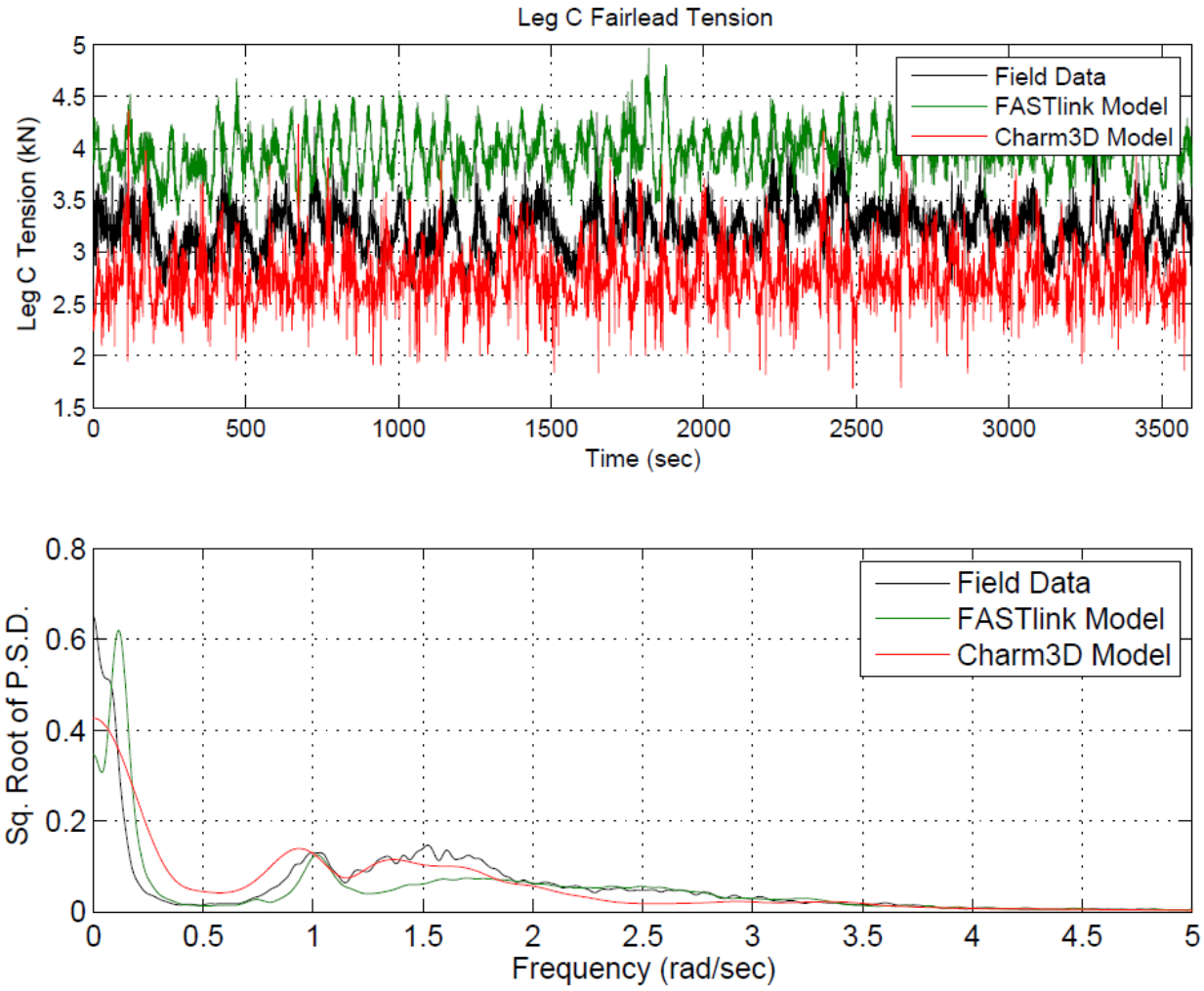

Figure 138: Leg C Tension. Time history (top) and power spectral density (bottom) shown for DLC 1.6.

6.4.6.3.3 SLC

For the Survival Load Case, the RMS responses are shown in Table 40, and the time history and spectral density results are plotted in Figure 139, Figure 140, and Figure 141. It is clear from Figure 139 that the survival load case produces extremely high tensions on Leg A with respect to the results seen in other legs and design load cases. The RMS tension is 11.47 kN, more than thrice as high as any other measurement seen in this study. It is also clear from Figure 139 that the simulations are only able to partially capture these extreme tensions.

One possible explanation for this under-prediction could be an error in the recorded alignment of environmental conditions. To test this hypothesis, a revised version of the OrcaFlex+FAST model was simulated in which it was assumed that all environmental loads are aligned with Leg A. The results are shown in Figure 142. Much better agreement between the field data and the simulation model is observed both in the time history and the spectral density results.

In addition to better agreement of Leg A, this revised model also produces better agreement with Leg C, which the simulation models significantly over-predicted. This result is shown in Figure 143.

Table 40: RMS of fairlead tension for field data, Charm3D+FAST model, and OrcaFlex+FAST model; SLC.

	Field Measurement RMS	Charm3D+FAST		FAST+OrcaFlex	
		RMS	Difference (%)	RMS	Difference (%)
Leg A (kN)	11.47	5.76	-50%	6.94	-39%
Leg B (kN)	1.93	1.99	3%	2.12	10%
Leg C (kN)	2.37	2.32	-2%	4.34	83%

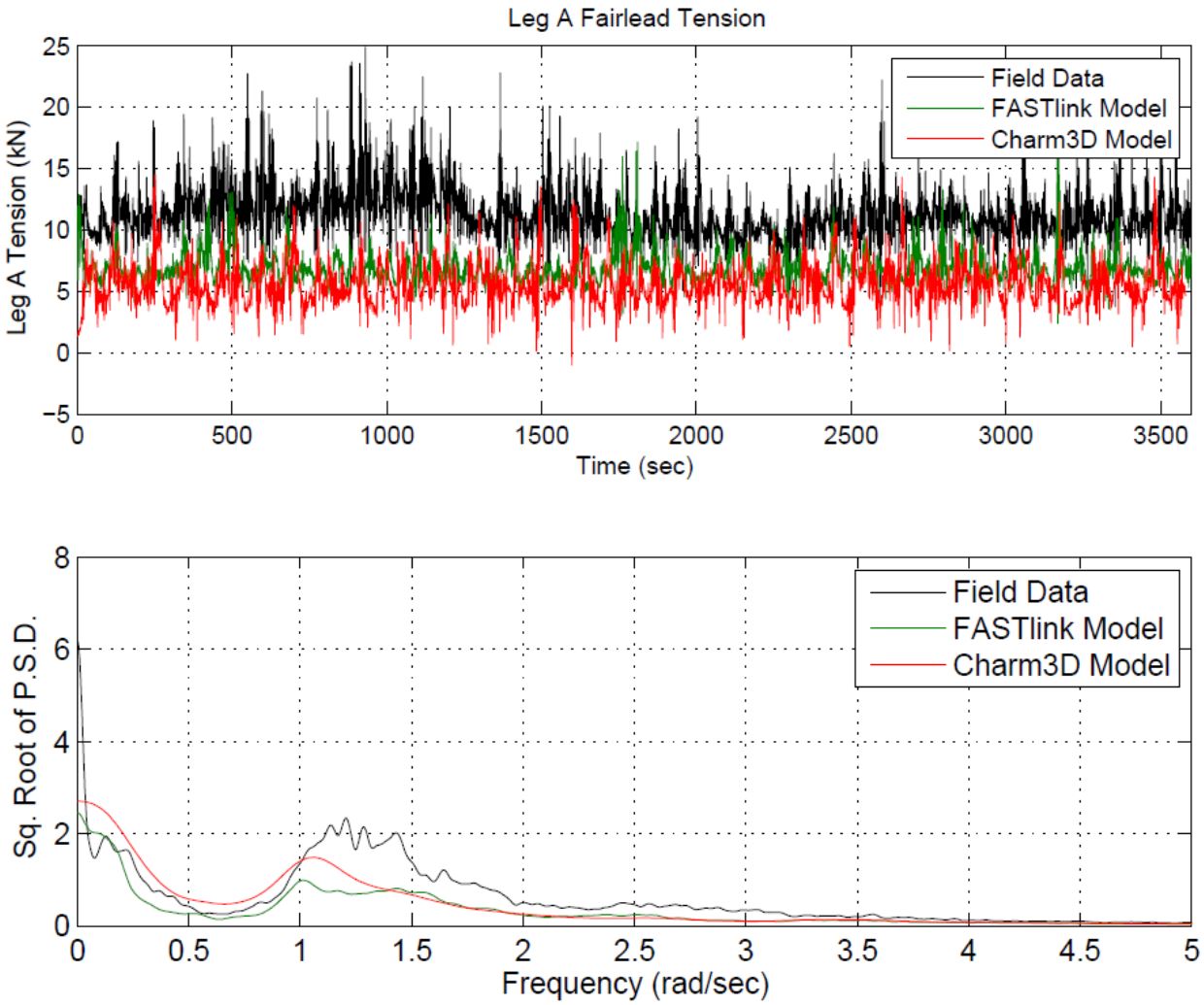

Figure 139: Leg A Tension. Time history (top) and power spectral density (bottom) shown for SLC.

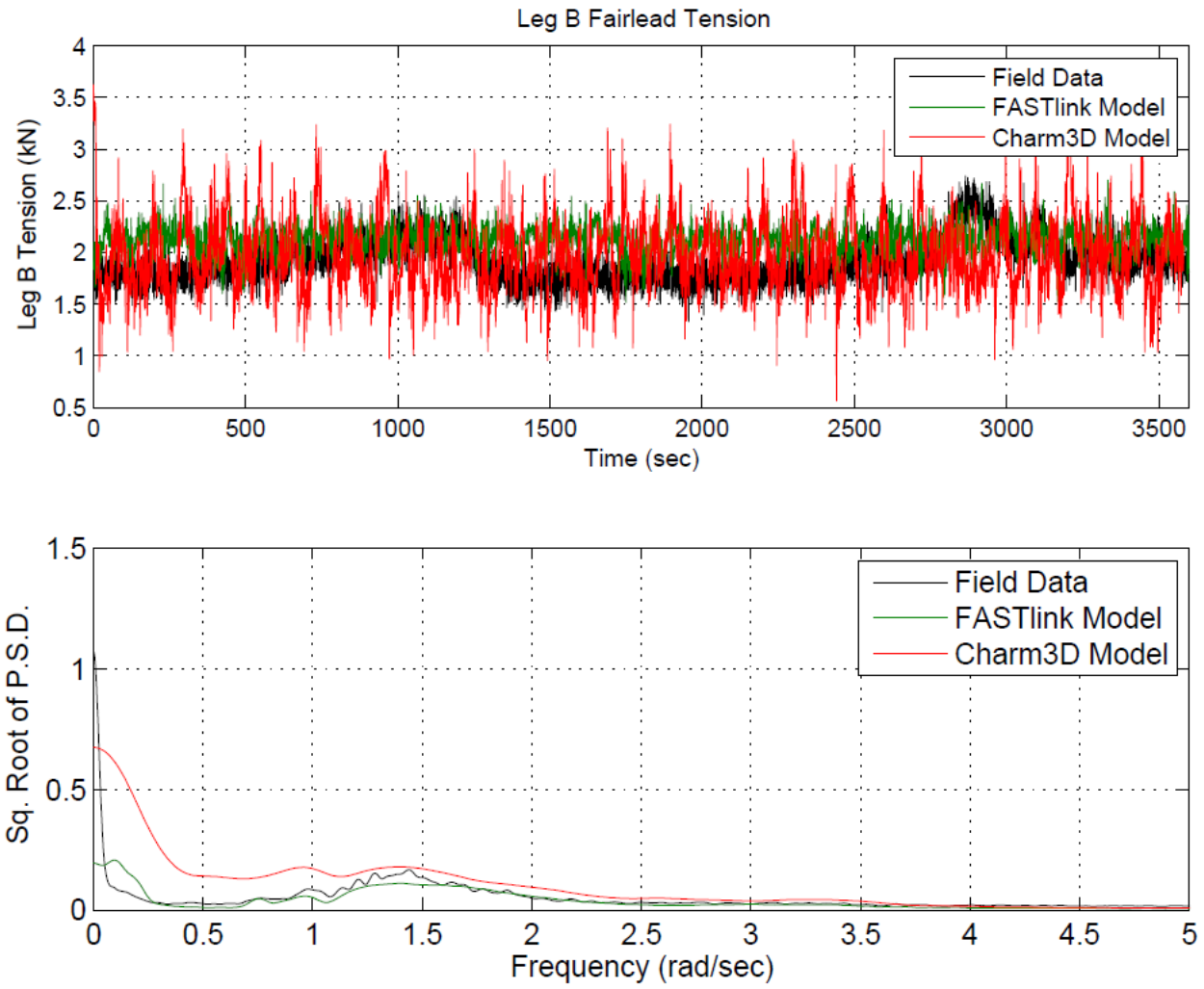

Figure 140: Leg B Tension. Time history (top) and power spectral density (bottom) shown for SLC.

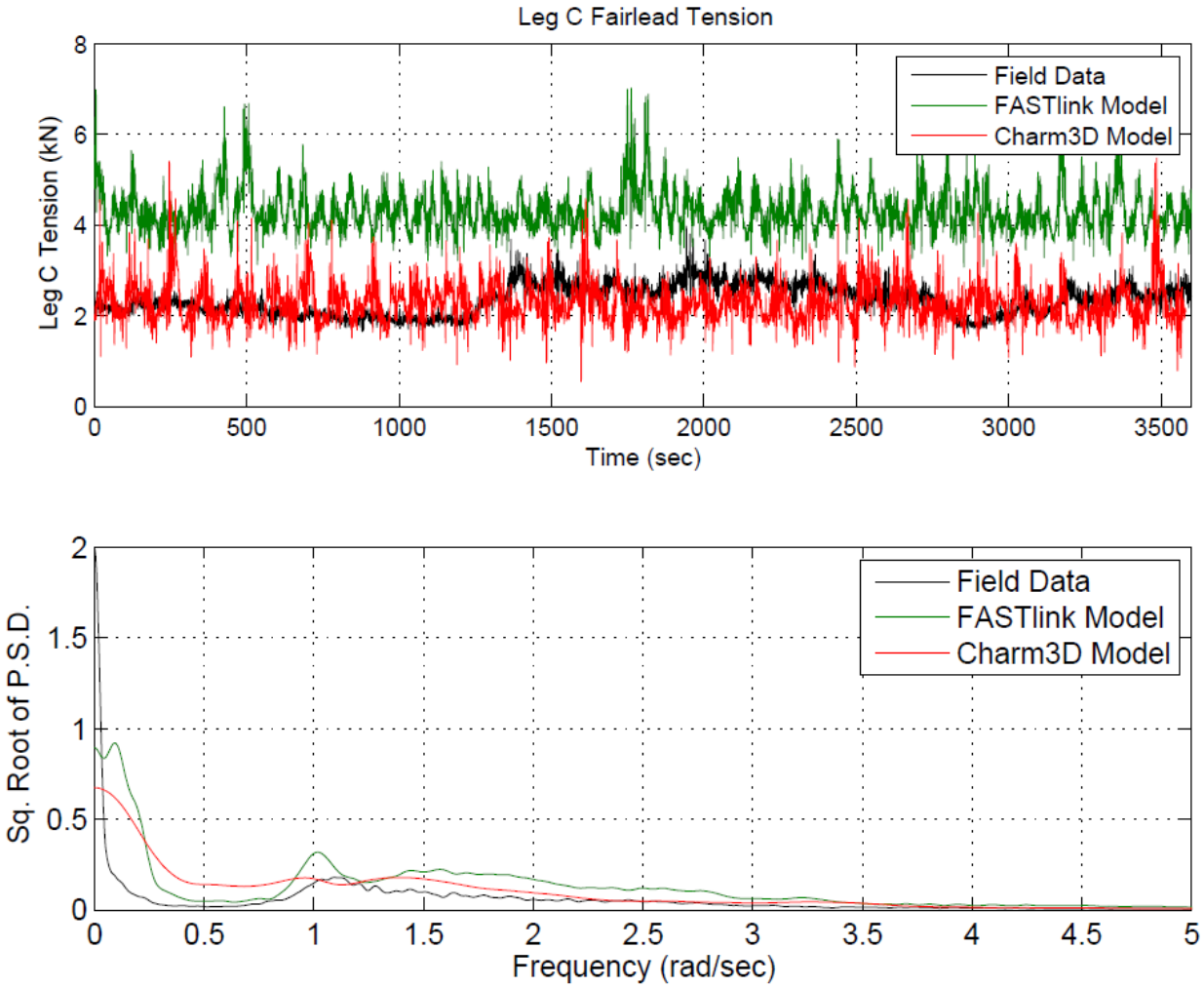

Figure 141: Leg C Tension. Time history (top) and power spectral density (bottom) shown for SLC.

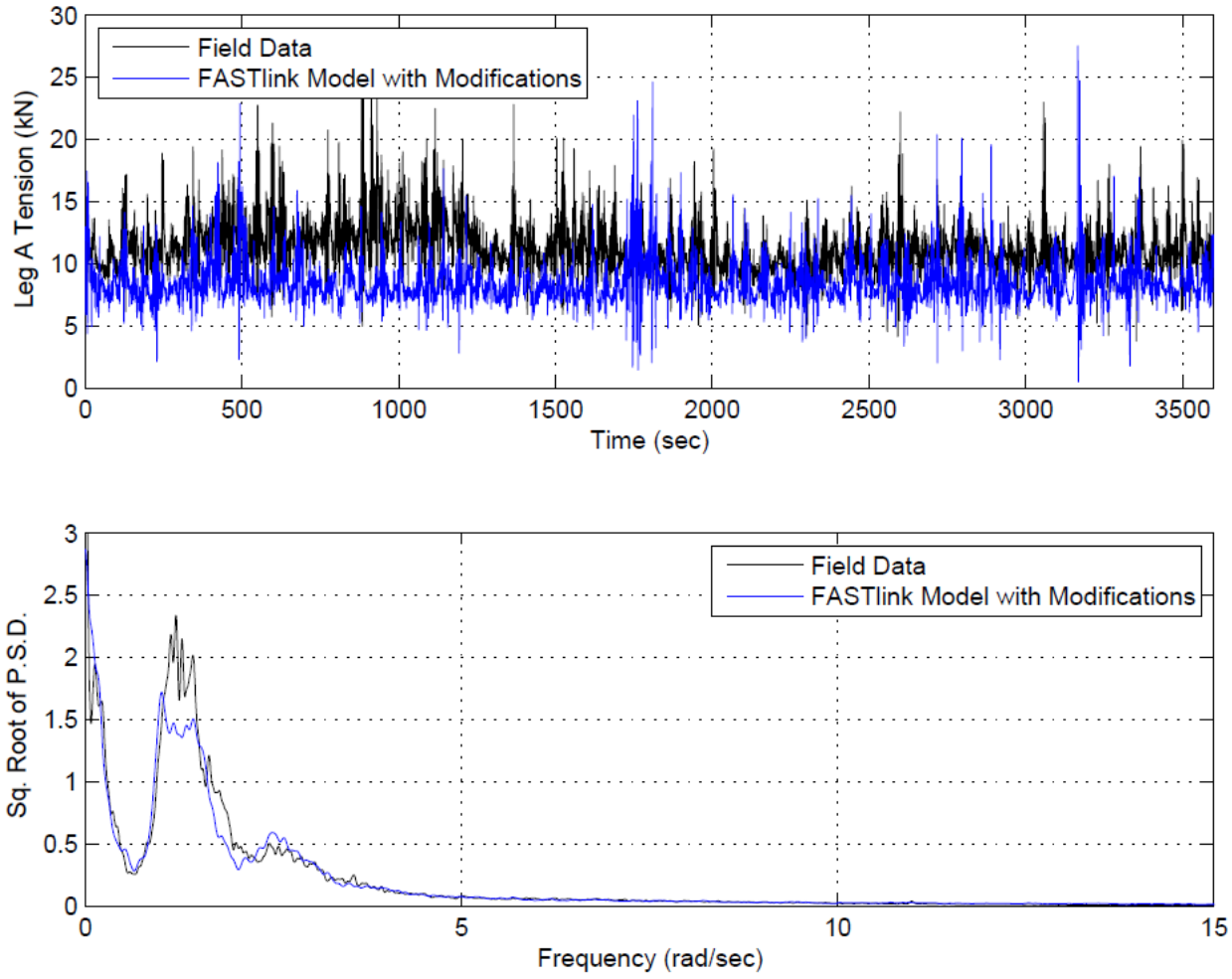

Figure 142: Leg A Tension with revised OrcaFlex+FAST model assuming aligned wind, wave, current, mooring leg.

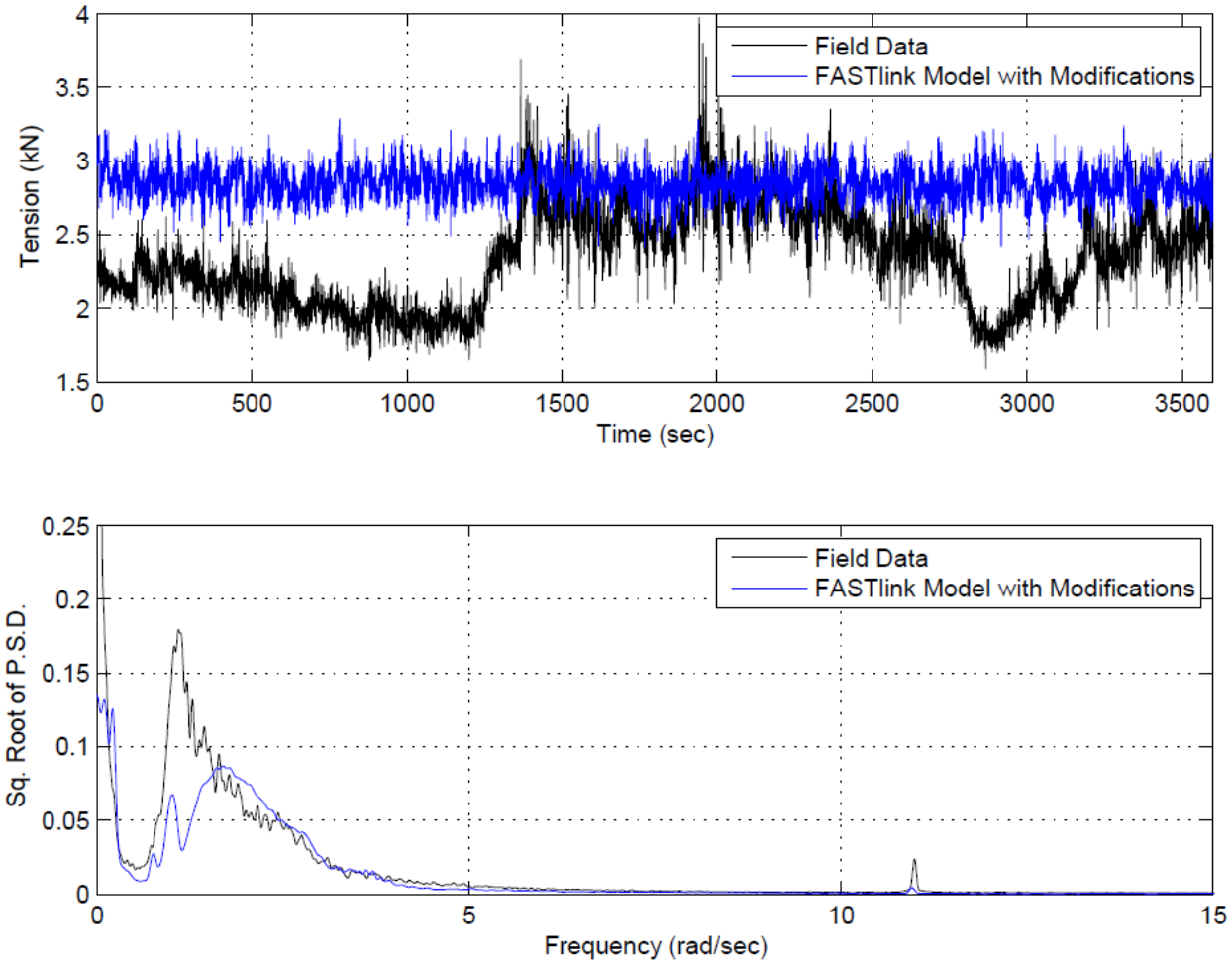

Figure 143: Leg C Tension with revised OrcaFlex+FAST model assuming aligned wind, wave, current, mooring leg.

6.4.7 Fatigue Study

6.4.7.1 Fatigue Predicted from Simulation and from Measured Data

For the three time periods for which the project team was provided field measurements, the accumulated fatigue damage was calculated in accordance with Miner's Rule. Fatigue damage on each mooring line was calculated for these time periods. This was done directly from the field data time history measurements of the fairlead tension, and for both simulation models. This section describes the process of predicting fatigue lifetime for the 1:8 scale model directly, rather than the hypothetical full scale model. Accordingly, while measured data may scale to extreme or survival load cases at the full scale, it is not considered too extreme to be used for fatigue calculation at the 1:8 scale.

As specified in API-RP-2SK, fatigue damage is calculated for the cyclic loading of a mooring system using a T-N approach. Miner's Rule, given by Equation (28) is used to calculate the damage ratio, *D:*

$$D = \sum \frac{n_i}{N_i} \qquad (28)$$

In this equation, n_i represents the number of cycles in each tension range, and N_i represents the number of cycles to failure over the same interval. API-RP-2SK strongly advises against a quasi-static approach in fatigue calculation, which is in part why OrcaFlex and Charm3D were used in simulations.

Tension fatigue is calculated based on a T-N curve of the form:

$$NR^M = K \quad (29)$$

In which N is the number of cycles, R is the ratio of tension to breaking load, and K and M are T-N parameters provided in API-RP-2SK, Table 3.

Alternatively, DNV-OS-E301 uses a stress based approach for mooring line fatigue calculation. The fairlead stresses are computed from tension cycles by applying a cross-sectional area of $2\pi d^2/4$. Fatigue curve parameters are summarized in Figure 144. For this case study the DNV fatigue methodology was used.

201 The following equation can be used for the component capacity against tension fatigue:

$$n_c(s) = a_D s^{-m}$$

This equation can be linearised by taking logarithms to give:

$$\log(n_c(s)) = \log(a_D) - m \cdot \log(s)$$

$n_c(s)$ = the number of stress ranges (number of cycles)
s = the stress range (double amplitude) in MPa
a_D = the intercept parameter of the S-N curve
m = the slope of the S-N curve

The parameters a_D and m are given in Table F1 and the S-N curves are shown in Fig.6.

Table F1 S-N Fatigue Curve Parameters

	a_D	m
Stud chain	$1.2 \cdot 10^{11}$	3.0
Studless chain (open link)	$6.0 \cdot 10^{10}$	3.0
Stranded rope	$3.4 \cdot 10^{14}$	4.0
Spiral rope	$1.7 \cdot 10^{17}$	4.8

Figure 144: Fatigue calculation methodology and coefficients. Source: DNV-OS-E301.

Fatigue tension cycles were calculated using a rainflow counting routine within the WAFO Matlab toolbox (WAFO, 2000). For each of the three storm conditions, the fatigue damage was calculated. A sensitivity study showed that the damage calculated using API parameters is 154% of the damage calculated using DNV parameters in each case. This is indicative of the high variance inherent in fatigue damage estimation. Fatigue is a process that occurs over long duration, and is extremely sensitive to input parameters and assumptions.

The fatigue damage accrued in one hour was calculated from the field measurements, the FAST+OrcaFlex simulation, and the Charm3D+FAST simulation. The result is shown in Table 41 for the conditions labeled DLC 1.2, Table 42 for DLC 1.6, and Table 43 for the Survival Load Case. This represents damage to the 1:8 VolturnUS mooring system, while the conditions are labeled with respect to the full scaled system.

Of note is the observation that the fatigue damage accumulated during the Survival Load Case exceeds all other cases by almost four orders of magnitude. This suggests that even if such a response has a return period of one year, it still contributes to the total fatigue damage disproportionately. A similar result was found in the literature by Kiecke and Zhang (2011). This study uses real world data to study the fatigue damage on a Gulf of Mexico spar. It is found, through examination and extrapolation of three storm events, that a hurricane, occurring once in 20 years, contributes 80% of the total fatigue damage accrued over that time period.

Table 41: Fatigue damage on each leg, calculated from field measurements, Charm3D+FAST simulation, and FAST+OrcaFlex simulation. DLC 1.2.

	Field Measurement	Charm3D+FAST	FAST + OrcaFlex
Leg A	2.51E-11	1.94E-11	1.70E-11
Leg B	6.12E-10	3.85E-10	4.44E-10
Leg C	2.63E-10	1.61E-10	2.44E-10

Table 42: Fatigue damage on each leg, calculated from field measurements, Charm3D+FAST simulation, and FAST+OrcaFlex simulation. DLC 1.6.

	Field Measurement	Charm3D+FAST	FAST + OrcaFlex
Leg A	4.79E-09	2.34E-08	4.09E-09
Leg B	2.26E-09	7.15E-09	1.30E-09
Leg C	9.85E-09	2.87E-08	5.60E-09

Table 43: Fatigue damage on each leg, calculated from field measurements, Charm3D+FAST simulation, and FAST+OrcaFlex simulation. SLC.

	Field Measurement	Charm3D+FAST	FAST + OrcaFlex
Leg A	1.69E-05	4.93E-06	2.71E-06
Leg B	6.32E-09	3.54E-08	4.04E-09
Leg C	9.30E-09	1.23E-07	9.13E-08

6.4.7.2 Simulated Lifetime Calculation

In lieu of existing field measurements for long-term fatigue damage, a parametric fatigue study was undertaken using the OrcaFlex+FAST model. Simulations were run under a variety of environmental conditions in accordance with specifications in the ABS Guide for Building and Classing Floating Offshore Wind Turbine Installations.

ABS specifies several fatigue load cases. Design Load Case 1.2 and Design Load Case 6.4 were used in this investigation. These design load conditions do not represent discrete storms but account for the joint distributions of wind speeds up to the one year return period, and the

corresponding joint sea-state distributions. Associated with these are normal current and tidal water level ranges.

A complete fatigue analysis requires a full wave scatter table. Environmental data, including current speeds, significant wave heights, dominant wave periods, and associated wind speeds were derived from the Northeastern Regional Association of Coastal and Ocean Observing Systems (NERACOOS, http://www.neracoos.org/datatools/historical/graphing_download).

The wave scatter table used for the analysis is shown in Figure 145, including the occurrence probability for each combination of significant wave height and dominant wave period.

Dominant Wave Period (s)		0.0 - 2.0	2.0 - 4.0	4.0 - 6.0	6.0 - 8.0	8.0 - 10.0
Significant Height (m)	0.0 - 0.2	9.9%	23.8%	14.2%	15.8%	3.3%
	0.2 - 0.4	1.2%	20.9%	0.8%	0.4%	0.0%
	0.4 - 0.6	0.0%	6.2%	0.2%	0.0%	0.0%
	0.6 - 0.8	0.0%	2.2%	0.3%	0.0%	0.0%
	0.8 - 1.0	0.0%	0.3%	0.2%	0.0%	0.0%
	1.0 - 1.2	0.0%	0.1%	0.1%	0.0%	0.0%

Figure 145: Wave scatter table for Buoy F02: DeepCwind Castine Test Site.

NOTE: Although the bin sizes in wave scatter tables published by NDBC and other agencies tend to be self-consistent, there does not appear to be an industry-accepted procedure for determining scatter table bin sizes. The sizes in Figure 145 were chosen to spread out the data while not creating cells with such a low probability as to be useless and possibly misleading.

The relationship between significant wave height and mean wind speed is shown in Figure 146. The best fit curve was found to be linear. For fatigue calculation, the 75% Prediction Interval (upper dashed line) was assumed, as a conservative approach.

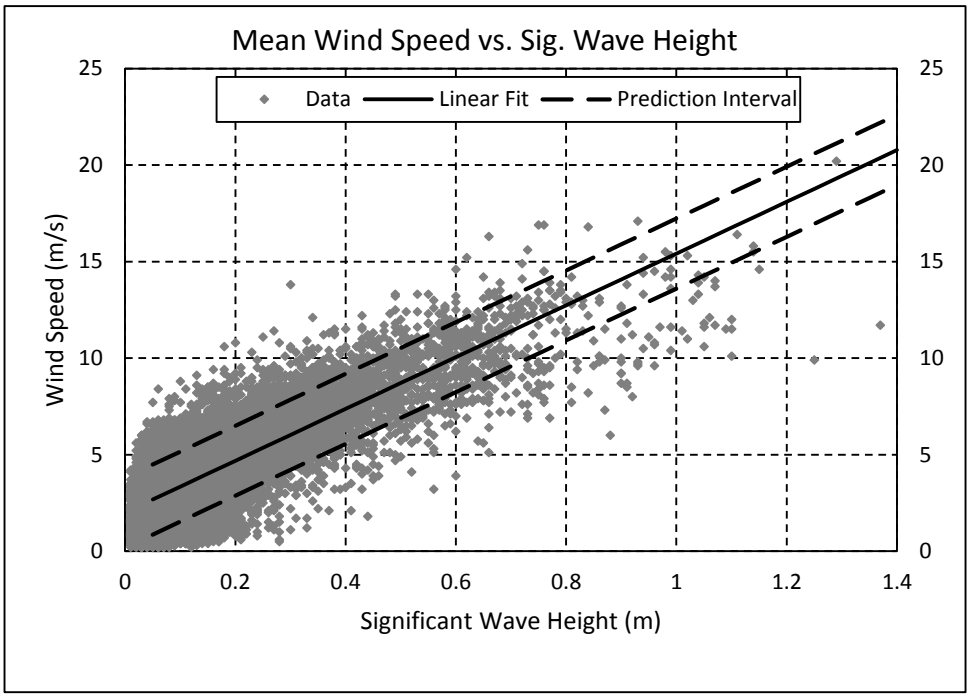

Figure 146: Plot of mean wind speed vs. significant wave height and plots of Logarithmic trend line, with +/- 75% Prediction Intervals.

Current velocity and heading was found to be tidal, as shown in Figure 147. A heading of 0° represents a flood tide condition, while a heading of 180° is an ebb tide. The 95th percentile current velocity of 0.48 m/s was assumed.

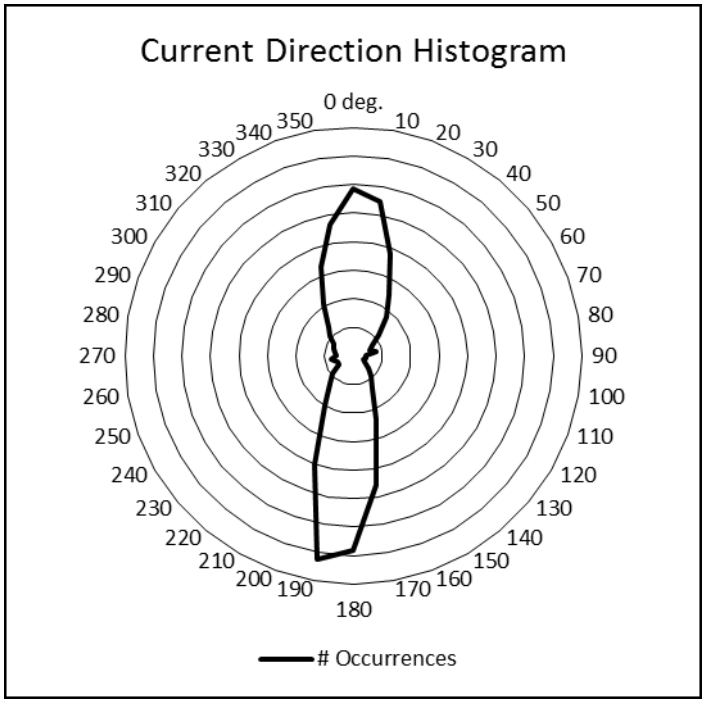

Figure 147: Histogram of hourly current direction measurements, taken from Buoy F02.

Finally, typical tidal ranges were estimated from historical tide charts in Castine, ME (http://me.usharbors.com/monthly-tides/Maine-Midcoast/Castine/). The mean change in water level between high and low tide was found to be 3.19 m.

A single wave heading, coming from the south, was assumed. API RP-2SK recommends using several wave heights, however, the VolturnUS site is located near the mouth of the Penobscot River. The most severe seas are expected to originate at sea, and can only reach the VolturnUS from a southerly direction.

6.4.7.3 Corrosion and Abrasion Prediction

In order to study the effects of corrosion and abrasion on fatigue, a simplified prediction of the decrease in chain bar diameter was made. The diameter loss due to corrosion was calculated using the model, and coefficients, described by Melchers (2008), and Melchers (2005). This corrosion prediction is dependent on the annual mean temperature, taken to be 9.2° C, based off of estimates from NOAA buoys in the Gulf of Maine. With this model, a loss of diameter of 3.1 mm over a 20-year lifetime is assumed.

In addition to corrosion degradation, material loss due to abrasion between chain links is expected to occur. It is assumed that the maximum abrasion will occur near the fairlead, where chain tension is the highest. According to Shoup and Mueller (1984), and Brown et al. (2010), abrasion is a function of contact tension, relative motion between chain links, material hardness, and a non-dimensional wear coefficient.

A simplified calculation was able to predict the worn volume from the fatigue simulations. Using the methods discussed by Shoup and Mueller (1984), the worn volume between chain links was calculated from a time series of tension and angular motion measurements:

$$Volume = \sum_{i=1}^{N-1} \frac{T_{i+1} + T_i}{2} (\varphi_{i+1} - \varphi_i) r K \qquad (30)$$

Where T_i represents the fairlead tension, and φ_i represents the difference in declination angle (in radians) between the first two chain links at time *i*. The ratio of wear coefficient to material hardness is *K*, and is taken from experimental data reported by Shoup and Mueller (1984). The nominal link diameter is *r*. This is the formulation of Archard's Equation presented as Equation 3 by Shoup and Mueller (1984).

The loss of radius corresponding to the worn volume is calculated by assuming that the diameter loss occurs over an area specified by the radius, i.e. $Diameter = Volume * \pi r^2$, where *r* is the bar radius. This method is a simplification of the geometry of the chain link crown; a more detailed methodology is laid out by Brown et al. (2010).

Combining the predicted corrosion and abrasion loss, the normalized reduction in diameter is plotted in Figure 148, compared with a nominal reduction of 0.4 mm/yr, which is a typical value specified in offshore standards.

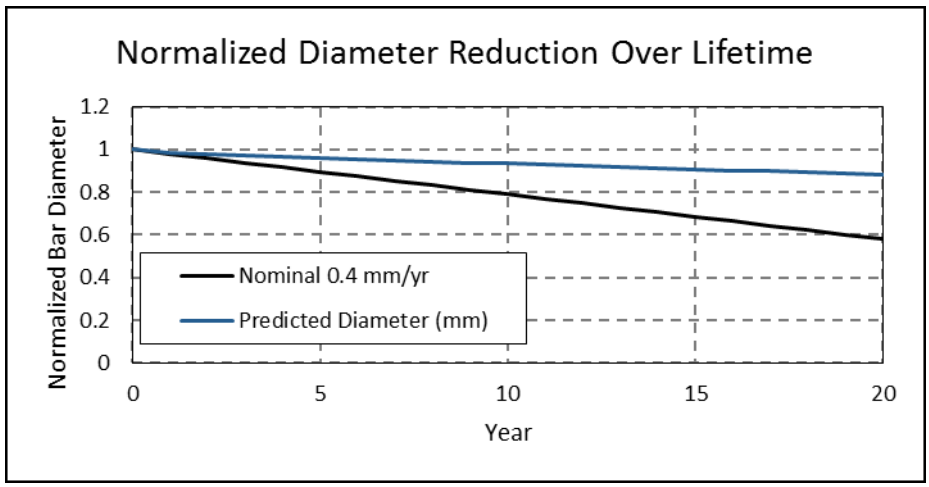

Figure 148: Predicted corrosion from literature models compared with typical nominal corrosion rate from offshore standards.

According to Figure 148, the nominal corrosion rate of 0.4 mm/yr. is conservative, however it may prove to be non-conservative under different conditions (as has been reported in the literature), including:

- Tropical locations, where the water may be several times warmer on average, which has been shown to speed up corrosion.
- Locations where microbiological activity may cause pitting corrosion, which often occurs much more rapidly and more deeply than uniform corrosion.
- Systems with tighter mooring systems in deeper water, where higher fairlead tensions occur, leading to greater wear.
- Conditions in which corrosion and abrasion interact with each other. An example of this is discussed by Melchers et al. (2007), in which regular abrasion prevents the build-up of a layer of rust, thus speeding up corrosion as the chain link surface remains in aerobic conditions.

6.4.7.4 Fatigue Lifetime Prediction

For the environmental conditions described, total of 68 OrcaFlex+FAST simulations were run. These simulations accounted for all assumed variations in wind speed, sea-state, water depth, and current heading. From the results of these simulations, fatigue damage was calculated in accordance with Miner's Rule. S-N parameters were selected from DNV-OS-E301.

From simulated OrcaFlex+FAST results, the hourly damage was calculated on Leg A (the downwind leg). The annual damage was calculated according to the probabilities of occurrence specified in Figure 145. The result is shown in Figure 149. The maximum damage occurs at a dominant wave period of 5.00 s, and a significant wave height of 1.10 m (colored red in the figure). It is noteworthy that, while this sea-state only occurs 0.1% of the time, it accounts for over half of the annual damage that occurs on Leg A.

	1.00 s	3.00 s	5.00 s	7.00 s	9.00 s
0.10 m	6.5E-09	1.8E-08	4.1E-09	2.0E-08	6.9E-09
0.30 m	3.3E-07	8.1E-07	2.0E-08	9.2E-08	
0.50 m		2.2E-06	9.7E-08		
0.70 m		2.8E-06	1.2E-06		
0.90 m		1.2E-06	5.7E-06		
1.10 m		1.3E-06	1.8E-05		

Figure 149: Scatter table showing predicted annual damage for each scatter cell.

The expected fatigue lifetime was calculated using the assumed corrosion and abrasion losses discussed in the previous section. It is assumed that each year the diameter of the chain link decreases due to corrosion and abrasion. This decrease causes increased stress from fairlead tensions over time, despite being under the same environmental excitation. The decrease in diameter is not modeled in OrcaFlex+FAST simulations, it is only assumed in fatigue calculations done in post-processing.

In addition, fatigue lifetime was calculated assuming (1) no corrosion in the chain, and (2) that the chain has corroded 50% of the value expected over its lifetime. This later assumption is in accordance with DNV OS-E301, Section 2 F302. The results are shown in Table 44 for both of the corrosion assumptions shown in Figure 148. In each case, the mooring line is expected to survive a nominal fatigue lifetime of 20 years.

Comparing the fatigue prediction from the two corrosion assumptions, it is observed that corrosion assumptions have a large impact on fatigue damage calculations. Using 50% of the expected corrosion for lifetime calculations is a valid approximation if the predicted corrosion model is used, however it underestimates the fatigue damage when a nominal corrosion rate of 0.4 mm/yr. is assumed.

Even though these lifetime numbers are large, they represent estimates of reliability rather than absolute predictions of time-to-failure. As such they are useful design metrics.

Table 44: Predicted cumulative damage and fatigue lifetime under different corrosion assumptions.

	Predicted Corrosion/Abrasion		Nominal Corrosion/Abrasion Rate	
	Cumulative Damage	**Lifetime (years)[1]**	**Cumulative Damage**	**Lifetime (years)[1]**
Lifetime Corrosion Assumption	1.10e-03	1,910	5.10e-3	412
No Corrosion	6.81e-04	2,930	6.81e-3	2,930
50% Corrosion	1.05e-03	1,900	2.80e-3	714

[1] *Assuming a safety factor of 10 for non-redundant system without regular inspection.*

6.4.7.5 Snap Loads Effect on Fatigue Life

Snap loads on mooring lines are observed during survival sea-state which is caused by large motion of the floater. Snap events are characterized by low frequency of occurrence and high magnitude. Although there are only few snap events during the one-hour storm, However, we found that mooring line tension history with snap events have higher exceedance probability at high tension range than the mooring line tension history without snap events. That means snap loads should be considered as part of effect on the fatigue life.

In this case study, no snap events are observed during the SLC condition. This is possible because the mooring lines of VolturnUS were conservatively designed to have extraordinary lengths of line on the seafloor. To investigate the effect of the mooring line length on snap events, and the snap loads effect on fatigue life, we conducted a parametric study of line length.

The minimum mooring line length with no uplift on the anchor can calculated by Equation(31), below (Faltinsen,1999).

$$S_{min} = d\sqrt{\frac{2T_t}{wd} - 1} \quad (31)$$

Here T_t is the maximum tension that can be expected in a survival condition. d is the water depth and w is the weight per unit length of the line. For a maximum tension value of 24 kN (recorded in one of the lines during SLC) the minimum line length is evaluated to be 135 m. The as-deployed lengths of LEGA, LEGB and LEGC were 309m, 277m and 198.5m respectively.

Long line lengths imply that a significant part of the line rests on the seabed for much of the time. The laid lengths on the seabed for LEGA, LEGB and LEGC are estimated to be 278m, 235.5m and 168.7m respectively. Moreover, snap events are not observed in the field data under survival sea-state. In this case study, we artificially decrease line length from the original condition (LEGA, LEGB and LEGC were 309m, 277m and 198.5m respectively) to the minimum line length (LEGA, LEGB and LEGC were all 135m) to investigate the occurrence of snap events, as shown in Table 45.

Table 45 Line lengths for four cases in sensitivity study.

Case	Line Length (m)		
	LegA	LegB	LegC
1	309	277	198.5
2	250	250	250
3	200	200	200
4	135	135	135

For each case, the pretension of each mooring line are the same as the field data (LegA, LegB and LegC were 3.1kN, 3.4kN and 2.4kN respectively). Figure 150 through Figure 152 shows the comparison of mooring tension under four cases for LegA, LegB and LegC respectively.

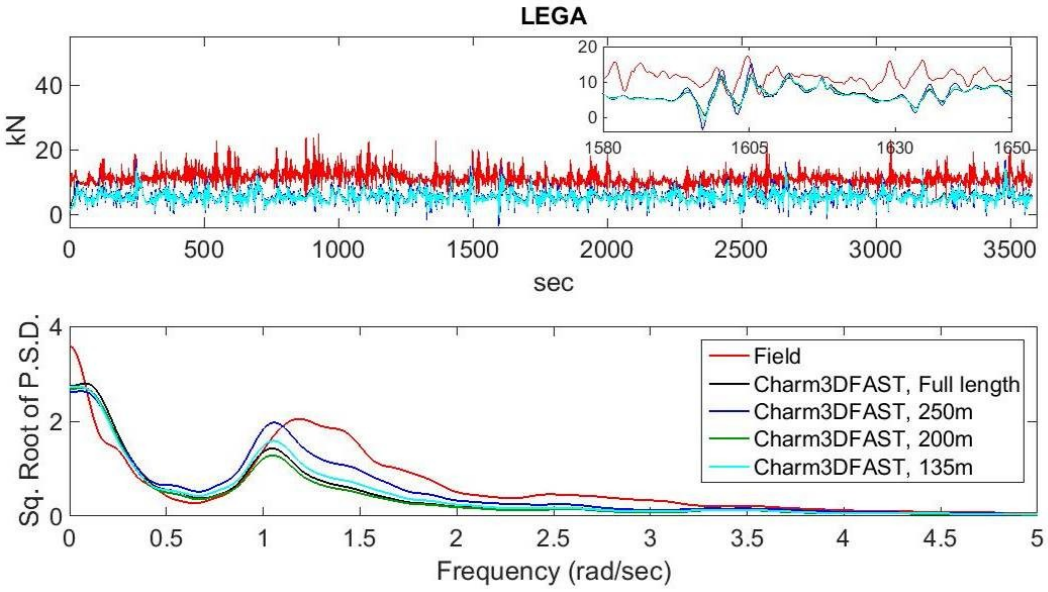

Figure 150 Mooring line tension, LegA, four different line lengths

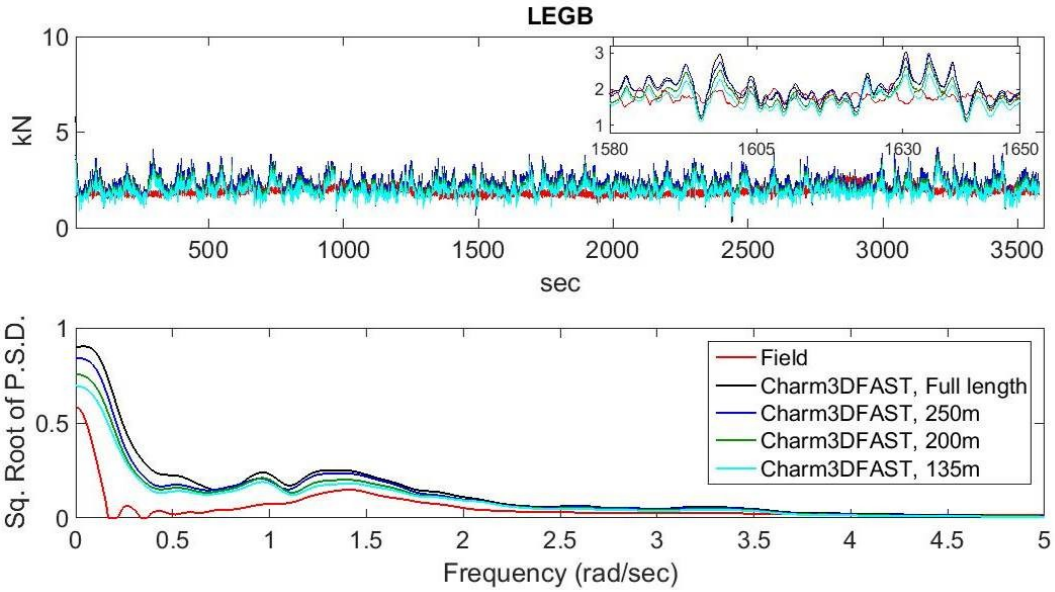

Figure 151 Mooring line tension, LegB, four different line lengths

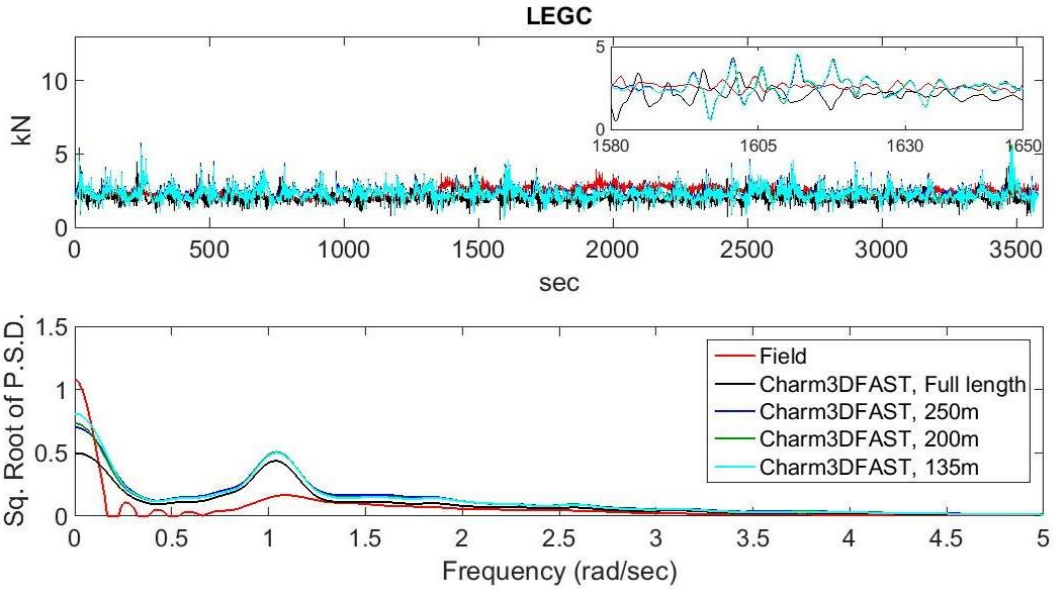

Figure 152 Mooring line tension, LegC, four different line lengths

Snap events are observed in LegA. Table 46 shows the occurrence of snap load on LegA in each case. Two snap events are observed in the full length case, while there is no snap event is observed in field data. Line length of 250m found more snap events than three other cases, and line length of 200m does not found any snap events. Four snap events are observed in the minimum length case. We found that there is no trend of occurrence of snap events with decreasing line length. Moreover, for cases 2 and 4 there were isolated time instants where negative tension forces are observed implying an error accumulation in the simulation run. Thus, some numerical modeling problems continue to persist and results around these negative tension events were removed from further analysis.

Table 46 Occurrence of snap events for four cases simulating 1 hour episodes

Case	Number of Snap Events
1	2
2	21
3	0
4	4

In this study, we only consider line length as the only one factor of snap events. However, there are several factors of snap events, such as water depth, mooring line stiffness, mooring line density and so on, which should be included in the parameter study of snap events. Although we did not find the trend of mooring line length effect on occurrence of snap events, snap events effect on fatigue life could be investigated by these modeling results.

Miner's rule is one of the most widely used cumulative damage models for failures caused by fatigue. To apply Miner's rule, T-N curve is required to calculate the damage. The minimum N of the current T-N curve is 200, however the snap load with the low frequency and high strength is not in this region. In our study, less than 30 snap events were observed during simulations of

one hour episodes. The simple approach is to extend the T-N curve to the y-axis with the same slope. To study snap load effect on fatigue life, the fatigue life comparison between 1-hour mooring tension history includes snap loads and without snap loads. Table 47 shows the occurrence of snap events, the fatigue damage and damage ratio of Case 1-4. The damage ratio is defined as damage of each case divided by damage of case 3 which is without snap events. We found that even if there were only two snap events during a 1 hour storm, the damage increased to 1.34 times the damage without snap events.

Table 47 Occurrence of snap events, fatigue damage and damage ratio of Case 1-4. Each simulation represents a 1 hour episode.

Case	Number of Snap Events	1-hour Fatigue Damage	Damage ratio
1	2	3.46×10^6	1.34
2	21	8.97×10^6	3.48
3	0	2.58×10^6	1
4	4	4.36×10^6	1.69

6.4.7.6 Comments on quality of simulation results

In general, comparison between simulations and field data was made difficult by lack of precise information needed from the field for the simulations. It is typical of field measurements to not have such level of detail commonly available. However, the research team worked closely with ASCC scientists and with the software developers to bring convergence into issues of conflict. Notwithstanding these issues, the overall comparison was satisfactory at many places, while some issues were of concern.

Motion response prediction by software compared favorably with field data. OrcaFlex+FAST was within 50% of statistics for DLC 1.6, while Charm3D/FAST did comparatively well for the SLC condition. Differences in other load cases went as far as 100% and higher. Perhaps more relevant to this project is the prediction of mooring line tensions, which the software estimates to within 50% in most cases of relevance, except for SLC where Leg A predictions were considerably lower than field data. The team extensively researched this particular case. Such a large force magnitude was found to be inconsistent with the general tension range of the line (pre-tension was typically about 1 – 2 kN), and none of the software simulations could capture this large value.

6.4.7.7 Comments on software tools

Stability, Usability, Functionality of OrcaFlex+FAST

Findings by NREL (Masciola et al., 2011) suggest that the FAST/OrcaFlex coupling tool produces results consistent with FAST's quasi-static cable model. This investigation considered simple cases, using the NREL Hywind 5 MW Baseline model. Viselli et al (AWEA, 2014) find that FAST by itself is inadequate to reproduce field measurements for the VolturnUS 1:8-scale model.

For the present study, while agreement between OrcaFlex+FAST measurements and field data was mixed, OrcaFlex+FAST was found to be largely stable and functional.

Simulation Run-Time

As noted by Masciola et al. (2011), high-fidelity modeling requires simulation speed to be sacrificed. While simulation speed can be increased by increasing the time step, a high time step also decreases accuracy and may cause instabilities in the models. In the present study, it was found that a coupled OrcaFlex+FAST simulation is slower than a FAST simulation and an OrcaFlex simulation without the coupling.

Balancing the Time-Step between Simulators:

OrcaFlex+FAST simulations were run with an OrcaFlex time-step of 0.0125s, and a FAST time-step of 0.0125s as well. This value was based on a brief sensitivity study to achieve high time-step without loss of accuracy. Flexibility modes of the blades were disabled to allow for faster time-step. This was not done in de-coupled FAST simulations. The simulations in FAST, when de-coupled from OrcaFlex, were run with a time- step of 0.0025 s. Similarly, the simulations in OrcaFlex, when de-coupled from FAST, were run with a time-step of 0.05s.

Selecting time-steps between FAST and OrcaFlex is up to the user. No clear rules are stipulated. One area needing further investigation involves defining a method to select time-step length. In terms of stability, the time-step has a profound effect on the solution, and in general, a smaller time-step implies greater simulation stability.

OrcaFlex GUI

The Graphical User Interface (GUI) available through OrcaFlex allows easy management of platform hydrodynamic properties and cable configuration. Once the simulation is run with OrcaFlex+FAST, the simulation file can be used to gain appreciation of the platform and mooring motions through three-dimensional rendering, although the turbine dynamics are not animated in OrcaFlex.

The OrcaFlex+FAST tool appears suitable for a multitude of offshore wind turbine designs, including semi-submersibles and TLPs, whether the mooring lines are taut or slack.

6.4.8 Conclusions

Simulations were run with Charm3D+FAST and OrcaFlex+FAST to compare against three one-hour field measurement periods. In general, good qualitative agreement was observed between simulation and field data. Several discrepancies were observed and discussed.

The most notable discrepancy between simulation models and field measurements was a severe under-prediction in loads in the taut mooring line in the Survival Load Condition. However, better agreement was achieved by adjusting current and wave headings to align with Leg A. This suggests several things.

- Disagreement between simulation models and field data could be attributed in part to uncertainties or errors in reported environmental conditions. Unfortunately it is difficult or impossible to verify this.
- Simulation models show that the mooring system is extremely sensitive to environmental inputs. This effect is likely enhanced for shallow water, slack mooring systems with light platforms, which are all typical characteristics of FOWTs. Additionally, FOWT mooring systems are less likely than other offshore systems to have redundancies. Therefore, higher sensitivity in selection of environmental conditions is likely required to ensure that extreme events are accounted for in preliminary design.

A parametric fatigue lifetime calculation was conducted, based on available field measurements for environmental parameters. A number of significant conclusions are drawn from the fatigue study.

- Under the assumptions of Miner's Rule, it is found that severe storms contribute a disproportionate amount of damage, even when accounting for their low likelihood of occurrence. Similar observations have been reported in the literature (Kiecke and Zhang, 2011). This raises the question of whether even more unlikely storms (with return period > 1 year) need to be taken into account when calculating fatigue damage. Such Survival Load Cases are not required to be considered in design standards.
- Consistent with findings in the literature, the present study finds that corrosion tolerances reported in design standards may not be conservative. An approximation of corrosion and abrasion degradation in the VolturnUS chain was determined from methodology proposed in the literature.
- In one case, assuming 50% of the expected corrosion when calculating fatigue lifetime substantially over-estimated the lifetime compared with a similar calculation in which the corrosion damage at each year was accounted for. An assumption of 65-70% would have been more accurate in this case.

7 Conclusions

The designer faces a number of challenges in predicting the fatigue life and failure mechanisms of the mooring systems of FOWT installations:

- Fundamental Theory:
  - High scatter observed in fatigue lifetime calculations.
  - Fatigue damage is sensitive to extreme events and to corrosion and abrasion.
  - Miner's Rule is hard to validate in an offshore mooring setting.
  - Fundamental research on system level corrosion and abrasion needed.
  - Extreme events including snap loads require special treatment in statistical fatigue calculations.

- Software Tools: Limitations, accuracy, level of integration between modules, and customer support
  - Industry lacks high-fidelity tools for prediction of mooring chain material loss.
  - Simulation results are particularly sensitive to input parameters such as sea-states, relative headings, and even random number seeds that determine the starting wind gust and wave component heights and phases.
  - FAST, Aqwa, OrcaFlex, Charm3D are each good simulation tools provided the environment and FOWT inputs are well understood.
  - Coupling of Aqwa/OrcaFlex/Charm3D to FAST is incomplete, not well supported.
  - Coupling between OrcaFlex and FAST v8 should be developed, and fidelity of FAST v8 mooring module should be compared with OrcaFlex+FAST.

- Data Sources:
  - VolturnUS case study presented challenges due to large scope, shallow water, and light platform with scaled down turbine.
  - Initial proposal to use Gulf of Maine Statoil turbine data did not materialize due to shift in local political climate which prevented that project from moving forward.
  - Future research could be done with full VolturnUS data set to examine fidelity of software tools in predicting fatigue lifetime (as calculated using Rainflow Counting and Miner's Rule).

7.1 Problems with Fundamental Theory

7.1.1 Theory: Statistical Fatigue Analyses

Accepted practice is to apply a single statistical distribution to all degradation processes, but as case studies in this project have shown, small discrepancies in mooring tensions between simulation data and field data can correspond to a large difference in predicted fatigue damage.

Miner's Rule is hard to validate in an offshore mooring setting. Fatigue is a process that takes years or decades to occur, and in the field such long term experiments are rarely practical. In addition, the concept of "damage" is hard to quantify. Destructive testing can be done to assess

residual breaking loads of mooring components, but this is difficult within the context of ongoing field experimentation. A study of crack propagation can provide useful fatigue damage measurement, but is challenging to measure reliably on offshore mooring components.

Complete and Accurate Environmental Data: Classical fatigue damage calculations were found to be extremely sensitive to environmental assumptions, possibly even more so in shallow water, where FOWTs are likely to be sited, than in deep water. Good knowledge of the local environment is essential to even preliminary, high level design. That information includes:

- Wave + wind probability distribution
- Wave + wind heading distribution
- Current speed + heading
- Tidal water depth variations

Results from case studies in this project show that large, survival case storms can dominate fatigue calculations. It is possible that component stresses from extreme storms will result in snap events that violate the assumptions of independence between stress events, but that is a subject for additional research. The ABS FOWT guidelines do not consider survival conditions in fatigue design load cases, except for TLPs.

Traditional fatigue analyses were used to predict the lifetime of mooring systems in this project, and a large amount of scatter was observed in the results. Specifically, the percent difference between the damage calculations based on experimental data and those based on simulated data is larger than the percent difference between the RMS values of mooring tension from experimental data and from simulation results.

Extreme Stress: Another way to look at classical fatigue analysis is to consider it useful for a component subjected to frequent stresses well below its breaking strength, but that is never subjected to extreme loads. Unfortunately that description does not fit the mooring system on an offshore wind turbine, which will be exposed to extreme events on an infrequent basis. This team has found that the loads from these extreme events (e.g. hurricanes) will dominate the fatigue load calculations and dominate the actual failure mechanisms in the system.

Light Loading: This project team has found that classical fatigue analysis as implemented using rainflow event counting and Miner's rule may be useful as a long term reliability prediction tool, but that it is less useful as a predictor of failures in mooring systems. For components that are lightly loaded such as the mostly-downwind leg of a mooring system, the loads will be below Fatigue Limit States, a lower limit to the stress that contributes to fatigue. In an ideal system without corrosion an infinite number of cycles below a metal's Fatigue Limit State can occur without fatigue failure. Statistical fatigue life calculations on lightly load mooring components can predict extremely long fatigue lives. Other mechanisms such as uneven corrosion or uneven loads, microbial induced corrosion and other factors could cause failures well before the predictions.

7.1.2 Fatigue Analysis based on Corrosion and Abrasion

Corrosion, abrasion mechanisms on mooring systems are extremely complex and not well understood at the system level

Abrasion: This study has demonstrated a new way to predict abrasion in chain-based catenary mooring systems. The USCG ATON buoy case study has shown that mooring system material loss due to abrasion can exceed classification society rules by an order of magnitude. This finding is consistent with reports in the literature of extreme material loss due to abrasion, corrosion, microbial influenced corrosion, and many other failure mechanisms.

This study suggests that abrasion mechanisms play multiple roles in determining the life of a mooring component. Section 7.4 discusses this in detail and concludes that system lifetime predictions for mooring components have to be done on a region by region basis. It is not enough to consider interlink abrasion; abrasion between metal components and the seafloor have to be considered.

Corrosion: This study has shown that under certain circumstances it is possible to predict material loss in mooring system components by looking at publically available data on metallic and organic contaminants in the seawater. While corrosion studies have been performed before by researchers and joint industry projects on chains and other mooring components, more work is required so that design methodology can be codified in classification rules. Multiple theories exist describing corrosion mechanisms, and these theories need to be compared and integrated into a system level corrosion prediction mechanism that takes into account the validity of each corrosion theory for specific regions of mooring components. For example, corrosion in chain lying on the sea floor will be influenced by the seabed chemical composition, whereas corrosion in chain in the water column might be influenced more by microbiologically induced corrosion.

7.1.3 Theory: Fatigue Analysis based on Snap Loads

From prior experience, project team members have noted that extreme tensions in mooring components can arise from snap events in which the line tension goes from essentially slack to a significant percentage of breaking strength. Research has shown a relationship between snap events and micro-fractures. Especially during survival conditions snap load events can result in excessive damage to mooring system components. [2]

As shown in this report, tension events experienced during extreme storms can have an inordinately large effect on the cumulative fatigue damage. If these high tension events are snap events, then there is a strong chance that the damage from these events are higher than would be expected from linear fatigue theory.

Analysis in this project shows that snap tension events have a different probability distribution as compared to that of cyclic maxima. Recognizing the potential for excessive damage from snap events, the project team has concluded that recommended approaches to low cycle/high stress fatigue overly simplify damage in mooring components, and over predicts the lifetime of these components. Accordingly better methods are required to predict the likelihood of snap loads and the impact of snap loads on individual components.

[2] ABS FOWT guidelines do not include recommendations to consider survival load conditions in fatigue analysis except in the case of TLPs.

7.2 Conclusions Regarding Software Design Tools

The project team found that commercial software tools are reasonably accurate, provided that the inputs (environmental, mooring, platform, turbine) are known and accurate.

On the other hand results from the case studies show that:

- Serious technical limitations exist in the tools
- They exhibit uneven levels of accuracy
- There is relatively poor integration between modules, especially program systems made of programs from different sources
- Some of the tools are very specialized and the developing organizations offer weak customer support.

System-level abrasion and corrosion are not addressed in the common software tools. The project team identified no high-fidelity SW tools for prediction of mooring chain or wire rope material loss covering the span from anchor to fairlead. Corrosion and abrasion are more important for systems deployed in shallow water than for deep water systems, and most FOWT systems are deployed in shallow water.

There appear to be no software systems with seamless integration between all of the physics modules, including those modeling turbine motion, wind loads, wave loads and mooring system behavior.

The software tools evaluated in this project appear to be targeted toward deep water floating systems. This project team found that long-scope, shallow water mooring systems are not well modeled in ANSYS Aqwa or Charm3D. OrcaFlex seems to handle the long-scope, shallow water case slightly better, but the developer still needs to put effort into predicting the initial conditions to insure that the simulator converges.

7.2.1 ANSYS Aqwa

NOTE: The project team had access to ANSYS Aqwa version 14.5. Enhancements to the program system beyond this version are not described in this report.

Aqwa is a 3D potential flow program from ANSYS. The program is integrated in the ANSYS Workbench environment so that designs can be created with ANSYS Design Modeler and meshed with an ANSYS surface meshing tool.

Aqwa can be used as a tool for generating frequency dependent hydrodynamic databases consisting of added mass, damping, and Froude-Krylov force coefficients in six fully-coupled degrees of freedom. The program also calculates hydrostatic restoring force coefficients. These dynamic and static coefficients are imported into an OrcaFlex model for accurate simulation of wave-based dynamic effects.

Aqwa can also be used as a stand-alone tool to predict the seakeeping behavior of free-floating and moored systems. The basic system can calculate motion Response Amplitude Operators (RAOs), responses to input sea states, and motion and load statistics. By adding the optional non-linear "Cable Dynamics" module the system can also simulate mooring lines using a finite element methodology.

Table 48 Benefits and Issues of ANSYS Aqwa Program System

Benefits	Issues

• Can calculate accurate RAOs and system responses
  ○ Results are well validated and calibrated against measured data
• Aqwa Graphical Supervisor (AGS) supports animation, standalone analyses, mesh generation for ships
• Convolution-based time-domain simulation to capture non-linear behavior mixed with linear (wave) dynamics
• Complete solution including meshing, potential flow modeling, time-domain cable dynamics modeling
	• Program can be sensitive to mesh. Design components (e.g. keels, bulbs) may need slight separation from vessel body to eliminate meshing errors.
	• (Pro/Con) Aqwa chooses frequency spacing in RAOs based on energy concerns. It can be difficult to get Aqwa to simulate specific frequencies other than the ones it chooses algorithmically
	• Limited access to Aqwa/AGS hydrodynamic coefficient database
	  ○ OrcaFlex has to import hydrodynamic coefficients by parsing Aqwa listing files
	• Aqwa with Cable Dynamics can difficulty converging on solutions if one or more lines are sufficiently slack

In this project Aqwa was used both for generating hydrodynamic databases for OrcaFlex and as a standalone tool for the ATON buoy case study. The case study consisted of simulating 54 different buoy locations. The simulation models included the buoy "can" type, water depth and mooring chain type. The system was automated so that the expected responses for each cell in an annual wave scatter diagram could be combined to calculate a single vertical and lateral energy value. After some script debugging, Aqwa worked well in this application. All 54 buoys are constructed with a small set of standard buoy "cans," so the design creation and meshing tasks could be finished ahead of the bulk simulations.

At the time of this report ANSYS is working with one of their customers to develop an Aqwa-FAST coupling, but that has not yet been released.

7.2.2 NREL FAST

The FAST software tool from the National Renewable Energy Laboratory (NREL) calculates wind turbine performance including rotor and generator, nacelle motion, and tower bending in response to turbine excitation.

Table 49 Benefits and Issues of NREL FAST Program System

Benefits	Issues

• Open source tool
• Can be tailored to specific cases including control algorithms
• Includes physics models for blades, turbine, tower, platform and simple mooring system
• Includes tools for inflow wind calculations
• Pretty good documentation and support Lots of papers on FAST
  ○ Lots of examples available
  ○ Very Good on-line Wiki
  ○ Very fast response from NREL staff
  ○ Source code available (slightly cryptic)
	• Written in Fortran
	  ○ Little Fortran expertise outside of academic environment
	  ○ If extensions or scripting required, most commercial tools use Java or Python
	• FAST v7 neglects wind loads on the turbine tower and platform (FAST v8 includes support for tower wind loads)
	  ○ Problem for small prototypes (e.g. 1/8 Scale VolturnUS)
	  ○ Problem for high wind conditions due to pitch control
	• FAST v8 not coupled to Aqwa, OrcaFlex or Charm3D

7.2.3 NREL FAST Coupled with Specialized Hydrodynamics Mooring Software

Individually FAST, Aqwa, OrcaFlex, Charm3D are good simulation tool provided the environment and FOWT inputs are available and accurate. All of the coupled systems exhibit benefits and drawbacks to some degree.

Table 50 Benefits and Issues of NREL FAST Coupled with Other Software Modules

Benefits	Issues

• Coupled systems do work most of the time
• In most cases results are accurate for engineering purposes
	• 10x performance hit over individual tools
	• All or part of human interface becomes unusable (back to text files)
	• Potential instabilities
	  ○ Yaw instability
	  ○ Hard to tell if certain behaviors are due to simulation artifacts or reality
	• No customer support for integrated system
	• Undependable update cycle
	  ○ Not connected to commercial SW update cycle
	  ○ Depends on government funding and priorities
	• Documentation limited
	  ○ Some support through NREL online forum, focus is on FAST
	  ○ Orcina and Coastal Dynamics do not support coupled version (at least not directly)
	• Wind loads on tower are not modeled directly. In this project these loads were modeled as time-dependent Applied Loads.
	  ○ Based on API wind load assumptions
	  ○ Not coupled to platform motion or change in wind direction

7.2.4 Orcina OrcaFlex

OrcaFlex by Orcina is a very robust, user-friendly tool for simulation of complex mooring systems in a wide variety of offshore applications. The OrcaFlex time-domain simulator predicts the motions and loads of moored floating systems.

Table 51 Benefits and Issues of Orcina OrcaFlex Program

Benefits	Issues

• Superior for simulating complex mooring systems including lines with very long laid lengths and seafloor contact friction
• Finite-element solver for mooring lines is more robust than quasi-static solvers
  ○ Includes inertia, added mass, torsion of lines
  ○ Can better model slack lines
• Program has flexibility in assignment of line node spacing
  ○ Nodes do not need to be evenly spaced
  ○ Useful for modeling composite mooring systems, moorings with large laid length with little motion
• API allows manipulation of simulation cases, pre-processing, post-processing of large batch jobs with external software
• Documentation and support are very good
	• It is difficult to directly specify pre-tension values of mooring lines
	• Little built-in functionality to model wind/current loads based on design standards
	• Linear platform hydrostatics is assumed
	• In the VolturnUS 1/8-scale case study OrcaFlex had difficulty with:
	  ○ Indeterminacy of initial azimuth angle of laid length
	  ○ Folded lines at touchdown caused by very slack conditions

7.2.5 OrcaFlex+FAST

The OrcaFlex time-domain simulator is connected to FAST v7 through the OrcaFlex+FAST program. The combined system can predict the motions and loads of moored FOWTs.

Table 52 Benefits and Issues of NREL FAST Coupled with OrcaFlex

Benefits	Issues

• Full coupling between mooring + platform + wind turbine models
  ○ Time-dependent turbine thrust and torque loads
  ○ Time-dependent, finite element solver for mooring lines
  ○ Time-dependent, convolution integral calculation of platform response
  ○ Platform hydrodynamics based on external linear potential flow solver
• OrcaFlex GUI is available for hydrodynamic model development
• For shallow water systems with large laid length, such as VolturnUS case study:
  ○ Seafloor friction model is useful for long laid length
  ○ Finite element mooring model is able to simulate slack mooring lines beyond what quasi-static solver can do
	• Limited use of OrcaFlex Graphical User Interface (GUI)
	  ○ All turbine/nacelle/tower parameters have to be entered using text file
	• Challenges encountered during VolturnUS case study:
	  ○ Challenges included: extreme shallow water depth, very high scope, light-weight system
	  ○ High laid length: system sensitive to initial azimuth angle of lines
	  ○ One line slack in all time periods investigated (no horizontal tension)
	  ○ Simulation indeterminate, unstable if lines fold back at touchdown
	• Tower loads modeled as time-dependent applied loads
	  ○ Based on API wind load assumptions
	• Documentation and Support
	  ○ No OrcaFlex+FAST manual, although there are some documents describing how to build and run the system
	• FASTLink (coupler) module was written by 3rd party (no support)

7.2.6 Charm3D

Charm3D from Ocean Dynamics offers good performance and a friendly human interface for simulating deep water offshore structures. The project team found it to be challenging to use Charm3D for FOWTs, primarily because the program has difficulty simulating long-scope, shallow water moorings systems.

Table 53 Benefits and Issues of Charm3D Program

Benefits	Issues

• Good design creation facility
  ○ System includes program for generating and editing ship/FPSO vessels and free-surface panel models
  ○ Can create truss and plate models using Morison's drag model
• Built-in WAMIT module for hydrodynamic coefficients
  ○ Creates mesh for WAMIT for Spar, TLP/SEMI, FPSO
  ○ Alternative: User can generate external WAMIT mesh by hand
• Charm3D system has a good human interface and good graphical output capabilities including animation
	• Limited wind force generation capability
	  ○ Can generate wind force on an object as defined by API RP 2A, Eqn. 2.3.2-7
	• Limited documentation and support
	  ○ Manuals for Charm3D and HARP systems
	  ○ Offshore Dynamics Inc. provided good, but very limited telephone support
	• Design and analysis of taut/catenary mooring systems is somewhat limited. Two options are:
	  ○ Given line length, pretension of each line, Charm3D calculates anchor locations
	  ○ Given the line length (or vessel offset) and anchor locations, Charm3D calculates the pretension[3]
	• Charm3D cannot simulate a design without a mooring system:
	  ○ Cannot run static analysis without mooring lines
	• Can only generate RAO by running individual regular waves

Offshore Dynamics offers a statistical fatigue analysis module, but this was not made available to the project team.

7.2.7 Charm3D+FAST

The Charm3D+FAST program system works. It can simulate the complete FOWT system from wind blade to mooring system, and the results appear to be reasonably accurate. Since the system is based on Charm3D, the hydrodynamics database is created internally using the WAMIT program.

There are a number of issues with the implementation of Charm3D+FAST. The combined system does not have the quality and usability characteristics of a polished commercial program, but with some extra effort the project team was able to get results and validate the results against measured data.

[3] This option was not available to the project team and proved to be a barrier in simulating the VolturnUS 1/8-Scale system.

Table 54 Benefits and Issues of NREL FAST Coupled with Charm3D

Benefits	Issues

• Full coupling between mooring + platform + wind turbine models
  ○ Time-dependent turbine thrust and torque loads
  ○ Time-dependent, finite element solver for mooring lines
  ○ Time-dependent, convolution integral calculation of platform response
  ○ Platform hydrodynamics based on external linear potential flow solver
• Charm3D GUI is available for model development
  ○ Text files have to be hand edited for use in coupled environment
• Charm3D system includes WAMIT so hydrodynamic/hydrostatic coefficients can be calculated in Charm3D and saved for coupled system
	• The Graphical Human Interface (GUI) of Charm3D cannot be used in the coupled system. All input is in the form of text files:
	  ○ Charm3d: "charm3d.in," "charm3d.wv"
	  ○ "fast.fst", "xx.wnd" for FAST (same files for standalone FAST)
	  ○ Animation is not available in Charm3D+FAST
	• Environmental conditions are defined by "charm3d.wv" input file
	  ○ Contains hydrodynamic database, geometry and environmental data
	  ○ Large "charm3d.wv" file must be rebuilt for every wave condition
	• Significant convergence problems simulating 1/8-scale VolturnUS system because of long mooring line lengths on the sea-floor
	• Difficult to import measured wave data
	  ○ Wave data must be trimmed
	  ○ Wave spectrum created from data using WAVE SPECTRUM (FFT) program
	• Documentation and Support
	  ○ There appears to be no Charm3D+FAST manual (have to study example files)
	  ○ Developer who provided the software system was not familiar with Charm3D+FAST

7.3 Conclusions: Measured Field Data

The project team found that good knowledge of the local environment is essential even for preliminary, high level design, much less detailed design. Simulation results were extremely sensitive to sea-states and to the relative headings between storm directions and the mooring system. A small change in wind, wave or current directions can have a profound effect on the mooring line tension predictions, and especially on the statistical fatigue life predictions for mooring systems. This sensitivity means that changes in the random number seeds that determine starting wind gust and wave component heights and phases can result in large differences in simulation results.

To expect accurate results, the design engineer should consider:

- Wave + wind probability (cross-correlation) distributions
- Wave + wind relative heading probability distributions
- Detailed information on current speed, heading, variability, and gradient in water column

- Tide-driven water depth variations

Unfortunately additional information may play a large role in determining the life expectancy of a FOWT installation. Anchor tensions may depend on exact bathymetry of the site, taking into account specific rocks near the touchdown point. It may be that wind, wave and current conditions are well understood and documented, but that the correlation between the data is not known. In general this may not be a problem, but it certainly is for extreme event simulation.

To study the behavior of deployed FOWT systems, it is critical to get good environmental, motion and mooring data. As this project team learned that task is made difficult because:

- If data exists, unlikely that data has been reviewed and converted for use by outside researchers. Different data sources may have incompatible formats, sampling rates, data drop conventions, and so on. The data must be aligned and packaged in a single, seamless package for use by researchers.
- It is difficult to collect real-time data on forces, moments, and motions from FOWT systems. The environment is somewhat hostile and such a system is a long way from repair staff. Accordingly any data acquisition system has to be complete (measure more, not less), and reliable. To the extent that data collection is considered important, key sensors should be redundant.
- The primary motivation of the developer is to show that their FOWT system can generate an economic return, not to collect data for research. Nonetheless it is critical for this industry that developers have an incentive to collect data so that we can understand how these complex systems behave. Funds should be allocated by the developer or supporters to support data collection.

7.3.1 Input Data for VolturnUS Case Study

The VolturnUS 1/8-scale system was designed to provide useful information on the behavior of the turbine, tower, platform and mooring system. Unlike the other components, the driving force behind the mooring system design was that it should never fail, not that it would experience scaled loads or tension events. The mooring chains had a very large scope to protect the platform, cost prohibitive in a full size system. The mooring system is difficult to simulate because most of chain is on seafloor, not under tension. Further, the large-scope system was never exposed to snap loads, which limits its usefulness for extreme event fatigue analyses.

A complication in describing the environment for the VolturnUS 1/8-scale system is that this prototype was deployed in 65-feet of water at mean low tide. The model had a draft of about 8.2 feet so the depth under the model at low tide was about 56.8 feet. A typical tide range of 10-feet at that location means that the depth under the model varied by about 17.6% over a tide cycle. Instantaneous load measurements will be significantly affected by the change in depth. Data provided by the VolturnUS team indicate that downwind mooring lines were slack much of the time, but even so the suspended weight will change more than 17% simply due to the tide variation. It is important to consider the effect of tides when logging and reporting load information.

A great deal of effort went into scaling the VolturnUS 1/8-scale system so that the motion behavior would reflect the full size system. The platform and small turbine were scaled properly

for ideal wind and waves, but unfortunately component fatigue based on mooring loads, do not scale well.

After data is collected it has to be checked for validity (e.g., drop-outs, calibration drift and so on) and it has to be packaged in a form that is useable by outsider researchers. That task is extremely time-consuming, so the VolturnUS team only was able to supply this project team with three one-hour snapshots of VolturnUS motion and mooring data out of a year of deployment. Statistical fatigue analysis depends on long-term data, so the project team simulated the FOWT system motion to demonstrate the fatigue analysis process in Section 6.3.3.1. In the future, this project team recommends that the full complement of VolturnUS data be studied to examine fidelity of software tools in predicting fatigue lifetime.

7.4 Conclusions: Abrasion and Corrosion

The project team investigated the mechanisms of corrosion and abrasion from both a material science perspective and a system level perspective. A single mooring system exists in multiple environments starting with the seafloor, traversing the water column, and often ending in the splash zone near the FOWT fairlead. Abrasion with the seafloor could be the dominant material loss mechanism for mooring components in the chafe zone on the seafloor. Corrosion (rust) or metal-to-metal abrasion may be the dominant mechanisms for components in the splash zone near the fairlead. From the literature and from our observations regarding the USCG ATON case study, other mechanisms such as classical metal fatigue and microbiologically induced corrosion (MIC) can play major roles in the lifetime of a mooring system component in the water column, and these mechanisms could dominate the wear for mooring system components.

In the USCG ATON buoy case study the material loss due to abrasion dramatically exceeded classification society rules. That loss was concentrated at the chafe zone where buoy motions result in chain/substrate interactions over a portion of the chain. Elsewhere, material loss was found to be consistent with corrosion models. The project team concluded that industry-standard ways of predicting the material loss in mooring components and of predicting the lifetime of mooring systems are overly simplified and inaccurate. By recognizing that there are different failure mechanisms factors affecting different portions of a mooring system the designer can make a much more accurate prediction as to the mooring life.

During this project, a dynamic, energy-based method was shown to be able to predict chafe-zone abrasion in chain-based catenary mooring systems (refer to Section 6.2.4.10). The method is shown to be effective for steel chain mooring lines deployed at a site with a sandy seafloor. It may be that the method is also effective in sites with mud, rock or shell seafloors, but more research is required.

Consistent with reports in literature of extreme material loss due to abrasion, corrosion, microbial influenced corrosion, linear regression models that relate the presence of certain chemical and biological contaminants to material loss in mooring chains were shown to apply to the ATON buoy mooring systems. With additional data and a more comprehensive data regression effort, regression-based models could be used to predict mooring component material loss in the water column with reasonable accuracy.

The project team recommends that the operational lifetime of a mooring system should be calculated by breaking the system down into regions, estimating the life of each region, and combining the results (refer to Table 55).

Table 55 Predicting mooring lifetime based on dominant wear mechanisms

Region	Wear Mechanism
Mooring line at anchor	If uplift and seafloor dragging forces expected, use energy abrasion model.
Idle line on seafloor	Estimate corrosion based on hydrology (temperature/current/chemical/biological mechanisms) and existing literature prediction models
Line in chafe zone (touchdown region)	Energy abrasion model.
Line in water column	Estimate corrosion based on hydrology (temperature/current/chemical/biological mechanisms) Estimate chain link abrasion from models in the literature
Line in splash zone	Corrosion based on temperature, oxygen content Estimate chain link abrasion from models in the literature
Line at fairlead	Statistical metal fatigue analysis based on expected tension cycles Estimate chain link abrasion from models in the literature

Without additional research that could show coupling between wear mechanisms, the designer should assume that the region of the mooring system with the shortest lifetime will determine the life of the entire system. More work is required so that this design methodology is robust enough to be codified in classification rules.

The design methodology should consider all regions of the mooring system, and should address each region with the most appropriate software tool or technology. More work is required to calibrate and validated the following methods of corrosion and abrasion prediction:

- Pure corrosion models exist in the literature (see reference section of this report)
    - Typically regression models that predict mooring component material loss using site hydrology data (especially if the regression data set can be expanded and improved). These models need to be enhanced with models that recognize the chemical and biological environment on the seabed itself.
- Chain link abrasion models exist in the literature
    - By taking into account the metal type, tension levels and total rubbing energy it should be possible to predict interlink abrasion with reasonable accuracy.
- Seafloor abrasion from this report
    - This report shows that it is possible to predict abrasion at the touchdown point based on buoy and mooring topology. At present this is limited to sites with sandy bottoms, but it can be expanded to include other bottom types.
- Nominal corrosion allowances from classification rules
    - Nominal corrosion allowances should be revised based on existing and future literature to more accurately predict damage from corrosion and abrasion.

Existing allowances are overly simplified and possibly excessively low depending on the site environment.

Additional research and predictive tools are required in order to have confidence in calculations that predict lower corrosion/abrasion rates than do classification rules. The project team recommends that the designer should use the larger of (1) predicted local corrosion and abrasion from the technologies described above, or (2) classification rules for design purposes.

7.5 Conclusions: Classification Society Design Rules

The society rules considered in this report include API (API-RP-2SK), DNV (DNV-OS-E301, DNV-OS-E302, DNV-OS-E304, and DNV-OSS-101), and ABS (ABS FOWT Guide, ABS FPI Rules, ABS Publications 82 and 104). Methodologies from these industry standards were followed during simulation and fatigue calculations. For general fatigue calculation of mooring systems, all of the society rules advise the use of damage calculation in accordance with Miner's Rule. Relevant T-N and S-N curves are available and were used for the present work for damage calculation.

Society rules recommend that material degradation through corrosion and abrasion be taken into account when considering mooring fatigue. Nominal corrosion and abrasion rates are presented in the society rules and are summarized in Table 1 of this report. As has been discussed here and in the literature, these nominal corrosion rates are, in many cases, non-conservative. This can be detrimental and dangerous.

However for FOWTs, it is also important that nominal corrosion rates not be too conservative. FOWTs are typically lighter weight than other offshore floating systems, and moored in shallower water. If the mooring system is overdesigned due to onerous corrosion requirements, the financial impact will be disproportionately larger than it would be for larger, deeper systems.

Therefore a conclusion of this report is that more accurate prediction tools for corrosion and abrasion degradation are required in the offshore industry in general, and especially for light-weight, shallow-depth FOWT systems. This must be reflected in future classification society rules.

7.5.1 American Bureau of Shipping (ABS)

The primary ABS guidelines for FOWT mooring fatigue include the ABS FOWT Guide and the ABS FPI Rules. Fatigue analysis methodologies for position mooring systems are discussed in the ABS FPI Rules, section 6-1-1/3.7. Fatigue is to be calculated following Miner's Rule for damage accumulation, and methodology is to be in accordance with API-RP-2SK. Similarly, ABS FOWT Guide section 8-3/3 specifies that corrosion and abrasion allowances are to be in accordance with API-RP-2SK.

Fatigue design margins are specified in the ABS FOWT Guide, section 8-3/5 for both redundant and non-redundant systems. Design margins are further refined based on whether the system is inspectable and repairable.

Design load cases for fatigue are specified in the ABS FOWT Guide sections 8-2/3.1 and 5-2/3. Operating conditions DLCs 1.2 and 6.4 were used for fatigue calculations in all of the case studies examined in this report. Other DLC fatigue fault, temporary, and parked/startup conditions include DLC 2.4, 3.1, 4.1, 7.2, and 8.3.

For fatigue calculation, these DLC conditions represent a large percentage of the likely expected operating conditions. However there is no recommendation to include any wind conditions or sea states with return period beyond one year. As was found in this report, extreme environmental conditions can play a disproportionate role in traditional fatigue calculation, even when their high return periods are accounted for. Consideration of these extreme events blurs the line between fatigue damage calculation and analysis of mooring storm/extreme event survival. A possible solution would be to consider events with a return period up to the design lifetime of the mooring system.

ABS Publications 82 and 104 describe low cycle-high stress fatigue analyses of FPSO structural components, and use an S-N rather than T-N approach. This approach suggests extending the S-N curve to the low cycle range for welded joints of an FPSO. A similar procedure is recommended for incorporating snap loading of mooring lines, however several parameters needed to conduct such analyses are missing from current sources of knowledge.

References

American Bureau of Shipping, 2014. Rules for Building and Classing Floating Production Installations.

American Bureau of Shipping, 2013. Guide for Building and Classing Floating Offshore Wind Turbine Installations.

ABS Guide for building and classing Floating Production Installations, Publication 82, 2010.

ABS, Guide for spectral-based fatigue analysis for floating production, storage and offloading (FPSO) installations, Publication 104, 2010.

7.5.2 American Petroleum Institute (API)

Fatigue analysis of mooring systems is considered in API RP-2SK Section 6, with example calculations included in Appendix J. API fatigue calculation methodology was followed in each of the Kyushu, DeepCwind, and VolturnUS case studies, and is discussed in those sections.

API recommends fatigue analysis in accordance with Miner's Rule for damage accumulation, based on relevant T-N curve parameters presented in Table 3 and 4, and Figure 13 of API RP-2SK. Consideration of low-frequency fatigue damage may be incorporated in several ways, including (1) summation of low and high-frequency components, (2) spectral fatigue calculation of a combined low and high-frequency spectrum, and (3) time domain cycle counting. In the case studies presented in this report, the third option was implemented as it represents the most accurate method.

Corrosion and abrasion allowances are given (see Table 1 of this report) in section 7.6 of API RP-2SK. In general, the values presented in this section are consistent with what is reported in other design standards. For fatigue calculation, API recommends accounting for expected corrosion loss at each period considered. Broad guidance is provided on expected corrosion trends, but is not sufficient to make calculations of anticipated corrosion loss for a specific site.

References

American Petroleum Institute, 2005. Design and Analysis of Stationkeeping Systems for Floating Structures: Recommended Practice 2SK, 3rd Edition.

7.5.3 Det Norske Veritas (DNV)

DNV's operating standard for position mooring systems is DNV-OS-E301. Operating standards OS-E302, OS-E303, and OS-E304 provide specifications for chain, fiber rope, and wire rope systems, respectively. As specified in DNV-OS-E301, fatigue calculation follows a stress-based approach (i.e. use of S-N curves is prescribed), in accordance with Miner's Rule.

Nominal corrosion and abrasion tolerances are specified in DNV-OS-E301. Tolerances are summarized in Table 1. It is noteworthy that an allowance of 0.8 mm/yr. is recommended in the Norwegian continental shelf, which is higher than other tolerances from the society rules reviewed in the present report. A corrosion accumulation of 50% of the expected lifetime amount is recommended. It was observed in this report that under certain conditions, this can predict a damage calculation lower than if annual diameter is change is considered.

Guidelines for monitoring and replacement of chains due to excessive corrosion and abrasion are found in DNV-OSS-101. For mooring chains, a loss of 10% of diameter due to corrosion/abrasion necessitates replacement of chain links. For fiber rope, it is required that no contact between rope and seafloor occur, to minimize abrasive damage. Similarly, wire rope must be protected from corrosion (DNV-OS-E304).

Recommendations for snap loads on crane wires during lifting and lowering operations are made in DNV RP-H103. Criteria are set for the allowable percentage of dynamic loads in relation to static (pre-tension) loads to avoid slack conditions of a wire. A similar criterion is derived and used for snap loading on mooring lines. Formulae for snap loads as given in DNV RP-H103 are not directly applicable and no similar approaches could be adopted.

References

Det Norske Veritas, 2008. Offshore Standard DNV-OS-E302: Offshore Mooring Chain.

Det Norske Veritas, 2009. Offshore Standard DNV-OS-E304: Offshore Mooring Steel Wire Ropes.

Det Norske Veritas, 2010. Offshore Standard DNV-OS-E301: Position Mooring.

Det Norske Veritas, 2012. Offshore Service Specification DNV-OSS-101: Rules for Classification of Offshore Drilling and Support Units.

Det Norske Veritas, 2013. Offshore Standard DNV-OS-E303: Offshore Fibre Ropes.

Det Norske Veritas, 2011, Recommended Practice DNV RP-H103: Modelling and analysis of marine operations.

8 Recommendations

8.1 Recommendations for Improving Guidelines and Current Practice

Snap Loads: FOWT mooring systems by their very nature of light pre-tension in shallow water have a higher susceptibility to snap loads. DNV RP-H103 recommends that snap loads should be avoided for all crane wires during marine operations. A good design practice would be to avoid snap loads for FOWT mooring lines, but such a requirement may be impractical for a variety of reasons, including permitting requirements that may force a designer to use a smaller mooring circle thus potentially exposing the system to snap conditions.

The recommendation of the research team is to incorporate snap load induced fatigue by a low cycle high stress fatigue analysis approach similar to that recommended by ABS Publication 104 for fatigue analysis of FPSO structural components, and use an S-N rather than T-N approach. The approach requires extending the SN curve to the low cycle range, such as an example shown below for welded joints of an FPSO. Snap load, by its very nature of being a shock load, has the potential to induce plastic deformation to a mooring line. This can occur when the stress induced by such a shock exceeds the yield stress of a mooring chain link, or in the case of a rope, some vulnerable strand. In order to obtain a similar curve as shown in the figure for mooring lines, more research is needed on plastic corrections due to snap.

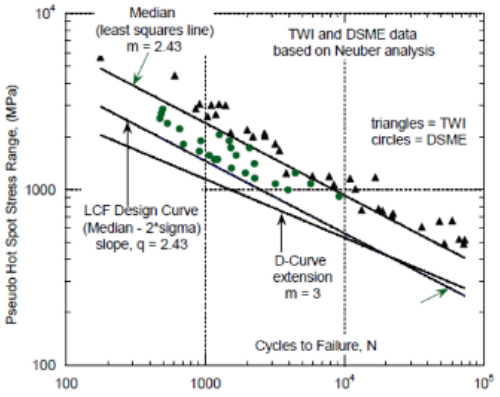

S-N Curve Based on Test Data

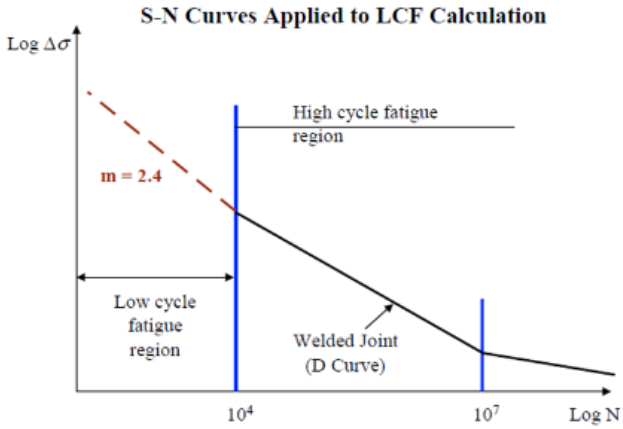

Material	N<10^4	
	Log a	m
Welded Joint	12.18	2.4

Figure 153: Modified SN curve for welded joints of an FPSO that are subjected to low cycle fatigue from loading and unloading of cargo. Original figures from ABS Pub 82, modified and presented by Basu (2014).

The recommended procedure as summarized by the flow chart in Figure 154 is to examine a mooring line time history for the following snap conditions:

$T_i \leq 0.9\,T_0$

$T_j > 0.9\,T_0$

Here *i* and *j* correspond to time instants which are no more than one-half period apart (mean or peak). Such snap episodes are grouped together and examined in a process similar to low cycle high stress fatigue (ABS Pub. 104).

The total fatigue damage due to both low cycle and high cycle (wave-induced) stress can be calculated by :

$$\mathrm{DM}_{comb} = \frac{\mathrm{DM}_{LCF}^2 + 2\delta \mathrm{DM}_{LCF}\mathrm{DM}_{HCF} + \mathrm{DN}_{HCF}^2}{\sqrt{\mathrm{DM}_{LCF}^2 + \mathrm{DM}_{HCF}^2}} \quad (32)$$

where

δ = long term stress scale factor

DM_{LCF} = low cycle fatigue damage

DM_{HCF} = wave induced high cycle fatigue damage

δ can be determined from long term statistical distributions of stress ranges. ABS Pub 104 recommends a value of 0.02 for welded joints.

Following API RP 2SK, the tension ranges to be used in fatigue analysis require a safety factor of 3.0. The corresponding factor of safety to be used for snap loading also requires further research.

Abrasion and Corrosion: Figure 155 shows the flow chart for fatigue calculation including abrasion and corrosion. Corrosion and abrasion degradation will decrease the diameter of the chain link each year of service life, which means S-N parameters (which depend on bar diameter) must be a function of service life, and annual fatigue damage will not be constant.

For a single year Miner's Equation for fatigue damage calculation takes the form:

$$D = \sum_{\substack{annual\\ rainflow\\ cycles}} \frac{1}{N} = \sum_{\substack{annual\\ rainflow\\ cycles}} K s^M \quad (33)$$

Where *N* is the number of cycles to failure, *s* is the chain stress level, and *K* and *M* are S-N curve parameters. If corrosion and abrasion are taken into consideration, then *K*, *M*, and *s* may be assumed to be time-dependent.

$$D = \sum_{i=1}^{L} D_i = \sum_{i=1}^{L} \left(\sum_{\substack{annual\\ rainflow\\ cycles}} K(i) s(i)^{M(i)} \right) \quad (34)$$

Here D is the lifetime damage calculation, and D_i is the annual damage. Estimation of corrosion and abrasion is difficult, as there is no industry-accepted protocol that is robust and dependent on local site conditions. This report has examined two primary mechanisms of abrasion:

1. Abrasion that occurs between chain links
2. Abrasion caused by seafloor motion.

Few approaches exist in the literature for predicting interlink abrasion. The project team chose to use Archard's Equation which describes abrasion as a function of chain link tension and motion between chain links. Tension and motion can be determined from simulated behavior of the FOWT system.

There is similarly very little discussion in the literature on seafloor abrasion. It is likely that this type of abrasion is not always a significant factor, dependent on the likelihood of chain dragging on the seafloor. If seafloor abrasion is likely to occur, a method for predicting such abrasion has been suggested in this report.

Corrosion is dependent on environmental conditions of the site and less so on motions and loads. Corrosion can be predicted by considering the chemical and biological environment at the site including both the water column and the seafloor. Some simple empirical predictive models for corrosion exist in the literature. This project has shown that regression models can be an effective way to predict corrosion using environmental characteristics.

Corrosion and abrasion must be considered at each section of the mooring line (fairlead, splash zone, suspended region, touchdown region, laid region), as the mechanisms that drive material loss vary among those regions.

From predictive models, corrosion and abrasion may be estimated for a given site. However, because of the simplistic nature and high uncertainties in current models, nominal corrosion/abrasion allowances in classification society rules must also be considered. When predictive models produce lower corrosion rates than classification society rules, it is recommended that nominal allowances be used as a conservative approach. Applicable safety factors must be taken into account as well for fatigue damage calculations.

A suggested procedure for including corrosion and abrasion effects in component life predictions is shown in Figure 155.

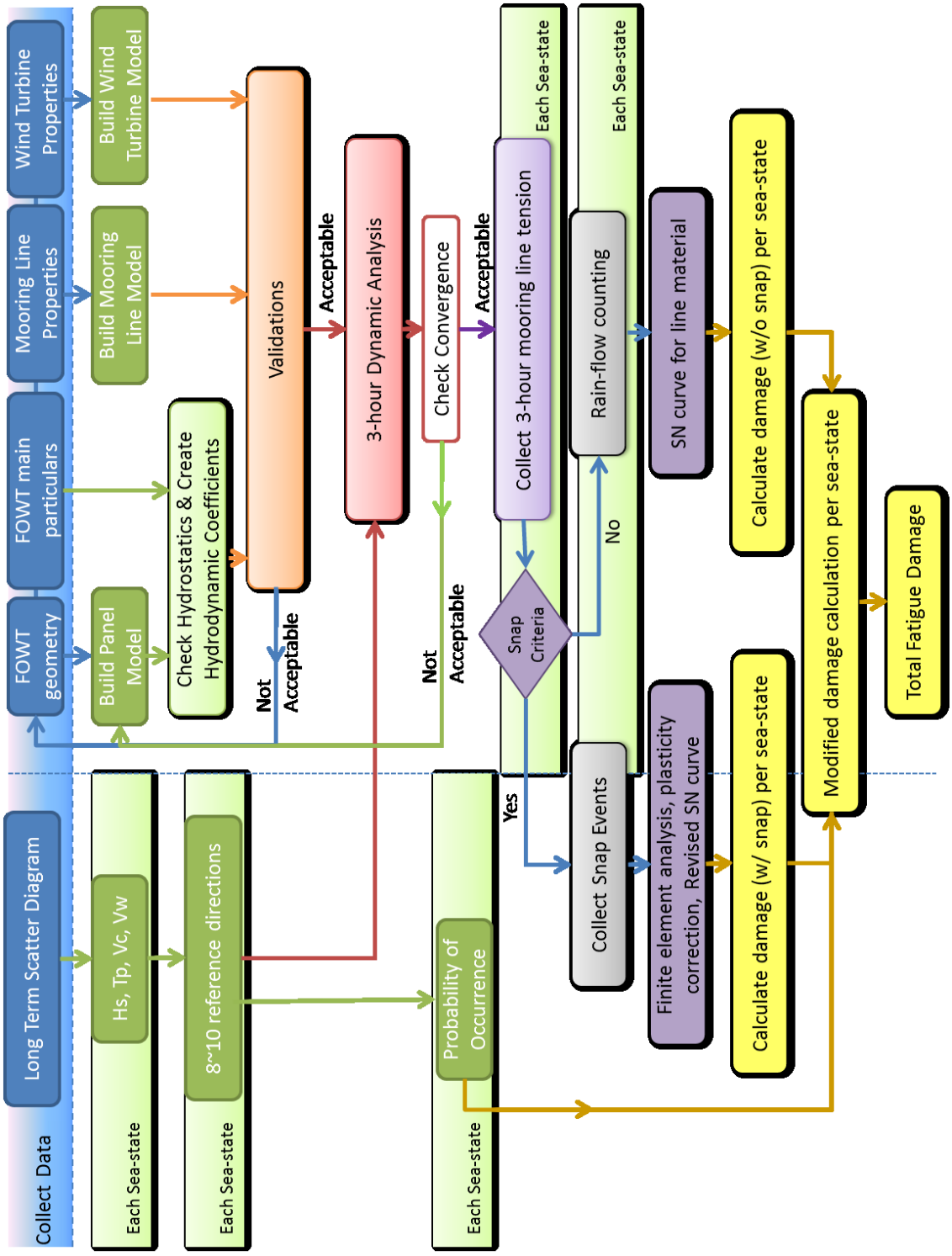

Figure 154: Flow chart of fatigue analysis with snap events.

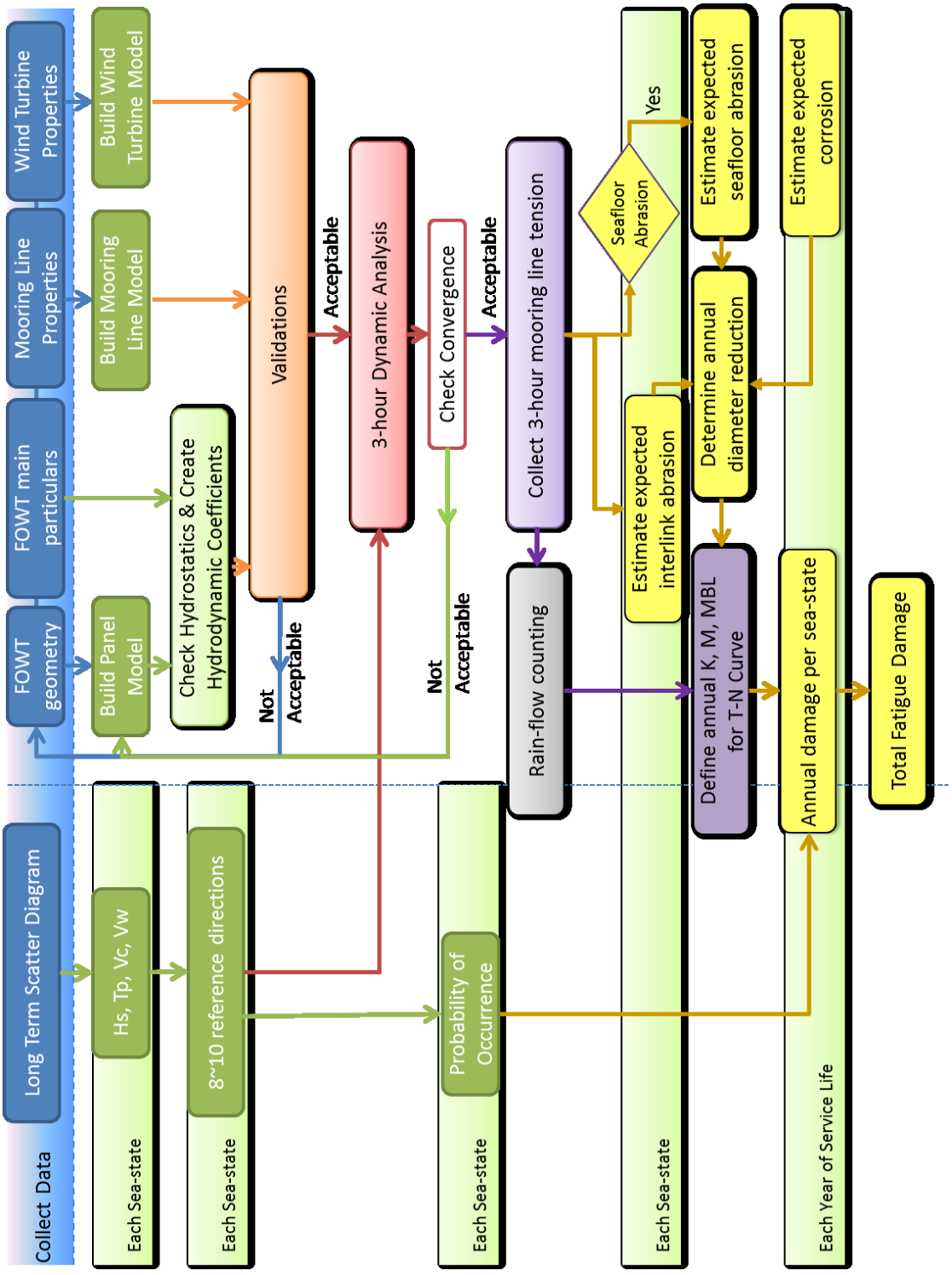

Figure 155: Flow chart of fatigue analysis with corrosion and abrasion

8.2 Recommendations for Future Research

As shown by results and conclusions from the case studies in this project, the ability to predict snap loads, abrasion and corrosion in FOWT mooring systems shows great promise with respect

to predicting failures in such systems. A number of topics and issues considered in this project require additional research and development. A short summary of topics mentioned in this report follows.

8.2.1 Statistical Fatigue Analysis Research Topics

- Do storm events have disproportionally high effect on calculated fatigue damage? Is this adequately accounted for in design standards?
- Compare the simulation error in RMS/Significant tensions to the simulation error in Miner damage calculation. Is the error amplified? Should safety factors be adjusted accordingly?

8.2.2 Snap Load Research Topics

- What is the definition or criteria for defining snap loads for FOWT mooring systems? Is there a way to predict the probability of snap loads on FOWT mooring systems?
- What are the causes and effects of snap loads in FOWT mooring systems? What are the dynamics of mooring lines including distributed loads during extreme non-linear tension events.
- Does a snap load cause excessive damage to a component or damage that is different than traditional fatigue damage? If so what are the mechanisms? How do those mechanisms vary from metal to metal and from metal to synthetic material?
- How much damage occurs during snap events and is it significant with respect to the system life? If so, does a modified safety factor neededfor mooring system design when the snap loads are considered?
- How do snap loads effect the lifetime prediction in Palmgren-Miner damage calculation and if so, why? What is the definition of the design S-N curve in the low cycle region where snap loads appear?

8.2.3 Corrosion and Abrasion Research Topics

- What are failure mechanisms for mooring components on the seafloor? What is the chemical and biological environment of the seafloor and how does that affect the total lifetime of that section of a mooring system?
- How important is oxidization in each regime of a mooring component? How can the damage be predicted?
- Does the loss of strength in a mooring component depend on the reduction in cross sectional area due to material loss from corrosion or abrasion? Do stress concentrations due to pitting result in more loss of strength than a uniform reduction around the circumference of the component?
- How do concentrations of chemicals such as nitrogen, phosphate, silicate and oxygen affect corrosion of mooring components? Is the corrosion temperature dependent? Is it dependent on the luminosity at the depth of the component?
- How does biologically induced corrosion affect the overall life of a mooring system component? Does it matter compared with conventional oxidation material loss? How can MIC be predicted and under what circumstances does it matter?

- How can the mechanical characteristics of the seafloor be defined so that seafloor abrasion can be predictable for all types of seafloors? What are the tribological mechanisms that cause material to be removed from chain or rope?

8.2.4 Building and Integrating FOWT Analysis Software

The project team struggled to use existing coupled software systems to simulate floating offshore wind turbines. These systems consist of commercial software coupled with government/academic software. There are issues of:

- Software ownership and responsibility
- Documentation, support and training
- Input / Output mechanisms. There is a cost to the industry in terms of data preparation and value of the results if I/O is via text files.
- Quality of the integration. Does it get the right answer? Under what conditions?
- Flexibility of the system. What features are lost from the individual tools when they are coupled?
- Data transfer between tools. Who is responsible for solving for platform motions? Who controls the time-step? Who writes the results or displays it through a user interface?

The existing integration between OrcaFlex and FAST was performed by a third party, Principle Power, because they needed a software solution. That integration is open source and not fully supported by any particular entity. The project team does not know who integrated Charm3D and FAST, although papers on the subject have been written by researchers at Texas A&M. It is likely that Ocean Dynamics is responsible for the integrated product.

NREL has developed a new version of FAST (version 8) that has advantages in terms of software architecture and flexibility in supporting new physics domain solvers. At the time of this report, Version 8 has not been integrated with Aqwa, Charm3D or OrcaFlex.

This project recommends that funds be allocated to support the commercial integration of this software with other tools. This integration should be performed by one or more entities that are end-user-oriented, not purely academic. Further, this project recommends that the combined system or systems be marketed and supported by a commercial entity funded at least in part by commercial end users. There should be a cost to the customer for the integrated solution as they have a vested interest in the quality of the results. As with other large software systems, it is expected that marketplace pressures would push the combined system to address the issues mentioned above.

8.2.5 Recommendations for Development of New Data Sources

By far the largest barrier to demonstrating the ability of software tools to predict fatigue and failure in mooring systems for FOWTs is that field data does not exist or is inaccessible. Accordingly it behooves the industry and government to create special projects to collect and distribute such data. The data must be comprehensive and accurate, and all of the appropriate environmental data must be collected to go along with the response data.

The challenge of using proprietary data for public research can be met in a number of ways. First, research can be performed on exemplar systems such as dummy FOWT platforms deployed and moored with anchoring systems that are similar to FOWT systems (e.g. catenary chain-based systems). This sort of experiment and data collection can be performed by

academic institutions with ocean engineering departments, and would benefit the FOWT industry and students from the academic institutions alike.

Second, research can be performed by research/commercial partnerships such as a commercial wind farm developer and a commercial or academic research partner. Of course the largest challenge in such a project is defining what information will be available from the wind installation, what can be done with the data, and what terms of privacy are required to maintain the confidential nature of the data.

Third, research can be performed by joint industry partnerships (JIPs), typically comprised of developers, designers, academic partners and regulatory partners. Although such partnerships usually include a public institution, often the data is still considered proprietary and is not released to the public. Accordingly the data may only benefit the JIP members. On the other hand, the conclusions will usually be made public, so the industry at large will benefit from this sort of work even if individual companies are not JIP members.

Finally, research can be performed by a government laboratory such as DoE NREL, possibly with industry partnerships. Such a governmental organization would be interested in promoting the FOWT industry as a whole, so it is more likely that important data would be made available to all members of the FOWT industry.

9 Acknowledgements

The project team is grateful to the U.S. Bureau of Safety and Environmental Enforcement (BSEE) for providing funding for this project under contract E13PC00019.

The project team wishes to acknowledge the contribution of the Advanced Structures & Composite Center (ASCC) of the University of Maine for providing data and support for our case studies of the 1/50-scale DeepCwind system and the 1/8-scale VolturnUS system. Support provided by H. Dagher, A. Viselli, A. Goupee and C. Allen are acknowledged.

The project team also wishes to acknowledge the support of Prof. Utsunomiya of Kyushu University, who answered technical questions in support of our case study about their spar buoy FOWT system.

Finally the project team wishes to acknowledge the support of the US Coast Guard, including the crew of the USCGC Abbie Burgess, the USCGC Willow, and the Boston Sector for providing maintenance records and samples of retired mooring chain from an ATON buoy.

10 References

(ABS), "Floating Wind Turbines," American Bureau of Shipping, Corporate Offshore Technology, Renewables, Houston, Texas. BSEE TA&R 669 (Contract M11PC00004), May 2012.

(ABS), Guide for Building and Classing Floating Offshore Wind Turbine Installations. American Bureau of Shipping, Houston, Texas, USA, 2013.

(ABS), Guide for building and classing Floating Production Installations, Publication 82, 2010.

(ABS), Guide for spectral-based fatigue analysis for floating production, storage and offloading (FPSO) installations, Publication 104, 2010.

Allan, S., et al. 2013. Mooring system life extension using subsea inspection technologies. Offshore Technology Conf. , OTC 24184. 2013.

_, American Petroleum Institute. Design and Analysis of Stationkeeping Systems for Floating Structures. Recommended Practice 2SK, Third Edition, October, 2005.

(Aqwa), *Aqwa Theory Manual*, ANSYS, Inc., Cannonsburg, PA, Release 15, November 2013.

Ayers, Ray R. and Aksu, Saltuk B., Test Results on the Effect of Cyclic Wear of Polyester Sub Ropes. Offshore Technology Conf., Rio de Janeiro, Brazil. 2011.

Ayers, R. R., Del Vecchio, C.J. Effects of fiber rope – seabed contact on subsequent rope integrity. Offshore Technology Conf., Houston, TX. 2013.

Banfield, S., et al, Fatigue Curves for Polyester Moorings - A State-of-the-Art Review, Offshore Engineering Conf., 12175, Offshore Technology Conf. 2000.

Bae, Y.H. and Kim, M.H. "Rotor-floater-mooring Coupled Dynamic analysis of Mono-Column-TLP-type FOWT (Floating Offshore Wind Turbine)." *Ocean Systems Engineering*, Vol. 1, No. 1 (2011) 95-111. 2011.

Bae, Y.H., Kim, M.H., Im, S.W. and Chang, I.H. "Aero-Elastic-Control-Floater-Mooring Coupled Dynamic Analysis of Floating Offshore Wind Turbines." *21st Int'l Offshore and Polar Engineering Conf.,* Maui, Hawaii, USA, 2011a.

Bae, Y.H., Kim, M.H., Yu, Q. and Kim, K. "Influence of Control Strategy to FOWT Hull Motions by Aero-Elastic-Control-Floater-Mooring Coupled Dynamic Analysis." *21st Int'l Offshore and Polar Engineering Conf.,* Maui, Hawaii, USA, 2011b.

Banfield, et al. Durability of polyester deepwater mooring rope. *Offshore Technology Conf*., Houston, Texas. 2005.

Basu, R. Fatigue in marine structures, Seminar notes, University of Maine, 2014.

Brown, M.G., Comley, A.P., Eriksen, M., Williams, I., Smedley, P., Bhattacharjee, S. Phase 2 Mooring Integrity JIP – Summary of Findings. Offshore Technology Conference, Houston, Texas, OTC 20613. 2010.

Brown, M.G. 10 years experience of North Sea FPSO moorings repair, renewal and life extension work. *SPE Offshore Europe Oil and Gas Conf. and Exhibition*, Aberdeen, UK, pp. 1-11. 2013.

Brown, R. R., Kohler, C.A. Corrosive-Wear of Buoy Chain. Report No. CG-D-17-88, U.S. Coast Guard Research and Development Center, Avery Point, Groton, CT. 1988.

(BSH), "Global Climatology and Atlantic Ocean Atlas," Bundesamt für Seeschifffahrt und Hydrographie, Germany [http://www.bsh.de/en/Marine_data/Observations/Climate/WOCE-AIMS/WGHC/, downloaded 29-June-2015].

Coulling, A.J., Goupee, A.J., Robertson, A.M., and Jonkman, J.M. Importance of second-order difference-frequency wave-diffraction forces in the validation of a FAST semi-submersible floating offshore wind turbine model. Proc. of the ASME 32nd Intl. Conf. on Ocean, Offshore and Arctic Engineering, OMAE2013-11072, Nantes, France. 2013.

DNV, Det Norske Veritas, Recommended Practice for Modelling and analysis of marine operations, 2011.

DNV, Det Norske Veritas. *Offshore Standard: Position Mooring*. Offshore Standard DNV-OS-E301. 2010.

DNV, Det Norske Veritas. *Modeling and Analysis of Marine Operations*. DNV-RP-H103. Hovik, Norway. 2011.

Duggal, A.S and Fontenot, W.L. Anchor Leg System Integrity – From Design through Service Life, Offshore Technology Conf., Houston, TX, pp. 1-15. 2010.

Faltinsen, O.M. *Sea loads on ships and offshore structures.* Cambridge University Press, Cambridge, UK, 1990.

Fletcher, S. L. et al. Material Innovation for Ultra-Deepwater Performance of Long Term Mooring Cables, OTC 20471, Offshore Technology Conf., Houston TX. 2010.

Fontaine, E., Armstrong, R., Potts, A., Melchers, R.E., Chaplin, C.R., Francois, M. Semi-empirical modeling of seawater corrosion of wire rope. Proc. of the 19th Intl. Offshore & Polar Engineering Conf., Osaka, Japan. 2009.

Fontaine, E., et al. Investigation of severe corrosion of mooring chain in West African waters. Proc. of 22nd Intl. Offshore and Polar Engineering Conf., Rhodes, Greece, pp. 389-394. 2012.

Flory, J., Banfield, S.J. Durability of polyester ropes used as deepwater mooring lines. *OCEANS IEEE*. 2006.

Gobat, J.I., Grosenbaugh, M.A.. Dynamics in the touchdown region of catenary moorings. Intl. Journal of Offshore and Polar Engineering, 11(4), pp. 273-281. 2001

Guedes Soares, C., Garbatov, Y., Zayed, A., Wang, G. Non-linear corrosion model for immersed steel plates accounting for environmental factors. Proc. of Society of Naval Architects and Marine Engineers (SNAME) Marine Technology Conference & Expo, Jersey City, NJ. 2005.

Halkyard, J. *Design and Analysis of Floating Structures, 3rd Edition*, Houston, Texas: John Halkyard & Associates. 2013.

Hall, A., Trower, A. Mooring system integrity: deteriorative mechanisms on mooring systems and appropriate inspection techniques. OTC 22615, Offshore Technology Conf., Rio de Janeiro, Brazil. 2011.

Heredia-Zavoni, E. Risk assessment for structural design criteria of FPSO systems. Part II: Consequence models and applications to determination of target reliabilities, Marine Structures, 28, pp. 50-66. 2012.

Hsu, W., Thiagarajan, K.P., MacNicoll, M., Akers, R. Prediction of Extreme Tensions in Mooring Lines of a Floating Offshore Wind Turbine in a 100-Year Storm. Proc. of the ASME 34th Intl. Conf. on Ocean Offshore and Arctic Engineering, OMAE2015-42015, St. John's, Newfoundland, Canada. 2015.

Kiecke, A., Zhang, J. Estimate of Mooring Line Damage Accrued by a GOM Truss Spar Based on Field Measurements. Proc. of the 21st Intl. Soc. of Offshore and Polar Engineers (ISOPE), Maui, HI. 2011.

Kimball, R., Goupee, A., Coulling, A., Dagher, H., 2012, Model Test Comparisons of TLP, Spar-buoy and Semi-submersible Floating Offshore Wind Turbine Systems, *Proc. SNAME Annual Meeting.* 2012.

Kobayashi, J., Takeshi, Y., Yoshida, K. Corrosion fatigue of heavy-duty coated and cathodically protected steel for TLP tendons. OTC 5614, Offshore Technology Conf., Houston, TX. 1987.

Koo, B., Lambrakos, K., Goupee, A., Kimball, R. Model Tests for a Floating Wind Turbine on Three Different Floaters, Proc. 31st Int. Conf. Ocean Offshore Arctic Eng, OMAE 2012, Paper 83642, Rio de Janeiro. 2012.

Little, B. J., Lee, J. S. *Microbiologically Influenced Corrosion*. Vol 3 of Wiley Series in Corrosion. ISBN 0470112441, 9780470112441, John Wiley & Sons, 2007.

Liu. F. C. Snap Loads and Bending Fatigue in Diving Bell Handling Systems, Offshore Technology Conf., Houston, TX. 1981.

Ma, K., et al. A historical review on integrity issues of permanent mooring systems. Offshore Technology Conf. OTC 24025. 2013.

(MARIN), Maritime Research Institute Netherlands. DEEPCWIND Floating Wind Turbine Model Tests Final Text Report. 2011.

Markussen, B.H., et al. Wear of nylon hawsers on rollers, pulleys, and fairleads. OTC 4765. Offshore Technology Conf., Houston, TX. 1984.

Martin, H. R. Development of a Scale Model Wind Turbine for Testing of Offshore Floating Wind Turbine Systems. Thesis, B.S. Civil and Environmental Engineering, Univ. of Maine, Orono 2011.

Martin, H., Kimball, R., Viselli, A., Goupee, A. Methodology for Wind/Wave Basin Testing of Floating Offshore Wind Turbines, *Proc. 31st Int. Conf. Ocean Offshore Arctic Eng*, OMAE 2012, Paper 83627, Rio de Janeiro. 2012.

Masciola. M. et al. Assessment of the Importance of Mooring Dynamics on the Global Response of the DeepCwind Floating Semisubmersible Offshore Wind Turbine, Intl. Offshore and Polar Engineering Conf., Anchorage, AK. 2013.

Masciola, M., Robertson, A., Jonkman, J., Driscoll, F. Investigation of a FAST-OrcaFlex Coupling Module for Integrating Turbine and Mooring Dynamics of Offshore Floating Wind Turbines. *Intl. Conf. on Offshore Wind Energy & Ocean Energy*, Beijing, China, NREL/CP-5000-52896. 2011.

Matsuishi, M. and Endo, T. Fatigue of Metals Subjected to Varying Stress. Proc. of the Kyushu Branch of Japan Society of Mechanics Engineering, Fukuoka, Japan, pp. 37-40. 1968.

Melchers, R.E. The effect of corrosion on the structural reliability of steel offshore structures. *Corrosion Science*, vol. 47, pp. 2391-2410. 2005.

Melchers, R.E., Wells. T. Models for the anaerobic phases of marine immersion corrosion. *Corrosion Science*, vol. 48, pp. 1791-1811. 2006.

Melchers, R.E., Moan, T., Gao, Z. Corrosion of working chains continuously immersed in seawater. J. Mar. Sci. Technol. vol. 12, pp. 102-110. 2007.

Melchers, R.E. Corrosion wastage in aged structures. In Paik, J.K. & Melchers, R.E. (ed), *Condition assessment of aged structures*. 2008.

Morandini. et al. Consistent Integrity of Mooring System, Proc. of 19th (2009) Intl. Offshore and Polar Engineering Conf., Osaka, Japan. 2009.

(NERACOOS) Northeastern Regional Association of Coastal and Ocean Observing Systems, "Graphing and Download." URL: http://www.neracoos.org/datatools/historical/graphing_download. Retrieved August, 2015.

Niedzwecki, J.M. and Thampi, S.K. Snap Loading of Marine Cable Systems, Applied Ocean Research, 13(1), pp. 2-11. 1991.

(Orcina LTD). OrcaFlex User Manual Version 9.7a. Daltongate, Cumbria, LA12 7AJ, UK. 2013.

Otten, J.D., Leite, S. Thunder Hawk mooring rope particle ingress, break, and fatigue testing. *Offshore Technology Conf*., Houston, Texas. OTC 24080. 2013.

Paik, J.K., Kim, S.K., Lee, S.K. Probabilistic corrosion rate estimation model for longitudinal strength members of bulk carriers. Ocean Engng, vol. 25 (10), pp. 837-860. 1998.

Paik, J.K., Melchers, R.E. (ed) *Condition assessment of aged structures*, Cambridge, England: Woodhead Publishing Limited. 2008.

Potts, A.E., et al. Factors influencing the endurance of steel wire ropes for mooring offshore systems. OTC 5718, Offshore Technology Conf., Houston, TX. 1988.

Qin, S., Cui, W. Effect of corrosion models on the time-dependent reliability of steel plated elements. Marine Structures, vol. 16, pp. 15-34. 2003.

Ridge, I.M.L., Chaplin, C.R., Zheng, J. Effect of degradation and impaired quality on wire rope bending over sheave fatigue endurance. Engineering Failure Analysis, 8, pp. 173-187. 2001.

Salancy, A. M., et al. Offshore Single Point Mooring Systems For Import of Hazardous Liquid Cargoes Offshore Southern California, Intl. Offshore and Polar Engineering Conf., Honolulu, HI. 1997.

Seo, M. et al. Wear and fatigue of nylon and polyester mooring lines. Textile Res. J. 67 (7), pp. 467-480. 1997.

Shah, A. A., et al. A methodology for assessing the reliability of taut and slack mooring systems against instability, Ocean Eng. 32, pp. 1216-1234. 2005.

Shoup, G.J., Mueller, R.A. Failure analysis of a calm buoy anchor chain system. Offshore Technology Conference, Houston, Texas, OTC 4764, pp. 451-456. 1984.

Stiff, John J., et al. Fatigue of Mooring Chain in Air and Water - Results and Analysis. OTC 8147, Offshore Technology Conf., Houston, TX. 1996.

Takayama, T., Tokubuchi, K. Economical Design of Elastic Chain for Mooring Through the Numerical Simulation. Proceedings of the Twelfth International Offshore and Polar Engineering Conference, Kitakyushu, Japan. 2002.

Tokubuchi, K. and Takayama, T. "Economical Design Procedures of Buoy Mooring System Considering the Effect of Elastic Chain on Impulsive Tension," *Proc. of Civil Engineering in the Ocean*. Vol. 21 (2005) P 1107-1112, released 2011.

Uhlig, H.H., Revie, R.W. Corrosion and Corrosion Control: An Introduction to Corrosion Science and Engineering, 3rd Edition. John Wiley & Sons, New York. 1985.

(USCG) CH-7 TO AIDS TO NAVIGATION MANUAL – TECHNICAL, COMDTINST M16500.3A, Apr. 6, 2010.

(USHarbors). Castine Tides - Sep/2015. (n.d.), http://me.usharbors.com/monthly-tides/Maine-Midcoast/Castine/. Retrieved August, 2015.

Utsunomiya, T., Matsukuma, H., Minoura, S., Ko, K., Hamamura, H., Kobayashi, O., Sato, I., Nomoto, Y., Yasui, K. On Sea Experiment of a Hybrid Spar for Floating Offshore Wind Turbine Using 1/10 Scale Model. Proc. of ASME 29th Intl. Conf. on Ocean, Offshore and Arctic Engineering, Shanghai, China, OMAE2010-20730. 2010.

Utsunomiya, T., Yoshida, S., Ookuba, H., Sato, I., Ishida, S. Dynamic Analysis of a Floating Offshore Wind Turbine under Extreme Environmental Conditions. Proc. ASME 31st Conf. on Ocean, Offshore & Arctic Engineering, Rio de Janeiro, Brazil, OMAE2012-83985. 2012.

Utsunomiya, T., Sato, I., Yoshida, S., Ookubo, H., Ishida, S. Dynamic Response Analysis of a Floating Offshore Wind Turbine Durign Severe Typhoon Event. Proc. ASME 32nd Intl. Conf. on Ocean, Offshore & Arctic Engineering, Nantes, France, OMAE2013-10618. 2013.

Utsunomiya, T., Yoshida, S., Kiyoki, S., Sato, I., Ishida, S. Dynamic Response of a Spar-Type Floating Wind Turbine at Power Generation. Proc. ASME 33rd Conf. on Ocean, Offshore & Arctic Engineering, San Francisco, California, OMAE2014-24693. 2014.

Vlasblom, M.P., Bosman, M.R.L. Predicting the creep lifetime of HMPE mooring rope applications. OCEANS 2006 IEEE. 2006.

(WAFO-Group). WAFO – a MATLAB toolbox for analysis of random waves and loads: tutorial for WAFO version 2.5. Sweden: Center for Math. Sci., Lund Univ. Lund: 2011.

(WAMIT). *WAMIT user manual*, WAMIT, Inc., 2013.

(WOCE), "Ocean Circulation and Climate: World Ocean Circulation Experiment," WOCE International Project Office, Report No. 154/97, August 1997 [http://www.nodc.noaa.gov/woce/wdiu/wocedocs/brochure97.pdf, downloaded 19-June-2015].

Yaghin, A.L., Melchers, R.E. Wear of Axially Loaded Chains in Dry and Wet Conditions. Proc. of the 25th International Ocean and Polar Engineering Conference (ISOPE), Kona, HI. 2015.

APPENDIX 1. USCG ATON Buoy Data

Table 56 USCG ATON Buoys: Principle Characteristics

	Name	Location		USCG ATON Buoy		Chain Type / Length	Nearest Metocean Buoy	
		Lat (˚N)	Lon (˚W)	ATON Type	Hull Type		Dist. (km)	ID
Northern New England	3-fathom ledge	43.90	68.70	RW "EI" Mo (A)	8x26	225' all 1.5" often mudded in	28.58	F01
	Wooden Ball Island	43.84	68.83	R "10"	8x26	350' all 1.5"	26.63	F01
	PenBay East LWB "PBA"	43.93	68.66	RW "O!" Mo (A)	8x26	180' all 1.5" - not sure of '05 replacement	29.58	F01
	Manana Island LWB 14M	43.76	67.37	R "2"	9x35	85' 1.62", 90' 1.5", 90' 1.62"	50.21	M01
	Boston Lighted Buoy B	42.38	70.78	R "2"	9x35	180' all 1.5"	11.19	44013
	Portland LWB P	43.53	70.09	R "2"	9x35	170' all 1.5	4.03	44007
	Boon Island Ledge LWB 22A	43.41	70.41	R "2"	8x26	180' all 1.5"	25.55	44007
	Buzzards Bay Mid Channel LBB	41.51	70.83	RW "BS" Mo (A)	8x26	180' of 1.5" - one measurement	20.67	BUZM3
	Sakonnet River LWB SR	41.43	71.22	G "1"	8x26	180' total, 1.5" chafe	16.19	BUZM3
	Marshall Point	43.92	69.18	R "2"	8x26	85' 1.62", 90' 1.5", 90' 1.62"	20.98	F01
East Coast	Narragansett Bay LWB	41.38	71.39	RW (NB) Mo (A)	9x35	315' all 1.5" - 2/15/00 1.5"	30.11	BUZM3
	Point Judith LWB	41.31	71.47	R "2"	8x26	170' all 1.5	38.06	BUZM3
	SW Ledge LWB	41.11	71.67	R "2"	9x35	180' all 1.5"	56.58	44017
	Jones Inlet LWB	40.56	73.59	RW "JI"	9X35	135' total. 1.75" chafe	130.77	44017
	Ambrose Channel	40.46	73.84	RW "A" Mo (A)	9x35	270' total, 1.5" chafe	153.33	44017
	NY Harbor S Approach	40.38	73.83	Y "B"	9x32	225' total, 1.75" chafe	154.32	44017
	Barnegat Inlet	39.74	74.06	R "2"	8x26	180' all 1.5"	152.67	44009
	Barnegat Inlet	39.76	73.99	R "2"	8x26	180' all 1.5"	157.00	44009
	Five Fathom Cape May	38.97	74.53	R "2FB"	8x26	180' all 1.5"	58.60	44009
	Cape Henlopen	38.77	75.02	RW (CH) Mo (A)	9x35	225' all 1.5"	44.29	44009
	Delaware Bay Approach	38.46	74.70	Y "D"	9x35	225' all 1.5"	0.00	44009

	Name	Location		USCG ATON Buoy		Chain Type / Length	Nearest Metocean Buoy	
		Lat (˚N)	Lon (˚W)	ATON Type	Hull Type		Dist. (km)	ID
	Chincoteague	38.00	75.02	R "6"	8x26	135' all 1.5" - inconsis. Data	58.29	44009
	Wimble Shoals	35.60	75.32	R "10"	8x26	350' all 1.5"	66.01	41025
	Cape Hatteras	35.15	75.29	R "12"	8x26	180' all 1.5"	18.51	41025
	Cape Lookout	34.30	76.40	R "14"	8x26	165' all 1.5"	120.83	41025
	Cape Fear Frying Pan	33.61	77.92	R "4FP"	8x26	180' all 1.5" - one measurement	25.21	41013
	Cape Canaveral Hetzel	28.64	80.35	R "8"	8x26	150' all 1.5" - poor data	20.55	41009
	West Palm Beach	26.77	80.01	RW "LW" Mo (A)	8x26	180' all 1.5"	195.40	41009
	Miami Beach	25.77	80.08	RW "M"	8x26	270' all 1.5"	305.98	41009
	Key West	24.46	81.80	RW "KW" Mo (A)	8x26	305' total, 1.5" chafe	423.84	42003
Carib	Mayaguez	18.16	67.34	R "8"	8x26	180' all 1.5"	1743.49	41009
Carib	Culebra Bajops Grampus	18.26	65.20	R "2"	8x26	180' all 1.5"	1905.27	41009
Carib	Sail Rock St. Thomas	18.28	65.11	G "1"	8x26	180' total, 1.5" chafe	1911.20	41009
G of Mex	St Andrews Bay	30.09	85.77	RW "SA"	8x26	135' all 1.5"	151.90	42039
G of Mex	Mobile Bay	30.13	88.07	RW "M" Mo (A)	8x26	180' of 1.5"	252.35	42039
G of Mex	Galveston Approach	29.18	94.46	RW "GA" Mo (A)	8x26	135' all 1.5"	7.38	42035
G of Mex	Matagorda Ship Channel	28.20	96.09	RW "MSC" Mo (A)	8x26	225' all 1.5" - two measurements	79.45	42019
G of Mex	Brownsville Channel	26.07	97.11	RW "BS" Mo (A)	8x26	180' of 1.5" - one measurement	108.45	42020
West Coast	San Diego	32.62	117.25	RW "SD" Mo (A)	8x26	270' total, 1.75" chafe	74.52	46086
West Coast	Pt. Buchon	35.24	120.91	R "16"	9x35	440' total, 1.75" chafe	27.66	46011
West Coast	Cypress Point	36.58	121.99	R "22"	8x26	340' total, 1.75" chafe - good rec.	48.76	46042
West Coast	Pt. San Pedro	37.47	122.51	RW "PP" Mo (A)	8x26	260' total, 1.75 chafe	34.89	46012
West Coast	San Francisco	37.75	122.69	RW "SF" Mo (A)	9x35	520' total, 1.75" chafe	13.23	46026
West Coast	Noyo Approach	39.43	123.83	RW "NA" Mo (A)	9x35	325' total, 1.75 chafe - poor rec.	24.32	46014

	Name	Location		USCG ATON Buoy		Chain Type / Length	Nearest Metocean Buoy	
		Lat (˚N)	Lon (˚W)	ATON Type	Hull Type		Dist. (km)	ID
	Columbia River	46.18	124.18	RW "CR" Mo (A)	9x35	483' total, 1.88 chafe	25.51	46029
	Cape Flattery Duntze	48.41	124.75	R "2"	9x35	760' total, 1.88 chafe	9.02	46087
AK	Kulichkof Rock	57.00	135.45	R "2"	8x26	85' 1.62", 90' 1.5", 90' 1.62"	59.54	46084
AK	Khaz Breaker	57.52	136.13	R "2"	9x35	360' all 1.5 (but used 1.75")	102.32	46084
AK	Yakutat	59.53	139.95	R "2"	9x35	270' of 1.75" 90' 1.5" riser	182.36	46083
AK	Egg Island (Cordova)	60.29	145.72	RW "EI" Mo (A)	8x26	225' all 1.5" often mudded in	61.59	46061
HI	Honolulu	21.28	157.88	RW "H" Mo (A)	9x35	230' of 1.5, 165' of 5.5"C nylon	357.30	51003
HI	Kaneohe Bay	21.52	157.80	RW "K" Mo (A)	8x26	270' of 1.5", bot 90' 1.12" Screwy record	380.54	51003
Pac	Taema Bank	14.67	170.67	G "1"	8x26	132' all 1.5"	1190.20	51003
Pac	Tanapag Harbor	15.20	145.67	R "T"	8x26	225' all 1.5", end-for-end 2012	765.80	51004

Table 57 USCG ATON Buoys: Water Characteristics

	Name	Bottom Type	Water Depth (m)		50th Percentile from Wave Scatter Table	
			Actual	Simulated	Tmod, s	Hsig, m
Northern New England	3-fathom ledge	rock	21.9	20	4.75	0.54
Northern New England	Wooden Ball Island	rock	44.2	40	4.75	0.54
Northern New England	PenBay East LWB "PBA"	mud	55.8	60	4.75	0.54
Northern New England	Manana Island LWB 14M	mud	88.4	90	4.60	1.23
Northern New England	Boston Lighted Buoy B	mud	30.8	30	4.90	0.73
Northern New England	Portland LWB P	mud	44.2	40	5.25	0.87
Northern New England	Boon Island Ledge LWB 22A	rock	31.1	30	5.25	0.87
Northern New England	Buzzards Bay Mid Channel LBB	mud	17.1	20	4.53	0.92
Northern New England	Sakonnet River LWB SR	rock	22.6	20	4.53	0.92
Northern New England	Marshall Point	rock	33.8	30	4.75	0.54
East Coast	Narragansett Bay LWB	mud	32.9	30	4.53	0.92
East Coast	Point Judith LWB	mud	19.8	20	4.53	0.92
East Coast	SW Ledge LWB	sand	17.7	20	4.87	1.15
East Coast	Jones Inlet LWB	sand	11.0	10	4.87	1.15
East Coast	Ambrose Channel	mud	22.9	20	4.87	1.15
East Coast	NY Harbor S Approach	mud	20.1	20	4.87	1.15
East Coast	Barnegat Inlet	mud	21.3	20	5.05	1.05

	Name	Bottom Type	Water Depth (m)		50th Percentile from Wave Scatter Table	
			Actual	Simulated	Tmod, s	Hsig, m
	Barnegat Inlet	mud	21.3	20	5.05	1.05
	Five Fathom Cape May	mud	19.8	20	5.05	1.05
	Cape Henlopen	mud	27.4	30	5.05	1.05
	Delaware Bay Approach	sand	28.3	30	5.05	1.05
	Chincoteague	sand	16.5	20	5.05	1.05
	Wimble Shoals	sand	31.4	30	5.06	1.25
	Cape Hatteras	sand	18.9	20	5.06	1.25
	Cape Lookout	sand	29.9	30	5.06	1.25
	Cape Fear Frying Pan	sand	18.9	20	4.97	1.15
	Cape Canaveral Hetzel	shells	26.5	30	5.14	1.06
	West Palm Beach	sand	25.9	30	5.14	1.06
	Miami Beach	rock	39.0	40	5.14	1.06
	Key West	sand	35.1	40	4.67	0.96
Carib	Mayaguez	sand	15.8	20	5.14	1.06
Carib	Culebra Bajops Grampus	sand	21.6	20	5.14	1.06
Carib	Sail Rock St. Thomas	mud	27.4	30	5.14	1.06
G of Mex	St Andrews Bay	sand	19.8	20	4.37	0.91
G of Mex	Mobile Bay	sand	18.3	20	4.37	0.91
G of Mex	Galveston Approach	mud	16.8	20	4.26	0.87
G of Mex	Matagorda Ship Channel	mud	27.7	30	4.65	1.12
G of Mex	Brownsville Channel	sand	14.0	10	4.72	1.15
West Coast	San Diego	gravel	31.7	30	6.79	1.38
West Coast	Pt. Buchon	gravel	45.1	50	7.01	1.89
West Coast	Cypress Point	shells	39.0	40	7.15	2.02
West Coast	Pt. San Pedro	shells	35.7	40	7.07	1.92
West Coast	San Francisco	sand	33.5	30	7.00	1.69
West Coast	Noyo Approach	rock	45.1	50	7.10	2.19
West Coast	Columbia River	sand	61.0	60	6.68	2.01
West Coast	Cape Flattery Duntze	rock	93.3	90	7.16	1.81
AK	Kulichkof Rock	rock	43.3	40	6.59	2.28
AK	Khaz Breaker	rock	43.9	40	6.59	2.28
AK	Yakutat	rock	43.0	40	6.40	2.06
AK	Egg Island (Cordova)	mud	22.9	20	6.06	1.27
HI	Honolulu	sand	95.1	100	6.42	2.07
HI	Kaneohe Bay	coral	37.5	40	6.42	2.07
Pac	Taema Bank	coral	25.6	30	6.42	2.07
Pac	Tanapag Harbor	coral	32.9	30	6.20	2.23

Table 58 USCG ATON Buoys: Hydrology Characteristics

Name		Temperature (Degr C)		Salinity (g/kg)	Oxygen (ml/l)	Silicate (umol/kg)	Nitrate (umol/kg)	Phosphate (umol/kg)
		50 Perc	Mean					
Northern New England	3-fathom ledge	9.36	Unknown	31.10	6.77	6.06	2.92	0.60
	Wooden Ball Island	9.36	Unknown	30.77	6.74	6.08	2.89	0.60
	PenBay East LWB "PBA"	9.36	Unknown	31.10	6.77	6.06	2.92	0.60
	Manana Island LWB 14M	10.83	Unknown	32.02	6.80	5.94	2.89	0.61
	Boston Lighted Buoy B	9.40	10.00	31.63	Unknown	Unknown	Unknown	Unknown
	Portland LWB P	9.40	9.60	31.20	6.61	5.74	2.67	0.58
	Boon Island Ledge LWB 22A	9.40	9.60	31.10	Unknown	Unknown	Unknown	Unknown
	Buzzards Bay Mid Channel LBB	12.30	12.00	31.77	Unknown	Unknown	Unknown	Unknown
	Sakonnet River LWB SR	12.30	12.00	31.77	Unknown	Unknown	Unknown	Unknown
	Marshall Point	9.36	Unknown	30.77	6.74	6.08	2.89	0.60
East Coast	Narragansett Bay LWB	12.30	12.00	31.79	Unknown	Unknown	Unknown	Unknown
	Point Judith LWB	12.30	12.00	31.79	Unknown	Unknown	Unknown	Unknown
	SW Ledge LWB	12.00	12.80	32.03	6.19	3.20	2.14	0.46
	Jones Inlet LWB	12.00	12.80	30.31	Unknown	Unknown	Unknown	Unknown
	Ambrose Channel	12.00	12.80	30.00	Unknown	Unknown	Unknown	Unknown
	NY Harbor S Approach	12.00	12.80	30.00	Unknown	Unknown	Unknown	Unknown
	Barnegat Inlet	14.40	14.50	31.47	Unknown	Unknown	Unknown	Unknown
	Barnegat Inlet	14.40	14.50	31.47	Unknown	Unknown	Unknown	Unknown
	Five Fathom Cape May	14.40	14.50	32.10	5.96	3.63	1.40	0.38
	Cape Henlopen	14.40	14.50	31.80	Unknown	Unknown	Unknown	Unknown
	Delaware Bay Approach	14.40	14.50	32.22	5.81	3.51	1.28	0.36
	Chincoteague	14.40	14.50	31.11	5.64	3.66	1.05	0.33
	Wimble Shoals	22.60	22.10	32.59	4.91	2.26	0.50	0.20
	Cape Hatteras	22.60	22.10	34.17	4.84	2.03	0.43	0.17
	Cape Lookout	22.60	22.10	35.07	4.79	2.01	0.38	0.14
	Cape Fear Frying Pan	23.00	22.80	35.05	4.75	2.31	0.32	0.12
	Cape Canaveral Hetzel	25.30	25.20	36.05	4.69	2.48	0.36	0.12
	West Palm Beach	25.30	25.20	36.03	4.67	1.96	0.35	0.10
	Miami Beach	25.30	25.20	36.12	4.67	2.14	0.44	0.09
	Key West	27.20	27.10	36.00	4.81	2.17	1.36	0.08
Carib	Mayaguez	25.30	25.20	35.66	4.65	2.10	0.62	0.06
	Culebra Bajops Grampus	25.30	25.20	35.66	4.66	1.82	0.65	0.05
	Sail Rock St. Thomas	25.30	25.20	35.66	4.66	1.82	0.65	0.05
G of Mex	St Andrews Bay	24.80	25.00	34.40	5.19	1.83	1.58	0.10
	Mobile Bay	24.80	25.00	32.97	5.22	1.91	1.61	0.19
	Galveston Approach	23.40	22.80	31.99	3.60	1.97	0.97	0.23
	Matagorda Ship Channel	25.10	25.00	34.05	4.64	1.50	0.84	0.19

Name		Temperature (Degr C)		Salinity (g/kg)	Oxygen (ml/l)	Silicate (umol/kg)	Nitrate (umol/kg)	Phosphate (umol/kg)
		50 Perc	Mean					
	Brownsville Channel	25.10	24.80	34.68	4.99	1.12	0.80	0.18
West Coast	San Diego	17.10	17.40	Unknown	Unknown	Unknown	Unknown	Unknown
	Pt. Buchon	13.70	13.80	33.44	5.89	3.57	1.48	0.44
	Cypress Point	12.90	13.10	33.29	5.95	5.30	2.98	0.57
	Pt. San Pedro	13.00	13.10	33.16	5.98	6.24	3.77	0.64
	San Francisco	12.40	12.50	33.16	5.98	6.24	3.77	0.64
	Noyo Approach	11.90	12.00	32.95	6.04	6.63	3.88	0.69
	Columbia River	12.00	12.10	29.91	6.27	11.29	3.60	0.69
	Cape Flattery Duntze	10.20	10.20	30.33	6.36	16.52	5.79	0.95
AK	Kulichkof Rock	8.80	9.40	30.99	6.77	22.85	9.19	1.14
	Khaz Breaker	8.80	9.40	31.09	Unknown	Unknown	Unknown	Unknown
	Yakutat	9.60	9.70	30.87	6.98	24.63	9.85	1.15
	Egg Island (Cordova)	7.90	8.60	Unknown	Unknown	Unknown	Unknown	Unknown
HI	Honolulu	26.30	26.30	34.93	Unknown	Unknown	Unknown	Unknown
	Kaneohe Bay	26.30	26.30	34.93	Unknown	Unknown	Unknown	Unknown
Pac	Taema Bank	26.30	26.30	34.49	4.67	1.44	0.09	0.13
	Tanapag Harbor	25.50	25.50	34.52	4.89	2.28	0.28	0.20

Table 59 Abrasion Records for USCG ATON Buoys

	Name	Abrasion Loss Rate (in/yr)		
		Mean	S.D.	# Samples
Northern New England	3-fathom ledge	0.23	0.07	2
	Wooden Ball Island	0.35	n/a	1
	PenBay East LWB "PBA"	0.15	0.06	3
	Manana Island LWB 14M	0.38	n/a	1
	Boston Lighted Buoy B	0.13	0.00	2
	Portland LWB P	0.14	0.06	3
	Boon Island Ledge LWB 22A	0.12	n/a	1
	Buzzards Bay Mid Channel LBB	0.13	0.11	2
	Sakonnet River LWB SR	0.09	0.04	2
East Coast	Marshall Point	0.18	0.09	3
	Narragansett Bay LWB	0.16	0.01	4
	Point Judith LWB	0.17	n/a	1
	SW Ledge LWB	0.13	0.05	4

	Name	Abrasion Loss Rate (in/yr)		
		Mean	S.D.	# Samples
Carib	Jones Inlet LWB	0.16	0.04	5
	Ambrose Channel	0.12	0.04	4
	NY Harbor S Approach	0.14	0.04	4
	Barnegat Inlet	0.18	0.08	3
	Barnegat Inlet	0.18	0.08	3
	Five Fathom Cape May	0.18	0.10	3
	Cape Henlopen	0.05	0.01	2
	Delaware Bay Approach	0.02	n/a	1
	Chincoteague	0.20	n/a	1
	Wimble Shoals	0.28	0.03	4
	Cape Hatteras	0.21	0.02	2
	Cape Lookout	0.22	0.02	2
	Cape Fear Frying Pan	0.18	n/a	1
	Cape Canaveral Hetzel	0.15	0.03	2
	West Palm Beach	0.09	0.01	3
	Miami Beach	0.12	0.06	3
	Key West	0.14	0.04	3
	Mayaguez	0.12	0.04	4
	Culebra Bajops Grampus	0.13	0.05	5
	Sail Rock St. Thomas	0.15	0.02	4
G of Mex	St Andrews Bay	0.12	0.05	2
	Mobile Bay	0.12	0.01	2
	Galveston Approach	0.26	0.18	2
	Matagorda Ship Channel	0.24	0.14	2
	Brownsville Channel	0.22	n/a	1
West Coast	San Diego	0.23	0.14	2
	Pt. Buchon	0.14	0.04	4
	Cypress Point	0.81	0.46	4
	Pt. San Pedro	0.19	0.05	3
	San Francisco	0.15	0.04	5
	Noyo Approach	0.17	0.10	4
	Columbia River	0.20	n/a	1

	Name	Abrasion Loss Rate (in/yr)		
		Mean	S.D.	# Samples
AK	Cape Flattery Duntze	0.10	n/a	1
AK	Kulichkof Rock	0.10	n/a	1
AK	Khaz Breaker	0.18	n/a	1
AK	Yakutat	0.07	0.04	5
AK	Egg Island (Cordova)	0.11	0.06	3
HI	Honolulu	0.22	0.18	4
HI	Kaneohe Bay	0.28	0.05	3
Pac	Taema Bank	0.14	0.10	4
Pac	Tanapag Harbor	0.13	0.07	3

APPENDIX 2. CASE STUDY DETAILS

A2.1. Static offset tests

The platform model was given an initial offset in x and y directions, and the mooring line tension were measured. A plot of tension vs. offset provides the restoring force characteristics of the mooring system. Figures 7 and 8 show the comparison of mooring line restoring force in x and y direction between OrcaFlex+FAST simulations, Charm3D+FAST simulations and experimental results. Offset values are incremented by 5 m in accordance with experiments. The simulation results are in good agreement with each other, and show good agreement with experimental results for lines 2 and 3. Tensions measured from simulations of line 1 are slightly larger than the tests. Since line 1 is collinear with the x-axis, it is heavily loaded and displays strong nonlinearity in the simulation, which was not captured in the experiments. The modified stiffness of mooring line, 581.6 ×103 kN, is applied to coupled Charm3D+FAST module to fit the static offset test, while the experimental mooring line consists of a linear spring located at the anchor. In addition, the mooring line drag coefficient, 2.4, recommended by DNV (2010) for stud-less chain is applied to the OrcaFlex+FAST and the Charm3D+FAST model.

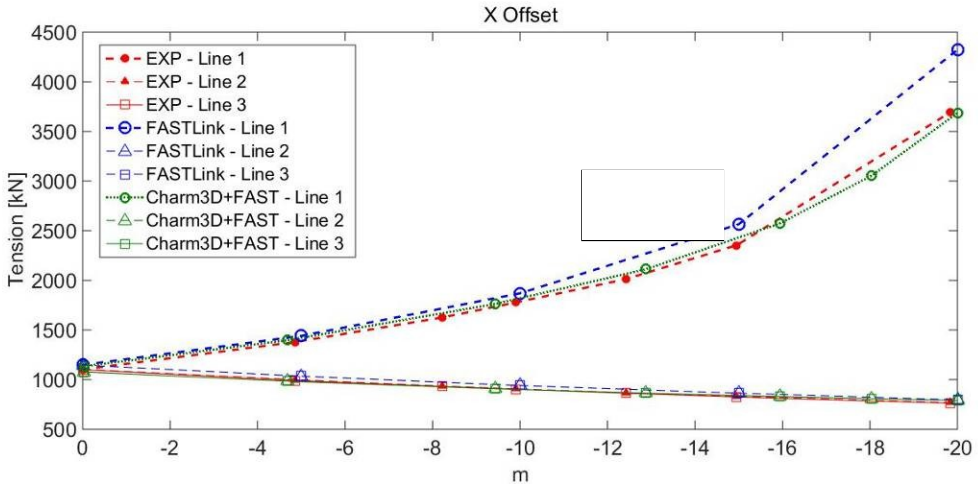

Figure 7 Comparison of mooring line restoring force in x direction between OrcaFlex+FAST, Charm3D+FAST and test data

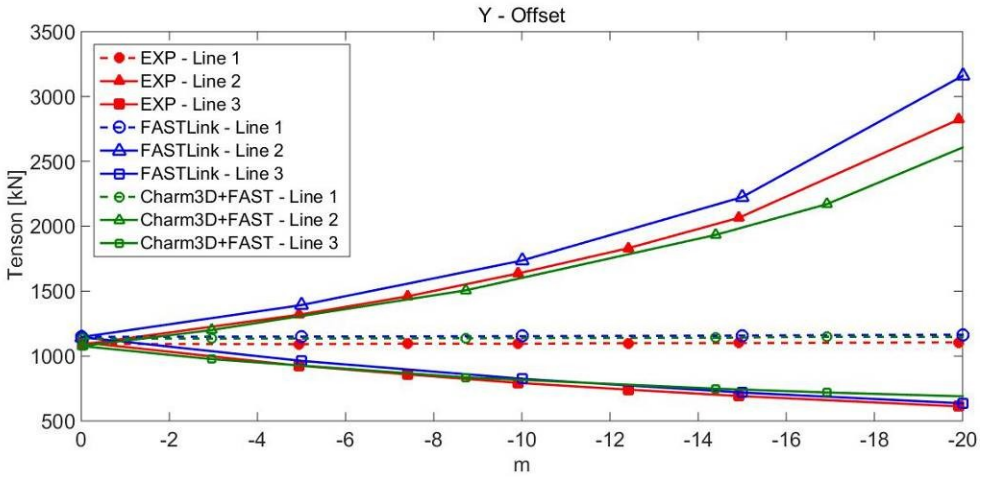

Figure 8 Comparison of mooring line restoring force in y direction between OrcaFlex+FAST, Charm3D+FAST and test data.

A2.2. White Noise Tests and Response Amplitude Operators (RAO)

The RAO of a floating platform in a degree of freedom describes the response amplitude per unit wave amplitude as a function of wave frequency. In regular wave tests, several regular waves of different frequencies are applied to the structure and the latter's responses are measured. This method is applied to the Charm3D+FAST model. Seventeen simulations with several different wave periods range from 5 to 25 s and every simulation's duration is 500 seconds.

The RAO is:

$$R_i = M_i/H_i \text{ , for } i = 1, 2, \dots, N \qquad (1)$$

Where $R_i$is the RAO, M_i is the response of the structure, H_i is the regular wave ampitude and the index $i = 1, 2, \dots, N$ denotes the components at regular frequencyf_i, here N=17.

Alternatively, a random wave condition based on a white noise spectrum is applied to the structure to obtain responses at various frequencies simultaneously. The latter approach is adopted in the experiments, and was mimicked in OrcaFlex+FAST. The white noise power spectral density (PSD) given by Si has energy spread evenly over the frequency range from 0.033 to 0.25 Hz (period 4 – 30 s). The RAO is then calculated as

$$R_i = (P_i/S_i)^{\frac{1}{2}} \text{, for } i = 1, 2, \dots, M/2 \qquad (2)$$

The PSD of the structure is Pi, and the index $i = 1, 2, \dots, M/2$ denotes the components at frequencies f_i, which are integer multiples of the FFT's fundamental frequency.

Figures 9 - 11 show the comparison of the RAOs in surge, heave and pitch motions respectively. These RAOs are obtained without wind effects but include the three mooring lines for model tests and simulation tests. Both surge and heave RAOs show good agreement between experimental data and simulation results. For pitch RAO, there is excellent agreement for period range from 5 to 14 s, beyond which the simulations agree with each other, and consistently

differ with experiments. This is likely due to decrease in wave amplitude at lower frequencies (approaching the end of the white noise spectrum) in experiments which leads to an artificially higher RAO (division by a small number).

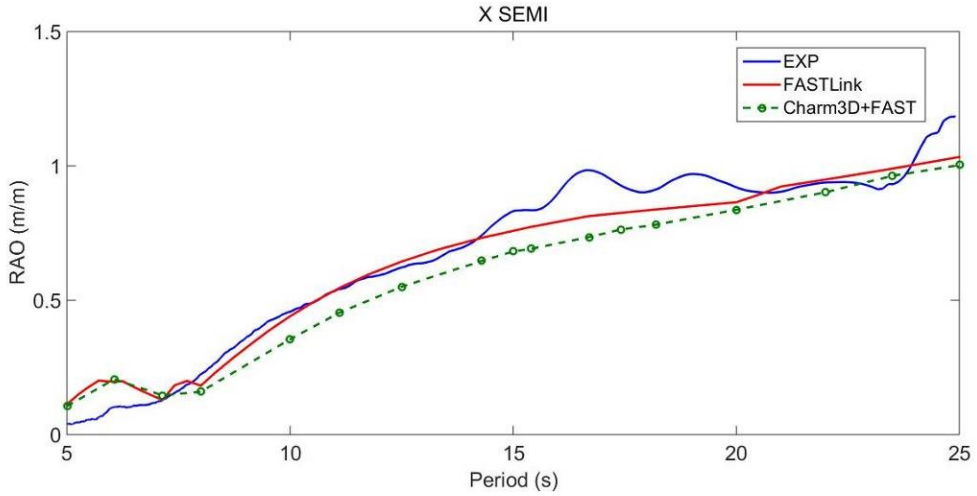

Figure 9 Comparison of RAO in surge between OrcaFlex+FAST, Charm3D+FAST and test data

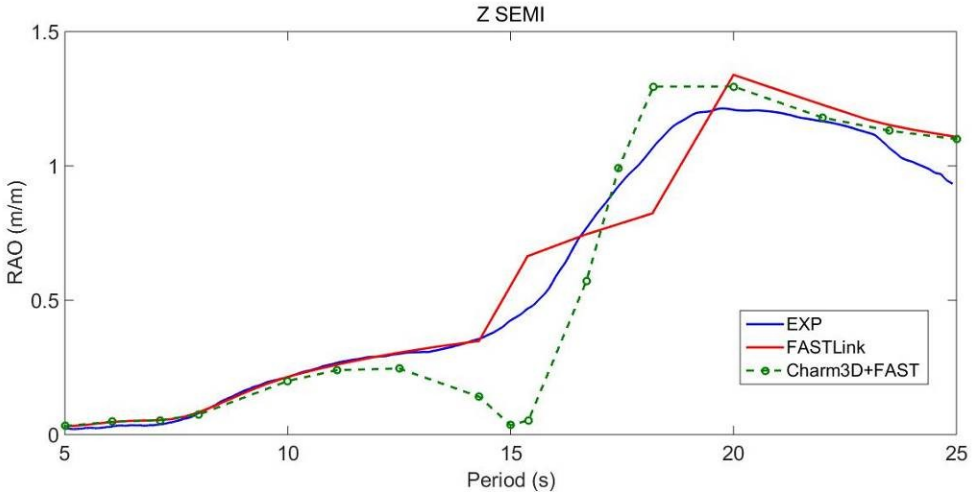

Figure 10 Comparison of RAO in heave between OrcaFlex+FAST, Charm3D+FAST and test data

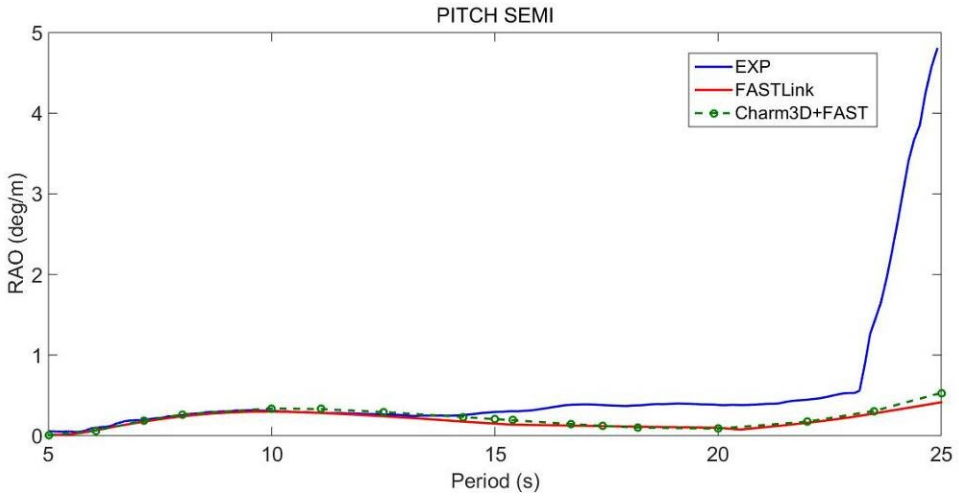

Figure 156 Comparison of RAO in pitch between OrcaFlex+FAST, Charm3D+FAST and test data

A2.3. Natural period, damping and free decay tests

For the semi-submersible platform, flow separation induced drag is a large component of the total hydrodynamic damping. However, OrcaFlex and Charm3D+FAST use potential flow theory to model the hydrodynamics forces, which defines the radiation loads for structures without viscous effects. As such, the linear radiation damping was augmented with a viscous damping model. The platform viscous damping and linear damping are replaced by the equivalent linear viscous damping.

$$B_{eqij} = B_{1ij} + B_{2ij}\frac{8}{3\pi}A_{ij}\omega_{ij}, \qquad i,j = 1,2,\cdots 6$$

Where B_{eqij} are the equivalent linear viscous damping coefficients, B_{1ij} and B_{2ij} are the linear and quadratic damping coefficients, A_{ij} are amplitudes and ω is the frequency. B_{1ij} and B_{2ij} were determined via the platform motion free-decay tests. The values for the equivalent damping coefficients were evaluated and applied to the OrcaFlex+FAST and Charm3D+FAST simulations.

Figure 157, Figure 158 and Figure 159 show the comparison of free decay in three directions between basin tests and simulations. The natural periods of surge, heave and pitch are calculated for both experimental results and OrcaFlex+FAST simulation, and show good agreement. The difference of natural period in heave of OrcaFlex+FAST and basin tests and of Charm3D+FAST and basin tests are 0.56% and 0.57% respectively. The difference of the pitch natural period of OrcaFlex+FAST and basin test and of Charm3D+FAST and basin tests are 0.37% and 2.23% respectively. There is 2.7% difference of natural period in surge motion between test results and OrcaFlex+FAST simulation, and 7.01% difference of natural period in surge motion between test results and Charm3D+FAST. In Figures 11 and 12, the simulations decay quicker than the tests. This is possible because the simulation use linear damping which overestimates the damping at lower amplitude motions.

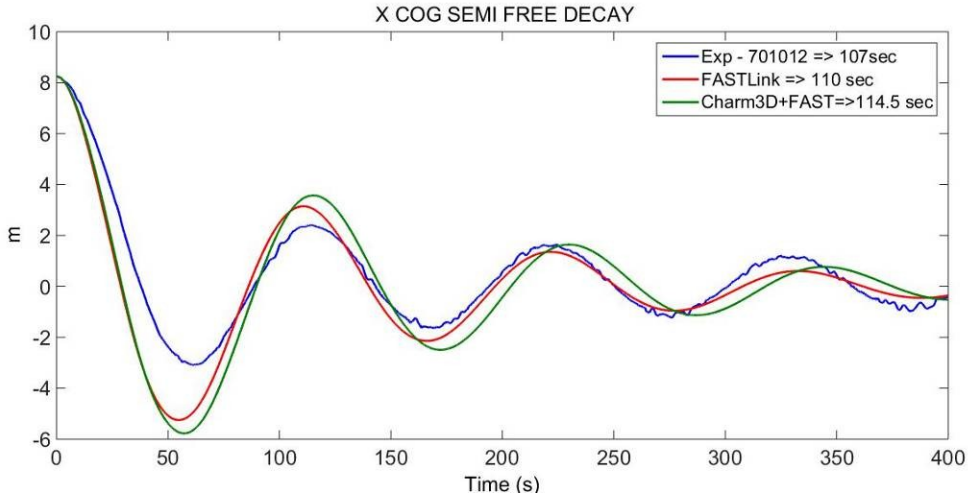

Figure 157 Comparison of free decay in surge between OrcaFlex+FAST (FASTLink), Charm3D+FAST and test data

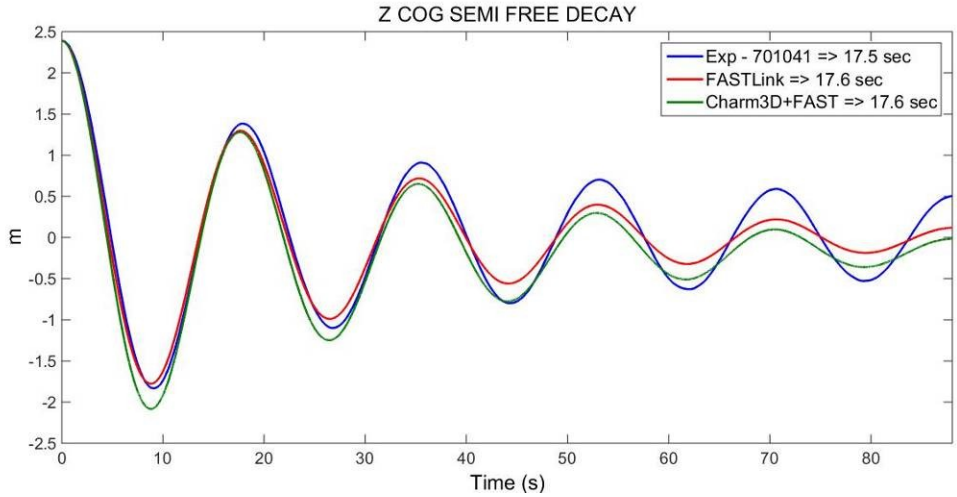

Figure 158 Comparison of free decay in heave between OrcaFlex+FAST (FASTLink), Charm3D+FAST and test data

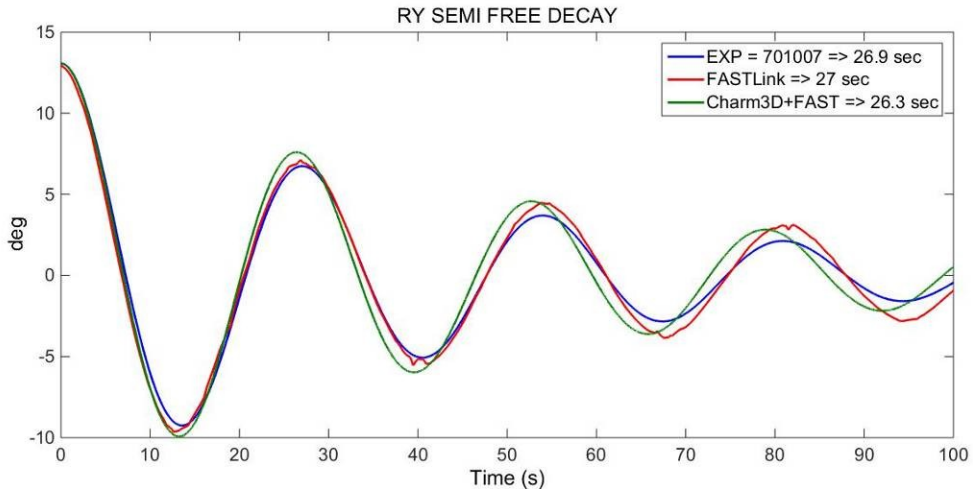

Figure 159 Comparison of free decay in pitch between OrcaFlex+FAST (FASTLink), Charm3D+FAST and test data